1998

Performance of a Boussinesq model for shoaling and breaking waves : a comparison with large scale laboratory data

Ozanne, Francoise

Performance of a Boussinesq Model for Shoaling and Breaking Waves

A comparison with large scale laboratory data.

Françoise Ozanne

A thesis submitted to the University of Plymouth
in partial fulfilment for the degree of

Doctor of Philosophy

School of Civil and Structural Engineering
Faculty of Technology

November 1998

Copyright Statement

This copy of the thesis has been supplied on condition that anyone who consults it is understood to recognise that its copyright rests with its author and that no quotation from the thesis and no information derived from it may be published without the author's prior consent.

Performance of a Boussinesq model for Shoaling and Breaking Waves
A comparison with large scale laboratory data
Françoise Ozanne

ABSTRACT

In this thesis, a nonlinear model predicting hydrodynamics data for waves shoaling and breaking on a beach is reproduced and extensively tested with laboratory data. The model is based on the 1D Boussinesq equations as derived by Madsen *et al.* (1991) and Madsen and Sørensen (1992), with the free surface elevation and the depth-integrated velocity as variables. It allows slowly varying bathymetries and contains additional high order terms to improve the frequency dispersion for shorter wave periods, and thus also to improve the shoaling properties of the model. Wave breaking is modelled using the concept of a surface roller as formulated by Schäffer *et al.* (1993). It is assumed that bottom friction is negligible. A large scale laboratory experiment (Supertank), designed in particular to obtain data to test the validity of wave propagation models, provides the wave and current data. Wave evolution over a complex bathymetry is examined for 4 cases. The data include conditions for long and short waves, and regular and irregular waves.

During the model evaluation, emphasis is put on the study of parameters of importance to sediment transport, including (orbital) velocity, undertow and wave shape prediction. The latter encompasses velocity and elevation skewness, kurtosis and asymmetry. It is found that, despite an overestimation of the depth-averaged horizontal velocity in some cases, the predicted velocity moments and undertow are in good agreement with the data. Using a bispectral analysis, it is shown that the nonlinear transfers of energy amongst the low order harmonics are well reproduced, but that errors are introduced in the treatment of the high order super-harmonics. As a result, the short waves tests are found to yield better results than those for long waves. A sensitivity analysis on the free parameters introduced in the simulation of wave breaking is carried out. It appears that the results are mostly sensitive to the critical wave front slope ϕ_B , and in particular that the elevation and velocity skewness and kurtosis predictions are very sensitive to this parameter.

LIST OF CONTENTS

LIST OF SYMBOLS

a_i amplitude of the i*th* harmonic
a typical wave amplitude
A_η total elevation asymmetry
A_U total velocity asymmetry
A_f complex Fourier coefficient
$b(f_1, f_2)$ bicoherence estimate
$B(f_1, f_2)$ bispectral estimate
B frequency dispersion parameter
c phase velocity
C_r Courant number
d total water depth ($=h+\eta$)
$E[\,]$ expected value or average operator
f wave frequency
f_p frequency of spectral peak
f_N Nyquist frequency
f_δ surface roller shape parameter
FBL length of the flat bed section seaward of the slope
g gravitational constant ($=9.81 m/s^2$)
h still water depth
$Hrms$ root mean square wave height
$Hmax$ maximum wave height
k wave number ($=2\pi/L$)
K_η elevation kurtosis
K_U velocity kurtosis
L wave length
L_r beat length due to interactions between first and second harmonics
mwl mean water level
M momentum flux
p pressure
sponge layer constant
P depth-integrated velocity, or volume flux
$P(f_j)$ power spectral estimate
S beach slope parameter ($=h_x L/h$)
S_η total elevation skewness
S_U total velocity skewness
T wave period
T_p peak wave period
t_B time at which wave breaking is initiated
t time
t^* rate of decay parameter
u horizontal velocity in x-direction
u_o core horizontal velocity in x-direction
$\overline{u}$ depth-averaged velocity
U mean current in x-direction
$\hat{U}max_{on}$ mean maximum onshore depth-averaged velocity
$\hat{U}max_{off}$ mean maximum offshore depth-averaged velocity
$\hat{U}_{on}$ mean onshore depth-averaged velocity

U_{off}	mean offshore depth-averaged velocity
U_r	Ursell number
w	vertical velocity component
x	horizontal co-ordinate
z	vertical co-ordinate
α	shoaling coefficient (sec. 3.3.4)
	filter coefficient (sec. 3.5.5)
$\beta(f_1, f_2)$	biphase
δ	roller thickness
$\bar{\delta}$	mean roller thickness
Δx	spatial increment
Δt	temporal increment
ε	nonlinearity parameter ($= a/h$)
ϕ	breaking wave critical wave front slope
ϕ_B	initial angle
ϕ_o	terminal angle
η	free surface elevation
μ	dispersion parameter ($= (h/L)^2 \approx h/(gT^2)$)
μ_i	sponge layer parameter
μ_{max}	sponge layer constant
ν	kinematic viscosity
ρ	fluid density
swl	still water level
mwl	mean water level

LIST OF TABLES

LIST OF FIGURES

Figure 6.3c Effect of profile smoothing on the cross-shore variation of the observed and predicted elevation skewness S_η (left column) and elevation asymmetry A_η (right column) estimated from the bispectral analysis. For runs B1 (top panels), and B2 (bottom panels).

Figure 6.3d Effect of profile smoothing on the cross-shore variation of the observed and predicted velocity skewness S_U (left column) and velocity asymmetry A_U (right column) estimated from the bispectral analysis. For runs B1 (top panels), and B2 (bottom panels).

Figure 6.4a Predicted and observed A_η (top raw) and A_U (bottom raw) *versus* ε (left column) and *versus* μ (right column). $\phi_B = 20°$, all four runs are plotted for each gauges.

Figure 6.4b (top plot) predicted and observed S_η and A_η as a function of Ur. (bottom plot). Predicted and observed S_U and A_U as a function of Ur. $\phi_B = 20°$, all four runs are plotted for each gauges/current meter arrays. The plain lines are the parameterization proposed by Doering and Bowen (1995).

Figure 6.5 Dimensional real (left panels) and imaginary (right panels) parts of the bispectrum, run A1, gauge 13 (just before breaking). The top panels are the model predictions, the bottom panels are the observations. Note that the imaginary part has been multiplied by a factor of -1.

Figure 6.6 Same as Figure 6.5, gauge 19.

Figure 6.7 Identification of the 12 triads selected for investigation. The dotted lines indicate the integration limits for each single wave triad.

Figure 6.8 Spatial evolution of the normalised contributions to skewness for a selection of 12 triads, run A1. Also shown are the total skewness (panel (1,1)), and the skewness arising from wind-wave frequencies only (panel (1,2)).

Figure 6.9 Spatial evolution of the normalised contributions to asymmetry for a selection of 12 triads, run A1.

Figure 6.10 Spatial variation of the skewness of a standing wave field consisting of two harmonics with amplitudes 0.3m and 0.15m. $T = 8$s, $L = 50$m.

Figure 6.11 Predicted *versus* observed normalised contributions to skewness for a selection of 12 triads, for the 4 studied cases. Also shown is the total skewness (panel (1,1)). $\phi_B = 20°$.

Figure 6.12 Predicted *versus* observed normalised contributions to skewness from (left column) low order interactions, and (right column) high order interactions, for the 4 studied cases. (top panels) $\phi_B = 17°$, (middle panels) $\phi_B = 20°$, (bottom panels) $\phi_B = 26°$.

Figure 6.13 Predicted *versus* observed normalised contributions to asymmetry for a selection of 12 triads, for the 4 studied cases. Also shown is the total skewness (panel (1,1)). $\phi_B = 20°$.

Acknowledgements

I would like to thank my supervisors; **Andrew Chadwick**, in the Civil Engineering department, University of Plymouth, for his support and encouragement; **David Huntley**, at the Institute of Marine Studies, University of Plymouth, for his approachability, interest and guidance, and for stimulating discussions; and **David Simmonds**, in the Civil Engineering department, University of Plymouth, for many helpful discussions and advice, and for providing the bispectral analysis program.

I would also like to extend my sincere thanks to **Dr A. G.L. Borthwick**, Department of Engineering Science, Oxford University, and **Prof C.A. Fleming**, Sir William Halcrow and Partners, for agreeing to be my examiners and for the detailed attention given to the thesis.

I extend my thanks to **Michael Brorsen**, in the Civil Engineering department, Aalborg University, for his invaluable help with the implementation of the model, and to **Jane McKee Smith**, USACE Waterways Experiment Station, for kindly providing the Supertank data.

I would also like to express my thanks to my colleagues in the Civil Engineering department, University of Plymouth, in particular **Suzana Ilic**, whose library introduced me to the world of numerical modelling.

I am grateful to **Andy McMullin**, at the Business School, and **Mark Flamank**, at the School of Computing, University of Plymouth, for their efficient and altruistic assistance, in particular for providing me with access to an FTP site and UNIX workstations.

Finally, my special thanks go to Jason, for his support, care and patience and my parents, pour leur encouragement, devouement et leur confiance en moi.

Author's declaration

The work described in this thesis was carried out in the School of Civil and Structural Engineering at the University of Plymouth. At no time during the registration for the degree of Doctor of Philosophy has the author been registered for any other University award. All the material described herein is the original work of the author unless otherwise acknowledged.

This study was financed with the aid of the University of Plymouth.

A programme of advanced study was undertaken, which included attendance at two short courses and a two month sabbatical to Aalborg University, Denmark, as a visitor researcher. The SCSE and IMS seminars and the three conferences detailed below were attended.

Courses attended: Coastal Engineering and Shoreline management, University of Plymouth, Sept. 95.

Waves and wave modelling (R. Dalrymple), Nonlinear waves (P. Liu and J. Kirby) and Field measurement techniques (E. Thornton), ICCE '96, Sept. 96.

Conferences attended: ICCE '96, Orlando

Coastal Dynamics '97, Plymouth

ICCE '98, Copenhagen (self-funded)

Publications: Ozanne F, Chadwick A.C., Huntley D.A. and McKee Smith J. (1997). Wave transformation in the nearshore zone: comparison between a nonlinear model and large scale laboratory data. *Coastal Dynamics '97*, ASCE, 295-304.

External contacts: Michael Brorsen, Civil Eng. dept., Aalborg University, Denmark

Jane McKee Smith, USACE Waterways Experiment Station, USA

F. Ozanne

Françoise Ozanne

15 11 98

CHAPTER 1 INTRODUCTION

In the past twenty years, the progress made in the development of numerical models that simulate wave transformation in the nearshore zone has been considerable. This was made possible thanks to the parallel developments achieved in computing technology. Much of the interest in the development of these numerical models was motivated by the need for tools that provide hydrodynamic data for the design of, for example, offshore structures, harbours, and coastal defence schemes. Indeed, increased human activity and interest both in the open sea and in the coastal zone have resulted in increased needs for data for the design of such structures. Since there may be not enough time and/or money to carry out an adequate wave measurement programme as part of a design process, numerical and physical wave modelling techniques offer good alternatives. The development and testing of numerical models are therefore essential if the model is going to be used as part of the design process.

An important part of the tackling of coastal problems lies in the prediction of sediment transport in the nearshore zone. Sediment displacement is the result of short wave (orbital) motion, long wave motion and net flows, and the interactions between them. In particular, the net shoreward velocity, associated with wave skewness, and the return flow (or undertow), associated with wave-induced mass transport, play an essential part in the morphological dynamics of a beach. To further our understanding of the processes that change the coastlines, and thus be able to predict them, it is essential that the hydrodynamics of the surf zone be understood, and simulated accordingly.

As surface gravity waves shoal, the wave field undergoes a substantial evolution from its deep water state owing to weak frequency dispersion and consequent nonlinear triad interactions. The study of the transformations of wave spectra typically show that narrow band spectra develop secondary peaks at harmonics of the peak frequency and broadband spectra show an increase of energy over a wide range of frequencies higher than most of the energetic part of the spectrum (Elgar and Guza, 1985a). In other words, energy is (nonlinearly) transferred from the incident wind waves to both higher and lower frequencies. For the length scale considered here, these energy transfers are predominantly

the result of triad interactions, which may be described as an energy exchange between 3 interacting wave modes[1]. Nonlinear interactions between a pair of wave components with frequencies and wave numbers (f_1, k_1) and (f_2, k_2) theoretically force secondary waves with the sum and difference frequency and wave number ($f_1 \pm f_2$) and ($k_1 \pm k_2$) (super- and sub-harmonics respectively). Thus, in the frequency domain, nonlinearities may result in important cross-spectral energy transfer in relatively short distances, and a wave field for which the phase relationship between some of the Fourier components is no longer random (the Fourier components become coupled). In the time domain, higher harmonic generation and their interactions cause surface elevation and orbital velocity time series to become increasingly asymmetrical. The waves become asymmetrical with respect to the horizontal; they become steep, sharp crested with broad troughs. This is termed *skewness* (skewed profile). The waves also tend to become asymmetrical with respect to the vertical, i.e. pitched forward. This is termed *asymmetry* (asymmetric profile).

Nonlinear waves are quantified by non-zero third and higher order moments, that is a non-Gaussian distribution. The effect of wave shape changes on sediment transport has long been recognised. For example wave skewness in the surf zone is reflected in onshore velocities that are greater than the offshore velocities, and is generally thought to result in a net onshore sediment movement over a wave period. These effects have been incorporated in widely applied cross-shore sediment transport models based on the energetics approach developed by Bailard (1981), and modified by Guza and Thornton (1985). The later authors used field experiments to examine the relative significance of the velocity moments used in Bailard's model. They found that suspended and bed load transport are dominated by the third and fourth order moments respectively, or, in normalised form, the *skewness* and the *kurtosis*.

While there is no doubt that the skewness does affect sediment transport, the details of this relationship are not clear. The hypothesis that wave skewness results in net onshore movement is made assuming that sediment transport responds instantaneously to fluctuations in the near-bed velocity. However, the analysis of field data by Russell (1993) shows there may be a lag between a variation in the bed velocities and suspended sediment concentrations. This could result in offshore sediment transport instead of the expected onshore transport. Russell concluded that detailed time variation of flow velocities (not just

---

[1] Given the length scale necessary for tertiary waves forced by the interaction of three primary waves to develop, harmonic generation by weaker third order interactions is not investigated in this study.

wave-averaged quantities) are therefore likely to be required for (suspended) sediment transport predictions. This emphasises the importance of modelling wave skewness in order to get accurate predictions of sediment transport.

The undertow is another wave-induced process that is significant in the cross-shore sediment dynamics. It is defined as a seaward directed return flow which compensates for the shoreward directed mass flux above the wave trough level. It is driven by the local difference between the vertically non-uniform[2] shoreward directed component of radiation stresses and the vertically uniform offshore directed pressure gradient (due to set-up and run-up). The resulting vertical velocity profile is complex and depends upon the distribution of the turbulence under the waves. Model evaluations of the undertow may be found in e.g. Svendsen (1984b). This offshore flow is significant in sediment transport as it is recognised that it tends to carry sediment offshore, where a bar may form.

Given the complexity of the processes involved in the surf zone, the relationship between nonlinear nearshore hydrodynamics and consequent sediment dynamics is still mostly qualitative, but is nevertheless significant. The linear theory can therefore no longer be applied to the description of waves approaching the shoreline where the nonlinearities described above become significant or even dominant. High order wave theories or nonlinear models should thus be used to model wave motion in the final stages of shoaling and in the surf zone.

At the starting point of the development of models for the propagation of ocean surface waves are the Navier-Stokes equations, which adequately describe the motion of water for an incompressible fluid of constant density. It is only very recently that it has become possible to solve these equations directly (see e.g. Petit *et al.*, 1994). They are still very computationally demanding however, and the length of the computational domain is thus restricted. Various simplifications of the Navier-Stokes equations have been introduced, leading to various approximations. We are concerned here by approximations that (i) involve the integration over the depth of the Navier-Stokes equations, and (ii) retain some degree of nonlinearity, that is, shallow water waves models. The simplification of the problem by removing the vertical co-ordinate permits the treatment of a wider computational domain. Further assumptions may then be introduced that result in different

---

[2] Within the surf zone, gradients in the radiation stress that cause a shoreward directed mass-transport of water is confined to the region between the trough and crest levels.

systems of equations, with different applications. Thus, Airy (1845) derived the Nonlinear Shallow Water (NLSW) equations, applicable to non-linear non-dispersive waves. Boussinesq (1872) introduced the derivation of equations for weakly dispersive and weakly nonlinear waves travelling over a flat bed, the Boussinesq equations. The derivation of high order analytical solutions for nonlinear waves followed with the Korteweg-de Vries equations (Korteweg and de Vries, 1895).

The first steps towards the development of nonlinear wave theories were thus undertaken last century, but it was not until the late 60s, early 70s, when the rapid development of computers made numerical advances possible, that these theories were actually applied. Research in the development and application of the NLSW and Boussinesq equations has been continuous ever since. Much of the development of models based on the Boussinesq equations was spurred by the attraction of their capability to describe shoaling, refraction, diffraction, (partial) reflection, and, most importantly, wave-wave interactions. Indeed, the triad interactions responsible for the generation of harmonics are reproduced, and the wave shape evolution is therefore modelled. Results from a Boussinesq model were compared to a linear wave transformation model and field data by Elgar and Guza (1985a). They found that the Boussinesq model predicts the evolution of energy spectra more accurately than does the linear theory.

The classical Boussinesq equations describe the propagation of weakly dispersive and weakly nonlinear waves, that is fairly long waves in shallow water. Significant research accomplishments were made in the last 10 years, whereby emphasis has been placed on efforts to extend the applicability of the classical Boussinesq equations to shorter waves ('deeper' water) on one hand, and to the surf zone on the other hand. This extensive work has resulted in many different forms of the Boussinesq equations which have a different range of application, hence the term 'Boussinesq-type equations' used hereinafter. A detailed review of the developments achieved in wave modelling with the Boussinesq equations is given in chapter 2.

In the context of this study, the choice of a Boussinesq-type model was motivated by several aspects. First the models based on the most advanced equations are attractive in that they describe wave shoaling as well as wave breaking. Second, and not the least, the Boussinesq equations include (the lowest order of) nonlinearity and dispersion effects. They are thus

capable of simulating changes in the spectral shape and wave profile. Nonlinearity, reflected in vertical and horizontal asymmetry of the wave profile and velocity oscillations, was seen earlier to be a significant element in the prediction of sediment transport. The most immediate application of such models is thus the supply of hydrodynamic data necessary to drive sediment transport models. Lastly, previous studies have shown that this type of model yields good results for (i) first order surface elevation statistics, so that one can reasonably expect good results for velocity predictions, and (ii) wave shape in the shoaling zone for strictly weakly dispersive waves (Elgar and Guza, 1985a & b). Thus one can reasonably hope to obtain good results for higher order statistics in the surf zone.

The object of this thesis is to evaluate a Boussinesq-type model that predicts the hydrodynamics of waves shoaling and breaking on a beach by using large scale laboratory data. During this model evaluation, emphasis is put on the study of parameters of importance to sediment transport, including orbital velocities, undertow and wave shape predictions. The latter encompasses velocity and elevation skewness, kurtosis and asymmetry.

The organisation of this thesis is as follows: in Chapter 2, we shall survey the various developments, validations and applications of Boussinesq-type models. This chapter also identifies the needs for further research and presents the aims of this study. The theoretical foundations of water wave modelling using the Boussinesq equations are presented in Chapter 3 with the derivation of the equations. This chapter also gives a description of the solution method used to solve the equations, and a description of the preliminary testing of the model. Chapter 4 introduces the data and data analysis methods used. The numerical simulations and comparisons are presented and discussed in Chapter 5 (time domain analysis) and Chapter 6 (frequency domain analysis). Further discussion, a summary and conclusions are given in Chapter 7.

CHAPTER 2 DEVELOPMENTS and APPLICATIONS of the BOUSSINESQ EQUATIONS

2.1 Classical Boussinesq equations

2.1.1 Early developments and first applications

Boussinesq (1872) originally derived the Boussinesq equations by incorporating low order dispersive effects in the nonlinear shallow water equations for waves propagating over a horizontal bottom. It was only in the late 60's however that his theory started to be applied: Peregrine (1967), using a perturbation approach, extended Boussinesq's original formulation to describe the nonlinear transformation of irregular short waves in water of varying depth using the free surface elevation and the depth averaged horizontal velocity as dependent variables. His equations, for which he also proposed the first numerical solution, read:

$$\frac{\partial \eta}{\partial t}+\frac{\partial}{\partial x}\left[(h+\eta)\overline{u}\right]=0 \qquad 2.1a$$

$$\frac{\partial \overline{u}}{\partial t}+\overline{u}\frac{\partial \overline{u}}{\partial x}+g\frac{\partial \eta}{\partial x}=\frac{1}{2}h\frac{\partial}{\partial t}\left[\frac{\partial^2}{\partial x^2}(h\overline{u})-\frac{1}{3}h\frac{\partial^2 \overline{u}}{\partial x^2}\right] \qquad 2.1b$$

where η is the free surface elevation, $\overline{u}$ is the depth-averaged velocity, and h is the still water depth.

Subsequent work started with the development of numerical methods, and the study of their effect on the accuracy of the solution. Abbott and Rodenhuis (1972) showed the extreme sensitivity of the solutions to the equations to numerical errors, and the necessity of a high accuracy finite difference scheme. On the other hand, they showed that if sufficient accuracy can be obtained, solutions to the equations give good results. Abbott *et al.* (1978a & b, 1984) described a third order accurate finite difference scheme for the solution of a modified version of Peregrine's equations.

Numerical models based on Peregrine's equations (or equivalent formulations) were subsequently tested against laboratory data and analytical solutions (Abbott *et al.*, 1978a & b; Haugel, 1980; Schaper and Zielke, 1984; Madsen and Sørensen, 1984). Both the solitary

wave theory and the cnoidal theory are solutions to the Boussinesq equations and have been used to validate 1D models for horizontal beds. Abbott *et al.* (1978a & b) were among the first to develop a two-dimensional numerical model based on Boussinesq equations (System 21 'Jupiter'). Their model is able to describe shoaling, refraction, diffraction and partial reflection from porous structures (rubble mound breakwater). The latter is made possible by including a porosity factor. Madsen and Warren (1984) made a comparison of the solutions of the model developed by Abbott and co-workers with analytical solutions and physical model tests. They showed the prediction of such processes as shoaling, refraction, diffraction and partial reflection from piers and breakwaters is reliable and can be used 'confidently' for engineering practice when applied within its limits (these limits may be broadly defined here as a restriction to fairly long waves in shallow water, see section 2.1.2 for more detail). Two dimensional Boussinesq-type models have therefore been used for many years to simulate wave conditions inside a harbour due to incoming waves. These models can describe all the processes involved in the propagation of irregular, multidirectional finite-amplitude (nonlinear) waves over complex bathymetries, i.e. shoaling, refraction, diffraction and partial reflection.

Freilich and Guza (1984) were the first to study the simulation of wave-wave interactions and associated spectral evolution in shallow water with a Boussinesq-type model. On the basis of the original Boussinesq equations, they derived a new set of evolution equations for the amplitude and phase of Fourier components. These equations contain second order (quadratic) interaction terms that allow the transfer of energy across the wave spectrum over short distances in shallow water. They validated their model against field data for non-breaking irregular wave trains propagating on a constant slope. They showed that the evolution of the power spectra of normally incident shoaling waves may be predicted accurately. Their model, which is sometimes referred to as a nonlinear spectral model, was subsequently verified against field data and improved in several subsequent papers (Elgar & Guza, 1985a & b, 1986; Elgar *et al.*, 1990; Freilich *et al.*, 1990; Elgar *et al.*, 1997[1]). In particular, validation was successfully extended to the prediction of bispectra and surface elevation asymmetry and skewness for weakly dispersive shoaling wave.

---

[1] Elgar *et al.* (1997) also studied evolution of power spectra for breaking waves: they compared measured power spectra in the surf zone with predictions from a models solving the NLSW equations and obtained good agreement.

2.1.2 Range of application

The range over which the Boussinesq equations are valid depends on the main assumptions made in their derivation. Two small scaling parameters are shown to be important in evaluating the different forms of the Boussinesq equations (Peregrine, 1972). and hence defining their range of applicability:

ε , the ratio of wave amplitude to water depth ***a/h*** (a measure of the degree of nonlinearity of the waves);

μ , the square of the ratio of the water depth to the wave length $(h/L)^2$ (a measure of the degree of dispersion).

ε is assumed small and μ is assumed to be smaller or of the same order as ε (that is. the Ursell number $Ur = \varepsilon/\mu = O(1)$). In other words, the original form of the Boussinesq equations assumes that both dispersion and nonlinearity are weak and of the same order. This would tend to restrict the application of the equations to the propagation of small waves in shallow water. However, numerical testing has shown good results for high waves and also for waves propagating in intermediate depth waters (McCowan. 1981).

Dingemans (1997) proposed an upper limit for ε at 0.25 (weak nonlinearity), and an upper limit for μ at 1/50 (i.e. $h/L \leq 1/7$) (weak dispersion).

Many forms of the Boussinesq equations are found in the literature. This variety is due to the fact that there are many procedures to derive Boussinesq equations and almost as many resultant forms of the equations (see e.g. Dingemans (1997)). For example, the dependent variables can be chosen in different ways. Typical velocity variables may be the velocity at the surface, the depth integrated velocity or the bottom velocity. Also, since the nonlinear and dispersive terms are of higher order, they can be manipulated by invoking the linear long-wave equation (nearly horizontal flow equations) (Mei, 1989; Whitham, 1974; Long, 1964).

Within the weak nonlinearity and weak dispersion limit, the practical range of application of a variety of Boussinesq-type models was studied by McCowan (1978,1981.1985.1987), Witting (1984), Nwogu (1993). Madsen *et al.* (1991) and Madsen & Sørensen (1992). The fact that the Boussinesq equations are only applicable to relatively shallow water depths is a major limitation of their original form. McCowan (1987) and Madsen *et al.* (1991) evaluated sets of Boussinesq equations for their applicability to propagate waves with the correct celerity, McCowan using different levels of dispersive terms. and Madsen *et al.*

using equations expressed in terms of different velocity variables, both methods resulting in the comparison of models with different linear dispersion relations. According to McCowan (1987), except for $h/L_o < 0.05$, the accuracy of the phase celerity and group velocity (and therefore the applicability of the model) depends on the velocity variable used. For the commonly used form of the Boussinesq equations, expressed in terms of the depth-averaged velocity, to keep errors in the phase velocity less than 5%, h/L_o has to be less than 1/5. Similarly, Madsen *et al.* (1991) showed that the worst form of the equations, expressed in terms of the surface velocity, breaks down for h/L_o larger than 0.12. They found, as well as McCowan, that the equations based on the depth-averaged velocity exhibit the best h/L_o limits, with a 5 % error in the phase celerity and a 20% error in the group velocity for h/L_o = 0.22. It is therefore this form that the authors recommended. A subsequent analysis by Madsen and Sørensen (1992) shows that major errors in the embedded linear shoaling gradient occur when $h/L_o > 0.1$. From their study it appeared that the shoaling properties of a given set of equations also depends on the velocity variable used.

2.1.3 The need to improve the frequency dispersion properties of the classical Boussinesq equations

To use a Boussinesq model as an engineering tool, the extension of the application of the model to waves with larger h/L_o, or kh,(also referred to in the Boussinesq literature as 'deep(er) water waves', or 'short(er) waves') would be a valuable asset. Note that the extension to the description of shorter waves is required not only to simulate waves further offshore, but also to accurately simulate the shorter waves (high harmonics) resulting from triad interactions during shoaling and breaking.

Mei and Ünlüata (1972) have shown that the phase mismatch between the primary wave and its harmonics, Δ, controls the strength of the nonlinear interactions occurring over small length scales, and causes a modulation of the harmonic amplitudes. They showed, both experimentally and theoretically, that the smaller Δ, the stronger the interaction (and the larger the amplitude and beat length of the oscillations of the second harmonic). Since Δ decreases in decreasing depth (the waves become non-dispersive), the strength of the interactions is enhanced in decreasing water depths. The correct prediction of the strength of the interactions (i.e. the amount of energy exchanged among harmonics) therefore depends on the correct prediction of the phase mismatch.

Good dispersion prediction is also essential for the correct simulation of the phase celerity of the free high harmonics. Indeed, during shoaling increasing energy is transferred into

bound sub and super-harmonics which travel phase locked to the primary wave train. Part of the energy can be released as free harmonics (e.g. a wave travelling over a submerged bar), i.e. harmonics travelling according to their own dispersion characteristics. The dispersion characteristics of free higher harmonics is thus a major factor of wave evolution because it determines the wave shape. Even when the primary component corresponds to very long waves, the modelling of this process therefore requires good linear dispersion and shoaling properties.

Summary

When applied within their range of validity, the classical Boussinesq equations provide satisfactory results. Given the applicability analysis carried out by a number of researchers, further development of the existing models and extension of their range of application is necessary, in particular with respect to their *h/L* limitation. This work is described in detail in the following section.

2.2 Extension of applicability to shorter waves

Recently, a number of attempts have been made to extend the range of applicability of the original equations to deeper waters by improving the dispersion characteristics of the equations. Each of these studies is based on the finding reported above that the frequency dispersion properties of a given set of equations depends on the velocity variable used. This has resulted in a range of new forms of the Boussinesq equations where more second and third order derivatives were introduced.

It was Witting (1984) who first attempted to extend the range of applicability of the equations to deeper waters. He used the velocity at the free surface as the velocity variable and introduced improved dispersion characteristics. His new form of the Boussinesq equations is for one horizontal dimension, and gives excellent dispersion properties, but is unfortunately very difficult to extend to two dimensions (Madsen *et al.*, 1991).

Madsen *et al.* (1991) also derived a new set of Boussinesq equations introducing improved linear dispersion characteristics. Through direct manipulation of the dispersion terms, they obtained a model with extended accuracy in its dispersion relation. This procedure is

detailed in section 3.3. In terms of the depth-integrated velocity, or volume flux, P, the new equations are:

$$\frac{\partial \eta}{\partial t} + \frac{\partial P}{\partial x} = 0 \qquad 2.2a$$

$$\frac{\partial P}{\partial t} + \frac{\partial (P^2/d)}{\partial x} + gh\frac{\partial \eta}{\partial x} = (\frac{1}{3} + B)h^2 \frac{\partial^3 P}{\partial^2 x \partial t} + Bgh^3 \frac{\partial^3 \eta}{\partial x^3} \qquad 2.2b$$

The introduction of high order terms in the momentum equation includes a linear dispersion parameter B which is adjusted so as to match the dispersion relation of the linearised extended equations with a polynomial expansion of the exact[1] linear dispersion relation combined with the use of Pade's approximant. They found that B = 1/15 gave optimum results (fig. 3.2). In deep water, the new equations have a frequency dispersion relation that approaches the exact linear dispersion relation. In shallow water, it converges towards the standard Boussinesq equations. The new equations resulted in an increase of the practical deep water limit from h/L_o = 0.22 to h/L_o = 0.5 (with phase celerity errors restricted to 5% relative to Stokes 1st order theory). This new form is valid for irregular wave trains in two horizontal dimensions but assumes a flat bottom. Madsen and Sørensen (1992) extended Madsen *et al.* (1991)'s new form of Boussinesq equations to the simulation of waves propagating on a slowly varying bathymetry. For the same value of B, the new equations allow for a more accurate simulation of shoaling and refraction of irregular wave trains (fig 3.3).

Nwogu (1993) also improved the linear dispersion properties of the Boussinesq equations: bearing in mind that the level at which the velocity is evaluated determines the dispersion properties of the equations, he derived a new set of equations with the horizontal velocity evaluated at some arbitrary distance -αh from the still water level. The optimal elevation at which the velocity is evaluated is then determined by comparing the dispersion relation of the linearized modified Boussinesq equations to that given by Stokes linear theory. The optimum depth is found to be close to mid depth at -0.531h (equivalent to B = 1/17.5, Dingemans (1997)).

The difference in the frequency dispersion behaviour between B = 1/17.5 and B = 1/15 is not large. Dingemans (1997, p539) has shown that the choice B = 1/17.5 is best over the

[1] assumed to be Stokes's first order theory

range $0 < kh < \pi$, but it results in a less accurate phase velocity for very long waves ($0 < kh < \pi/2$) when compared to $B = 1/15$.

Both the linear dispersion parameter B introduced by Madsen *et al.* (1991) and the depth at which the velocity is evaluated in Nwogu's model may thus be regarded as frequency dispersion tuning parameters. Both Madsen *et al.* and Nwogu have shown that their 'extended' models are able to describe the propagation of waves from relatively deep water (e.g. $h/L_o = 0.49$) to shallow water. Nwogu's (1993) model was further tested by Wei and Kirby (1995a) who also devised an improved numerical scheme using a fourth-order predictor-corrector method. Testing included the simulation of random waves on a constant slope (1D) and regular waves propagating over a shoal (2D, standard test devised by Berkoff *et al.*, 1982). The results are good when applied within the weak nonlinearity limit.

It is relevant to note that Madsen *et al.* (1991) and Madsen and Sørensen (1992), as well as Nwogu (1993), looked at improvements on phase and group celerities for waves with kh up to π only. It is certain that these authors achieved great improvements on the application of the original equations; however, beyond that limit, it appears that the extended equations have an dispersion relation increasingly diverging from Stokes first order (figure 3.2 and 3.3). These extended models must therefore be used with caution for $kh > \pi$.

The conclusions reached by Mei and Ünlüata (1972) outlined in section 2.1.3 signal the importance of good linear dispersion characteristics for the simulation of nonlinear phenomena such as wave-wave interactions. Madsen and Sørensen (1993) investigated the performance of the extended equations for the simulation of higher harmonics generated during shoaling, and came to the same conclusion. They derived new evolution equations based on Madsen and Sørensen's (1992) model to simulate wave-wave interactions on constant depths and slowly sloping bottoms. They found remarkable improvements in the simulation of higher harmonics when compared to the classical Boussinesq equations. They also observed some underestimation of high harmonic amplitude in the shoaling region.

Studies of waves travelling over a submerged bar have been carried out to show the generation of bound harmonics over the bar and their release as free waves behind the bar. This situation provides a severe test for the extended models with regard to (i) their linear frequency dispersion characteristics, and (ii) their capability to model wave-wave

interactions. This experimental set-up was first investigated by Beji & Battjes (1994). They found that, for non-breaking cases, extended (improved linear dispersion characteristics) Boussinesq-type models can reproduce this process.

A comparison was made between flume experiments with the same geometry as in Beji and Battjes (1994), and computations with 7 (non-dissipative) Boussinesq-type models from various European institutes. The dominant difference between the models lies in their linear frequency dispersion relation, with some less significant differences in the nonlinear and bed slope terms. An interesting detail of this study it that the participants did not have access to the experimental data during testing. This collaborative work was compiled and reported by Dingemans (1994). Again the bed geometry was chosen in view of the possibility of assessing the models for their accuracy to predict a correct frequency dispersion for the free short waves generated (released bound waves) on the downwards slope of the bar. The study was thus designed not only to demonstrate the importance of the accuracy of frequency dispersion but also to establish which form of Boussinesq models performs best with this respect. It showed that indeed it was on the downward slope of the bar that the results were most divergent. Two models appeared to share the best performances, the model derived by Madsen and Sørensen (1992) being one of them. Note however that this study did not evaluate the performance of more advanced models subsequently developed such as that by Wei *et al.* (1995) for example (see section 2.4.2). An important conclusion was also drawn from this comparison: the primary property affecting the model performance is the accuracy of the frequency dispersion characteristics. The reproduction of higher order nonlinear effects is an important property, but is of little use if the model's frequency dispersion characteristics are not accurate.

Summary

The extensive research reported above has resulted in a number of extended forms of the Boussinesq equations applicable to waves with larger *kh*. The new equations have better linear frequency dispersion and shoaling properties, which were shown to be of importance for the simulation of nonlinear interactions. They thus offer a promising tool for wave shape prediction, and, if extended to the surf zone, for application to sediment transport prediction. Lastly, the importance of frequency dispersion, relative to amplitude dispersion, makes the application of the extended Boussinesq-type models to the surf zone conceivable despite the weak nonlinearity assumption.

2.3 Wave breaking

Wave breaking is one of the phenomena most difficult to describe mathematically. The modelling of the surf zone processes is typically based on highly simplified representations of broken waves. Surf zone modelling methods can be divided into two categories: the short wave-averaged models and wave-resolving models. In the wave-averaged models, the equations for conservation of mass and momentum are depth-integrated and time-averaged. Svendsen and Putrevu (1996) give an extensive review of these models. Wave-resolving models are time domain models that have the advantage of providing information about the phase motion in terms of both the elevation and the velocity. Their attraction also lies in their capacity to predict wave shape. They are reviewed in detail in this section.

The modelling of wave breaking is hampered by the difficulty in describing the breaking process. The modelling of two breaker types is breifly reviewed here: spilling breakers, which are observed when waves of large steepness are incident to a gently sloping beach, and plunging waves, which are observed on relatively steep beach slopes, with waves of intermediate steepness. After a wave has broken as a spilling or plunging breaker, a transition occurs in the so-called outer surf zone. For the spilling breaker, the forward slope of the wave top becomes unstable. A plume of water and air bubbles slides down the slope from the crest. The volume of the plume, or surface roller, increases, and the wave height decreases rapidly. For the plunging breaker, the crest of the wave moves forward and falls down at the trough in front of it as a single structured mass of water, or jet. The jet of water plunges down, and pushes up a very turbulent mass of water which continues the breaking process.In both cases, this transition in the outer surf zone is followed by the transformation of the wave into a bore-like wave in the inner surf zone.

The transition occurring in the outer zone involves rapid processes that are difficult to model. The inner part of the surf zone on the other hand can be described as a series of periodic bores. This gave rise to two concepts: the bore concept, applied with the nonlinear shallow water equations, and the roller concept, first introduced by Svendsen (1984a) in a wave-averaged model, and subsequently applied to a (phase-resolving) Boussinesq model.

The NLSW equations are valid for very shallow water (for all long wave theories, $\mu^{1/2} << 1$) but finite wave height ($\varepsilon = O(1)$). In this case, therefore, nonlinearity dominates over dispersion ($Ur >> 1$). These conditions hold in both the inner surf zone and the swash zone. The suitability of the NLSW equations for the modelling of the broken waves is further

enhanced by the fact that they admit bore-like solutions. They predict that the wave front will gradually steepen until it is vertical. The NLSW equations have already been used with great success to model inner and swash zones hydrodynamics (Hibberd & Peregrine, 1979). The main restriction for the use of the NLSW equations is that they can only be used for very shallow water and for the simulation of broken waves as they do not include frequency dispersion.

Boussinesq equations on the other hand include the balanced effects of lowest order frequency dispersion and amplitude dispersion. This tends to stabilise the waves profiles. This is in contrast with the NLSW equations, for which only amplitude dispersion is included, and for which, as a result, the wave front continuously steepens. The Boussinesq equations can therefore describe wave shoaling and pre-breaking stage. An extension of Boussinesq equations to describe wave breaking therefore seems attractive. Since in the derivation of the equations it is assumed that *H/h* is small, and since this parameter near the breaking point reaches values close to 1, its extension to the surf zone may seem contradictory. Despite this, several authors have extended their Boussinesq model to describe wave breaking without including additional (high order) terms to allow for more nonlinear waves. The results obtained from these new models are unexpectedly promising.

The extension of Boussinesq-type models to the surf zone requires two steps: the introduction of a breaking criterion and the inclusion of an energy dissipation term. Bearing in mind that Boussinesq-type models are time dependent models, which rules out e.g. energy-based wave breaking formulations such as Battjes & Janssen's (1978), three different concepts have been adopted to incorporate wave breaking and energy dissipation:

- the first is based on the eddy viscosity concept (Karambas and Koutitas (1992), Wei and Kirby (1995b));

- the second is based on the surface roller concept (Brocchini *et al.* (1992), Schäffer *et al.* (1993));

- the third concept was introduced by Svendsen *et al.* (1996) which accounts for vorticity.

Svendsen *et al.* (1996) carried out a theoretical comparative study of these 3 concepts. They concluded that in each case, the terms added to the equations resulted in remarkably similar effects, i.e. the Boussinesq equations respond equally to the different terms introduced in the

momentum equations. The models thus produce comparatively good results for the simulation of wave decay and wave shape evolution.

The surface roller concept is described in detail here since it is the method that is applied in this thesis. It was first applied in a phase-averaged model by Svendsen (1984a): the water body is split into two parts. The main part is part of the wave motion (i.e. orbital motion). The breaking is represented by a surface roller that travels on the front of each wave, at the wave celerity. Engelund (1981) used the analogy between the broken wave and a hydraulic jump to determine the volume (hence mass) of the surface rollers. Svendsen (1984a) applied this analogy to express the energy flux and radiation stress in a broken wave.

This concept was first introduced into a Boussinesq model by Deigaard (1989) who incorporated the effect of the roller as an additional pressure term in the depth-integrated momentum equation.

Schäffer *et al.* (1993) modified this approach to incorporate the effect of the roller as an additional momentum flux. Again, the surface roller is considered as a passive bulk of water riding on the front of the breaking wave. It is transported at the wave celerity while the orbital velocity of the flow below is assumed to be uniformly distributed over the vertical and is a lot smaller than the wave celerity (and hence smaller than the roller celerity). The vertical distribution of the horizontal velocity is thus non-uniform in the presence of rollers. The contribution from the roller is introduced as the excess momentum flux due to deviations from a uniform velocity profile. This is incorporated in the depth-integrated momentum equations as an additional convective momentum term. The development of this model is presented in section 3.4. Schäffer *et al.* (1993) thus derived a new set of equations for both the one and two dimensional cases. The breaking criterion is related to the water surface slope and the thickness of the roller is determined by simple geometrical considerations (after Deigaard, 1989). The one-dimensional model was tested and compared against experimental data (Schäffer *et al.*, 1993). The model gives a good prediction of the variation of the wave height and mean water level for regular as well as irregular waves breaking on a barred beach. The two dimensional model simulations appeared in later papers in which the model was extended to the swash zone (see section 2.4.3).

Summary

Despite the weak nonlinearity assumption, when provided with an appropriate dissipative mechanism and breaking criterion, the Boussinesq equations can be modified to describe

breaking waves. The different attempts made to include these criterion were described here. They were shown by Svendsen *et al.* (1996) to be equivalent. The first model validations, which were made in terms of surface elevation predictions, are promising.

2.4 Recent developments

Research in the development and application of the Boussinesq equation has been accelerating in the past 4 years and has experienced what one might call a 'Boussinesq Boom'. The developments presented in this section appeared during the late stage of the study presented in this thesis. These developments have included the extension of spectral models to reproduce energy dissipation, extension to the description of more nonlinear or dispersive waves, simulation of swash motion, percolation and first applications to sediment transport prediction.

2.4.1 Wave breaking and nonlinear spectral models

Eldeberky and Battjes (1995) observed, from laboratory experiments on waves propagating over a submerged trapezoidal bar, that the spectral evolution of breaking and non-breaking waves is similar. Breaking was found to simply re-scale the wave spectrum through energy dissipation without changing the spectral shape significantly. On the basis of these observations Eldeberky and Battjes (1996) devised a spectral model including wave breaking. Their model dissipates energy equally through the whole range of frequency. Comparison of experimental and numerical results for power spectra of random waves propagating over non-barred and barred profiles yielded good agreement. Chen *et al.* (1997) incorporated a frequency dependent energy dissipation mechanism in a Boussinesq model with improved dispersion (after Nwogu, 1993 and Chen and Liu, 1995) and compared their results with field data. The inclusion of the frequency dependence allows a more realistic weighting of breaking towards primary and high frequency bands, thus allowing low frequency energy to propagate through. This model resulted in improved skewness and asymmetry predictions when compared to frequency independent dissipation. No improvements were obtained for the power spectra, for which the results were also good if no frequency dependence was included [1].

[1] The insensitivity of the power spectrum predictions to the frequency dependence was found by Chen *et al.* to be due to the fact that the preferential reduction of high frequency energy is largely compensated by increased nonlinear transfers of energy to high frequencies.

2.4.2 Boussinesq models with improved nonlinearity

The standard Boussinesq equations are derived assuming that ε and μ are small (<<1) and of the same order ($\varepsilon/\mu = O(1)$). The extended equations described in section 2.2 have provided an extended limit on μ. In order to comply with $\varepsilon/\mu = O(1)$ however, if μ is to increase, then ε must increase as well. This is limited since the weak nonlinearity assumption remains. This was illustrated in Wei *et al.* (1995). To be able to fully exploit the advantages of these extended equations (i.e. use the full range of kh), the limit on ε must also be extended. For that reason, and also purely to be able to simulate a more nonlinear regime, Wei *et al.* (1995) derived a new set of Boussinesq type equations valid for fully (to second and third order) nonlinear dispersive waves (which they solved using the fourth order numerical scheme presented in Wei and Kirby (1995a)). Unlike the derivation of the Boussinesq equations so far, no assumption of small nonlinearity is made, and terms of $O(\varepsilon)$ in the $O(\mu)$ dispersive terms are retained (i.e. the nonlinear dispersive terms are not neglected). Their model also includes improved frequency dispersion as introduced by Nwogu (1993). It was applied to shoaling solitary waves and the propagation of undular bores over a flat bed, with strong nonlinearities. Wei *et al.* found significant improvements for wave height and phase celerity predictions. They also presented a rare evaluation of a Boussinesq model with respect to horizontal velocity predictions. Assuming a parabolic vertical distribution, they were able to estimate the profile for the horizontal velocity, which they compared to a fully nonlinear potential flow model (Grilli *et al.*, 1989). Both solutions were in good agreement. Again this showed much improvement over the weakly nonlinear Boussinesq equation with improved dispersion.

Wei and Kirby (1995b) extended Wei *et al.*'s model to the surf zone by introducing energy dissipation terms based on an eddy viscosity concept. They applied their model to random waves shoaling and breaking over a constant slope. Comparison of numerical and experimental results are good. Good agreements were found not only for wave heights, but also for third moment elevation statistics (elevation skewness and asymmetry).

2.4.3 Inclusion of swash oscillations

Madsen *et al.* (1994) extended the surf zone model by Schäffer *et al.* (1993) to the description of swash oscillations. Inclusion of the swash zone requires a number of modifications: first the swash zone is represented by incorporating a moving shoreline boundary condition. The dispersion terms are 'switched off' at the still water shoreline where the equations thus reduce to the nonlinear shallow water equations. Finally, the growth of

numerical instabilities is avoided by altering the numerical scheme in this region with the use of numerical filters. The first results show promising qualitative results for the run-up and reflected low frequency waves. This model was further tested by Sørensen *et al.* (1994) for 2D nearshore circulation. Again promising results are obtained for rip current generation and current circulation behind detached breakwaters. The model evaluation has been mostly qualitative.

Further qualitative testing of this model for regular and random waves was presented by Madsen *et al.* (1997a & b). In addition, they compared their results for run-up predictions to both laboratory data and predictions of a model based on the nonlinear shallow water equations. They obtained encouraging results. The spatial evolution of phase-averaged quantities such as the cross-sectional roller area, the radiation stress, energy flux and energy dissipation were found to be in good agreement with predictions by conventional phase-averaged wave models.

2.4.4 Higher order frequency dispersion

Models with higher-order frequency dispersion have recently been produced which involve the introduction of fifth order derivative terms (Schäffer & Madsen, 1995; Dingemans, 1997). To date, this work has been purely theoretical and no solution to the higher order equations has been proposed.

2.4.5 Latest applications: wave-current interactions & sediment transport prediction

A theoretical study of wave-current interactions with a Boussinesq model with extended linear frequency dispersion properties was carried out by Chen *et al.* (1998). Physical processes such as wave blocking by opposing current were modelled and shown to be in reasonable agreement with theoretical calculations. The model remains to be tested with measurements.

Finally, for completeness, the first applications of Boussinesq models to the prediction of beach profile evolution may be found in Karambas *et al.* (1995), Rakha *et al.* (1996) and Nwogu (1996). All those applications yield promising results !

2.5 Evaluation of the performance of Boussinesq models

The segmented nature of the developments of Boussinesq models has resulted in equally segmented model testing programmes. Apart from Dingemans's (1994) comparison of 7

			Shoaling			Shoaling and breaking			
	Author		Beji & Battjes (1994)	Wei et al (1995)	Bosboom et al (1996)	Wei & Kirby (1995b)	Svendsen et al (1996)	Madsen et al (1997a)	Madsen et al (1997b)
MODEL	improved dispersion		✓	✓	✓	✓		✓	✓
	improved nonlinearity			✓		✓			
	wave breaking					✓	✓	✓	✓
	swash					✓		✓	✓
DATA	type of experiment		L	A[1]	L	L	L	N / A	N / A
	wave input		Irregular	Regular	Regular	Irregular	Regular	Regular	Irregular
	bed profile	flat bed							
		constant slope		✓		✓	✓	✓	✓
		barred	✓[2]		✓[3]			✓[3]	
Model-data comparison	elevation	time series	✓	✓		✓	✓	✓	✓
		H, mwl		✓			✓	✓	✓
		wave envelope						✓	
		power spectrum	✓						✓
		skewness & asymmetry				✓			✓
		bispectrum evolution							
	velocity	velocity profile		✓	✓		✓		
		undertow						✓	
		time series			✓				
		third moments							
	others							radiation stress roller area energy dissipation	run up shoreline motion

Type of experiment:

numerical experiment only	N	comparison with analytical solutions	A
comparison with laboratory data	L	comparison with field data	F

Table 2.1 1D time domain Boussinesq models: summary of model-data comparisons.

[1] comparison with fully nonlinear potential flow model (Grilli et al, 1989)

[2] submerged bar as in Beji and Battjes (1994)

			Shoaling	Shoaling and breaking			
	Author		Elgar et al (1997)	Eldeberky & Battjes (1995)	Eldeberky & Battjes (1996)	Bosboom et al (1997)	Chen et al (1997)
MODEL	improved dispersion			✓	✓	✓	✓
	improved nonlinearity						
	wave breaking			✓	✓	✓	✓
	swash						
DATA	type of experiment		F	L	L	L	L / F
	wave input		irregular	irregular	irregular	irregular	irregular
	bed profile	flat bed					
		constant slope				✓	✓
		barred	✓	✓	✓	✓	✓
Model-data comparison	elevation	time series	✓		✓	✓	
		H, mwl	✓				✓
		wave envelope					
		power spectrum	✓	✓	✓		✓
		skewness & asymmetry	✓				✓
		bispectrum evolution	✓	✓ (biphase)			
	velocity	velocity profile					
		undertow					
		time series				✓	
		third moments				✓	
	others		energy dissipation				

Type of experiment:

numerical experiment only	N	comparison with analytical solutions	A
comparison with laboratory data	L	comparison with field data	F

Table 2.2 1D frequency domain Boussinesq models: summary of model-data comparisons.

different Boussinesq models with a single data set, the validation of Boussinesq models has consisted of the verification for the prediction of a variety of quantities with various data sets. Furthermore, validation has concentrated on elevation predictions, giving relatively very little attention to the prediction of velocities. In particular, three issues have been extensively addressed in the testing of the models, namely performance with regards to frequency dispersion, wave-wave interactions, and wave decay in the surf zone.

The validation of Boussinesq-type models to date is summarised in tables 2.1 and 2.2. Table 2.1 covers the most advanced time-domain Boussinesq-type models, and the range of the parameters studied in their evaluation. Table 2.2 displays the most advanced frequency-domain models, and their validations.

From table 2.1 it is clear that, in the past, the verification of Boussinesq-type models has been focused on surface elevation predictions, with attentions focusing on wave height (shoaling and decay) and mean water levels.

Bosboom *et al.* (1996) proposed a rare study of a Boussinesq model with respect to velocity predictions of non-breaking waves. This study consisted of the evaluation of regular waves propagating over a submerged bar. For surf zone models, the verification of velocity predictions with a Boussinesq model has been limited to Svendsen *et al.* (1996) and Madsen *et al.* (1997a). Svendsen *et al.*, assuming a parabolic velocity distribution of the horizontal velocity, compared predictions to laboratory measurements, and obtained acceptable agreement. Madsen *et al.* (1997a) applied Madsen *et al.*'s (1994) model to compare undertow predictions with laboratory measurements for one case of regular waves propagating on a constant slope. They found good agreement.

Besides a lack of evaluation of Boussinesq models with regards to velocity prediction, it is clear that wave shape prediction has received little attention. With the exception of Bosboom *et al.* (1996), who compared predicted velocity time series to laboratory measurements, it also appears that most evaluation of wave shape prediction has focused on elevation distortions. Wei and Kirby (1995b) and Madsen *et al.* (1997b) evaluated their respective time domain surf zone models for the prediction of elevation skewness and asymmetry, presumably through a bispectral analysis. Both these authors considered a single case of irregular waves on a constant slope. Their comparison yielded good results.

Frequency domain models have been mostly evaluated in terms of power spectrum predictions. Chen *et al.* (1997) extensively tested their new frequency domain Boussinesq model extended to the surf zone with field and laboratory data. In particular, their comparison included elevation skewness and asymmetry, but no velocity predictions. Bosboom *et al.* (1997) evaluated Eldeberky and Battjes's (1995) model for second and third order velocity moments. They tested two cases, one of short waves, one of long waves, propagating over a complex bathymetry. The best results were obtained for the long waves.

2.6 Objectives of this study

2.6.1 Model selection

The numerical model used in this thesis is based on the most advanced work existing at the beginning of this study, that is, the work carried out by Madsen and co-workers at the Danish Hydraulic Institute (DHI) in the early nineties, which produced state of the art Boussinesq-type models. It is based on the 1D Boussinesq equations as derived by Madsen *et al.* (1991) and Madsen and Sørensen (1992), with free surface elevation and depth-integrated velocity as variables. It allows slowly varying bathymetries and contains additional high order terms to improve the frequency dispersion for shorter wave periods, and thus also improve the shoaling properties of the model. Wave breaking is modelled using the concept of surface roller as formulated by Schäffer *et al.* (1993). It is assumed that bottom friction is negligible.

The methods of numerical modelling with Boussinesq-type equations may be classified into the time domain finite difference method, and the frequency domain methods. Freilich and Guza (1984) were the first to use a spectral approach. They were followed by Madsen and Sørensen (1993) and Eldeberky and Battjes (1995,1996). This method has the advantage of providing a simpler solution as the evolution equations are solvable with a Runge Kutta method. It has the disadvantage however of assuming non-reflective waves. It also results in a solution for the surface elevation only; an expression must be applied to subsequently determine the velocity (Bosboom *et al.*, 1997). The procedure applied to rewrite the equations from the time domain into the frequency domain also involve further assumptions of slowly varying complex amplitude. Lastly this method was found by Madsen and Sorensen (1993) to be very efficient for regular (or bichromatic) waves (i.e. for a finite number of harmonics), but very time consuming to solve for irregular wave trains (very

large number of harmonics). For these reasons the time domain model described above was preferred over Madsen and Sørensen's (1993) frequency domain model.

2.6.2 Aims of this thesis

With the exception of Wei and Kirby's (1995b) model, a common assumption for the Boussinesq models recently modified to include the description of breaking waves is that they can only describe waves with weak nonlinearity. This appears contradictory as breaking waves have reached a highly nonlinear regime. Despite this inconsistency, these models have yielded reasonable results with regard to wave decay and set-up. A better understanding of the strength and applicability of the model to the surf zone is needed. The primary purpose of this study is to investigate the behaviour of a Boussinesq model when applied beyond the limits of the assumptions made in the model derivation. The model will be evaluated for shoaling and breaking waves, with emphasis on the surf zone.

Every aspect of the performance of numerical models needs to be tested. Section 2.5 has identified the 'holes' in the validation of Boussinesq models so far. Little work has been presented on the evaluation of the model with respect to velocity predictions, and the prediction of vertical and horizontal asymmetry of the wave profile and velocity oscillations. The object of this study is to assess how satisfactorily these processes may be modelled using a Boussinesq type model.

Further research is also required in studying the effect the free parameters introduced in the simulation of wave breaking, which were arbitrarily chosen from laboratory and numerical experiments (section 4.1.3). No sensitivity analysis has been produced in the work presented by Schäffer *et al.* (1993), and later numerical investigations by Sørensen *et al.* (1994) and Madsen *et al.* (1994). In a recent paper, Madsen *et al.* (1997a) looked at the effects of changing these parameters, their aim being to improve the results for wave height and mean water level. The aim here is not only to improve the results by adjusting these parameters, but in so doing, to test the sensitivity of the solution to systematic changes in the parameters. In contrast with Madsen *et al.* (1997a), who focused on wave height and mean water level predictions, this sensitivity analysis will cover testing with respect to velocity prediction, and the shape of both the wave profiles and the velocity oscillations. The latter will be shown to be critical.

The starting point of a model validation is verification with analytical solutions and laboratory data. This should include sensitivity tests of any empirical parameters used, and testing of all aspects of model performance. The next step is the verification with field data. An intermediate stage has been adopted here where the model is verified with large scale laboratory data. The accuracy of the measurements can be accepted with more confidence than for small scale data, for which further errors are introduced due to surface tension. Furthermore, the similarity in the behaviour of numerical and physical tanks, in particular in terms of boundary conditions, produces a fair comparison. The validation of the model is also further pushed by the complexity of the bathymetry.

This study thus provides a thorough examination of the model's performance, with emphasis on predictions in the surf zone. To summarise, the objectives of this research are :

- to study dependence of the model on empirical (wave breaking) parameters;
- to evaluate the model with large scale laboratory data;
- to evaluate the velocity predictions as well as surface elevation predictions;
- to verify the model with respect to the prediction of third and fourth order statistical moments (time domain analysis) of elevation and velocity;
- to verify the model with respect to the prediction of third order spectra (bispectral analysis), i.e. prediction of wave harmonics and their interaction, and their effect on the shape of both the wave profiles and the velocity oscillations;
- to investigate the contribution of individual triad interactions to wave shape evolution;
- to compare the evolution of high order moments of velocity and surface elevation;
- to evaluate the performance of the model with respect to short wave simulation;
- to investigate the effects of the slowly varying bathymetry assumption on the predictions.

CHAPTER 3 - THE MODEL

3.1 Introduction

This chapter introduces the numerical model evaluated in this study. In section 3.2, two theories for non-linear shallow water waves are derived. Emphasis is put on the assumptions made in the derivations and the consequent limitations/range of application of the two approximations. Section 3.3 provides a discussion of the Boussinesq equation in the limit where $h/L \ll 1$ no longer holds. Analysis yields a set of modified Boussinesq equations valid for shorter waves. In section 3.4, a simple description of wave breaking is incorporated in the Boussinesq model by using the concept of surface rollers. Section 3.5 gives the outline of the numerical method used to solve the equations. Finally, in section 3.6, preliminary testing of the numerical model is described.

3.2 Equations for shallow water waves - Derivation

3.2.1 Introduction

There are various ways to derive equations for shallow water waves. The derivation of the equations illustrated here proceeds by vertically integrating the governing equations, and applying boundary conditions. The dependent velocity variable is thus the depth-averaged velocity. At some point in the derivations, assumptions have to be made about the vertical structure of the flow. Two important scaling parameters are useful in this process, namely μ and ε. The assumptions made about the vertical structure of the flow depend on the relative magnitude of these two parameters.

In this section, the derivation of the one dimensional (1-D) NLSW equations and 1-D Boussinesq equations from the vertical integration of the Euler equations is outlined. The derivation of the Boussinesq equations follows the method outlined by Schäffer *et al.*(1993). A derivation in non-dimensional form has the advantage of showing the relative magnitude of each terms with respect to frequency dispersion and amplitude dispersion. However, it was decided here to write the equations in dimensional form. Emphasis is placed on consideration of the principles and assumptions. Dingemans (1997) gives

extensive details on different model derivation methods, including a derivation with non-dimensional variables and using a perturbation series approach.

3.2.2 The Navier-Stokes equations - Integration over the depth.

The motion of an incompressible Newtonian fluid is well described by the Navier-Stokes equations which express the conservation of mass and momentum. The continuity and momentum equations are:

$$\frac{\partial u}{\partial x} + \frac{\partial w}{\partial z} = 0 \tag{3.1a}$$

$$\frac{\partial u}{\partial t} + u\frac{\partial u}{\partial x} + w\frac{\partial u}{\partial z} + \frac{1}{\rho}\frac{\partial p}{\partial x} - \nu\left(\frac{\partial^2 u}{\partial x^2} + \frac{\partial^2 u}{\partial z^2}\right) = 0 \tag{3.1b}$$

$$\frac{\partial w}{\partial t} + u\frac{\partial w}{\partial x} + w\frac{\partial w}{\partial z} + \frac{1}{\rho}\frac{\partial p}{\partial z} + g - \nu\left(\frac{\partial^2 w}{\partial x^2} + \frac{\partial^2 w}{\partial z^2}\right) = 0 \tag{3.1c}$$

where u and w are the horizontal and vertical particle velocity respectively, ρ is the fluid density, ν is the kinematic viscosity, g is the acceleration due to gravity, and p is the pressure. Figure 3.1 shows the definition of the geometrical quantities used throughout this derivation. η is the free surface elevation, h the still water depth, and d the total water depth. The Cartesian co-ordinate system is chosen so that the x-plane lies in the still water surface plane and is taken positive shoreward; z is positive upwards.

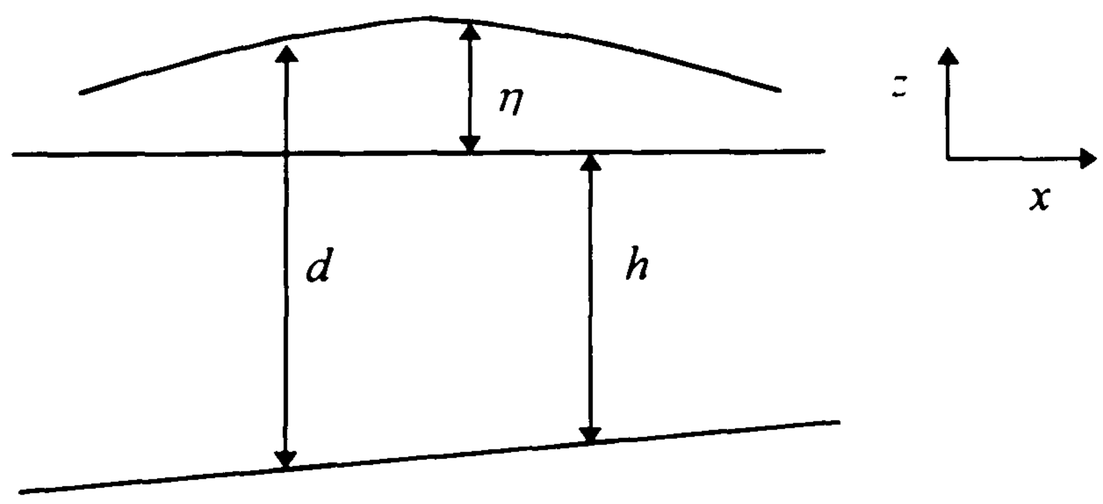

Figure 3.1 Definition of the geometrical quantities

The difficulty with these equations is that they are very computationally demanding to solve for complex problems such as wave description in the coastal area. In particular, water wave description is complicated by the unknown position of the free surface where a complex nonlinear boundary condition needs to be applied. To simplify the problem, some assumptions are made and the resulting equations are then an approximation of the chosen features of the flow.

First, an important assumption is frequently made: the fluid is assumed to be inviscid. The internal friction and the bottom boundary-layer friction arising from the water viscosity are neglected in view of the short length and time scales to be modelled, and assuming that the thickness of the boundary-layer is small compared to the water depth[1]. Neglecting the viscous forces, the governing equations reduce to the Euler equations.

The following boundary conditions are applied:

$$w|_s = \frac{\partial \eta}{\partial t} + u|_s \frac{\partial \eta}{\partial x} \qquad \text{at } z = \eta\,(x,t) \qquad (3.1d)$$

$$p|_s = 0 \qquad \text{at } z = \eta\,(x,t) \qquad (3.1e)$$

$$w|_b = -u|_b \frac{\partial h}{\partial x} \qquad \text{at } z = -h(x) \qquad (3.1f)$$

The subscripts *s* and *b* indicate that the variables are evaluated at the free surface and sea bed respectively. The physical principle imposed on the bounding surfaces states that once a fluid particle is on the surface, it remains there. This relates the kinematics of the particle motion on the surface to the changes in the surface levels, and results in the kinematic free surface boundary condition (3.1d), and, assuming a fixed bed, the kinematic bottom boundary condition (3.1f). A second physical property is applied to the free surface where it is assumed that the pressure is constant, and the surface tension effects are neglected. This gives the dynamic free surface boundary condition (3.1e).

The starting point for the derivation of the finite amplitude shallow water equation and Boussinesq equations is the integration of the continuity equation and the horizontal momentum equation from the sea bed *(z = -h)* to the instantaneous free surface *(z = η)*. This yields terms of the form e.g. $\int \partial / \partial x$ which are then transformed in terms of the form $\partial / \partial x \int$ using Leibnitz's rule:

$$\frac{d}{dx}\int_{\alpha(x)}^{\beta(x)} F(x,z)dz = \int_{\alpha(x)}^{\beta(x)} \frac{\partial}{\partial x}F(x,z)dz + F(x,\beta)\frac{d\beta}{dx} - F(x,\alpha)\frac{d\alpha}{dx}$$

The resulting extra terms that require an evaluation at *-h* and *η* (i.e. *α(x)* and *β(x)* respectively) are treated using the boundary conditions. The results of these integrations are presented in the following.

---

[1] note that in the extension of the model to the description of wave breaking (section 3.4), it is also assumed that the effects of wave breaking on energy dissipation dominate over the effects of viscosity.

By integration of the continuity equation from the sea bed to the free surface, and applying the kinematic boundary condition at the sea bed and free surface (equations (3.1f) & (3.1d)) we find :

$$\frac{\partial \eta}{\partial t}+\frac{\partial}{\partial x}\int_{-h}^{\eta} u\,dz=0 \tag{3.2}$$

Assuming that the bed is fixed (i.e. $\partial h/\partial t = 0$), integration of the horizontal momentum equation from the sea bed to the free surface and application of the continuity equation (3.1a) and the boundary conditions (3.1d-f) gives:

$$\frac{\partial}{\partial t}\int_{-h}^{\eta} u\,dz+\frac{\partial}{\partial x}\int_{-h}^{\eta} u^2\,dz+\frac{1}{\rho}\frac{\partial}{\partial x}\int_{-h}^{\eta} p\,dz-\frac{1}{\rho}p(-h)\frac{\partial h}{\partial x}=0 \tag{3.3}$$

Applying the continuity equation (3.1a) and the boundary conditions (3.1d-f), an expression for $p(z)$ can be obtained from the vertical integration of the vertical momentum equation:

$$p(z)=\rho\left[\; g(\eta-z)+\frac{\partial}{\partial t}\int_{z}^{\eta} w\,dz+\frac{\partial}{\partial x}\int_{z}^{\eta} uw\,dz-w^2(z)\;\right] \tag{3.4}$$

This expression for $p(z)$ can now be used to remove the pressure terms from the horizontal momentum equation. This requires some assumptions about the vertical structure of the flow to be made.

3.2.3 The non-linear shallow water equations

The NLSW equations, also called the finite amplitude shallow water equations, are derived assuming that $\varepsilon = O(1)$ and $\mu \ll 1$. The vertical acceleration is $O(\mu)$ and is therefore neglected, and the expression for $p(z)$ reduces to

$$p(z) = \rho g(\eta - z) \tag{3.5}$$

In other words, the pressure is hydrostatic to $O(\mu)$.

Ignoring the term $g\eta\partial\eta/\partial x$, substitution of (3.5) for $p(z)$ in the momentum equation (3.3) yields

$$\frac{\partial}{\partial t}\int_{-h}^{\eta} u\,dz+\frac{\partial}{\partial x}\int_{-h}^{\eta} u^2\,dz+gh\frac{\partial \eta}{\partial x}=0 \tag{3.6}$$

Equations (3.6) and (3.2) describe the motion of non-dispersive, non-linear waves. The phase celerity is independent of the wave number k, and is defined as $c^2 = g(h+\eta)$. This expression for c implies that the wave crest travels faster than the wave trough which leads

to the continual steepening of the wave front (as a result, the NLSW equations do not have solution of permanent form). This is known as *amplitude dispersion.* This steepening of the wave front can be balanced by allowing for some frequency dispersion: the effect of frequency dispersion is that the higher harmonics responsible for the steepening of the wave front travel much slower than the basic wave (the wave celerity is now a function of both local depth and wave number). From the derivation of the NLSW equations it is clear that these equations do not include frequency dispersion. The classical Boussinesq equations on the other hand allow for weakly dispersive, weakly non-linear waves.

3.2.4 The Boussinesq approximation

If it is assumed that $O(\varepsilon) \approx O(\mu) \ll 1$, terms of $O(\varepsilon)$ as well as terms of $O(\mu)$ are retained, and the high order non-linear and dispersive terms may be neglected[1]. Equation (3.4) reduces to

$$p(z)=\rho\left[g(\eta-z)+\frac{\partial}{\partial t}\int_{z}^{\eta} w\,dz\ \right] \tag{3.7}$$

This now exhibits frequency dispersion as a result of including the effect of the vertical acceleration ($O(\mu)$) on the pressure distribution, which is therefore no longer hydrostatic.

An expression for the vertical velocity w may be obtained from the continuity equation (3.1a) in terms of the horizontal velocity by vertical integration from the sea bed to an arbitrary level z:

$$w(z)=-\frac{\partial}{\partial x}\int_{-h}^{z} u\,dz \tag{3.8}$$

Substitution of equations (3.7) and (3.8) for $p(z)$ and $w(z)$ in the momentum equation (3.3) yields

$$\frac{\partial}{\partial t}\int_{-h}^{\eta} u\,dz+\frac{\partial}{\partial x}\int_{-h}^{\eta} u^2\,dz+gh\frac{\partial \eta}{\partial x}+\psi=0 \tag{3.9a}$$

where

$$\psi=-\int_{-h}^{0}\frac{\partial^2}{\partial x\,\partial t}\int_{z}^{0}\frac{\partial}{\partial x}\int_{-h}^{z} u\,dz\,dz\,dz \tag{3.9b}$$

Notice that all non-linear contributions to ψ have been neglected.

Let us define the depth-integrated velocity P, and the momentum flux M as

---

[1] Note that assuming $O(\varepsilon^2) \approx O(\mu)$ leads to the retention of some nonlinear effects in the dispersive terms, resulting in the so-called Serre equations.

$$P = \int_{-h}^{\eta} u dz \quad \text{and} \quad M = \int_{-h}^{\eta} u^2 dz$$

Assuming a uniform vertical distribution of the horizontal velocity, the expression for the dispersive term ψ then reduces to:

$$\psi = \frac{h^3}{6}\frac{\partial^3 u}{\partial x^2 \partial t} - \frac{h^2}{2}\frac{\partial^3 (uh)}{\partial x^2 \partial t}$$

while the momentum flux simplifies to

$$M = \frac{P^2}{d}$$

Since all non-linear contributions to ψ arising from the difference between d and h have been neglected, it is consistent to express the dispersive term as:

$$\psi = \frac{h^3}{6}\frac{\partial^3 (P/h)}{\partial x^2 \partial t} - \frac{h^2}{2}\frac{\partial^3 P}{\partial x^2 \partial t} \tag{3.10}$$

In terms of the depth-integrated velocity the horizontal momentum equation and continuity equation become:

$$\frac{\partial P}{\partial t} + \frac{\partial (P^2/d)}{\partial x} + gh\frac{\partial \eta}{\partial x} + \frac{h^3}{6}\frac{\partial^3 (P/h)}{\partial x^2 \partial t} - \frac{h^2}{2}\frac{\partial^3 P}{\partial x^2 \partial t} = 0 \tag{3.11a}$$

$$\frac{\partial \eta}{\partial t} + \frac{\partial P}{\partial x} = 0 \tag{3.11b}$$

The set of equations (3.11) describes the motion of weakly dispersive, weakly non-linear waves propagating over changing bathymetry. It is emphasised here that their derivation is based on the assumption that ε and μ are small and of the same order. The limiting cases are obtained for $\varepsilon << \mu$ (linear long waves) and $\varepsilon >> \mu$ (finite amplitude long waves).

The Boussinesq equations only differ from the NLSW equations by the third order derivative terms in the momentum equation. The derivation shows that it is this (dispersive) term that accounts for the effects of w on the pressure distribution. In contrast with the NLSW equations, it is possible to obtain solutions with permanent wave form.

At this point, the implications of the shallow water assumption ($\mu << 1$) need to be emphasised. First, it limits the application of the equations to fairly long waves. This may

be expressed as $h << L$, that is, this assumption also implies that the wave properties vary little in a distance of the same order as the depth (Peregrine, 1972). Dingemans (1997) demonstrates this statement by showing that the bottom slope h_x is at most $O(\mu^{1/2})$, that is, the slope should be at most so large that at least one wave length fits in the inhomogeneity region[1]. In the following, the bottom slope is assumed small, and as a result, higher order derivatives (profile curvature) and product of derivatives may be neglected. The momentum equation (3.11) simplifies to :

$$\frac{\partial P}{\partial t} + \frac{\partial (P^2 / d)}{\partial x} + gh\frac{\partial \eta}{\partial x} = \frac{h^2}{3}\frac{\partial^3 P}{\partial x^2 \partial t} + \frac{1}{3}h\frac{\partial h}{\partial x}\frac{\partial^2 P}{\partial x \partial t} \qquad (3.12)$$

The small bottom slope assumption implies that $h_x << \mu^{1/2}$. The application of (3.12) is therefore limited to slowly varying bathymetries ($h_x L/h << 1$).

These equations are equivalent to those derived using a perturbation approach and assuming that the horizontal velocity profile has a quadratic variation over the depth (Dingemans, 1997).

3.3 Improved linear frequency dispersion

3.3.1 Introduction

In section 3.2.4, a set of Boussinesq type equations was derived neglecting terms of $O(\varepsilon\mu, \mu^2)$, and expressed in terms of the free surface elevation and the depth-integrated velocity component. They are repeated here with, between square brackets, the relative order of magnitude of each terms:

$$\frac{\partial \eta}{\partial t} + \frac{\partial P}{\partial x} = 0 \qquad (3.13a)$$

[1] [ε]

$$\frac{\partial P}{\partial t} + \frac{\partial (P^2 / d)}{\partial x} + gh\frac{\partial \eta}{\partial x} = \frac{h^2}{3}\frac{\partial^3 P}{\partial x^2 \partial t} + \frac{1}{3}h\frac{\partial h}{\partial x}\frac{\partial^2 P}{\partial x \partial t} \qquad (3.13b)$$

[1] [ε] [1] [μ] [μ]

[1] defined by Dingemans (1997) as 'the region in which appreciable changes in water depth occur'. In other words, the length of the inhomogeneity region should be at least of the order of one wave length.

It is clear from the derivation of the Boussinesq equations that the resulting set of equations (3.13) are limited to fairly long waves with respect to the local water depth ($\mu << 1$). A direct consequence of this assumption is the incorrect representation of shorter waves. The steepening of the wave front as a wave travels in shallow water is a result of harmonic generation due to non-linear interactions, a process called amplitude dispersion (see section 3.2.3). The resulting higher harmonics, if correctly modelled, will have a tendency to counterbalance the steepening effect of the non-linear interactions by travelling slower than the fundamental wave, hence remaining behind it. These higher harmonics however may not be considered to be fairly long waves and their simulation by the present Boussinesq model (set of equations (3.13)) is questionable: the result of inaccurate frequency dispersion (terms $O(\mu)$) for shorter waves is that the computed wave form may be inaccurate.

Recently extensive research efforts have concentrated on improving linear frequency dispersion for Boussinesq type equations. This has resulted in a range of new forms of the Boussinesq equations where more second and third order derivatives (terms $O(\mu)$) were introduced. This work was reviewed in section 2.2. Here, the method proposed by Madsen, Murray and Sørensen (1991) will be followed.

Because the limitation to relatively shallow water is the primary factor affecting the applicability of the Boussinesq equations, it is important to understand the effect that the choice of the velocity variable has on the dispersion properties of the model. Thus, in section 3.3.2, the frequency dispersion properties of various forms of the Boussinesq equations for a flat bottom are studied. The modification of the Boussinesq equations to extend the accuracy of the dispersion relation is presented in section 3.3.3.

3.3.2 Frequency dispersion properties of the classical Boussinesq equations

In order to assess the frequency dispersion properties of a set of Boussinesq equations, and hence determine their relative depth limitation, the linear dispersion relation of the given equation is compared with the exact linear dispersion relation given by:

$$\frac{c^2}{gh} = \frac{\tanh kh}{kh} \tag{3.14}$$

Madsen *et al.* (1991) compared the dispersion characteristics of three sets of linearised Boussinesq equation expressed in terms of the depth averaged velocity $\bar{u}$ (set equivalent to

set (3.13) restricted to flat beds), the bottom velocity u_b and the mean sea level velocity u_m. Each of these sets of equations is limited to flat beds. The derivation of the equations and their respective linear dispersion relation can be found in their paper. The latter may be expressed as follows:

$$\frac{c^2}{gh} = \frac{1 + Bk^2h^2}{1 + (B + \frac{1}{3})k^2h^2} \tag{3.15}$$

where $B = 0$ for the equations in $\overline{u}$

$B = 1/6$ " u_b

$B = -1/3$ " u_m

Hence the level at which the velocity is evaluated determines the dispersion properties of the equation. It may be shown that, for small *kh*, the solution converges towards the exact linear dispersion relation. As *kh* increases however, the departure from Stokes first order theory (linear theory) is greater. A comparison of these phase celerities with the exact linear solution is shown in figure 3.2. It is clear that the equations in u_m give the worse results. For $kh > 1.75$, solutions to the dispersion relation cannot be found. The equations in $\overline{u}$ on the other hand yield the best phase properties. However, the phase errors for larger *kh* are still significant and limit the application of this model to small relative depths.

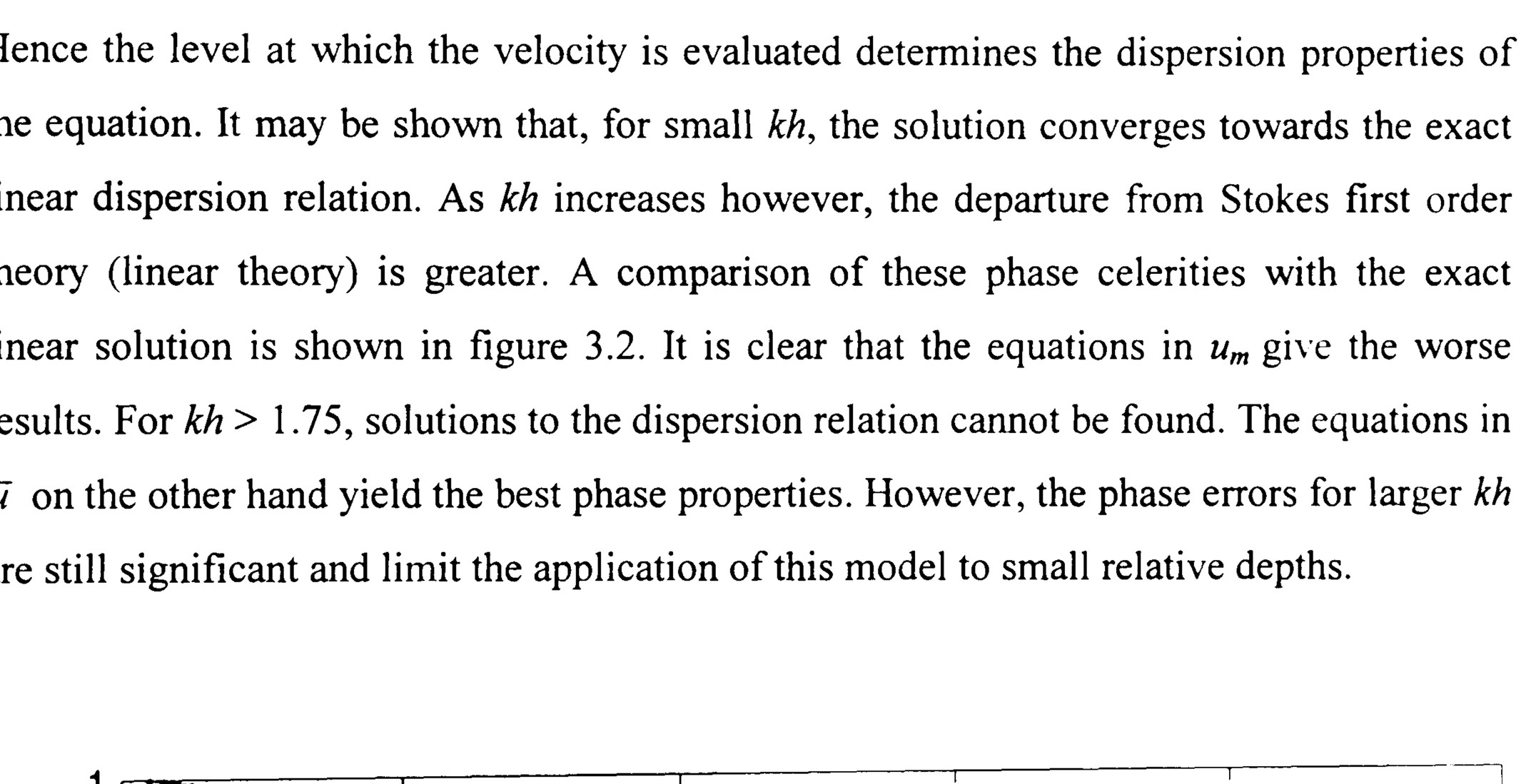

Figure 3.2 Comparison of phase celerities for various forms of the Boussinesq equations with Stokes first order theory. ------ $B = -1/3$, ------ $B = 0$, ——— exact, ... $B = 1/15$, ... $B = 1/6$. c is normalised with $(gh)^{1/2}$

In order to extend the applicability of the Boussinesq equations to larger *kh*, *B* may be considered as a curve fitting parameter chosen so that equation (3.15) follows equation (3.14) as closely as possible, over as wide a range of *kh* as possible. For this purpose, Witting (1984) suggested a method by which the optimum value of *B* can be obtained by comparing equation (3.15) with the Padé approximant of (3.14). A Padé expansion of c^2 of order [1/1] gives an expression for (3.14) of the same form as (3.15), with $B = 1/15$ (Madsen *et al.*, 1991). Figure 3.2 shows that, indeed, a dispersion relation with $B = 1/15$ gives a better agreement than with $B = 0$. Madsen *et al.* (1991) carried out the same analysis for group velocities, and came to the same conclusion.

3.3.3 Boussinesq equations with improved frequency dispersion

From section 3.3.2 it is clear that the derivation of the Boussinesq equations for which the coefficient *B* could explicitly be chosen (so as to fit Stokes first order theory) would be a great improvement. There are a number of ways by which this has been done (section 2.2). Madsen *et al.*'s (1991) approach was to directly manipulate the (high order) dispersive terms. Their method is illustrated here.

Since the non-linear and dispersive terms are of higher order, the linear long wave approximation

$$\frac{\partial P}{\partial t} + gh\frac{\partial \eta}{\partial x} \approx 0$$

may be used to manipulate terms of higher order without any loss of accuracy (Mei, 1989; Whitham, 1974; Long, 1964). By spatial differentiation, and neglecting second order spatial derivatives of the still water depth, we get:

$$\frac{\partial^3 P}{\partial x^2 \partial t} + 2g\frac{\partial h}{\partial x}\frac{\partial^2 \eta}{\partial x^2} + gh\frac{\partial^3 \eta}{\partial x^3} \approx 0 \qquad (3.16)$$

Addition of the product of Bh^2 times the left hand side terms in (3.16) to the standard Boussinesq momentum equation for slowly varying bathymetries gives:

$$\frac{\partial \eta}{\partial t} + \frac{\partial P}{\partial x} = 0 \qquad (3.17a)$$

$$\frac{\partial P}{\partial t} + \frac{\partial (P^2/d)}{\partial x} + gh\frac{\partial \eta}{\partial x} = (\frac{1}{3} + B)h^2\frac{\partial^3 P}{\partial x^2 \partial t} + Bgh^3\frac{\partial^3 \eta}{\partial x^3}$$

$$+ h\frac{\partial h}{\partial x}\left[\frac{1}{3}\frac{\partial^2 P}{\partial t \partial x} + 2Bgh\frac{\partial^2 \eta}{\partial x^2}\right] \qquad (3.17b)$$

This new set of equations has the dispersion relation (3.15); B can explicitly be chosen so as to fit (3.14) (optimum B = 1/15). Non-dimensionalisation shows that the left hand side terms in (3.16) are $O(\varepsilon,\mu)$, and are multiplied by $2\mu hB$. The terms added to the original Boussinesq equations are therefore $O(\varepsilon\mu,\mu^2)$ (Dingemans, 1997). Hence, for small kh, or long waves, these additional terms will have no effect: μ terms are small, hence the higher order terms introduced, which are $O(\varepsilon\mu,\mu^2)$, are very small and have no effect on the solution. On the other hand, for larger kh, or shorter waves (higher harmonics), the newly introduced terms $O(\varepsilon\mu,\mu^2)$ become significant.

3.3.4 Linear shoaling analysis

Madsen & Sørensen (1992) carried out a linear shoaling analysis on the modified equations. The linear shoaling coefficient, or linear shoaling gradient, is defined as

$$\alpha = \frac{a_x / a}{h_x / h}$$

where a is the wave amplitude, and the subscript x denotes differentiation with respect to space. Details of this analysis may be found in their paper. The resulting shoaling coefficients for the new set of equations (3.17) with B=0 and B=1/15 are compared to Stokes first order theory on figure 3.3. It is clear that the accuracy of the dispersion relation affects the linear shoaling behaviour of the model. The standard Boussinesq equations (B=0) lead to major discrepancies for kh larger than 1. The modified Boussinesq equations with B=1/15 however show an excellent agreement for kh as large as 4.5.

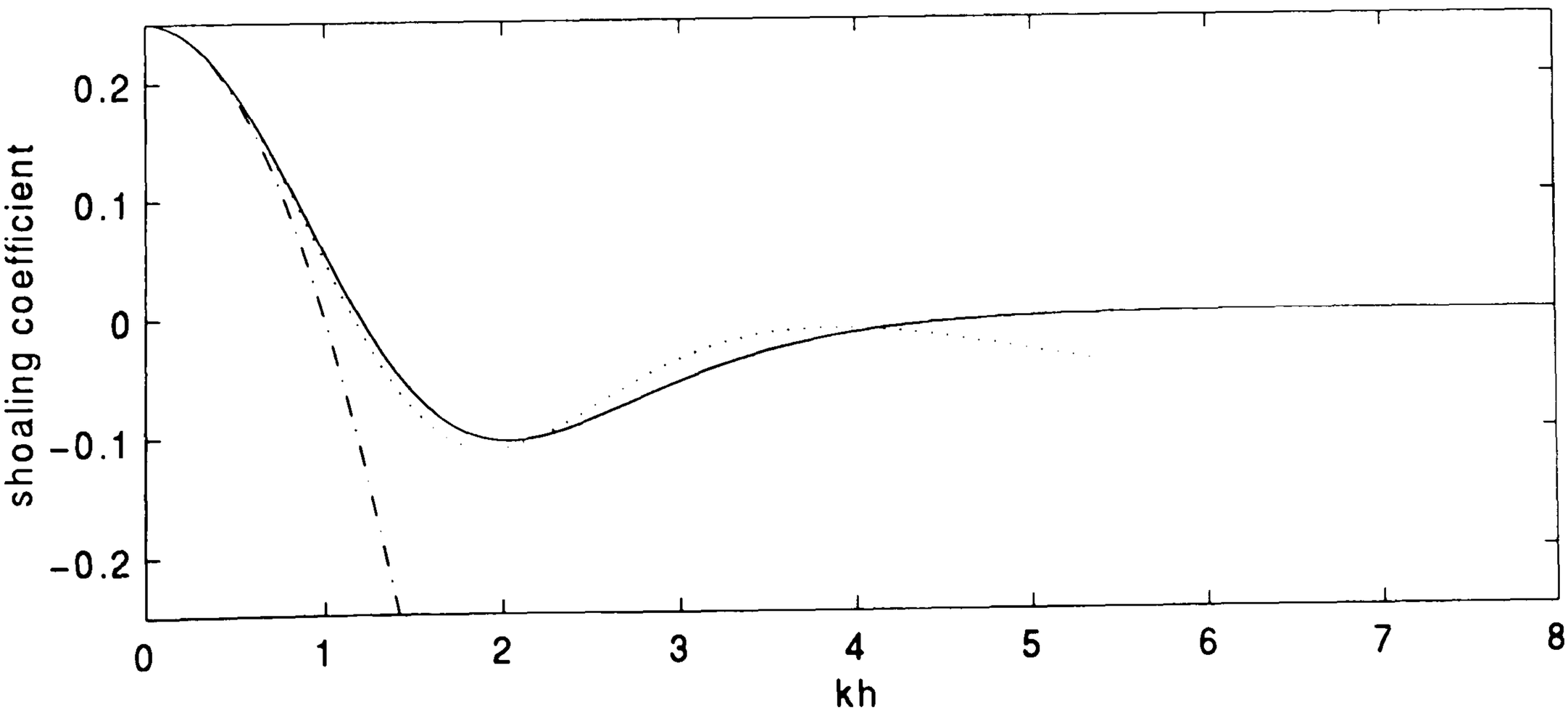

Figure 3.3 Comparison of linear shoaling coefficient α for equation (3.17) with B=0 (- - - - - -) and B=1/15 (.....), with Stokes first order theory (———)

Madsen and Sørensen have also shown a major dependence of the linear shoaling properties of the model on the bed slope terms, the removal of which resulted in large overestimation of the shoaling gradient. Dingemans(1997) carried out a shoaling analysis for 4 sets of Boussinesq equations having the same linear dispersion properties, but different bed slope terms. He came to the same conclusion as Madsen and Sørensen, and further shows that the equations with the bed slope terms as in Madsen and Sørensen's model yields the best shoaling properties.

3.4 Incorporation of wave breaking

3.4.1 Introduction of the effect of surface rollers in the momentum equation

Wave breaking is modelled using the concept of the surface roller as formulated by Schäffer *et al.* (1993). This concept assumes spilling breakers. The surface roller is regarded as a passive bulk of water being carried by the wave, at the wave celerity. The roller generation is assumed to introduce a non-uniform velocity profile. The effect of wave breaking is incorporated in the depth-integrated momentum equation through an additional convective term resulting from the new non-uniform velocity profile. Schäffer *et al.*(1993) follow the approach by Svendsen (1984a) whereby the vertical profile of the horizontal velocity is simplified to:

$$u = c \qquad \text{for} \qquad \eta-\delta \le z \le \eta$$

$$u = u_0 \qquad \text{for} \qquad -h \le z < \eta-\delta$$

δ is the roller thickness and is defined on figure 3.4., which also shows the new vertical distribution of the horizontal velocity u.

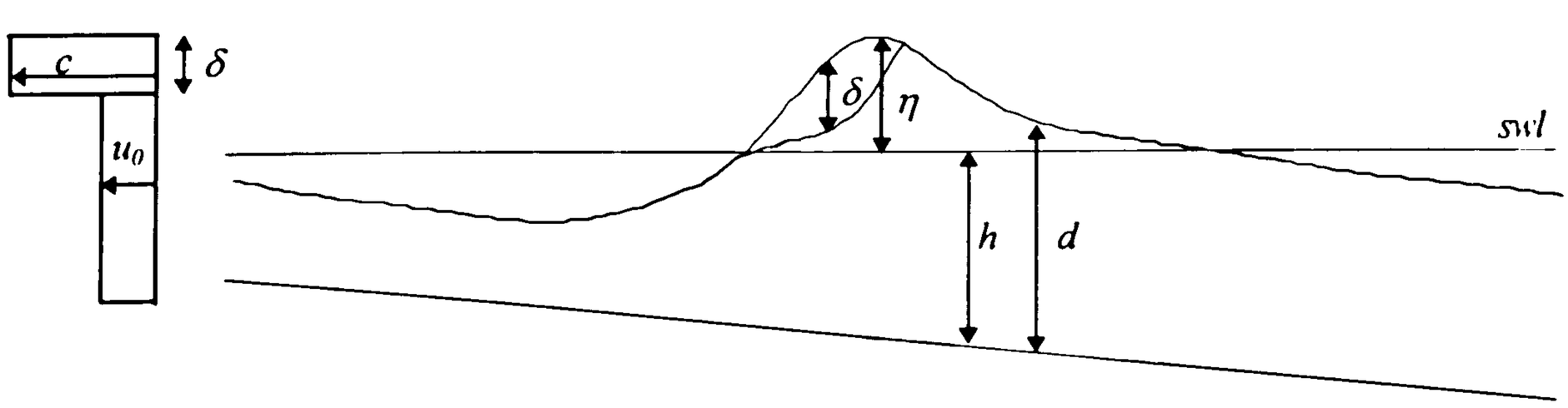

Figure 3.4 Definition sketch of a surface roller and assumed velocity profile in the presence of a roller

Introducing the new velocity profile into the expressions for the depth-integrated velocity $P = \int_{-h}^{\eta} u dz$ and the momentum flux $M = \int_{-h}^{\eta} u^2 dz$ gives

$$P = u_0(d-\delta)+c\delta \qquad \text{and} \qquad M = u_0^2(d-\delta)+c^2\delta \qquad (3.18\ a\ \&\ b)$$

Hence the effect of the surface rollers is introduced by accounting for the effect of the non-uniform velocity distribution. The excess momentum flux due to the non-uniform velocity distribution can now be defined as:

$$R = M - \frac{P^2}{d} = (c-u_0)^2\,\delta\left(1-\frac{\delta}{d}\right) \qquad (3.19)$$

(3.18a) rearranged gives an expression for $(c-u_0)$:

$$(c-u_0) = \frac{cd-P}{d-\delta}$$

which, substituted into (3.19), gives:

$$R = \delta\left(c-\frac{P}{d}\right)^2\left(1-\frac{\delta}{d}\right)^{-1} \qquad (3.20)$$

The governing equations therefore become:

$$\frac{\partial \eta}{\partial t} + \frac{\partial P}{\partial x} = 0 \qquad (3.21a)$$

$$\frac{\partial P}{\partial t} + \frac{\partial R}{\partial x} + \frac{\partial (P^2/d)}{\partial x} + gh\frac{\partial \eta}{\partial x} = (\frac{1}{3}+B)h^2\frac{\partial^3 P}{\partial x^2 \partial t} + Bgh^3\frac{\partial^3 \eta}{\partial x^3}$$
$$+h\frac{\partial h}{\partial x}\left[\frac{1}{3}\frac{\partial^2 P}{\partial t \partial x} + 2Bgh\frac{\partial^2 \eta}{\partial x^2}\right] \qquad (3.21b)$$

3.4.2 Geometrical definition of the surface roller - breaking criterion

The breaking criterion, which is related to the local slope of the water surface, determinates the thickness of the roller δ from simple geometry: breaking is initiated when the local slope of the free surface ϕ reaches a threshold ϕ_B. The water above the tangent of the slope $\tan\phi$ is assumed to belong to the roller, thus defining δ. ϕ then exponentially decays to ϕ_o as described by equation (3.22). This time variation of ϕ is chosen by virtue of the fact that breakers often transform rather quickly into the bore-like stage:

$$\tan\phi = \tan\phi_o + (\tan\phi_B - \tan\phi_o)\exp\left(-\ln 2\frac{t - t_B}{t^*}\right) \tag{3.22}$$

t^* controls the rate of decay of ϕ. t_B is the time at which breaking is initiated. The fourth parameter involved in the simulation of wave breaking is the roller shape parameter f_δ (figure 3.5). After the determination of the surface roller, δ is multiplied by f_δ purely to compensate for the simple way of separating the roller from the rest of the flow. Breaking ceases if the local slope becomes less than $tan\phi$ again. The waves are absorbed by a numerical sponge layer at the shoreline boundary (section 3.5.5). The model therefore assumes that there is no reflection from the inner surf zone and swash zone. This is a significant point which we will come back to in section 4.2.4 and throughout the thesis.

Finally, the excess momentum due to the surface roller requires the determination of the phase celerity c (equation (3.20)). In order to avoid the introduction of additional differential equations, an analytical expression for c was chosen as 1.3 the linear shallow water wave celerity $\sqrt{gh}$. This approximation is in agreement with the experiments carried out by Stive (1980).

Figure 3.5 Geometrical definition of a surface roller.

Although this is a simple wave breaking model that relies on several empirical parameters and that still assumes weakly non-linear waves, Schäffer *et al.* (1993) showed its capabilities to predict various quantities and simulate various surf zone processes. Initiation and cessation of wave breaking, cross-shore evolution of the wave height and mean water level, horizontal shift between the break point and the point at which the set up in the mean water level is initiated are all reasonably well predicted. Computed and measured time series of surface elevation were also directly compared and indicated satisfactory wave shape and harmonic generation predictions. These validations were carried out for both regular and irregular waves measured in small scale laboratory experiments.

The main limitation of this model is that the wave breaking simulation relies on four empirical parameters. The figures recommended by Schäffer *et al.* for ϕ_B, ϕ_o, t^* and f_δ are 20°, 10°, T/10 and 1.5 respectively, where T is a typical wave period. One of the objectives of this study is to test the sensitivity of the model to these four free parameters. It is important to note that since this model is able to predict weakly nonlinear wave fields only, it tends to underestimate the wave height in the region of breaking. Consequently, the local slope of the water surface will tend to be underestimated in this region. The value recommended by Schäffer *et al.* for ϕ_B is therefore chosen smaller than the actual wave steepness at the breaking point.

3.5 The numerical scheme

3.5.1 Introduction

The numerical scheme used here is the one developed by Abbott *et al.* (1984) for the set of equations (3.13), and extended by Madsen *et al.* (1991) to solve (3.17). The equations are solved using a time centred implicit finite difference scheme on a space-staggered rectangular grid as described in figure 3.6. In the following, the subscript i indicates the horizontal co-ordinate ($x_i = \Delta x_1 + \Delta x_2 + \ldots + \Delta x_{i-1}$) and the superscript n indicates time levels ($t^n = n\Delta t$).

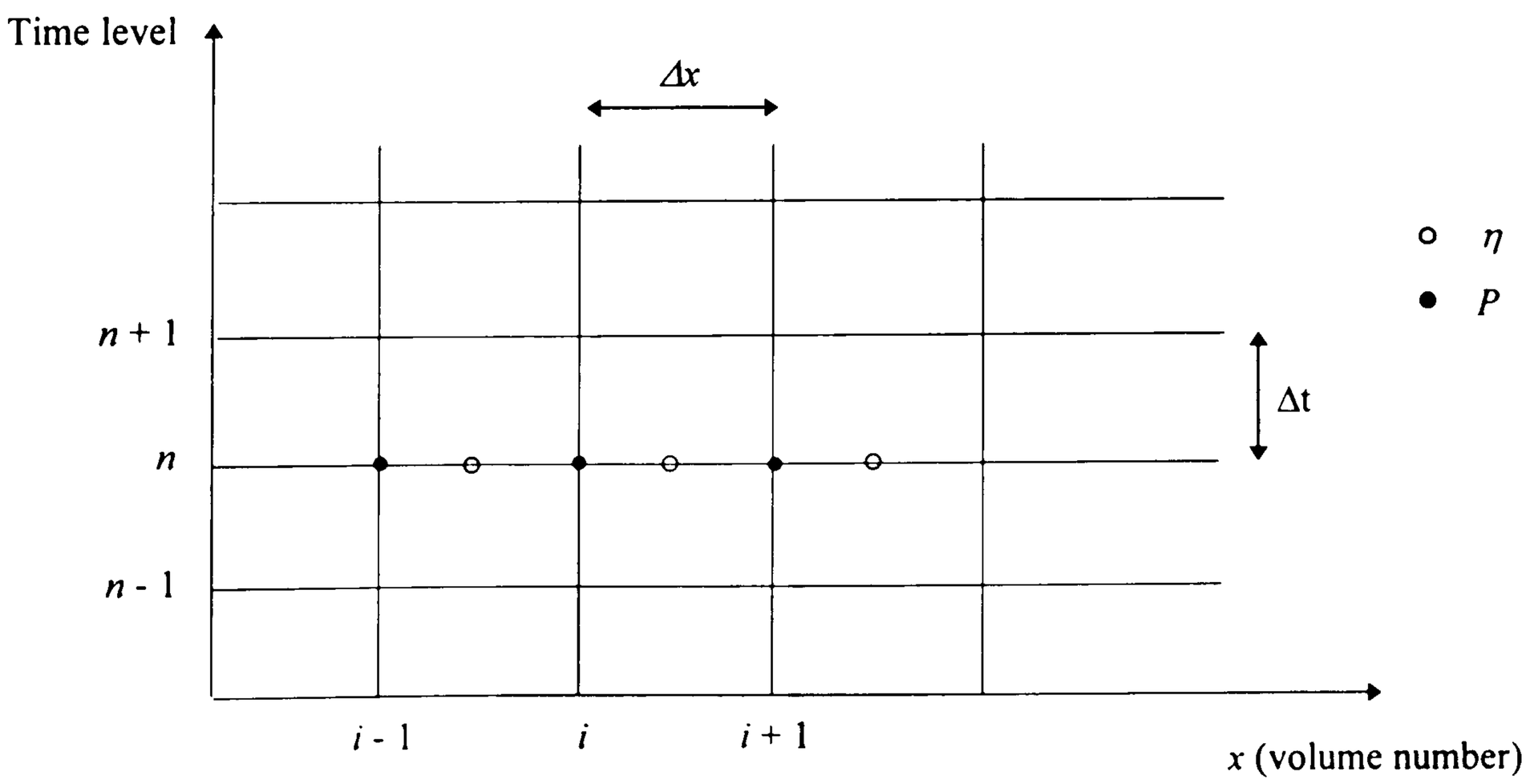

Figure 3.6 Computational grid

3.5.2 Finite difference approximation

The governing equations (3.21) are expressed in finite difference form using, as far as possible, a time-centred central difference implicit scheme:

$$\frac{\eta_i^{n+1}-\eta_i^n}{\Delta t}+\frac{1}{\Delta x}\left(\frac{P_{i+1}^{n+1}+P_{i+1}^n}{2}-\frac{P_i^{n+1}+P_i^n}{2}\right)\approx 0 \qquad (3.23a)$$

$$\frac{P_i^{n+1}+P_i^n}{\Delta t}+$$

$$\frac{1}{\Delta x}\left[\frac{\delta_i^n+\delta_i^{n+1}}{2}\left(1-\frac{\delta_i^n+\delta_i^{n+1}}{2d_i^{n+1/2}}\right)^{-1}\left(1.3\sqrt{gh_i}-\frac{P_i^n+P_{i+1}^n}{2d_i^n}\right)\left(1.3\sqrt{gh_i}-\frac{P_i^{n+1}+P_{i+1}^{n+1}}{2d_i^{n+1}}\right)\right]$$

$$-\frac{1}{\Delta x}\left[\frac{\delta_{i-1}^n+\delta_{i-1}^{n+1}}{2}\left(1-\frac{\delta_{i-1}^n+\delta_{i-1}^{n+1}}{2d_{i-1}^{n+1/2}}\right)^{-1}\left(1.3\sqrt{gh_{i-1}}-\frac{P_{i-1}^n+P_i^n}{2d_{i-1}^n}\right)\left(1.3\sqrt{gh_{i-1}}-\frac{P_{i-1}^{n+1}+P_i^{n+1}}{2d_{i-1}^{n+1}}\right)\right]+$$

$$\frac{1}{\Delta x}\left(\frac{P_{i+1}^{n+1}+P_i^{n+1}}{2}\frac{P_{i+1}^n+P_i^n}{2d_i^{n+1/2}}-\frac{P_i^{n+1}+P_{i-1}^{n+1}}{2}\frac{P_i^n+P_{i-1}^n}{2d_{i-1}^{n+1/2}}\right)+$$

$$g\frac{d_i^{n+1/2}+d_{i-1}^{n+1/2}}{2\Delta x}\left(\frac{\eta_i^{n+1}+\eta_i^n}{2}-\frac{\eta_{i-1}^{n+1}+\eta_{i-1}^n}{2}\right)-$$

$$(B+\frac{1}{3})\frac{(h_i+h_{i-1})^2}{4\Delta t\Delta x^2}\left(P_{i+1}^{n+1}-2P_i^{n+1}+P_{i-1}^{n+1}-P_{i+1}^n+2P_i^n-P_{i-1}^n\right)-$$

$$\frac{1}{3}\frac{h_i+h_{i-1}}{2}\frac{h_i-h_{i-1}}{\Delta x}\frac{1}{\Delta t}\left(\frac{P_{i+1}^{n+1}-P_{i-1}^{n-1}}{2\Delta x}-\frac{P_{i+1}^n-P_{i-1}^n}{2\Delta x}\right)-$$

$$Bg\left(\frac{h_i+h_{i-1}}{2}\right)^3\frac{1}{\Delta x^3}\left(\eta_{i+1}-3\eta_i+3\eta_{i-1}-\eta_{i-2}\right)^{n+1/2}-$$

$$2Bg\left(\frac{h_i+h_{i-1}}{2}\right)^2\left(\frac{h_i-h_{i-1}}{\Delta x}\right)\frac{1}{2\Delta x^2}\left(\eta_{i+1}-\eta_i-\eta_{i-1}+\eta_{i-2}\right)^{n+1/2}\approx 0 \qquad (3.23b)$$

where the surface elevations at time level n+1/2 are estimated explicitly from the continuity equation:

$$\eta_i^{n+1/2}=\eta_i^n+\frac{\Delta t}{2\Delta x}(P_i^n-P_{i+1}^n)$$

hence, assuming that the bed is fixed (i.e. $\partial\eta/\partial t=\partial d/\partial t$),

$$d_i^{n+1/2}=d_i^n+\frac{\Delta t}{2\Delta x}(P_i^n-P_{i+1}^n)$$

The discretisation of the wave breaking term $\partial R/\partial x$ also involved an explicit estimation of the total water depth at n+1 with:

$$d_i^{n+1} = d_i^n + \frac{\Delta t}{\Delta x}(P_i^n - P_{i+1}^n)$$

Following Verwey (1980), the nonlinear convective term $\partial(P^2/d)/\partial x$ was discretized assuming $(P^2)^{n+1/2} = P^n P^{n+1}$.

The above approximations suggest that care should be taken when choosing the time increment.

3.5.3 Truncation error correction

In the discretisation it is assumed that the variation of the flux and elevation can be described by Taylor series that are truncated after the 2nd order derivative terms. Abbott *et al.* (1984) pointed out that this truncation error is of the same order of magnitude as the dispersive term. In order to identify and eliminate these error terms, a truncation error analysis was performed. It gave rise to the following correction terms to the left hand side of equation (3.23b):

$$-\frac{\Delta t^2}{24}\frac{\partial^3 P}{\partial t^3} - gd\frac{\Delta x^2}{24}\frac{\partial^3 \eta}{\partial x^3} - gd\frac{\Delta t^2}{8}\frac{\partial^3 \eta}{\partial x \partial t^2}$$

which, invoking the linearised long wave equation (Abbott, 1978b) may be re-written

$$\left(gd\frac{\Delta t^2}{12} + \frac{\Delta x^2}{24}\right)\frac{\partial^3 P}{\partial^2 x \partial t}$$

3.5.4 Method of solution

The finite difference system of equation (3.23) may be rearranged in the form

$$a_k P_{i-1}^{n+1} + b_k \eta_{i-1}^{n+1} + c_k P_i^{n+1} = d_k$$

$$q_{k+1} P_{i-1}^{n+1} + a_{k+1} \eta_{i-1}^{n+1} + b_{k+1} P_i^{n+1} + c_{k+1} \eta_i^{n+1} + r_{k+1} P_{i+1}^{n+1} = d_{k+1}$$

in which η^{n+1} and P^{n+1} are the unknown variables, and the coefficients q, a, b, c, r and d are functions of known quantities $(P^n, \eta^n, \Delta t, \Delta x \ldots)$. At each time level, the finite difference equations may be assembled in the following matrix system:

$$\begin{bmatrix} 1 & & & & & & & \\ a_1 & b_1 & c_1 & & & & & \\ q_2 & a_2 & b_2 & c_2 & r_2 & & & \\ & & a_3 & b_3 & c_3 & & & \\ & & . & . & & & & \\ & & & . & . & & & \\ & & & & a_{II\bullet 2} & b_{II\bullet 2} & c_{II\bullet 2} & \\ & & & & & & 1 & \end{bmatrix} \begin{bmatrix} P_1 \\ \eta_1 \\ P_2 \\ \eta_2 \\ \\ \\ \eta_{II} \\ P_{II+1} \end{bmatrix} = \begin{bmatrix} * \\ d_1 \\ d_2 \\ d_3 \\ \\ \\ d_{II\bullet 2} \\ * \end{bmatrix} \tag{3.24}$$

where the first two rows of the matrix correspond to the first volume, and so on. The stars represent boundary conditions. In the present form, the model is restricted to flux boundary conditions only. An alternative will be introduced in section 3.5.5. This system of equations must be solved at each time step, yielding the new P and η values. It is first brought to a tri-diagonal form using the Gaussian elimination technique. The resultant (tri-diagonal) matrix is then solved using the double sweep method (Abbott and Basco, 1985).

3.5.5 Initial and boundary conditions

The initial conditions are those of a cold start. The surface elevation and computational velocity were set to zero throughout the computational domain at $t = 0$. Two alternatives were used for the wave generation boundary condition. Larsen and Dancy (1983) devised a method for generating the incident wave field inside the computational domain. This has the advantage of allowing the implementation of an absorbing seaward boundary using a so-called sponge layer. Alternatively, a wave generation boundary condition requiring the prescription of the surface elevation at the boundary was sought. This involves the calculation of the boundary flux from the continuity equation. (3.24) then reads:

$$\begin{bmatrix} 1 & & & & & & & \\ b_1 & a_1 & c_1 & & & & & \\ a_2 & q_2 & b_2 & c_2 & r_2 & & & \\ & & a_3 & b_3 & c_3 & & & \\ & & . & . & & & & \\ & & & . & . & & & \\ & & & & a_{II\bullet 2} & b_{II\bullet 2} & c_{II\bullet 2} & \\ & & & & & & 1 & \end{bmatrix} \begin{bmatrix} \eta_1 \\ P_1 \\ P_2 \\ \eta_2 \\ \\ \\ \eta_{II} \\ P_{II+1} \end{bmatrix} = \begin{bmatrix} * \\ d_1 \\ d_2 \\ d_3 \\ \\ \\ d_{II\bullet 2} \\ * \end{bmatrix}$$

Absorption at the shoreward boundary (and possibly at the seaward boundary) is based on the concept of sponge layers. The principle is that both the flux and the surface elevation

are (artificially and exponentially) damped to zero by division by μ_i at each time level. μ_i follows:

$$\mu_i = (\mu_{\max} - 1)\left(\frac{N+1-i}{N}\right)^p + 1$$

where μ_{max} and p are constants, N is the number of volumes in the sponge layer, and i is an index whereby $i = 1$ corresponds to the boundary volume. Therefore, $\mu = \mu_{max}$ at the boundary, and $\mu = 1$ at the beginning of the sponge layer, and in the rest of the computational domain.

Chen and Liu (1995) argue that 'the highest order of the spatial derivative in the equations derived by Nwogu (1993) is one order higher than that in the conventional Boussinesq equations. This creates a difficulty in specifying appropriate boundary conditions and increases the numerical effort for solving these new equations'. The same problem transpires with Madsen and Sørensen's model: inspection of equation (3.23b) shows that the calculation of the high order spatial derivatives (additional third order terms in x) at the first internal flux point requires the specification of the surface elevation outside the boundary. Madsen and Sørensen recommend the prescription of the surface elevation and curvature at the incoming boundary. In this study it was initially chosen to approximate the solution by applying these terms from the second internal flux point only. For the cases studied here, this has been found to give satisfactory results. This is despite the fact that, for 2 of the runs investigated, the input consists of short waves. The effect of the simplification made in the implementation of the high order spatial derivatives is further discussed in section 3.6.3.

3.5.6 Numerical filter

Schäffer *et al.* (1993) recommended that an implicit numerical filter be used in combination with the roller momentum in order to secure a smooth and stable solution. The stabilising low pass filtering effect is obtained by a slightly forward time-centring of the spatial derivatives in the mass equation, and is applied in the vicinity of a surface roller. A weighting parameter α is therefore introduced so that 3.23a becomes:

$$\frac{\eta_i^{n+1} - \eta_i^n}{\Delta t} + \frac{1}{\Delta x}\left(\frac{\alpha P_{i+1}^{n+1} + (2-\alpha)P_{i+1}^n}{2} - \frac{\alpha P_i^{n+1} + (2-\alpha)P_i^n}{2}\right) \approx 0$$

Notice that if $\alpha = 1$, the original finite difference equation is recovered.

3.6 Preliminary testing of the model

3.6.1 Introduction

The numerical model was implemented using Salford FORTRAN, in a Windows environment. This section describes the testing of the source code. By assuming that the waves are propagating in one direction only, the Boussinesq equations ((3.13) restricted to a flat bed, i.e. high order term in h_x neglected) can be reduced to the Korteweg-deVries (KdV) equation. The KdV equation has for solution a periodic wave of constant form. The surface elevation of these waves is described by the cn-function (one of the Jacobian elliptic functions), which led to the name 'cnoidal' waves as an analogy to 'sinusoidal' waves. The numerical model was therefore tested against cnoidal wave solutions for wave propagation over a flat bed in section 3.6.2.1 and cnoidal wave shoaling in section 3.6.2.2. Further evaluation of the model consisted in testing its improved dispersion properties, over a flat bed in section 3.6.3.1, and over a slowly varying bathymetry in section 3.6.3.2. These tests were aimed at reproducing the results obtained by Madsen *et al.* (1991) and Madsen and Sørensen (1992) respectively. Finally, the implementation of wave breaking was verified with the tests presented by Schäffer *et al.* (1993) and results are submitted in section 3.6.4.

For all of the following tests, a time series of surface elevation is specified as the seaward boundary condition.

3.6.2 Propagation of a cnoidal wave

3.6.2.1 Flat bed

The numerical model's capability to simulate the propagation of nonlinear waves over a flat bed was tested with the cnoidal first order theory (Svendsen, 1974). Comparison of the propagation of cnoidal waves in a channel with a flat bottom is shown in figure 3.7. The depth of the channel is 10 m, and its length is 500 m. The cnoidal waves are generated at the seaward boundary with a wave height of 1 m, and a wave period of 15.5 sec. (wave length 150 m). Thus, $L/h = 15$ ($h/L_0 < 0.2$) and $Ur = 22.5$, which is well within the limits of the cnoidal theory[1]. Figure 3.5 shows that the surface elevation time series predicted by the model are in good agreement with the cnoidal theory.

---

[1] defined by $L/h > 6\text{-}7$ and $Ur > 15$ (Svendsen, 1974)

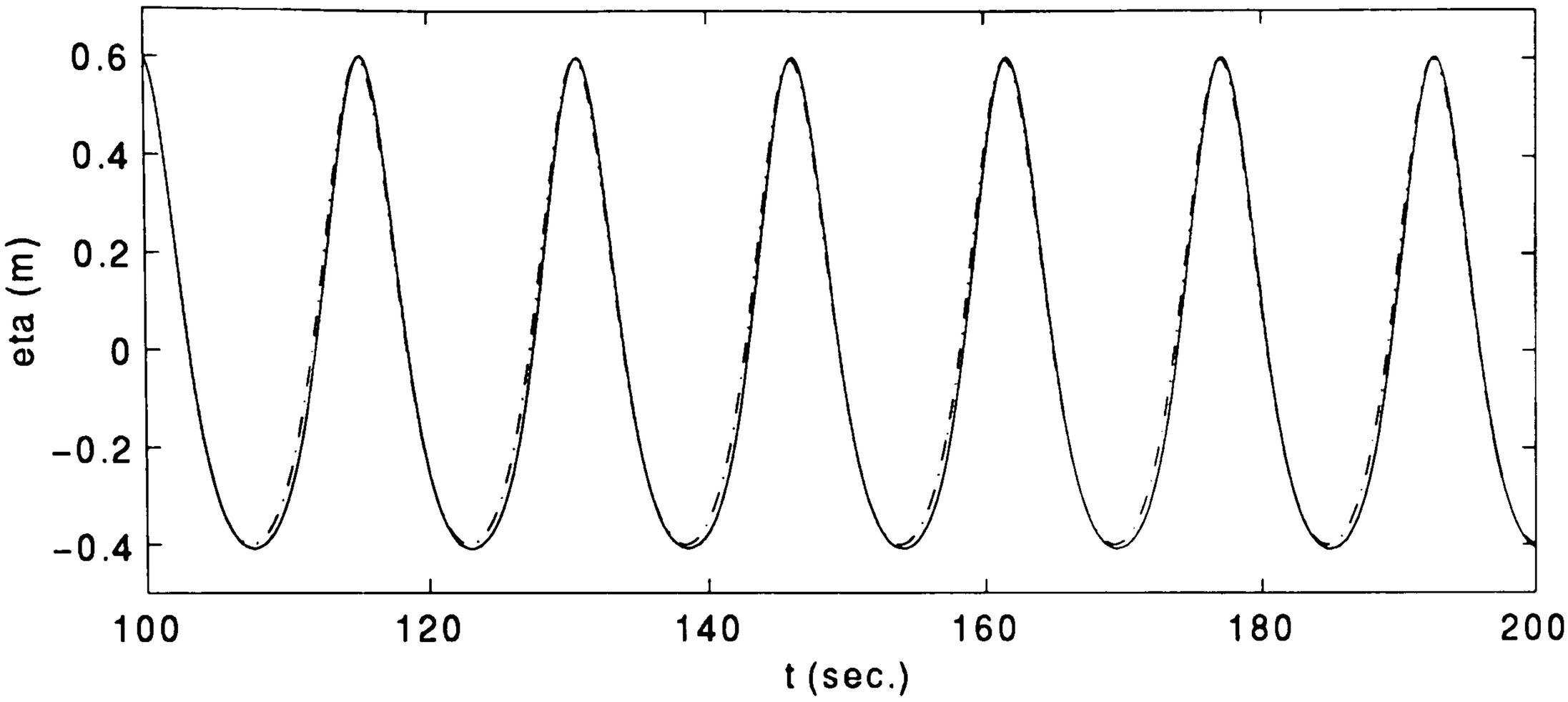

Figure 3.7 Wave propagation over a flat bed. Plot of theoretical (cnoidal, - - - - - -) and numerical (———) time series of the free surface elevation at x=300 m (H=1m, T=15.5sec., L=150m, Δx=2.5m, Δt=0.25sec.).

3.6.2.2 Sloping bed

The shoaling properties of the model for nonlinear waves were tested with the theory developed by Svendsen (1974) for cnoidal waves over a gently sloping bottom. At the seaward boundary, the depth of the channel is 10 m. The bed is flat for the first 140 m; it

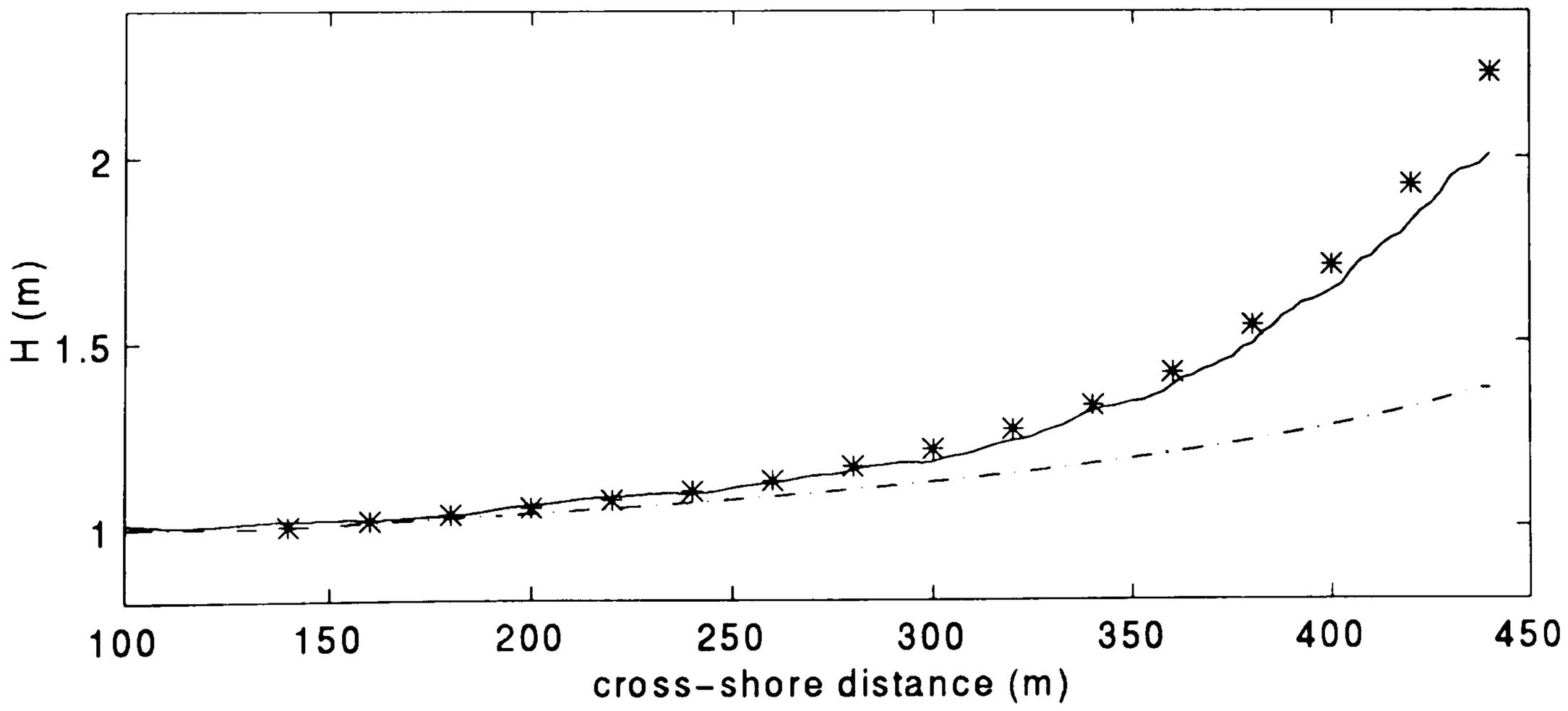

Figure 3.8 Wave shoaling test. Plot of theoretical (cnoidal, ✳ ; linear, - - - - - -) and predicted (———) wave height (H=1m, T=15.5sec., L=150m, Δx=2.5m, Δt=0.25sec., slope=1in53, slope starts at x=140m).

then has a constant slope of 1/53 from 140 m to 440 m. Finally, for the last 100 m the bottom is flat again with a water depth of 2.5 m. The same wave input is used as in the previous test, i.e. a wave height of 1 m, and a wave period of 15.5 sec, which was shown to be within the limits of the cnoidal theory. The wave height predicted by the linear theory is plotted along with wave height predicted by the cnoidal theory on figure 3.8. It confirms the well known fact that the cnoidal theory predicts a much faster increase in wave heights than the linear theory does. Figure 3.8 shows that the computed shoaling wave height is in good agreement with the cnoidal theory, with the exception of the last point for which H = 2m and the water depth is 2.5m, hence H/h = 0.8. This is an agreed figure for the wave breaking criterion, and therefore justifies the discrepancy between theoretical and predicted wave heights in this region where both the numerical and the analytical solutions fail.

3.6.3 Improved frequency dispersion

3.6.3.1 Flat bed

In order to verify the improved dispersion characteristics of the model, the following test case, proposed by Madsen *et al.* (1991), was studied: in a 4.2 m deep, 120 m long channel with a flat bed, a sinusoidal wave train was generated at the seaward boundary with H = 0.2 m and T = 2.5 sec., leading to h/L_0 = 0.43 (kh = 2.7). For this value of h/L_0, the standard Boussinesq equations ((3.13) or (3.17) with B = 0), lead to a phase celerity error of -12% (figure 3.2), while the improved equations with B = 1/15 lead to a celerity error of +1.7% only. This is illustrated in figure 3.9a (B=0) and 3.9b (B=1/15) where it is clear that the extension of the accuracy of the dispersion relation has resulted in a dramatic improvement of the model's performance for shorter waves.

It is notable however that the wave generation presents some irregularities even with B = 1/15, with the appearance of a 'hump' in the wave height for the first 7 m after generation. The wave height then stabilises at H = 0.22 m. This wave generation problem was anticipated in section 3.5.5. It is shown in section 3.6.3.2 that, in the case for which the condition $\mu \ll 1$ holds for the incident wave train, the wave generation is unaffected by the simplification made in the incorporation of the higher order spatial derivatives. For this case, the improved dispersion is still essential to the accurate description of the higher harmonic generated during shoaling and breaking. It appears from figure 3.9 that the simplification made in the implementation of the seaward boundary results in imperfections in the wave generation for cases where short waves are present in the prescribed incoming wave train. In the cases studied in this thesis however, wave

generation appeared to be affected by other more dominant factors. Wave generation is an essential part of a numerical model; it is also a difficult one which has incited considerable research. In the case of Boussinesq models, an intrinsic problem lies with the very fact that the model describes wave-wave interactions, and, as a result, the wave shapes tend to change constantly. This and the effects of wave reflection were found to dominate the accuracy of the wave generation in the cases studied in this thesis (section 5.6). It was thus decided *a posteriori* that the treatment of the seaward boundary[2] was reasonable in the context of this study.

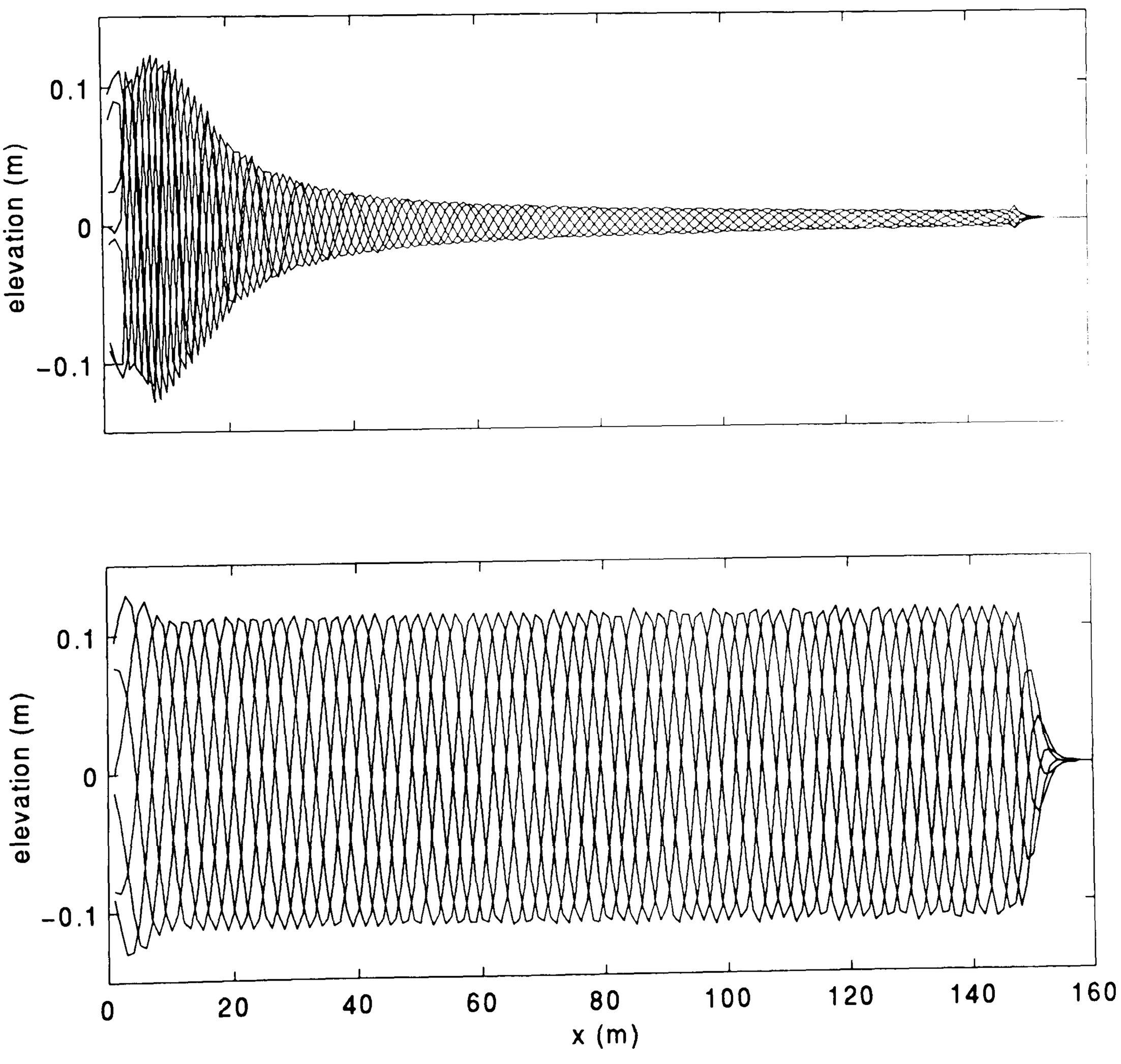

Figure 3.9 Wave propagation over a flat bed in deep water. Predicted surface elevation over 1 wave period. (top plot) B=0; (bottom plot) B=1/15 (H=0.2m, T=2.5sec., L=9.6m, Δx=0.75m, Δt=0.1sec.)

According to the linear theory, the theoretical wave length for this case is L_{th} = 9.65m. The wave length predicted by the model is slightly less at 9.5 m. The flux predicted by the

[2] c.f. section 3.5.5.

model is 0.43 m^2/s for the stabilised wave (H = 0.22 m). Again according to the linear theory, the theoretical flux for this case is P_{th} = 0.43 m^2/s, assuming a wave height of 0.22m. This demonstrates the good performance of the model for equivalent conditions. It also suggests that if an input wave height was sought by trial and error so as to obtain the prescribed wave height, the solution would yield good results. This method was applied by Wei and Kirby (1995).

Madsen *et al.* (1991) also verified the improved dispersion characteristics of the model with respect to wave group propagation and found the same spectacular improvement to the solution when B = 1/15.

3.6.3.2 Sloping bed

In order to test the shoaling properties of the model, Madsen and Sørensen (1992) conducted two test cases: with all nonlinear terms in the Boussinesq equations 'switched off', and with B = 1/15, a regular wave train with H = 0.1 m and T = 4 sec (deep water case) and T = 8 sec (intermediate water case) is set to travel over a 1/50 slope. The initial water depth is 13 m and the final water depth is 0.2 m. The bed is flat for the first 10 m. At the top of the slope, the waves are allowed to travel over a 50 m flat bed before reaching the sponge layer.

intermediate water

For the first test case, T = 8 sec., leading to kh = 1 (h/L_0 = 0.13) at the seaward end of the channel. Figure 3.10 shows a series of plots of surface elevation (covering one wave period), and a comparison between predicted and linear (Stokes first order) shoaling wave heights. The agreement is very satisfactory. The phase prediction of the model was checked by comparing the predicted number of waves in the channel with that predicted by Madsen and Sørensen. This proved satisfactory with 13 waves in both cases. From figure 3.2, it can be shown that for kh = 1, the relative error in the shoaling coefficient between linear theory and the Boussinesq equation with B = 0 is less than 1% (it is 0% for B = 1/15). Indeed, if this test is run with B = 0, it is found that the predicted wave is only slightly underestimated. This test thus demonstrates that indeed no loss of accuracy is incurred during the manipulation and introduction of the high order terms. Notice that for this case, the 'B-terms' in the Boussinesq equations being small, there is no problem of wave

generation, which confirms that the model may be used with confidence so long as $\mu << 1$ holds for the incident wave train.

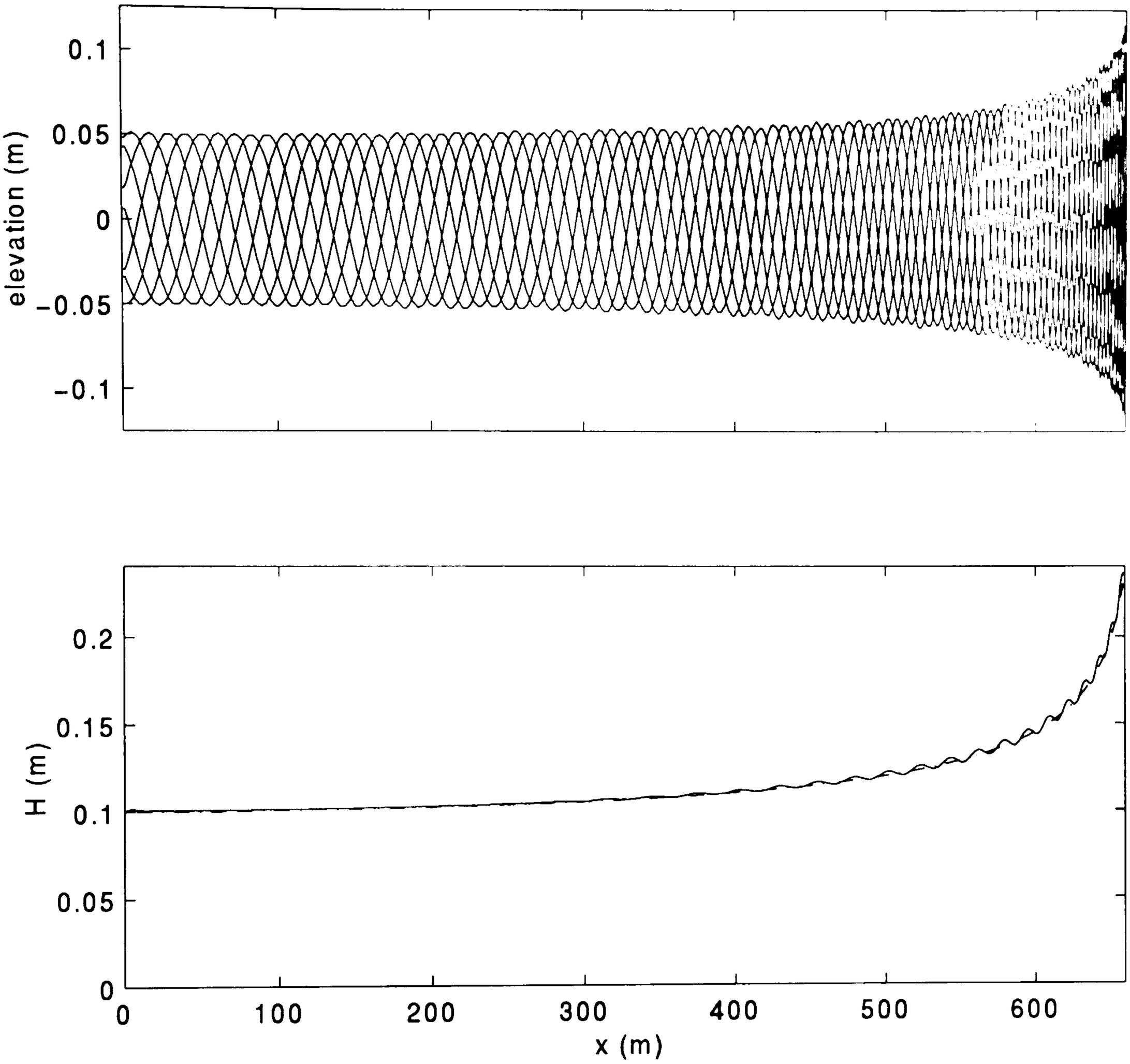

Figure 3.10 Wave shoaling in intermediate water. (top plot) predicted surface elevation over 1 wave period; (bottom plot) predicted (———) and theoretical (linear, - - - - - -) shoaling wave height (H=0.1m, T=8sec., L=78m, Δx=1m, Δt=0.16s, B=1/15).

deep water

For the deep water test case, T = 4 sec. , leading to kh = 3.3 (h/L_0 = 0.52) at the seaward end of the channel. Figure 3.11 shows a series of plots of surface elevation covering one wave period, and figure a comparison between predicted and linear (Stokes first order) shoaling wave heights. The resulting, stabilised wave height was 0.098 m. It is this figure that was used for the calculation of the linear shoaling. Again the agreement is satisfactory. The numerical predictions overestimate the linear theory in the late stages of shoaling (x >

625 m). The same crude check was carried out on the phase prediction as in the previous case. Both the results presented by Madsen and Sørensen (1992) and those obtained here predict the presence of 32 waves in the channel. A further check was made by comparing the predicted wave length at the location where the wave height is minimum ($x \cong 500$m). Madsen *et al.*'s results give $L_{Hmin} \cong 19$m, while the model reproduced for this study gives $L_{Hmin} \cong 20$m. Hence the phase simulation of the model is acceptable for this case.

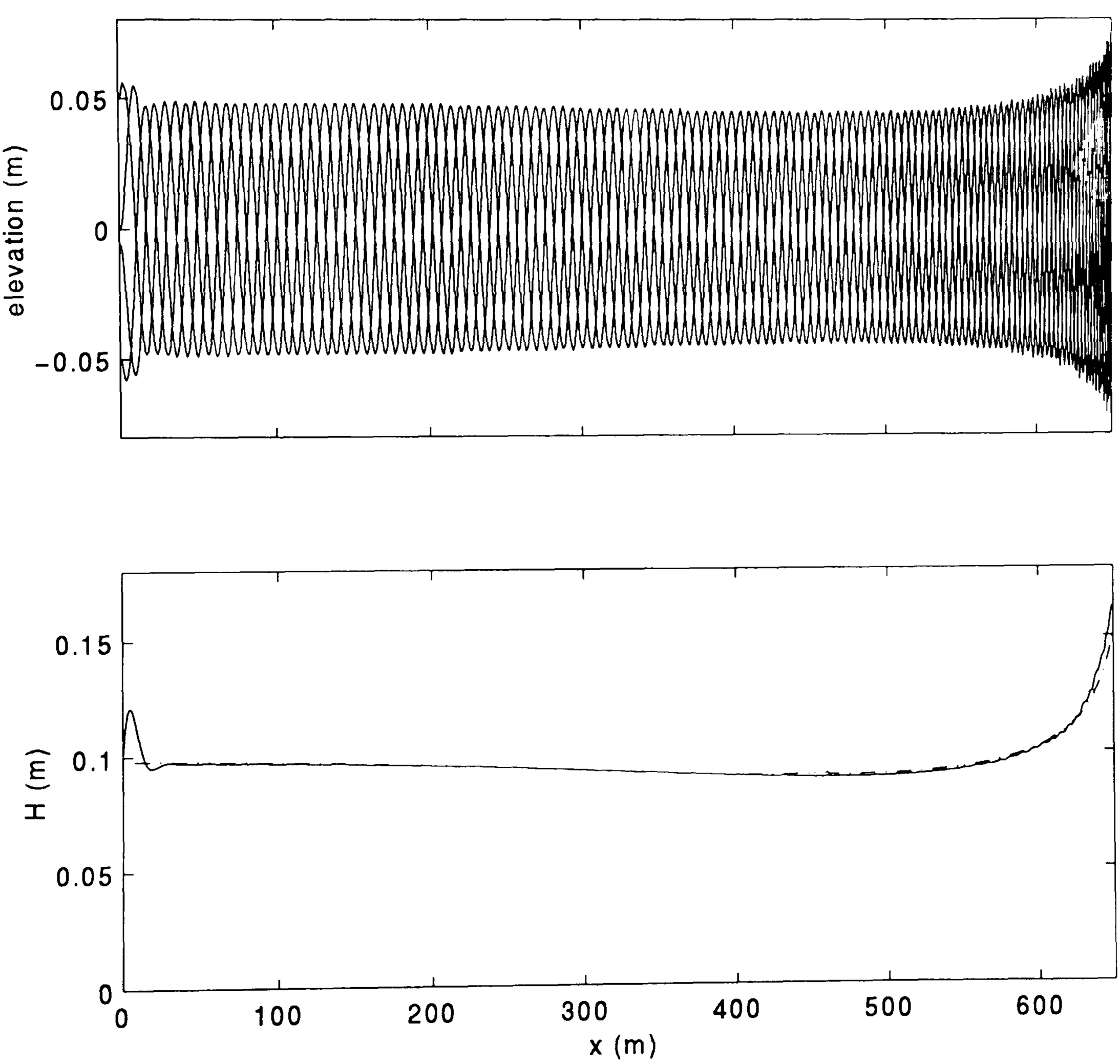

Figure 3.11 Wave shoaling in deep water. (top plot) predicted surface elevation over 1 wave period; (bottom plot) predicted (———) and theoretical (linear,------) shoaling wave height (H=0.1m, T=4sec., L=25m, Δx=1m, Δt=0.08s, B=1/15).

The undulations present in the predicted spatial variations of the wave height in figures 3.10 and 3.11 are also present in Madsen and Sørensen (1992)'s results. They attributed the presence of these oscillations to reflection from the sloping beach.

3.6.4 Wave breaking

A first impression of the capability of the model to simulate wave breaking is given in figure 3.12. A 0.7 m high cnoidal wave is generated very close to breaking point and propagates over a 1 in 40 slope from 1.1 m to 0.2 m deep. The waves are generated inside the domain at x = 12 m, and are absorbed by a 12 m sponge layer at each end of the numerical tank. This test shows that the model is capable of qualitatively reproducing wave decay, set-up and the development of asymmetric (bore-like) profiles.

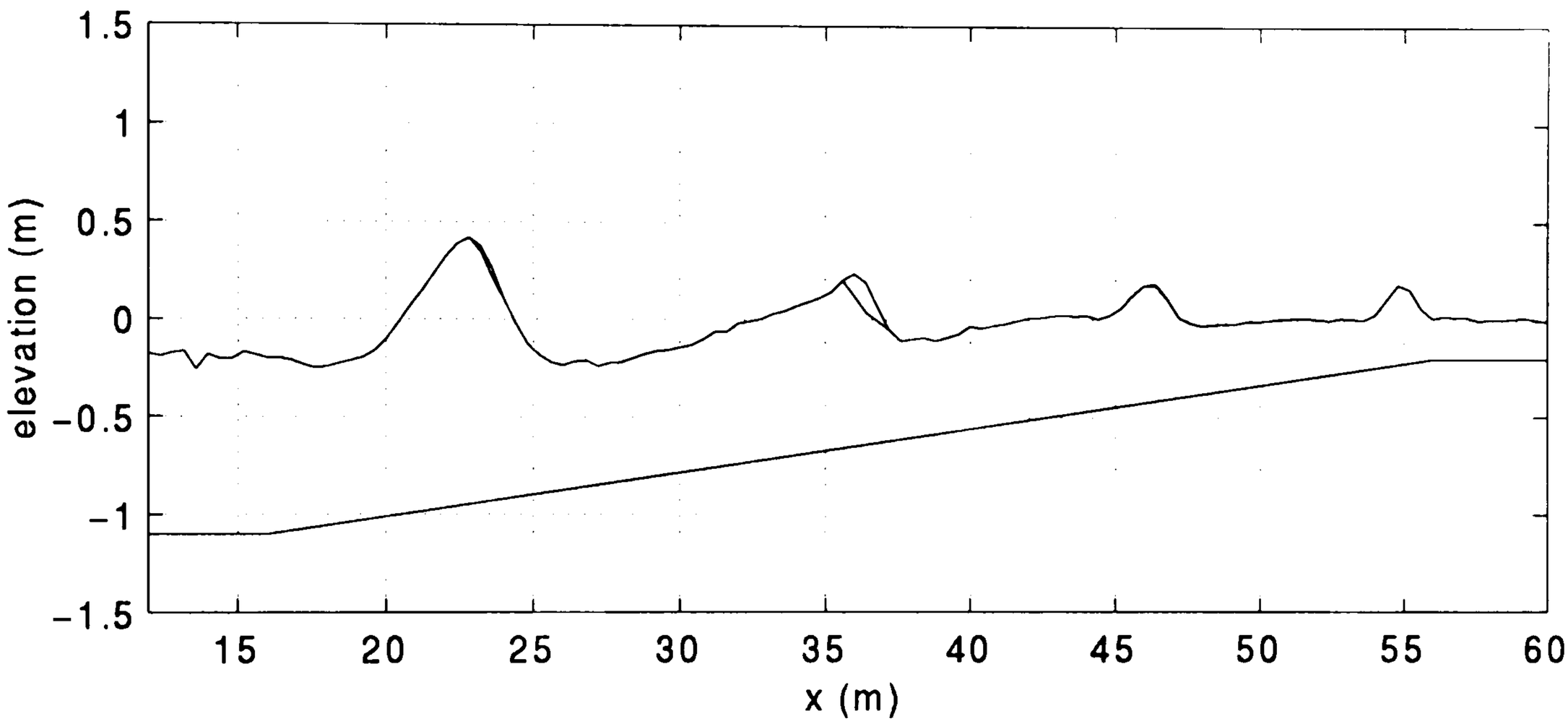

Figure 3.12 Wave breaking. Bathymetry and predicted surface elevation with surface rollers at t=24sec (H=0.7m, T=4sec., L=14.6m, Δx=0.4m, Δt=0.05sec.).

The next test involves the reproduction of the test presented by Schäffer *et al.* (1993). It consists of the comparison of the mean water level (*mwl*) and mean wave height prediction with measurements. The regular incident waves (H_0 = 0.12 m, T = 1.6 sec) are set to propagate over a bar (figure 3.13). The waves are generated inside the domain at x = 5 m, and are absorbed by a 5 m sponge layer at each end of the numerical tank. Figure 3.13 shows the predicted and measured mean wave heights across the channel. It appears that the wave height prediction in the region of the break point is underestimated. This was also observed by Schäffer *et al.* who suggested this is due to the fact that the Boussinesq equations used in this model are for weakly nonlinear waves only. In the breaking region, the assumption $\varepsilon << 1$ certainly does not hold. The maximum measured wave height is 0.152 m, corresponding to a water depth of 0.9 m, hence $H_b/h_b = 0.8$. Notice that, although the model does not predict the measured maximum wave height, (i) it still initiates

breaking at the same location as indicated by the measurements (this is because the breaking criterion as recommended by Schäffer *et al.* accounts for this under-estimation (section 3.4.3)), and (ii) it still predicts the wave decay well.

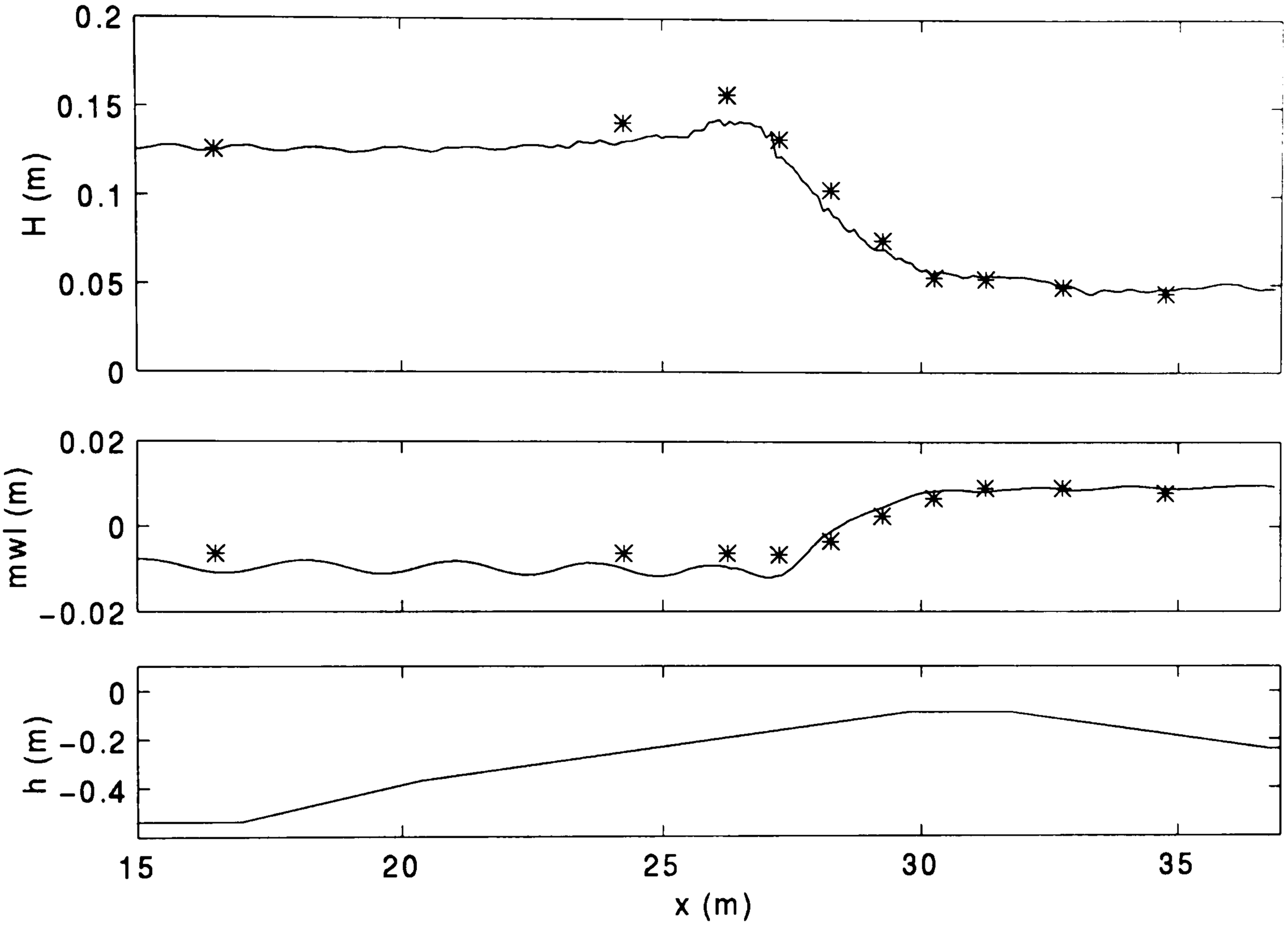

Figure 3.13 Wave breaking. (top plot) predicted (———) and observed (✳) mean wave height; (middle plot) predicted and measured mean water level; (bottom plot) bathymetry (H_0=0.12m, T=1.6sec., Δx=0.1m, Δt=0.05sec., B=0) .

Figure 3.13 also shows the predicted and measured mean water level. Again the results are most satisfactory and in accordance with Schäffer *et al.*'s. The change of gradient occurs at the correct location. The magnitude of the set-up is fairly well reproduced, as well as the lag between breaking point and change of gradient of mwl.

Summary

This preliminary testing of the model has involved comparison with analytical solutions and reproduction of the same tests as Madsen *et al.* (1991), Madsen and Sørensen (1992), and Schäffer *et al.* (1993). This series of tests has shown that the model reproduced for this study performs within the same accuracy as Schäffer *et al.* 's.

CHAPTER 4 - THE DATA and DATA ANALYSIS

4.1 Introduction

The data used for this study were collected during the SUPERTANK Laboratory Data Collection Project run in 1991 in the Wave Research Laboratory, Oregon State University (Kraus & McKee Smith, 1994). This experiment has the advantage of providing data for conditions comparable to those in the field with data unbiased by scaling distortions. The total length of the channel is 104 m, its width is 3.7 m and depth 4.6 m. It contained a 76 m long sandy beach. This data set was also chosen because it provides a comprehensive set of cross-shore wave and current measurements, in the shoaling zone and throughout the surf zone. In addition, the velocities were measured using current meters set in vertical arrays which permitted the investigation of any vertical variability of the flow. Section 4.2 gives details about the selected data collection and its characteristics (in a 'Boussinesq context'). The methods used for the time domain data analysis are described in section 4.3.

4.2 The Supertank data

4.2.1 Instrumentation and data collection

Figure 4.1 shows the experimental set-up, with a typical beach profile, and the location of the instrument stations. The co-ordinate system is chosen so that the x-plane lies in the still water surface plane and is taken positive shoreward with its origin at gauge 1. The free surface oscillations were measured using 16 resistance gauges (gauges 1 to 16) spaced 3.7 m apart, and 10 capacitance gauges (gauges 17 to 26) spaced 0.6 to 1.8 m apart. The array of resistance gauges extended from the toe of the beach to a water depth of approximately 0.5 m (which happens to be beyond the average breaking point for all the runs considered here). The array of capacitance gauges extended from the mid-inner surf zone to the maximum run-up limit. The numerical experiment stopped after the third capacitance gauge (i.e. gauge 19 on figure 4.1), where the sandy bed was never exposed. The most offshore wave gauge signal was used as input in the numerical model at the seaward boundary.

The velocities were measured using 18 Marsh-McBirney electromagnetic current meters deployed in depths of 0.3 to 1.8 m in vertical arrays of 1 to 4 instruments with a vertical spacing of 0.3 m. Each array was configured to share timing pulse to reduce electronic

interference. The arrays are labelled c1, c2 .... to c8 on figure 4.1. The cross-shore location of c3 varied by a few tenth of centimetres from run to run. As the model assumes that the horizontal velocity u is uniform over the depth, the additional information about the vertical structure of the flow permitted checks to be made of how applicable to the data the model is relative to this assumption.

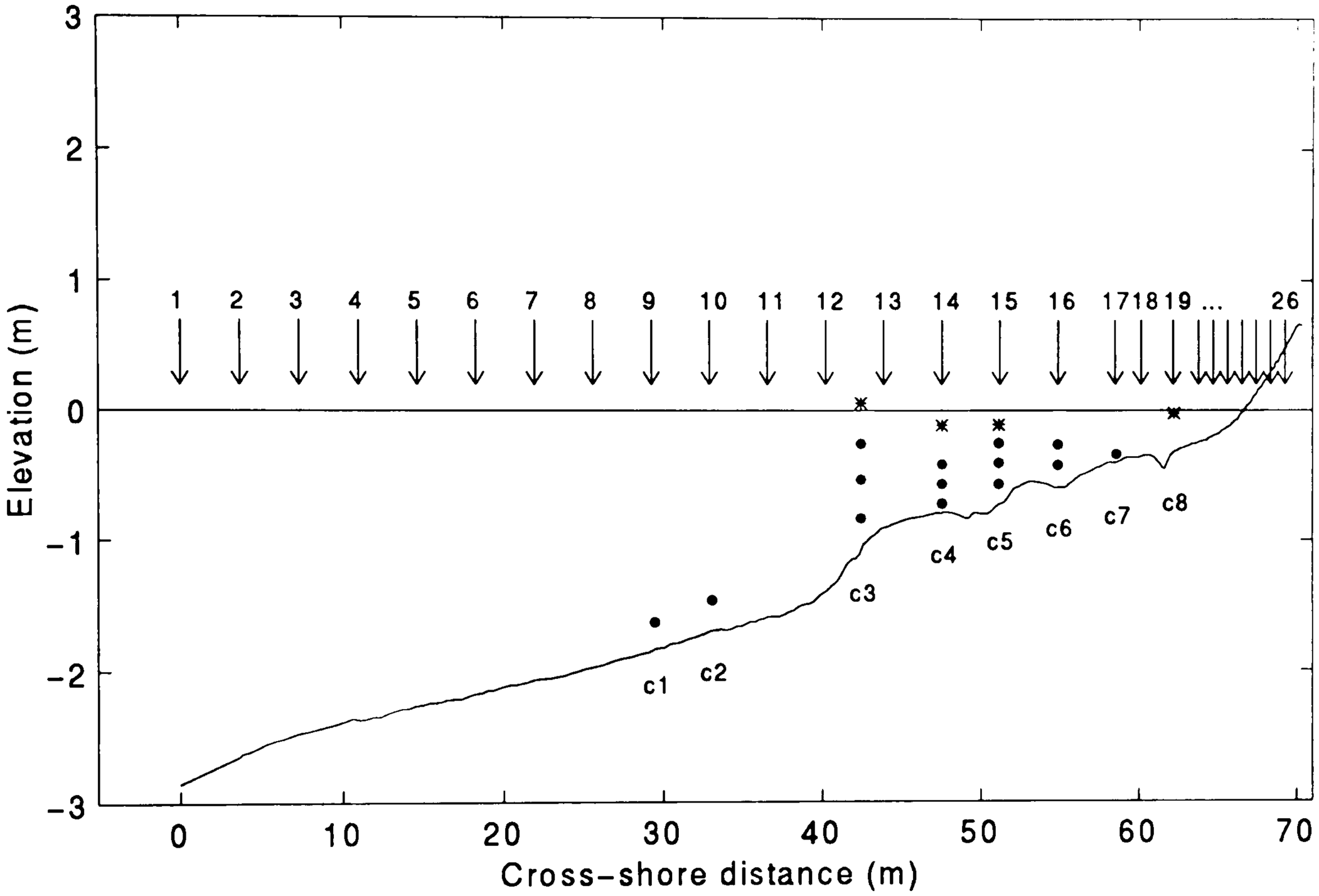

Figure 4.1 Experimental set-up. Wave gauges are numbered 1 to 26. Gauges 1 to 16 are resistance gauges, gauges 17 to 26 are capacitance gauges. The 18 electromagnetic current meters are represented by a dot or star. The arrays are labelled c1, c2 .. to c8. The profile at the beginning of run A1 and the still water level are drawn as plain lines.

The beach profile measurement was carried out in the centre line of the tank before each experiment with a typical horizontal spacing of 0.3 m, and with much finer resolution over features such as bars. Most tests were initiated with the final profile configuration of the previous test. It was the case for all the runs used for this study, for which the initial profile was therefore arbitrary. This also had the advantage of providing, for each run, the initial and final profiles. Any longshore variability was occasionally inspected by surveying the profile 0.9 m away from the walls (as well as in the centre line).

The digitally-controlled hydraulic wave generator was equipped to absorb outgoing energy (i.e. energy that was reflected from the beach) at the peak spectral frequency.

4.2.2 The selected data

The assumptions of weak nonlinearity, spilling breakers, no reflection from the region beyond gauge 19, and slowly varying bathymetry form the basis of the model. Obviously, the aim here being to assess the model for hydrodynamic predictions in the surf zone, the regime is expected to be highly nonlinear, and the weak nonlinearity assumption is expected to be violated. This section presents the selected data, and makes a preliminary analysis of its characteristics in terms of its application to the model.

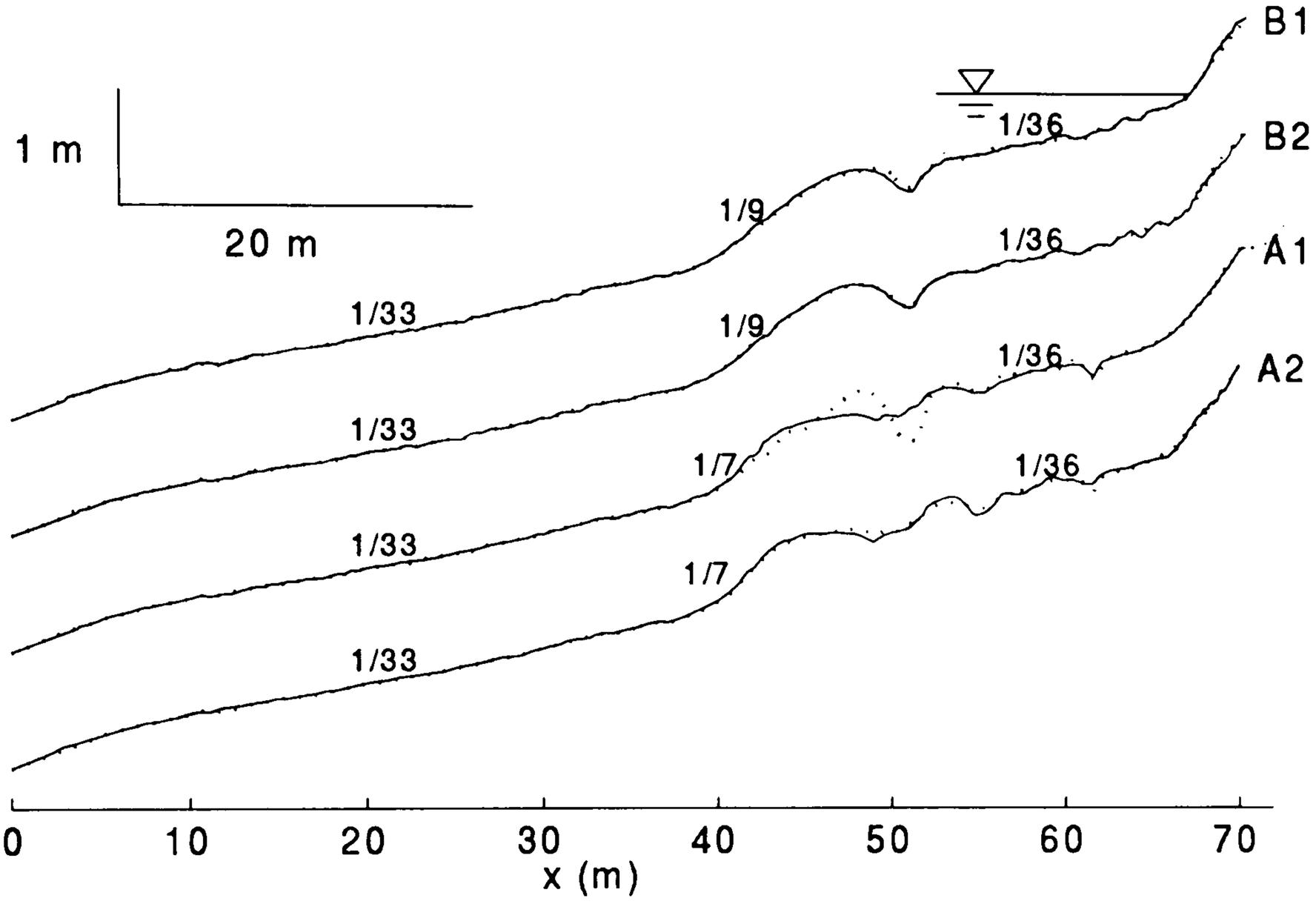

Figure 4.2 Beach profiles for all 4 runs. The profile at the beginning and end of each run are drawn as plain and dashed curves respectively.

The results of comparison with 4 runs are presented here: 2 of regular waves, and 2 of irregular waves (broad spectrum). The bed profiles for all 4 runs (figure 4.2) are complex and arbitrary. The main features for runs A2 and A1 are the presence one main bar and a smaller one inshore. The beach is fairly shallow, with a slope of 1 in 33 and 1 in 36 in front and beyond the main bar respectively. The seaward face of the bar has a 1 in 7 slope. The bathymetry for runs B2 and B1 is mainly characterised by a higher bar with a 1 in 9 seaward face. It also features a deep trough in the lee of the bar. Figure 4.2 also shows the beach profiles at the end of the (40 minutes) runs. It shows, with the exception of A1, that these runs resulted in little net sediment transport. It is therefore reasonable to assume the bed profile to be stable for the duration of the (numerical) tests (typically 3 minutes).

The wave characteristics of these runs are presented in table 4.1. The beach slope parameter S (= h_xL/h) is large ($S > 1$, i.e. $h_x > \mu^{1/2}$, in the breaking region). making the assumption of slowly varying bathymetry questionable. Furthermore, the typical wave period for both A1 and A2 being as high as 8 sec., S reaches values as high as 4 and significant reflection from the slope is anticipated.

		Hrms (m)	*Tp* (s)	S_o	S_{br}	Breaker Type	ε_o	ε_{br}	μ_o
A2 (A1215A)	irregular	0.6	8	0.5	4	plunge	0.1	0.26 (0.6)	0.005
A1 (A1216A)	regular	0.6	8	0.5	3.8	plunge	0.1	0.39 (0.57)	0.005
B2 (A1310A)	irregular	0.4	3	0.2	1.3	spill/plunge	0.07	0.24 (0.52)	0.03
B1 (A1311A)	regular	0.4	3	0.2	1.3	spill/plunge	0.07	0.39 (0.41)	0.03

Table 4.1 Wave characteristics. the subscripts '*o*' and '*br*' refer to the wave generation and breaking regions respectively. The breaker type is estimated with the surf similarity parameter computed using the outer surf zone slope and H_b/L_o. ε_o and ε_{br} are estimated based on *Hrms*/2. An estimation of ε_{br} based on *Hmax* is given in brackets. The run name in brackets indicates the Supertank run identification.

Shallow water waves are characterised by $\mu << 1$. An upper limit for μ is 0.02 (section 2.1.2). Thus the dispersion parameter μ ($\approx h/gT^2$) is typical of very long (primary) waves for A1 and A2, while B2 and B1 are characterised by a rather short primary wave. It was shown in section 3.6.3 that the generation of short waves resulted in discrepancies between the prescribed and the resulting wave train in the model. In these 2 cases however, *kh* is still low at 1.27. The absence of dispersive terms in *B*, which are therefore still relatively small, in the first two computational volumes, did not noticeably affect the wave generation. Verification against figures 3.2 and 3.3 shows that for $kh = 1.27$, the model with extended frequency dispersion accuracy should perform well for those short waves tests[1].

The degree of nonlinearity ε in the generation region is typical of weak nonlinearity. For decreasing water depth, the restriction on ε (and thus ε/μ) is increasingly violated. In the breaking region, the nonlinearity parameter ε based on Hrms ($\varepsilon = Hrms/2h$) reaches 0.26 and 0.24 for the irregular waves cases. The weak nonlinearity limit proposed by Dingemans (1997) (section 2.1.2) is thus slightly exceeded for A2. For the regular wave cases however,

[1] note that the upper limit for μ, or kh, proposed by Dingemans (1997), has been extended to 0.25, or π, respectively.

nonlinearity increases with an ε as high as 0.39. Computed with *Hmax*, ε ranges between 0.4 and 0.6 in the breaking region.

Strictly speaking, the model is only applicable for an Ursell Number $Ur = \varepsilon/\mu = O(1)$. In practice, acceptable results can be obtained with larger Ursell numbers. Dingemans (1997) found that good results are obtained for ε as high as 0.25 while μ should typically be smaller than 0.02 (for equations with no improved dispersion).

The breaker type that characterises the four experiments is that of plunging breakers. This goes against the intrinsic assumption of spilling breakers made in the extension of the model to the surf zone.

4.2.3 Approximation for the depth averaged velocity

The velocity variable output from the model is the depth-integrated velocity, from which the depth-averaged velocity is calculated. The measurements of the cross-shore velocity consisted of vertical arrays of 1 to 4 current meters, that is, measurements at fixed altitudes. In order to obtain an approximation of the depth-averaged velocity from the measurements, several options were available: it could be approximated by averaging over all current meters, ignoring the current meters located close to the free surface (i.e. ignoring the current meter with less than 100% immersion), or using the current meter closest to the theoretical depth-averaged velocity (at $\cong$ -0.4*h*, Dingemans, 1997) only. Inspection of the current data provides an answer.

The most shoreward 'array' (c8, consisting of one current meter only) measured very large velocities compared to its adjacent current meter (not shown). It is placed very close to the still water level and, despite the set up[1], it is expected to be occasionally emerged. Indeed the signal issued from this current meter is anomalous: it contains spikes and high frequency noise, a clear indication of the instrument becoming intermittently exposed. The results from this current meter should thus be used with caution, if at all. The same observation was made with the other three current meters located close to the still water level, and where the set down is greatest: namely the 'top current meters' of c4 and c5 (at 0.11m below the *swl*), and c3 (at 0.06m above the *swl*). They are represented by stars on figure 4.1. The above observations are illustrated here with fig 4.3 where the signal from

[1] e.g. B2: CM @ -0.024m below *swl*. set up = 0.01m. hence CM @ -0.034 below the mean water surface. At this location *Hrms* = 0.2m, assume 0.1m amplitude

the top current meter at c3 for condition B2 is plotted together with the signal of the current meter located directly below (middle top current meter, c3). The oscillations of this signal are much larger, particularly for the onshore velocities. Since the oscillations for both current meters are in phase, it is possible to use it in order to get an idea of the crest velocities occurring at this location. It is clear however that the uncertainties as to what this current meter is measuring prevent it being used in the comparison.

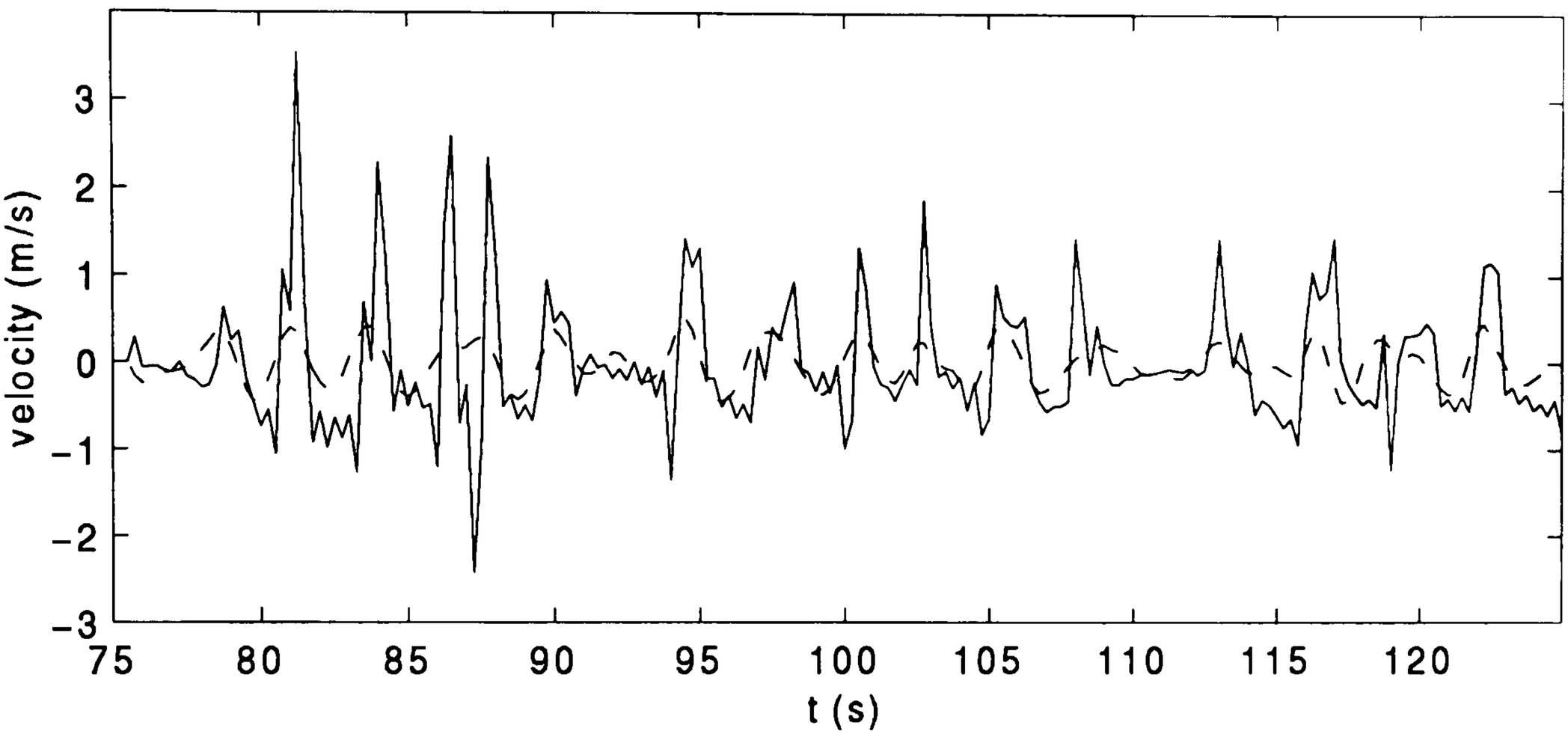

Figure 4.3 Observed velocity oscillations at array c3. ——— top current meter, - - - - - - middle top current meter. Positive velocities are directed onshore.

Figure 4.4 provides the statistical measures of the mean, standard deviation, skewness and kurtosis (defined in section 4.3) for each current meter, and for each run. For example, for run A1, panel (1,1)[1] shows the depth variation of the mean for, from left to right in the panel, c3, c4, c5 and c6. It appears that the top current meters of arrays c3, c4 and c5, indicated by a circle, almost systematically indicate large deviations from the otherwise fairly uniform through the depth velocity field. The third and fourth order statistics are particularly affected. The middle top current meters from these arrays also show some deviations, particularly for the standard deviation of array c3. These deviations are less significant however, and are ignored.

It is clear from figures 4.3 and 4.4 that the top current meters from arrays c3, c4 and c5, and the current meters from array c8 should not be included in the calculation of the measured depth-averaged velocity. The fairly uniform velocity profile that transpires from the analysis of the rest of the current meters indicates that an averaging over the said meters is acceptable. From here on, it is implicitly understood that the top current meters of arrays c3, c4 and c5, and the current meter of array c8 are disregarded, unless otherwise stated.

---

[1] the notation used throughout this thesis is such that panel(4,2) indicates the plot on row 4, column 2.

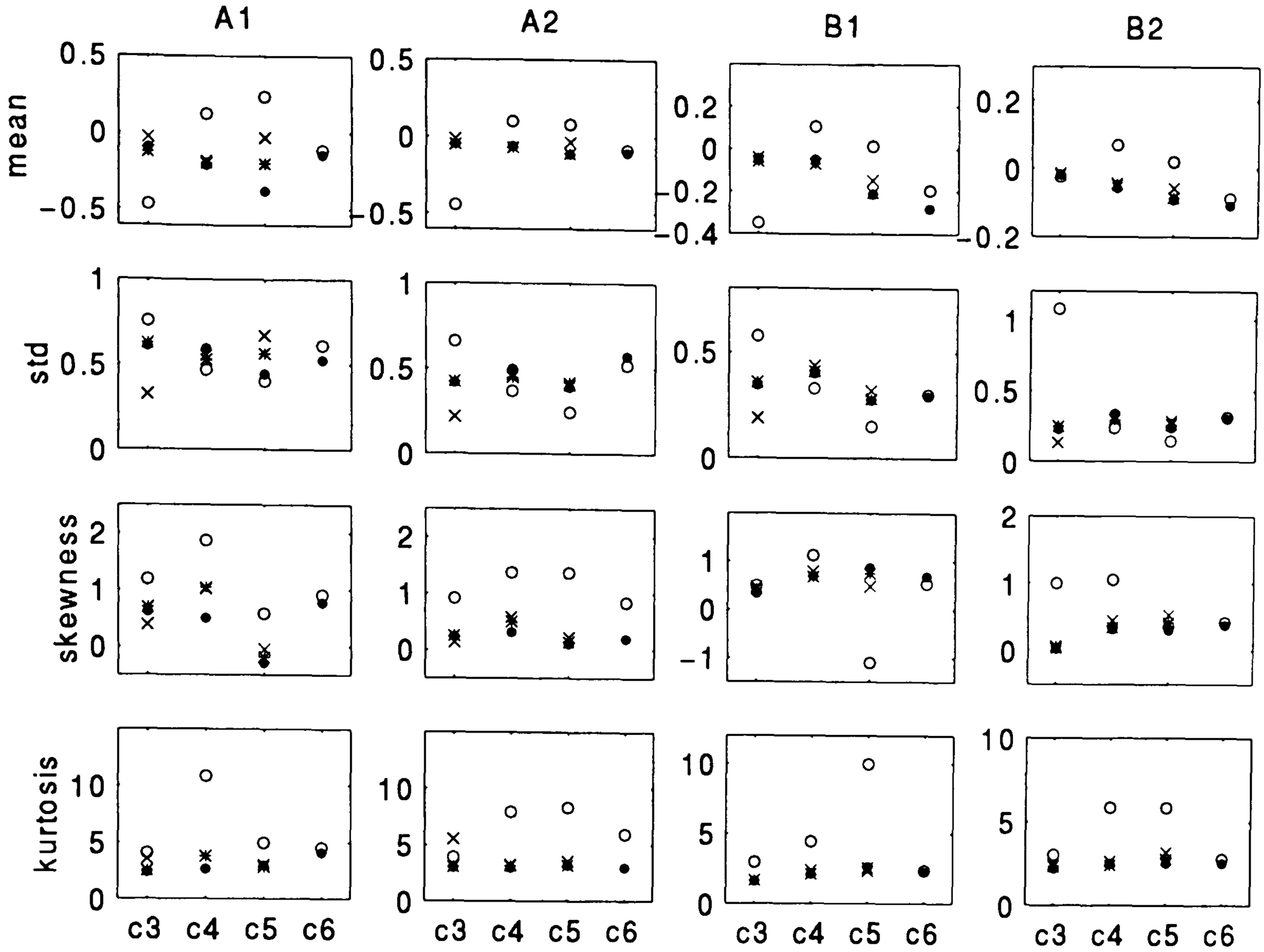

Figure 4.4 Vertical variation of the observed velocity statistics at four cross-shore locations (arrays c3, c4, c5 and c6). ○ Top current meter, × middle top current meter, ✳ middle bottom current meter, • bottom current meter. Columns, from left to right, are A1, A2, B1 and B2. Rows, from top to bottom, are the velocity mean, standard deviation, skewness and kurtosis.

Figure 4.4 reveals another interesting feature of the current data. For runs B2 and B1, despite the fact that we are dealing with shorter waves, the uniformity of the velocity field through the depth is indisputable. For runs A1 and A2, on the other hand, this uniformity is not as unequivocal. This is surprising as, for these two runs, the waves are very long ($\mu \ll 1$), which is characteristic of nearly horizontal flows. One would thus expect the assumption of horizontal velocity uniform over the depth to hold better for A1 and A2, than for B1 and B2.

4.2.4 Reflection from the shoreline

Reflection of a small fraction of the incident wave energy flux produces significant cross-shore variations in energy levels (Elgar *et al.*, 1997). Reflection from the region from gauges 19 (landward boundary of the model) up to the shoreline is a matter of concern, especially for A2 and A1. The typical wave period for both these runs is large (low wave steepness), and the foreshore is steep. This results in high values for the Irribaren number, and it is probable that significant reflection occurred in this region.

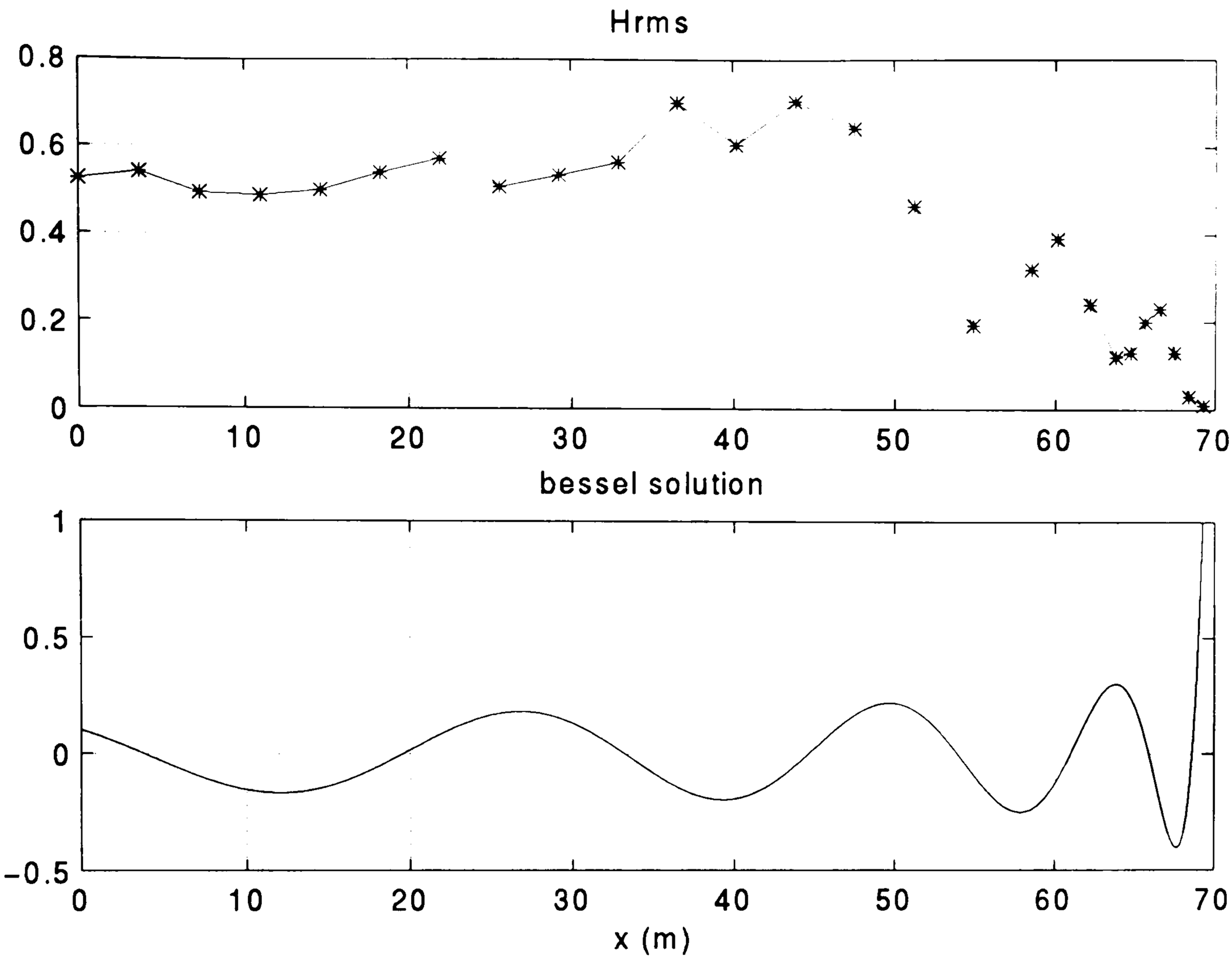

Figure 4.5 (top plot) cross-shore variation of the observed wave height, test A1. (bottom plot) Bessel solution with T = 8s and s = 1/36.

This presumption is confirmed by the fact that the cross-shore variation of the measured wave height shows clear modulations, especially in the inner surf zone and swash zone, where they are of a factor of two (figure 4.5). These modulations are characteristic of cross-shore standing waves. They appear to damp away offshore, further suggesting they may be due to reflected waves of which the amplitude is damped as they propagate offshore. In say 0.3 m water depth, the wave length of an 8 s. incident waves is about 14 m. Thus, the expected separation of nodes and antinodes is about 3.5 m. The separation between the wave staffs is therefore small enough to resolve the modulations in wave height due to reflection. A quick analytical solution (using a Bessel function) for the location of nodes and antinodes of a standing waves field was applied to this situation. A solution is given in figure 4.5. It indicates that a relatively good correlation can be obtained using $T = 8$ sec and a slope of 1/36. This indicates that the maxima and minima observed in the data are (physically) possible locations for nodes and antinodes, which further indicates that these oscillations may be the result of reflection[1].

---

[1] The possibility that these oscillations may be the result of wave reflection is strengthened in section 6.4, where it is shown that (i) the skewness arising from the self interactions at the peak frequency is

4.2.5 Summary

The data essentially consist of 2 conditions: long waves (A runs) and short basic waves (B runs), both conditions being investigated for irregular and regular cases. Each of these cases is identified in figure 4.6 with the observed surface elevation time series at gauge 1. Some characteristics of the data set fall outside of the domain of application of the model. This is inevitable and the model-data comparison will show the limitations of the model with respect to its assumptions.

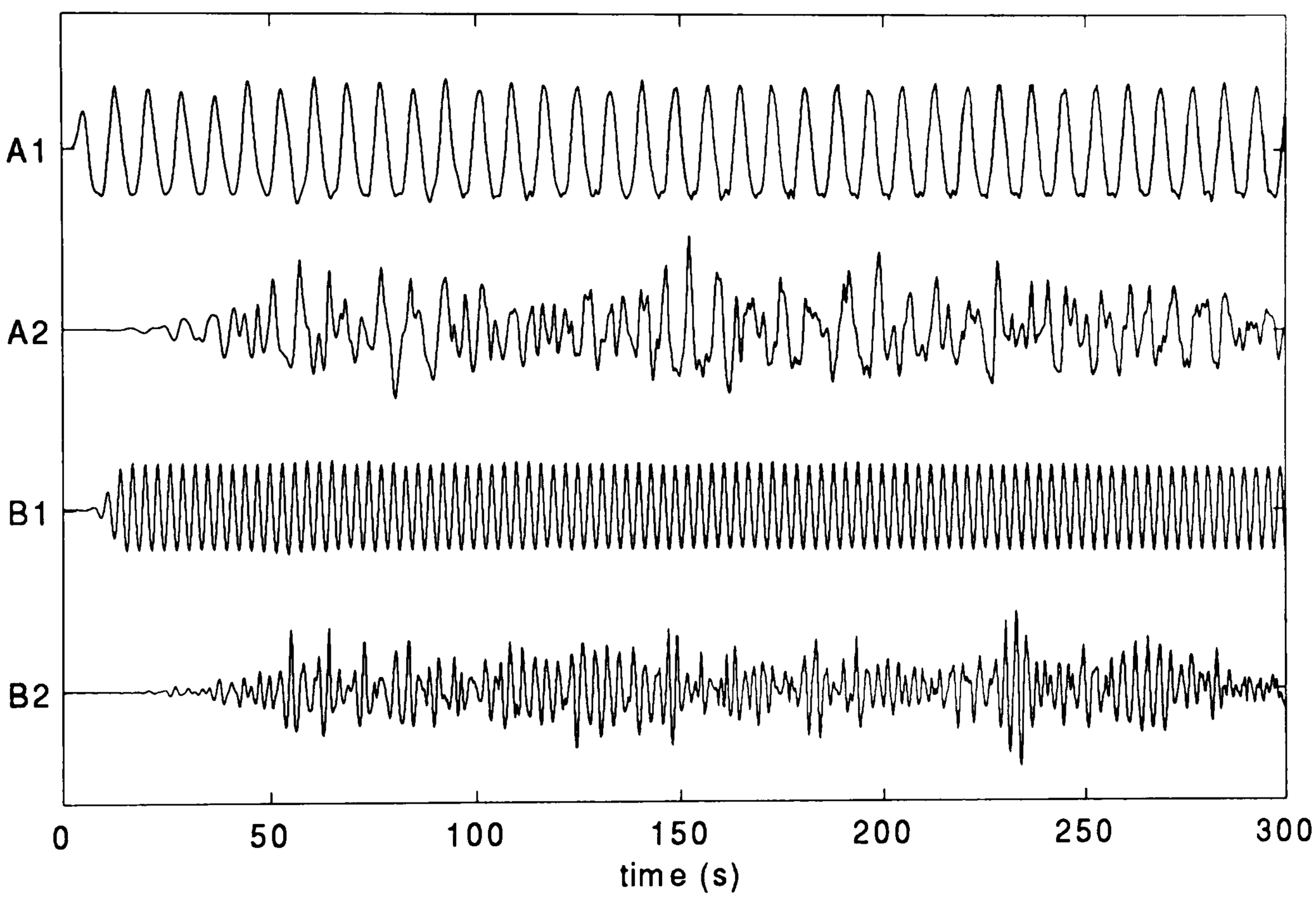

Figure 4.6 Observed time series of surface elevation at gauge 1 for all 4 data sets.

4.3 Data analysis

The sampling rate for the wave and current gauges was 16 Hz. A 10 Hz, fifth-order anti-aliasing Bessel filter was then applied to the resistance gauges and current meters data to eliminate noise and avoid aliasing. In addition, the data, as received, had already been decimated to 4 Hz. The generated time series were also decimated to 4 Hz. Both the predicted and observed time series were band pass filtered between 0.06 - 2 Hz.

(unexpectedly) negative at the location of minima in the measured Hrms (condition A1), and that (ii) a correlation is found between negative skewness arising from interactions amongst short waves and reflection.

It was emphasised in the introduction that in shallow water the first and second moments (mean and variance) are not sufficient to define the wave regime. In shallow water the waves become increasingly asymmetrical about both the vertical and the horizontal axis, thus resulting in skewed and saw-toothed wave shapes. The statistical distribution of the instantaneous surface elevation, or velocity, in this region can no longer be assumed to follow a normal distribution, and can no longer be expressed by the first two statistical moments only. The extent of the deviations from the normal distribution may be examined through two parameters:

the third central moment, or skewness: $$S = \frac{\sum (\eta - \overline{\eta})^3}{\sigma^3 N}$$

the fourth central moment, or kurtosis: $$K = \frac{\sum (\eta - \overline{\eta})^4}{\sigma^4 N}$$

where N is the number of data points and σ is the standard deviation of the random function of time $\eta(t)$. The normal distribution (distribution symmetric with respect to the mean value) has $S = 0$ and $K = 3$. The skewness gives information about the asymmetry of the statistical distribution. When, as is the case for shallow water waves, the mode of the distribution is located lower than the mean and the distribution has a long tail in the range greater than the mean, S takes a positive value. In terms of elevations, this implies that if $S > 0$, the wave crest heights are greater than the wave trough depths, and vice versa. In terms of velocities, $S > 0$ indicates that the velocity is skewed onshore (i.e. onshore velocities are high, with short duration, while offshore velocities are smaller, with longer duration). The kurtosis gives information about the peakedness of the statistical distribution. If the peak is higher than that of the corresponding normal distribution, then $K > 3$, in which case the distribution features long tails on both sides to compensate for the high peak. This suggests that if $K > 3$, the degree of variability in the instantaneous surface elevation is less. The physical meaning of the kurtosis is uncertain, but its importance with regards to suspended sediment transport has been shown to be significant (see chapter 1).

Besides the standard deviation[1], the skewness and kurtosis were thus systematically calculated for both elevation and velocity time series. In addition, the mean was calculated for the elevation time series, yielding the mean water level *mwl*.

---

[1] defined as the square root of the second central moment, or variance (m^2)

The time series analyses were carried out using a zero-upcrossing method to define individual waves. A wave is defined between two upward crossings of the water surface about the mean water level. The wave height is defined as the sum of the absolute values of the maximum and minimum elevation between two zero-upcrossings. Very small waves (H < 0.6 cm) were not identified as individual waves. They were included as part of the preceding wave. Analysis of elevation time series further involved calculation of maximum and minimum elevations and wave heights. Analysis of velocity time series also involved calculation of maximum onshore and offshore velocities.

The shoreward mass flux, concentrated above the wave trough level, is compensated in the laboratory by a seaward mean return flow, also called undertow. Since, in the surf zone, the shoreward mass flux of the waves is strongly enhanced by the breaking process (Svendsen, 1984b), the effect of the roller on the vertical distribution of the horizontal velocity must be included. Thus the undertow may be approximated as a depth-averaged quantity as the time average of u_o, which is defined from equation (3.18a) as:

$$u_0 = \frac{P - c\delta}{d - \delta} \tag{4.1}$$

Since the time average of the depth-integrated velocity is zero in the physical tank, and since, given the boundary conditions, the time average of the flux in the numerical tank is non-zero and positive, the average was removed from the depth-integrated velocity time series before applying equation 4.1. The time average of u_0 is then negative to compensate for the shoreward flux due to the surface roller.

The calculations for the observed undertow involves further approximations. It was found that (i) the measurements indicate a velocity field that is fairly uniform through the depth, and that (ii) the mean velocity for each of the current meters is negative. It may thus be assumed that each of these current meters measured undertow, and that the undertow is fairly uniform through the depth. The observed undertow was thus calculated from the averaging of all current meters.

A bispectral analysis was also performed on the data. It is described in detail at the beginning of chapter 6.

CHAPTER 5 MODEL - DATA COMPARISON: A TIME DOMAIN ANALYSIS

5.1 Introduction

5.1.1 Introduction

The developments and applications of numerical models based on the Boussinesq equations were reviewed in chapter 2. In this review it was emphasised that, to date, the validation of the Boussinesq model used in this study has essentially concentrated on surface elevation predictions, with particular focus on wave height and mean water level predictions. Given the importance of the knowledge of the velocity field for sediment transport predictions, it is surprising that very little work has been presented on evaluating the capability of this model (and Boussinesq models in general) to predict velocities. The wave shape is another element of importance for sediment transport predictions. Again no thorough study of the model with respect to wave shape has been produced.

In this chapter, both the surface elevation and depth-averaged velocity predictions are compared with large scale laboratory data (section 5.2). The assessment of the capabilities of the model is taken further in section 5.2.3, by comparing predicted and measured skewness and kurtosis, thus giving an indication of the model's potential to predict wave shape. In addition, the robustness of the model is assessed with respect to the free parameters involved in the simulation of wave breaking (sections 5.1.3 and 5.3). The implications and effects of the slowly varying bathymetry assumption made in the derivation of the equations are investigated in section 5.4. This is followed by a discussion on wave reflection in section 5.5, and an analysis of the treatment of the seaward boundary condition in section 5.6. Section 5.7 provides a summary and discussion.

5.1.2 Design of numerical experiments

Improved dispersion

In order to improve the description of the super-harmonics, all computations were performed with $B = 1/15$. This also proved essential for the correct shoaling of the primary waves in runs B1 and B2.

Mesh size and test duration

It is important that Δt and Δx be chosen small enough to provide an adequate resolution of the super-harmonics as well as the primary wave. For A1 and A2, Δt and Δx were set to 0.05 sec and 0.25 m respectively. B1 and B2 required a finer resolution, with Δt and Δx at 0.025 sec and 0.14 m, respectively. With these mesh sizes, the Courant number, defined as the ratio of the propagation velocity of the physical and numerical waves[1], $C_r = \frac{\Delta t}{\Delta x}\sqrt{gh}$, was equal to 1 at the deepest location. The number of grid points per wave length and wave period up to the fifth super-harmonic are tabulated in table 5.1.

Exp.	Harmonic	T (s)	points per wave period	L (m)	points per wave length
A1 & A2	1	8	160	40.7	163
	2	4	80	18.5	74
	3	2	40	6.2	25
	4	1	20	1.56	6
	5	0.5	10	0.39	1.6
B1 & B2	1	3	120	14.0	100
	2	1.5	60	3.5	25
	3	0.75	30	0.9	7
	4	0.375	15	0.22	1.6
	5	0.1875	7.5	0.05	-

Table 5.1 Number of grid points per wave length and wave period

The number of grid points available up to the third harmonic are adequate. Those for the fourth and fifth harmonics however are very low. This is not a problem for B1 and B2 since only the third harmonic develops in these tests (see chapter 6). It is not the case for tests A1 and A2, however, for which nonlinear interactions are intense, even in the shoaling region. Yet, increasing the wave resolution further by halving the mesh size (thus keeping C_r constant) did not improve the results. It is possible that yet a finer resolution may improve the results. Unfortunately this could not be attempted due to computer memory limitations. On the other hand however, observation of the cross-shore evolution of the power spectrum

[1] For numerical stability and accuracy, the time step Δt must be smaller than the time required for the modelled wave to travel over the distance Δx, i.e. $\Delta t < \Delta x\ (gh)^{1/2}$ (assuming wave celerity = $(gh)^{1/2}$).

for A1 shows that the fifth harmonic develops in a depth of about 1m. The maximum *kh* value for this harmonic is thus about 15, for which, despite improved dispersion characteristics, the model does not perform well anyway (figures 3.2 & 3.3). In view of the practical and theoretical limitations outlined above, the resolution of the fourth and fifth harmonics was considered acceptable.

The computations for runs A1 and A2, and B1 and B2 were performed for a duration of 300 sec and 175 sec respectively. This gave ample reserve to obtain permanent wave profiles at the shallowest station for both regular runs [1]. Note that, due to the very nature of the model, the stationarity of the wave profile is relative. Strictly speaking, the waves are non-stationary in time and space; this is inherently due to nonlinear interactions occurring. If nonlinearity and dispersion balance each other, the waves can be stable.

Wave generation

Since the initial conditions across the channel are those of a cold start, a slow start condition was prescribed in order to avoid the development of disturbances or instabilities. The waves were then allowed to travel over a flat bed section before reaching the toe of the slope. This was necessary in order to obtain a stable solution at this location. It had the disadvantage however of allowing the incoming wave field to transform, owing to nonlinear transfers of energy. The length of the flat bed sections were set to 20 m and 15 m for tests A and B respectively. The uncertainties in the wave generation are further convoluted by fact that no seaward propagating waves (i.e. waves reflected from the slope and/or the boundary) are allowed to leave the domain[2]. Wave generation is discussed in detail in section 5.6. The predicted and measured power spectra at gauge 1 are compared, for all four runs, on figure 5.1. It shows that the actual wave field compares reasonably well with the prescribed wave field. Some discrepancies between the prescribed and the actual wave field are noted for condition A1, for which the energy at the third harmonic frequency is overestimated. The energy at frequencies > 0.5 Hz are underestimated for A2.

---

[1] Eg.: for A1, the celerity of the fourth harmonic of the primary wave is $\frac{gT}{2\pi}$ =1.56 m/s., which thus travels the 82 m distance from the wave maker up to gauge 19 in 52 sec (making the conservative assumption that the third harmonic is present in the incoming wave field).

[2] note that besides the effect of nonlinear interactions and reflection on the wave generation, the treatment of the boundary coundition described in section 3.5.5 also contributes to errors.

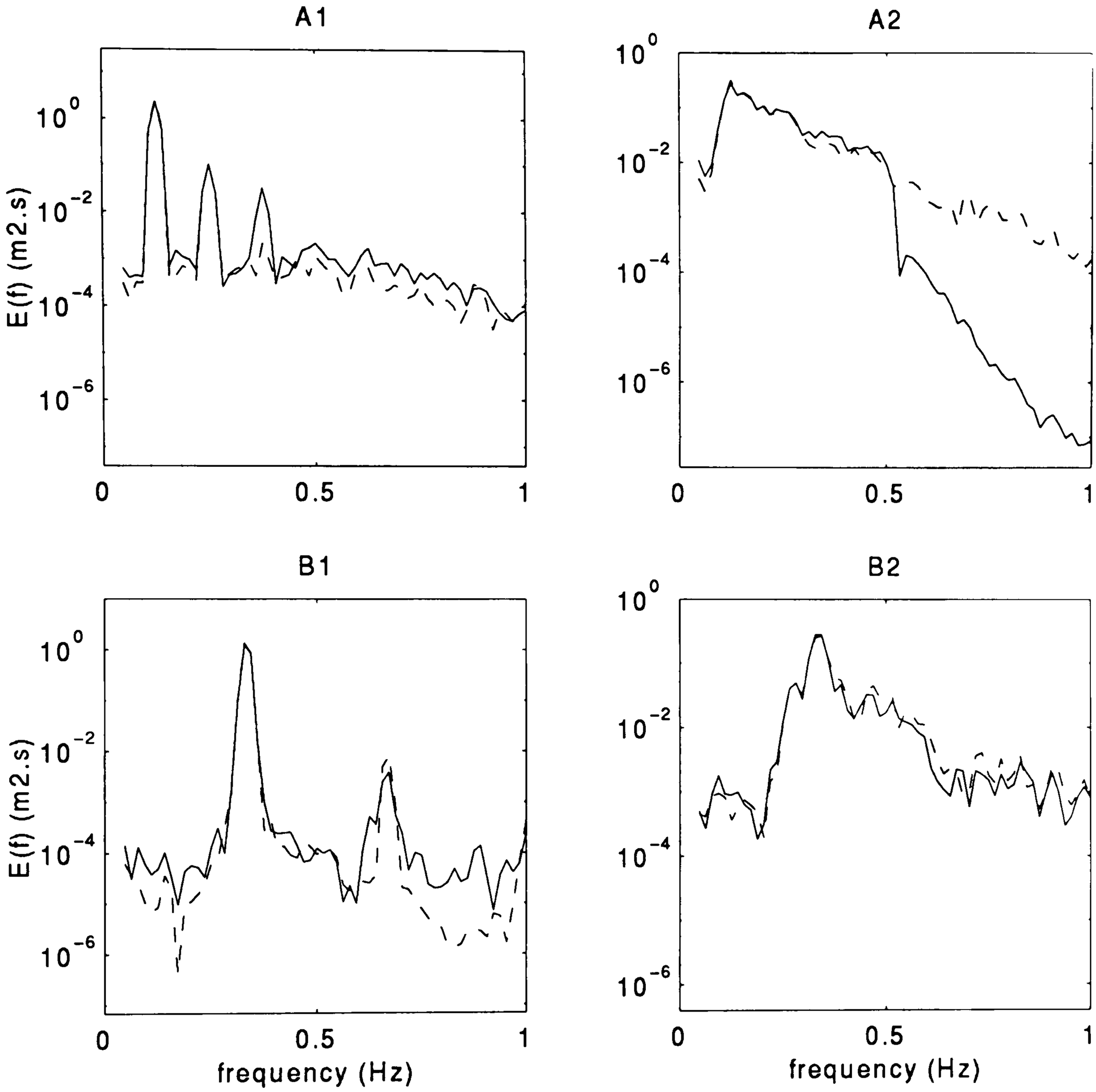

Figure 5.1 Predicted (———) and observed (exact) (------) power spectrum for each run at gauge 1.

Shoreward boundary condition: efficiency of the sponge layer

With the duration of the test chosen such that permanent wave profiles could establish throughout the channel, the possibility of waves reflecting from the shoreward boundary must be given consideration. The efficiency of the sponge layer was evaluated indirectly as follows: each run was initially performed with the outgoing boundary located such that the reflected waves could not manifest themselves in the domain of interest. This is exemplified here with tests A1 and A2: for a total duration of 300 sec. with a basic wave speed of approximately $(gh)^{1/2}$ = 4m/s (choosing a very conservative mean water depth of 1.6 m), the primary waves travel a distance of 1200m. Since the shoreward end of the domain of

interest is at 82 m from the incoming boundary, the use of a 560 m long horizontal bed beyond that domain prevented any reflected wave from perturbing the wave field. The results from these tests were then compared with the results from a test run with the same conditions except this time the horizontal bed section beyond the domain of interest was reduced to 5 m (minimum distance required in front of the sponge layer in order to avoid numerical instability)[1]. Both experiments resulted in almost exactly the same predictions, thus attesting to the remarkably high efficiency of the sponge layer.

5.1.3 Sensitivity to the free breaking parameters

The simulation of wave breaking involves the use of a number of parameters described in section 3.4. These are ϕ_B, ϕ_o, f_δ and t^*, for which the figures recommended by Schäffer *et al.* (1993) are 20°, 10°, T/10 and 1.5 respectively. ϕ_B controls the onset of wave breaking, whereas the remainder of the parameters control the rate of decay by controlling the roller thickness (equations (3.22) & (3.20)). These values were evaluated from laboratory measurements and subsequently 'adjusted' after numerical experiments. The relative uncertainty introduced in the estimation of these parameters is thus accentuated by the fact that some adjustments for the model limitations were made during this process. Indeed the model tends to underestimate the wave height in the region of breaking (Schäffer *et al.* 1993), thus underestimating the local slope of the water surface in this region. The value recommended by Schäffer *et al.* for ϕ_B was therefore chosen to be smaller than the actual wave slope at the breaking point, which is evaluated from laboratory data. An additional assumption was introduced in order to avoid complicating the numerical scheme: the phase celerity in equation (3.20) is approximated by $1.3(gh)^{1/2}$. Equations (3.20) & (3.21) show that this approximation affects the rate of decay by directly controlling the magnitude of the excess momentum due to the roller.

Sensitivity testing of the model with respect to the five parameters discussed above were carried out for all four data sets. This showed that the model is fairly robust with respect to ϕ_o, f_δ , t^* and the expression for c. Decreasing ϕ_o (to e.g. 7°) results in an increase of the roller thickness δ, hence an increase in the energy dissipation and rate of decay. A decrease of t^* has the same effect: decreasing t^* (to e.g. T/20) results in a steeper transition to ϕ_o , hence in an increase of δ. The effect of changing f_δ is more subtle. A small change in f_δ (to

---

[1] note that due to memory limitations, Δt and Δx were reduced to 0.05 s and 0.38 m for A1 and A2, and to 0.05 s and 0.22 m for B1 and B2. This applies to both experiments that are being compared here.

e.g. 1.7) has very little effect on the results. On the other hand, a large increase in f_δ (to e.g. 2.5) results in a milder wave height decay. This may appear contradictory at first since increasing f_δ directly increases δ. It may be interpreted as follows: as δ increases with increasing f_δ the energy dissipation increases, and the wave height decreases. If the initial decay is too strong, wave breaking may eventually stop. Note that a large decrease in ϕ_o and t^* may have the same effect. The analytical formulation of the phase celerity c was successively set to $(gh)^{1/2}$, $1.3(gh)^{1/2}$ and $1.5(gh)^{1/2}$. Again, very little change in the rate of decay with varying c was observed.

Testing of the model with respect to ϕ_B on the other hand shows more significant sensitivity to this parameter. This is not surprising since this parameter controls the breaking location as well as the roller thickness. In the following study, particular attention is therefore given to the effect of ϕ_B on the results. The computations presented here were initially run with ϕ_B, ϕ_o, f_δ and t^* set to 20°, 10°, T/10 and 1.5 respectively (section 5.2). They were subsequently run with a range of ϕ_B (section 5.3), chosen in view of two combined aims: to improve the results (by adjusting the location of breaking), and to test the sensitivity of the results to this parameter. The choice of ϕ_B was occasionally restrained by numerical stability problems.

Finally, testing of the model with respect to the numerical filter showed that the weighting parameter α had relatively little effect on the results (other than stabilising !). It was found that increasing α results in a slightly increased rate of decay.

5.2 Model-data comparison

5.2.1 Surface elevation (low order) statistics

The predicted and measured surface elevation statistics are compared in figure 5.2a (tests A) and 5.2b (tests B). For each run, these figures show the cross-shore variation of

- the mean water level (*mwl*) and standard deviation (top plots),
- the mean maximum and mean minimum elevations (centre plots), and
- *Hrms* (bottom plots).

Note that *Hrms* is plotted together with the mean roller thickness $\bar{\delta}$, which gives an indication of the location and intensity of wave breaking. *Hmax* is also shown for both irregular runs. The breaking point is located above the first bar, in the region of gauge 14 (x

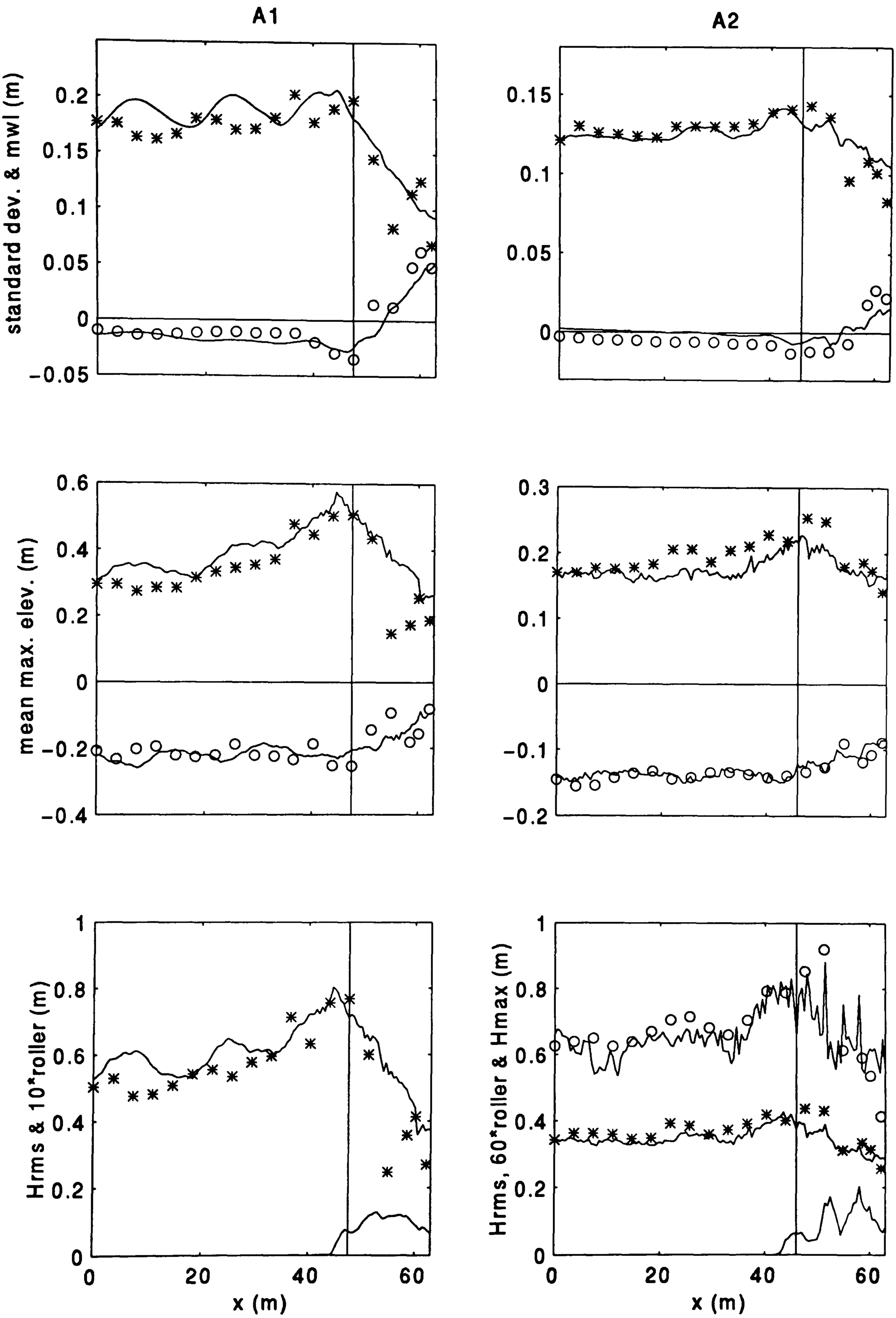

Figure 5.2a Cross-shore variation of the predicted (———) and observed (✳ ,○) surface elevation statistics for run A1 (left column) and A2 (right column). From top to bottom are the elevation standard deviation (✳), *mwl* (○), mean maximum crest elevation (✳), mean minimum trough elevation (○), *Hrms* (✳), and $\bar{\delta}$. *Hmax* (○), is shown for the irregular run. The vertical line at about 48 m indicates the bar crest location.

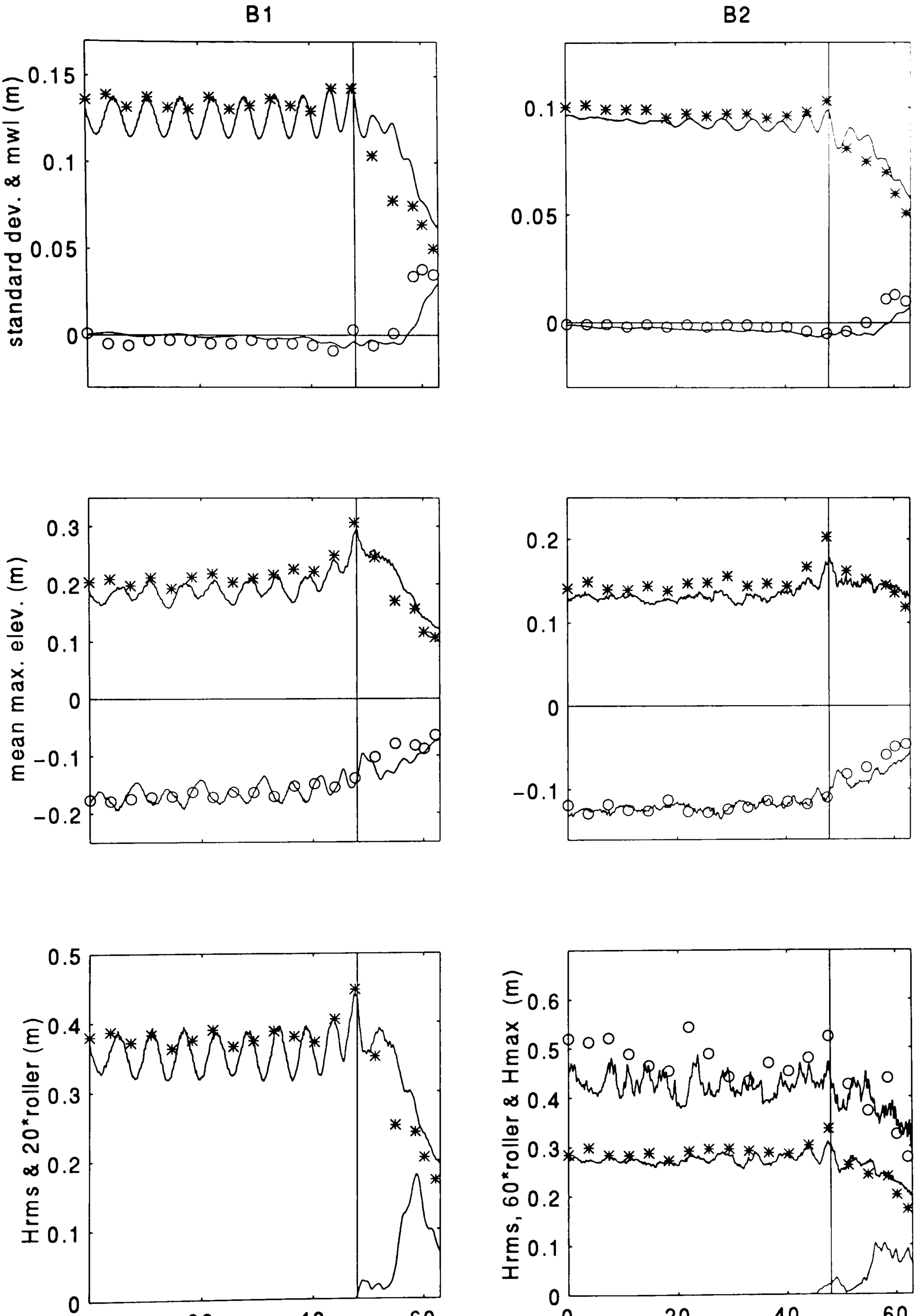

Figure 5.2b Cross-shore variation of the predicted and observed surface elevation statistics for run B1 (left column) and B2 (right column). Legend as in figure 5.2a.

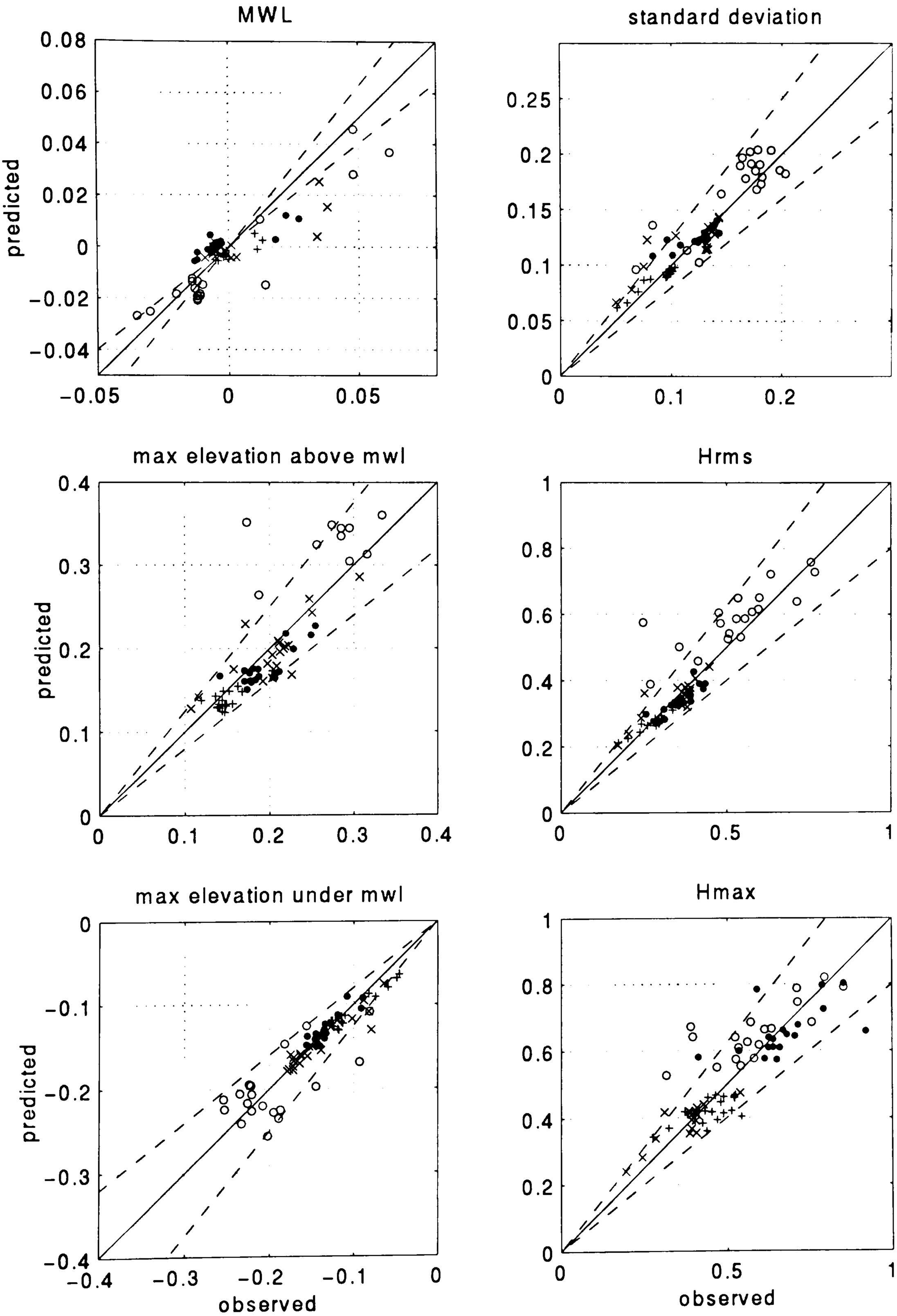

Figure 5.3 Predicted *versus* observed surface elevation statistics. ○ A1, ● A2, × B1, + B2. The solid and dashed lines correspond to perfect agreement and 20% difference respectively.

$\cong$ 47 m)[1]. The location of the bar crest is indicated by the vertical line. In the following, the domains seaward and shoreward of the vertical line will be referred to as the shoaling and breaking zones respectively.

The results show the development of oscillations in the modelled cross-shore variation of surface elevation statistics. These are discussed in detail in section 5.5. The predictions for the standard deviation and *Hrms* follow the same trends. The overall agreement for both these parameters is fairly good for all 4 tests. Note that the irregularity in the observations for A1, particularly for gauge 1, were shown to be due to reflection from the swash zone (section 4.2.4), which the model does not reproduce.

Both the standard deviation and *Hrms* tend to be overestimated in the surf zone for tests B. These over-estimations correspond to over-estimations of both the mean maximum and the absolute mean minimum elevations in that region. Inspection of the mean roller thickness reveals that some initial breaking occurs over the bar crest, but then stops over the bar trough to start again further onshore. The cessation of breaking allows the waves to shoal again, thus resulting in overestimated wave heights. No information on the location of breaking in the laboratory is available for this study. However, gauge 15 is located in the region of the trough and does not show signs indicating that breaking has stopped. Thus, given the spatial variation of the observed elevation statistics, it is suspected that breaking started over the bar crest and was continuous through the surf zone. It is shown in section 5.4 that the erroneous prediction of the breaking location is due to a violation of the mild slope assumption in the breaking region.

The results show an underestimation of *Hrms* and *Hmax* in the final stages of shoaling and in the outer surf zone for the irregular runs. Schäffer *et al.* (1993), Svendsen *et al.* (1996) and Madsen *et al.* (1997a) made the same observation. This appears to be a common feature of models expressed in terms of the depth-integrated velocity. Models with the depth-averaged velocity as a dependent variable tend to overestimate slightly the wave height (see e.g. Wei *et al.*, 1995). In the derivation of η-P and η-$\bar{u}$ models, high order nonlinear terms are neglected. As the waves shoal, these neglected terms become increasingly significant and (should) affect the solution. Table 4.1 shows that the nonlinear parameters based on Hmax for the irregular runs are very high. For condition A2, table 4.1 gives $\varepsilon = 0.1$ at gauge

[1] The interested reader is referred to table 3.1 for an indication of the wave height to water depth ratio at the breaking point ($= 2\varepsilon_{br}$).

1 and based on *Hrms*. ε based on *Hmax* is already as high as 0.2 at the toe of the beach. and reaches 0.6 at the average breaking point. The highest waves in the incoming wave train tend to be underestimated by the model, thus resulting in underestimated *Hrms*. Notice that the underestimation of the wave height is associated with an underestimation of the mean elevations above the *mwl*, whilst the predictions for mean elevation below the *mwl* are correct. It also appears that, for the same breaking parameter, the underestimation is greater for A2 than for B2. This, on the basis of the model limitations outlined above, may be explained by the fact the basic wave height for B2 is smaller (nonlinearity weaker) than that of A2. Besides a violation of the weak nonlinearity assumption, the wave height underestimation in the breaking zone may be the result of bad shoaling properties of the model for the high super-harmonics (large *kh*) inevitably present in the irregular runs. Since less high harmonics develop for B2, the improved performance of the model for that run (relative to A2) is again justified.

The irregular spatial variation of the wave heights (also seen in figures 3.8 and 3.13) is due to the fact that, due to wave-wave interactions, the wave shape constantly changes as the wave train propagates onshore. In the time series analysis, waves smaller than 6 cm are ignored (and assumed to belong to the preceding wave; see section 4.3). Thus, as the waves shoal, at e.g. $x = 30$ m, such a small wave, if less than 6 cm high, may be ignored. At say $x = 32$ m, if this wave has 'grown' to be larger than 6 cm, it is identified as an individual wave. This results in the wave at $x = 30$ m being divided into two smaller waves at $x = 32$m, and a decrease in the wave height. Of course the minimum wave height of 6 cm is arbitrary, and reducing it results in some smoothing in the spatial variation of the wave height[1].

The *mwl* predictions are not as satisfactory. The set up in particular is underestimated for all four runs, particularly the tests B1 and B2. For those two tests, the set-up underestimation may be partly explained by the fact that the breaking is predicted at the wrong location, that is, too far onshore. This was already seen to be the reason for the overestimation of the wave height. Since the set-up is related to the rate at which energy is dissipated, the wave height overestimation is associated with a late set-up.

An interesting feature of the model appears in the cross-shore variation of $\bar{\delta}$. The wave breaking simulation allows each wave to be treated individually. This is reflected in the

[1] note that the same minimum wave height was used for both the lab and numerical data.

irregular runs for which $\bar{\delta}$ indicates the successive breaking of the highest to the lowest waves. An attraction of this wave breaking model is that is allows wave breaking to cease if the water depth increases again. This can be useful in the case of waves breaking over a submerged bar for example. In the case of B1 and B2 however, the cessation of wave breaking in the bar trough is unrealistic.

Figure 5.3 shows the predicted versus measured elevation statistics for all four cases. The plain line and the two dashed lines represent perfect agreement and 20% difference between measured and computed data, respectively. It shows that despite the poor performance of the model for the *mwl*, the rest of the parameters are well predicted. Discrepancies up to 50% are noticed but typical errors are less than 10%. Close inspection shows that the points outside the 20% limit systematically belong to the surf zone.

5.2.2 Depth-averaged velocity (low order) statistics

The predicted cross-shore variation of the velocity statistics are compared to observations in figure 5.4a (tests A) and 5.4b (tests B). These figures display the cross-shore variation of, from top to bottom,

- the undertow,
- the standard deviation,
- the mean onshore and mean offshore depth-averaged velocities ($\hat{U}_{on}$ and $\hat{U}_{off}$, respectively), and
- the mean maximum onshore and mean maximum offshore depth-averaged velocities ($\hat{U}max_{on}$ and $\hat{U}max_{off}$, respectively).

The same oscillations as those observed in the elevation statistics appear. Again they will be discussed in section 5.5.

The undertow predictions are in good agreement with the approximation obtained from the observations. The results for the regular long waves test tend to over-estimate the undertow in the surf zone.

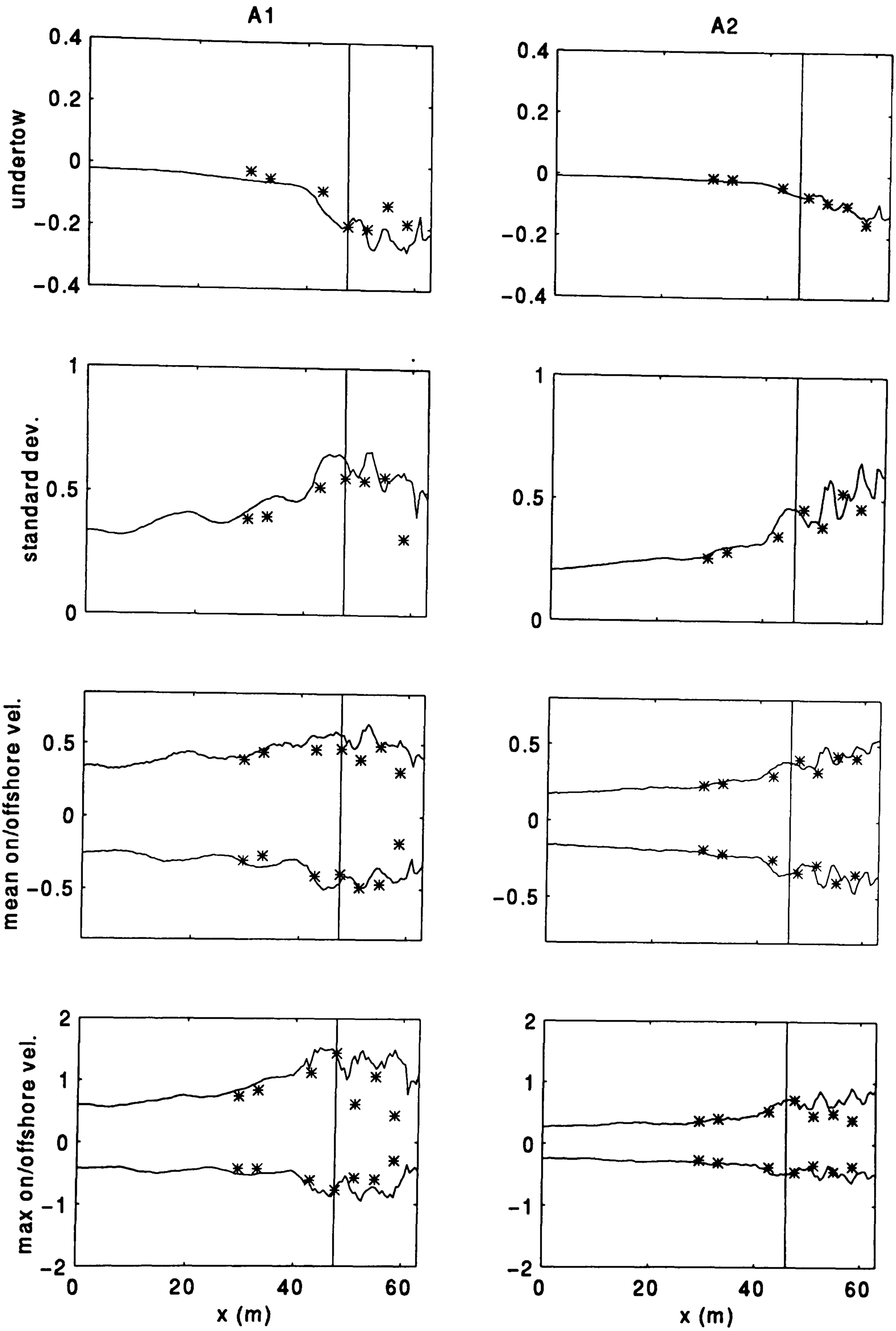

Figure 5.4a Cross-shore variation of the predicted (———) and observed (*) depth-averaged velocity statistics for run A1 (left column) and A2 (right column). From top to bottom are the undertow, velocity standard deviation, mean onshore and offshore velocities, and mean maximum onshore and offshore velocities. Onshore velocities are positive.

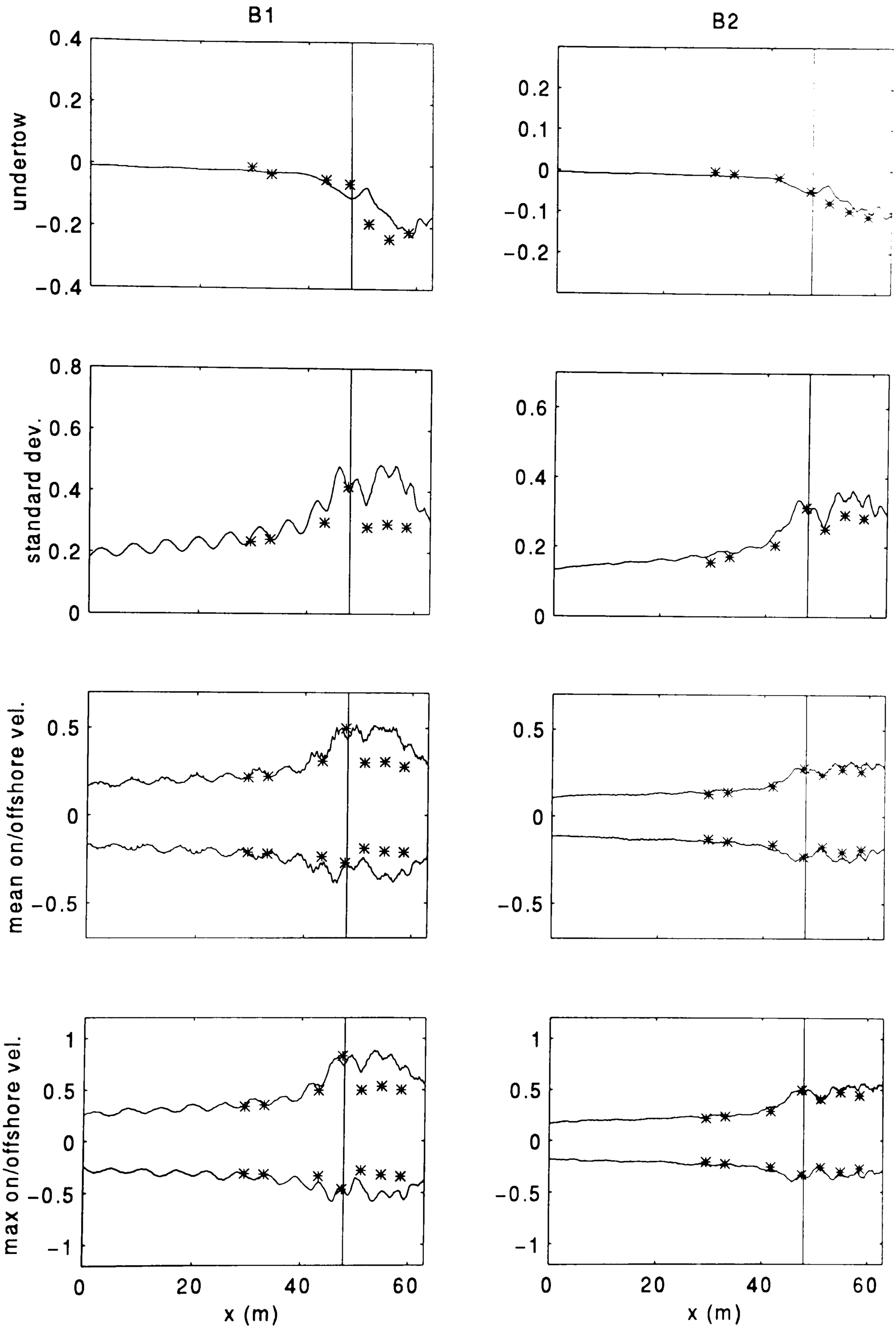

Figure 5.4b Cross-shore variation of the predicted and observed depth-averaged velocity statistics for run B1 (left column) and B2 (right column). Legend as in figure 5.4a.

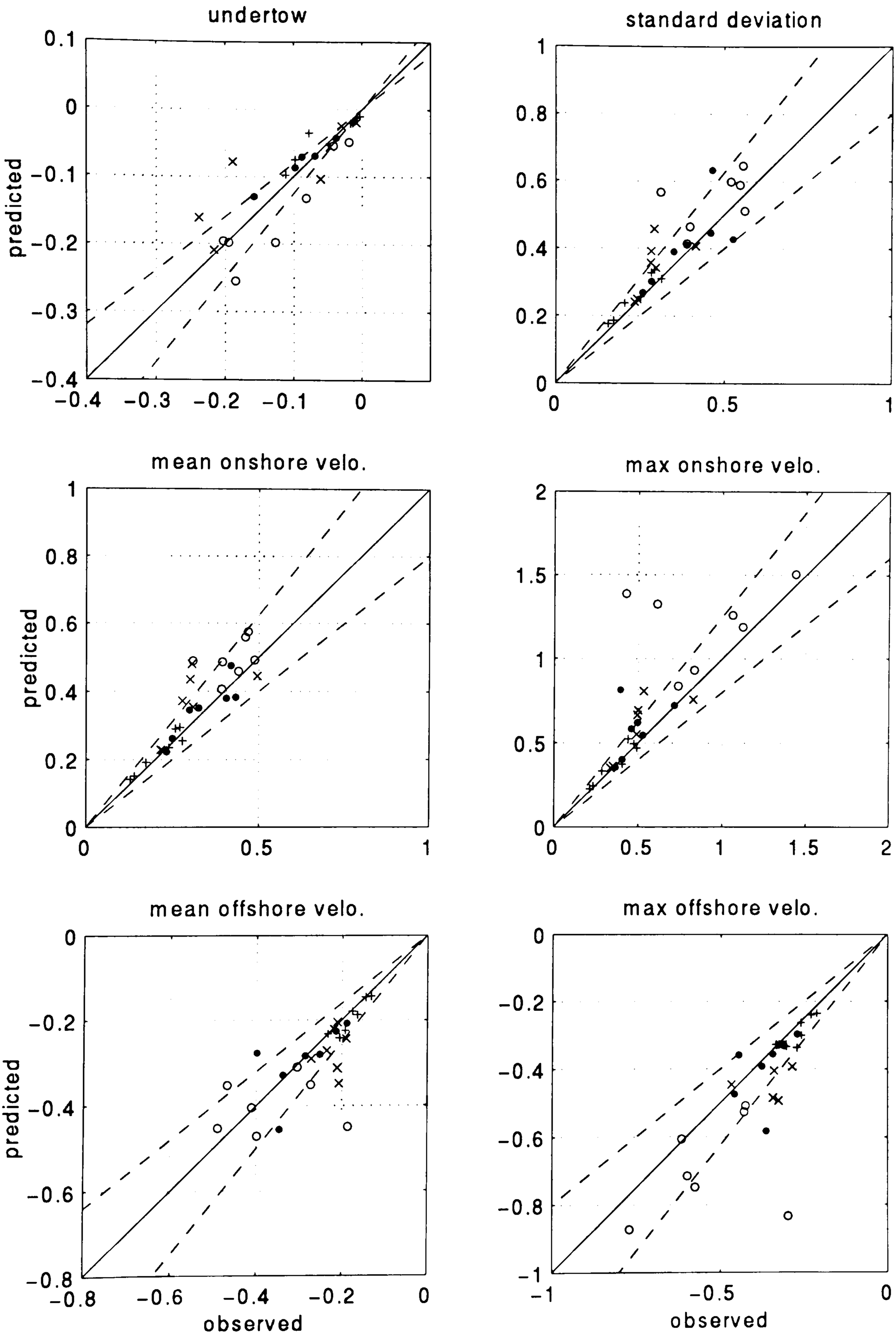

Figure 5.5 Predicted *versus* observed depth-averaged velocity statistics. Legend as in figure 5.3.

The predictions for both the offshore velocities, $\hat{U}_{off}$ and $\hat{U}max_{off}$, and the onshore velocities, $\hat{U}_{on}$ and $\hat{U}max_{on}$ are promising. The results are excellent for the irregular runs. The predictions for the regular runs tend to overestimate $\hat{U}_{on}$ and $\hat{U}max_{on}$ in the breaking zone. The eventuality that these over-estimations may be the result of the approximations made in the calculations of the depth-averaged velocity from the measurements deserves some attention. These approximations are described in section 4.2.3. Since the current meters are mostly located in the bottom half of the water column (figure 4.1), one may expect the calculations of the depth-averaged velocity from the measurements to be an underestimate. The uniformity of the velocity field suggests this may not be the case. Let us consider the current meters from c1 and c2. They were set in the bottom half of the water column, close to the bed. It was found that the calculation of the measured velocity at this location leads to a fairly good agreement with the predicted depth-averaged velocity at this cross-shore location. Furthermore, since, in theory, velocity profiles tend to become more uniform as the waves propagate into shallower waters, if the discrepancies were due to the approximations involved in the observed depth-averaged velocity, then they would increase with increasing water depth. It is not the case however, as it is in shallower water that the discrepancies are largest. It may thus be concluded that the approximation made in the calculation of the measured depth-averaged velocity is quite valid.

This overestimation of the onshore velocity was also observed by Wei *et al.* (1995) and Bosboom *et al.* (1996), who both found that this was associated with an overestimation of the crest elevation. Their tests consisted of regular non-breaking waves (Table 2.1). Note that their models are expressed in terms of η and $\overline{u}$, which tends to slightly overestimate shoaling (see section 5.2.1). Wei *et al.* proposed that the overestimation of onshore velocities, like the overestimation of the crest elevations by their model, is due to the limitation of the model to weakly nonlinear waves. It is particularly accentuated in the surf zone, which would support this hypothesis. Wei *et al.* (1995) compared the results from their weakly nonlinear model to those from their new 'fully' nonlinear model and found remarkable improvements, which also corroborates the above assumption.

As for the elevations, the plot of predicted against observed velocities (figure 5.5) shows general agreement within 20 %. Given that most of the model - data comparison for the velocities are located in the surf zone, the results are fairly good.

5.2.3 Wave shape prediction

5.2.3.1 Direct comparison of elevation time series

One of the attractions of time domain models like Boussinesq-type models is that their output consists of time series of surface elevation and velocities which can directly be compared to measurements, thus giving an indication of the ability of the model to simulate the wave shape. Both the measured and the computed time series of surface elevation are plotted for each regular test at three representative cross-shore locations in figure 5.6. The time lag between the measured and simulated time series was evaluated at gauge 1. The measured time series were subsequently shifted by that time lag for all gauges, hence making it possible to keep track of time information. The series are given for a duration of twice the wave period, starting after permanent wave profiles were obtained at gauge 19, and with a time increment of 0.25 sec, that is 32 and 12 points per wave period for A1 and B1 respectively.

The wave profile for A1 evolved significantly during shoaling. The discrepancies between the observed and simulated wave field at gauge 1 were already observed in figure 5.1 where it appeared that the energy at the third harmonic frequency is overestimated in the simulation. Indeed, this is reflected in the time series by a simulated wave profile showing signs of the presence of a super-harmonic. This appears to incite more nonlinear interactions which result in a steeper wave shape at gauge 14. Besides wave generation inaccuracies, the discrepancies between predicted and observed elevation time series can be explained by looking at figures 3.2 and 3.3. It is clear from these figures that the phase celerity and shoaling of waves for large *kh* cannot be well predicted.

Measured wave period is alternatively smaller (gauge 14) and larger (gauge 19) than computed. This may be the result of offsets in the cross-shore position of the wave gauges. The magnitude of the errors thus introduced depends on the wave celerity and the speed and intensity of wave shape changes. These are known to be rapid for run A1, and a small mismatch in the location of the physical and numerical wave gauges is likely to be the origin of these wave profile mismatches.

The reproduction of the wave shape for B1 is fairly good throughout the channel. The wave profile for this test barely evolved during shoaling, which is indicative of little triad interactions. The wave generation is reasonably good. Despite the improved dispersion

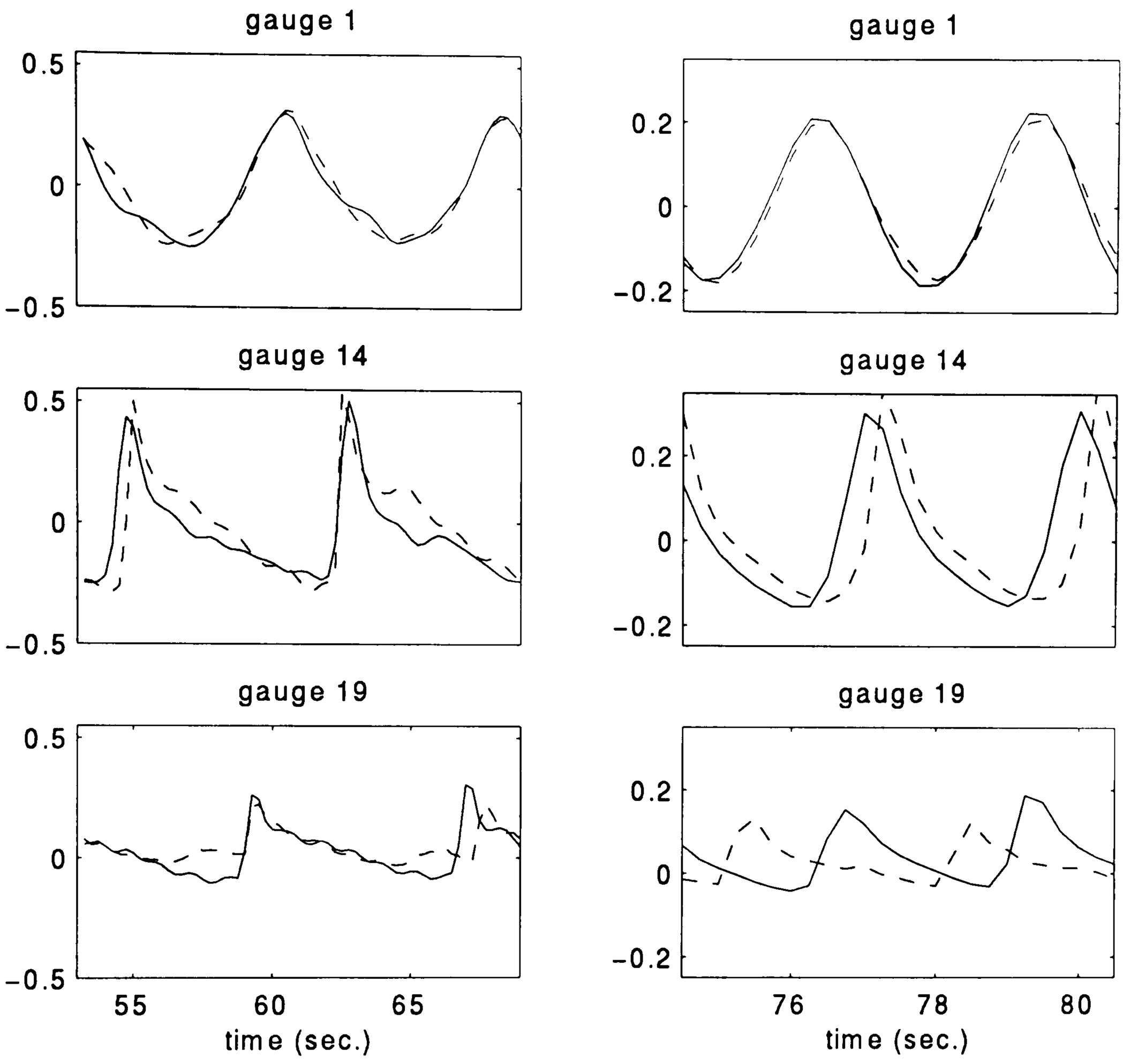

Figure 5.6 Predicted (———) and observed (------) wave profiles at three cross-shore locations for run A1 (left column) and B1 (right column). Wave breaking occurs around gauge 14. (top plots) gauge 1, x = 0m; (middle plots) gauge 14, x = 47.5m; (bottom plots) gauge 19, x = 62.2m.

characteristics introduced in the equations, there is a difference of phase celerity between the model and laboratory results: the waves appear to travel faster in the model than they actually did in the tank. This difference of phase celerity increases as the waves travel shoreward. Inspection of the wave shape (and power spectrum) evolution between gauges 1 and 8 shows dominance of the primary waves in this region, thus kh varies from 1.25 to 1.11 [1]. Given that B = 1/15, and according to figure 3.2, the phase error relative to Stokes first order theory (linear theory) between these two gauges is nil. Indeed both Stokes first order theory and equation 2.15 give c = 3.77 m/s at gauge 8. An evaluation of the actual celerity at this location was made using the signal from (laboratory) gauges 7 and 8, which are distant

[1] At gauge 1, L=14 m, h = 2.8 m. At gauge 8, L=11.3m, h=2m.

by 3.66m and between which little change occurs. This gave a wave celerity of 3.67 m/s. This solution differs from the Stokes first order theory towards which the parameter B was 'adjusted' for short waves, and explains the discrepancy.

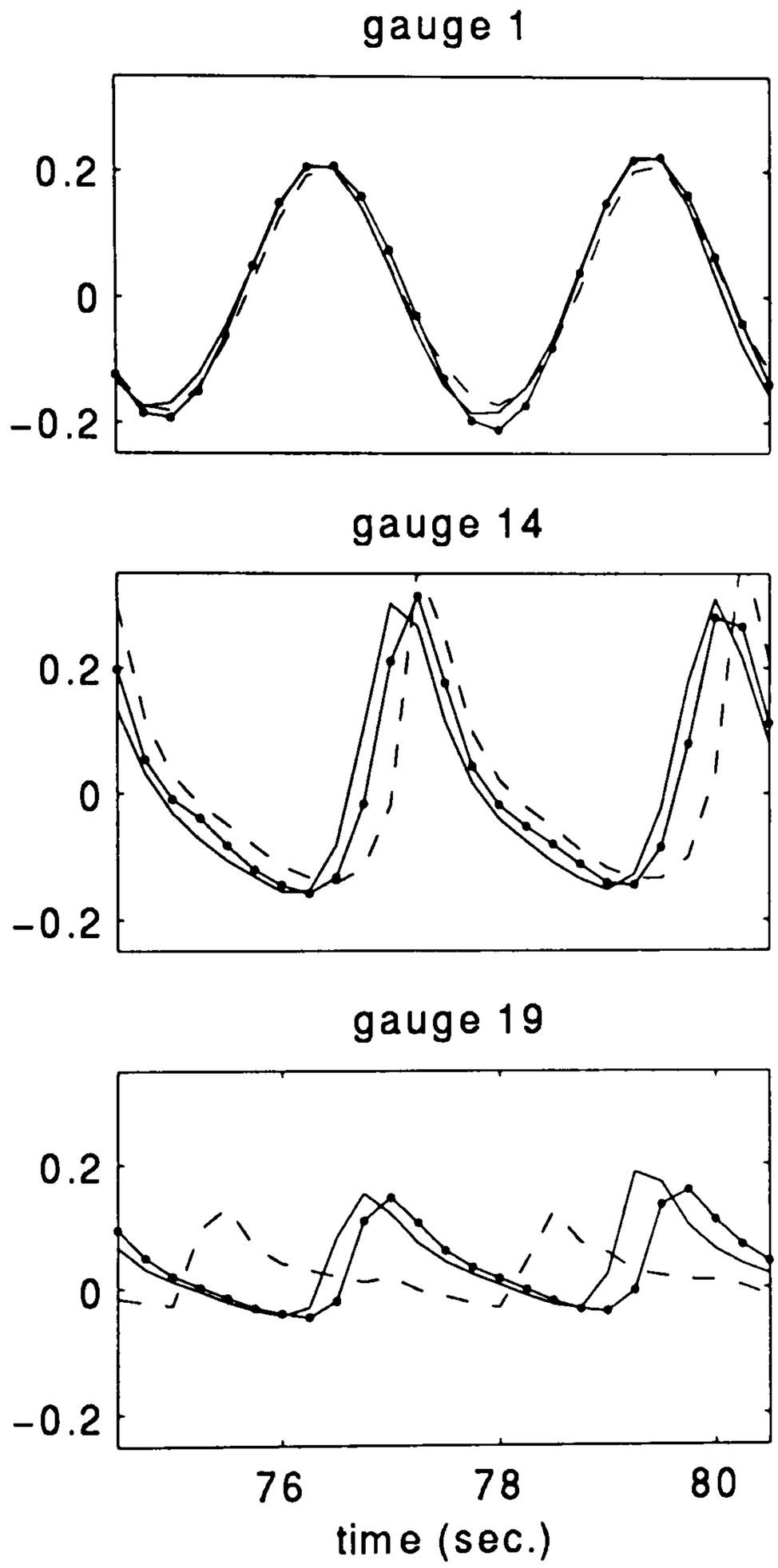

Figure 5.7 Wave profiles at three cross-shore locations for B1.
Predictions with B = 1/15 (———), B = 1/21 (—•—•—), and observations (- - - - - -).

The same test was run with B = 1/21 for which c is slightly reduced to 3.75 m/s [1]. It resulted in very little difference in the elevation statistics. It did however result in a slight improvement in the phase velocity prediction (figure 5.7).

[1] A value of 1/21 can be shown to yield better results for large kh. Over the whole range of kh however, B=1/15 yields the best results. Here (kh=1.25), theoretically, B=1/21 yields results that depart from Stokes's first order solution more than B=1/15. Since the actual celerity is somewhat smaller than Stokes's first order solution, and since B=1/21 yields a celerity (slightly) closer to the actual one, calculations with this value were attempted nevertheless.

Small errors in the predictions of the phase celerity, because they have a cumulative effect, may result in large discrepancies. Despite this deficiency of the model, the wave shape is very well predicted for test B1, and the over-prediction of the phase celerity is not a problem. It must be kept in mind however as the wrong prediction of an harmonic phase celerity may result in an incorrect wave profile prediction.

5.2.3.2 Elevation and velocity skewness and kurtosis

Elevation

The predicted and observed skewness and kurtosis of the free surface elevation, S_η and K_η respectively, are compared on figure 5.8 for all 4 tests. For each run, the spatial variations of S_η and K_η are comparable in shape, and the discrepancy between predicted and observed S_η is comparable to the discrepancy between predicted and observed K_η.

S_η and K_η for case A1 start increasing very early at about x = 10 m. For test B1 on the other hand, they are constant up to x = 35m, after which they start increasing. A1 is characteristic of long/shallow water for which the phase mismatch between fundamental and bound harmonics is smaller than for B1. The development of triad interactions for A1 and A2 occurs further offshore compared to B1 and B2. This is well reproduced by the model.

Let us first examine S_η and K_η in the shoaling zone. The agreement between predictions and data is fairly good. S_η and K_η tend to be underestimated for all runs, except A1. This underestimation is associated with an underestimation of the crest elevation (figure 5.2a & b). Clearly the underestimation of S_η and K_η is a result of the violation of the weak nonlinearity assumption. The slight overestimation of S_η and K_η for A1 on the other hand is associated with an overestimation of the crest elevation which will be discussed in section 5.6.

In the breaking zone, the spatial evolution of S_η and K_η becomes more variable. A common feature of the observed cross-shore variation of S_η and K_η for A2, B1 and B2 is an increase up to some distance after breaking, after which both parameters decrease. This is in agreement with observations based on field experiments by Guza and Thornton (1985). This pattern is not observed for A1 for which reflection was already seen to induce irregularities in the cross-shore evolution of the wave field.

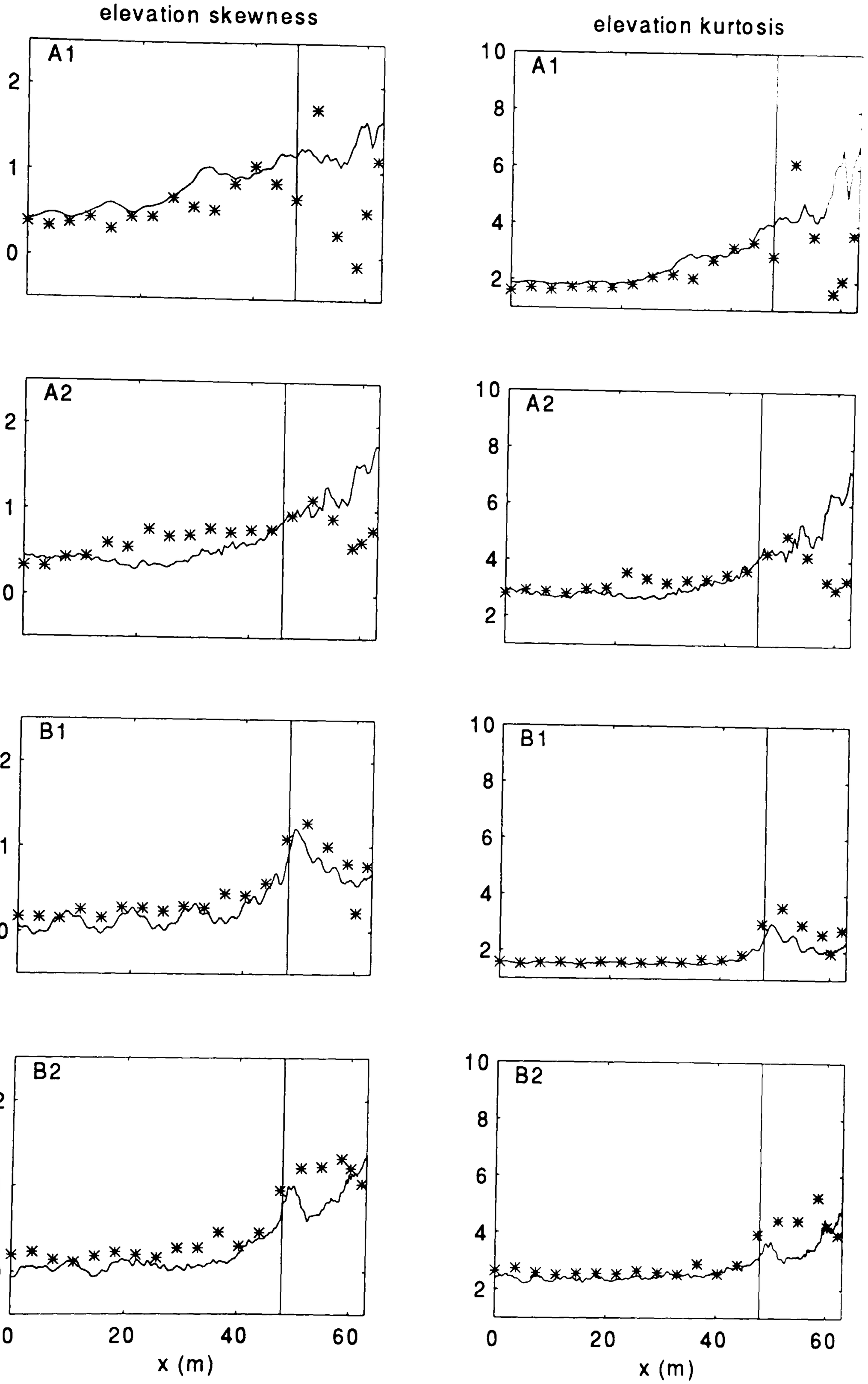

Figure 5.8 Cross-shore variation of the predicted and observed surface elevation skewness S_η (left column) and kurtosis K_η (right column), for, from top to bottom, A1, A2, B1 and B2. Legend as in figure 5.2a.

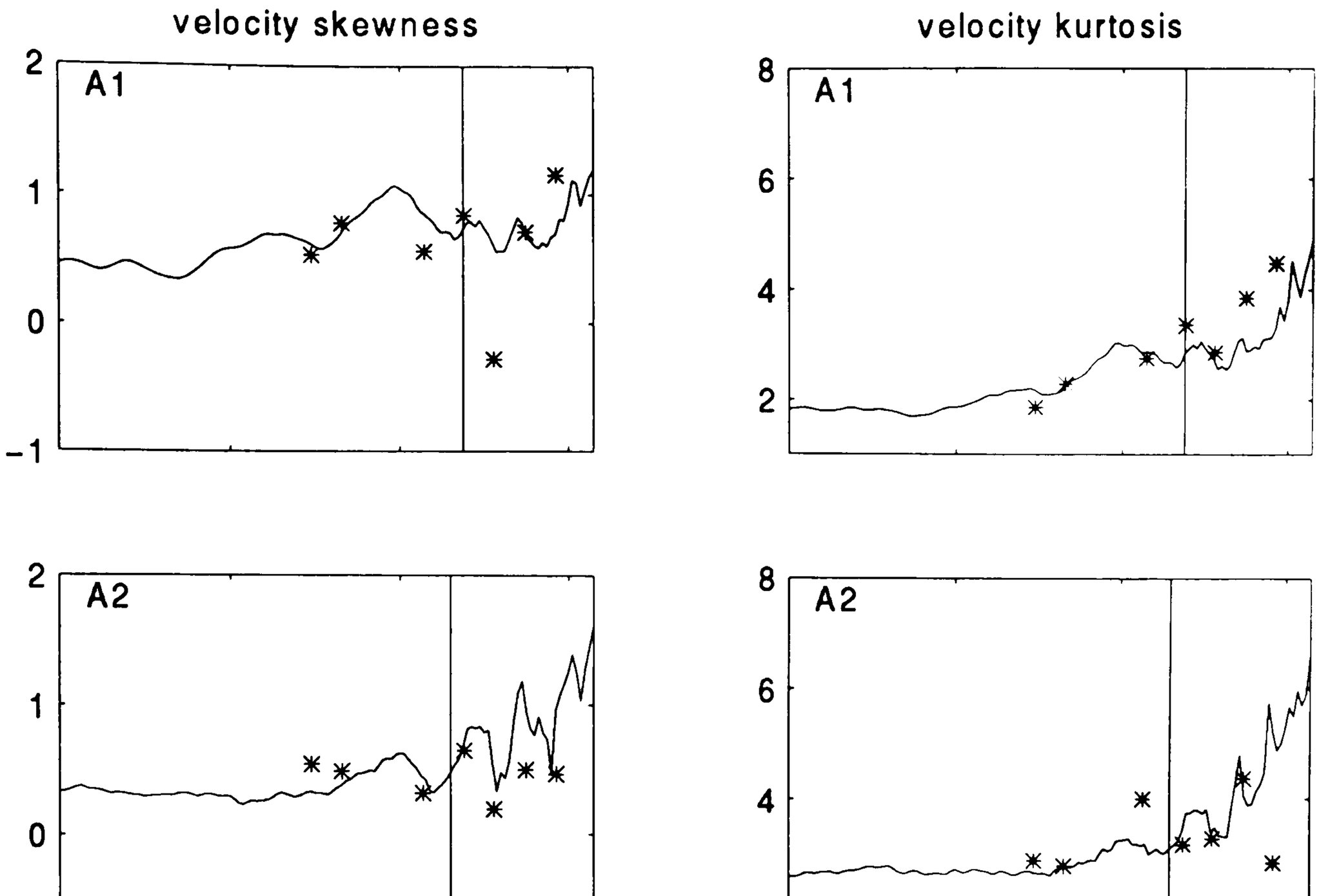

Figure 5.9 Cross-shore variation of the predicted and observed depth-averaged velocity skewness S_U (left column) and kurtosis K_U (right column), for, from top to bottom, A1, A2, B1 and B2. Legend as in figure 5.2a.

The predictions do reproduce this maximum for B1, for which direct observation of the time series already indicated matching wave shapes. For the other runs, the dominant trend indicates a general increase for the predictions of S_η and K_η. The simulated cross-shore variations of S_η and K_η for B2 are interesting in that they show a sudden decrease in the region of the bar trough. It was shown in section 5.2.1 that wave breaking is unrealistically predicted to cease at this location.

The possibility that this continual increase of S_η and K_η in the surf zone may due to boundary effects was investigated. The tests were run with a range of sponge layer parameters, and with variable length of flat bed in front of the sponge layer. This had no effect on the results. Reasons for the disagreements in the breaking zone, not only in magnitude but also in shape, were thus thought to lie in the model`s properties.

In the inner surf zone region, nonlinear effects increasingly dominate over dispersive effects. It is clear that the model is being applied beyond its limits. The presence of the dispersive terms tends to counter-balance the nonlinear terms: the effect of frequency dispersion is that the higher harmonics travel much slower than the basic wave. This results in a wave profile that is less steep (under-estimated asymmetry), which in turn may result in an overestimated skewness.

The nonlinear parameter ε can be shown to be continuously increasing in the surf zone. While the effects of the violation of the weak nonlinearity assumption in the surf zone are not clear, it is reasonable to suggest this violation may be responsible for discrepancies in the region.

A more definite cause for these disagreements is the presence of wave components with high *kh* generated during shoaling and breaking. From figures 3.2 and 3.3 it is clear that the model's performance with respect to predicting the phase celerity and shoaling of waves with *kh* larger than 5 is poor. A poor performance for high *kh* is thus reflected in a poor wave shape prediction. This is further discussed in section 5.7.

depth-averaged velocity

The predicted and observed skewness and kurtosis of the depth-averaged velocity, S_U and K_U respectively are compared in figure 5.9. The overall fit for S_U and K_U is very promising. The results for B1 exhibit some interesting features. While the predicted $\hat{U}_{on}$ and $\hat{U}_{off}$ are larger than the measured data, the S_U and K_U show excellent agreement with the data. In

other words, although the magnitude of the predicted velocities is larger than the measured ones, it appears that the shape of the velocity time series is well predicted.

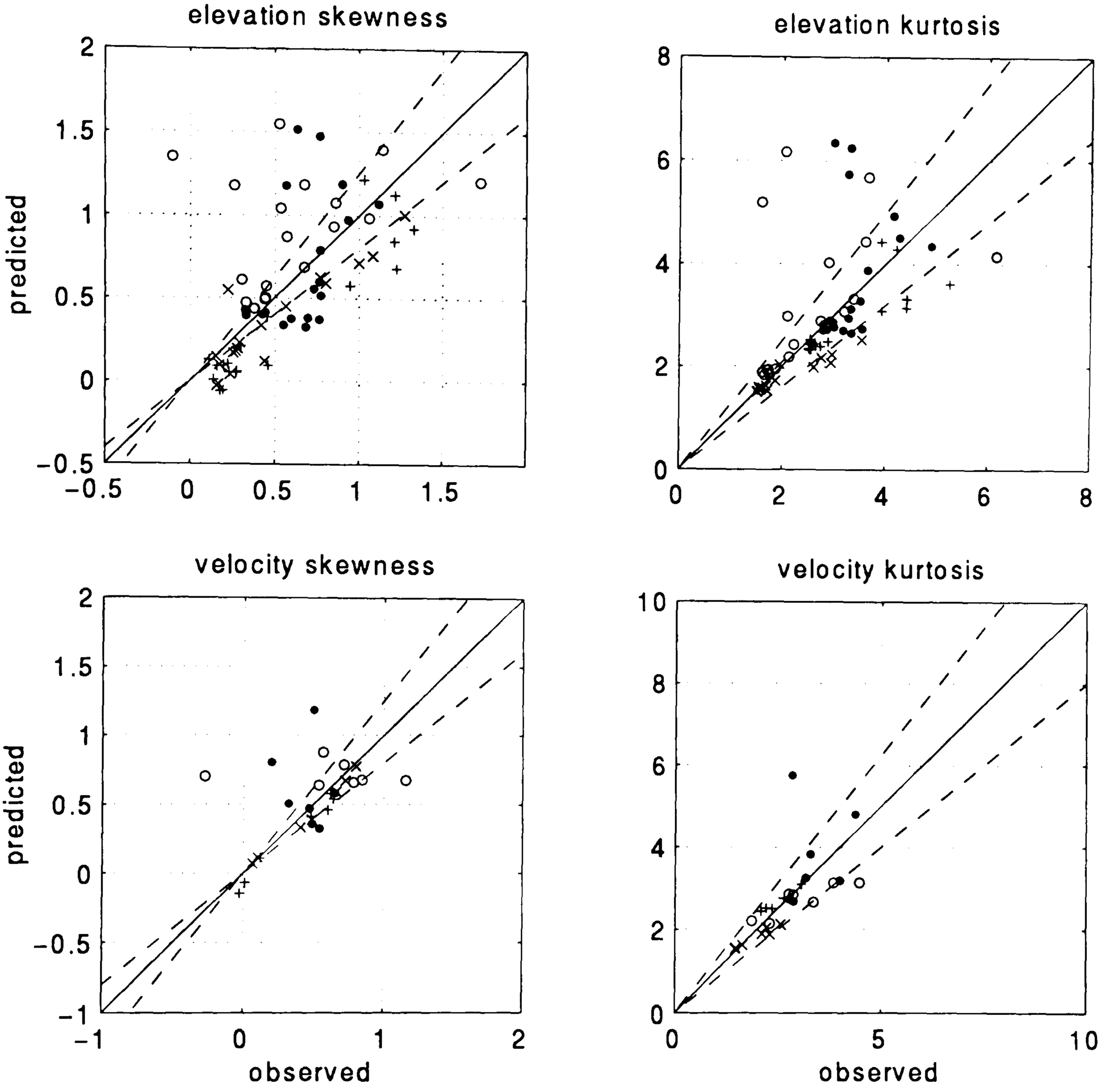

Figure 5.10 Predicted *versus* observed surface elevation (top row) and depth-averaged velocity (bottom row) skewness (left column) and kurtosis (right column). Legend as in figure 5.3.

Figure 5.10 shows a plot of predicted versus observed skewness and kurtosis. The largest discrepancies for S_η and K_η are for the largest skewness and kurtosis values, that is, data in the surf zone.

In terms of percentage difference between measurements and computed results, S_U and K_U are better predicted than S_η and K_η. This, combined with the fact that the discrepancies for S_η and K_η are greater in the surf zone, suggests that another possible cause for the

disagreements for the elevation statistics could be the difficulty of measuring free surface elevations in the surf zone. Turbulence and aeration make the free surface level difficult to determine. Furthermore, the performance of the resistance and capacitance wave gauges with respect to measuring wave shape is uncertain. For example, resistance gauges are known to distort the wave shape due to the finite distance between their two parallel wires (Hughes, 1993).

On the other hand, one may argue that the improved agreement for the velocity moments may be due to the fact that these are integrated quantities, and, as a result, irregularities may be smoothed out. Inspection of fig. 4.4 however shows that, for most cases, the velocity moments are fairly uniform though the depth. Furthermore, despite the fact that arrays c1, c2 and c7 (fig. 4.1) consist of one current meter only (i.e. no smoothing is made), the agreement between numerical predictions and measurements is good, even in the surf zone (array c7). It may thus be concluded that the averaging over three or two current meters at arrays c3, c4, c5 and c6 has not resulted in significant smoothing, and may not justify the improved agreement for the velocity moments.

5.3 Sensitivity to ϕ_B

The sensitivity to ϕ_o, f_δ, t^* and the analytical expression for c were qualitatively described in section 5.1.3. The effect of ϕ_B is greater in magnitude and is studied in detail in this section.

5.3.1 Surface elevation (low order) statistics

Figure 5.11 shows the effect of ϕ_B on the *mwl* (left column), the standard deviation (middle column), and $\bar{\delta}$ and *Hrms* (right column). The effect of ϕ_B on *Hrms* is as expected: increasing ϕ_B results in a shift shoreward of the breaking point, which is reflected by a shift shoreward of $\bar{\delta}$.

Let us first consider A1. As ϕ_B increases from 20° to 23° , the waves are allowed to shoal further. This results in a marginally better fit for Hrms. Increasing ϕ_B further to 26° results in a decrease and modulations in *Hrms* in the breaking zone. This is explained by the fact that allowing the waves to shoal further results in increased nonlinearity, thus increased generation of higher harmonics, with an eventual decrease of the wave period.

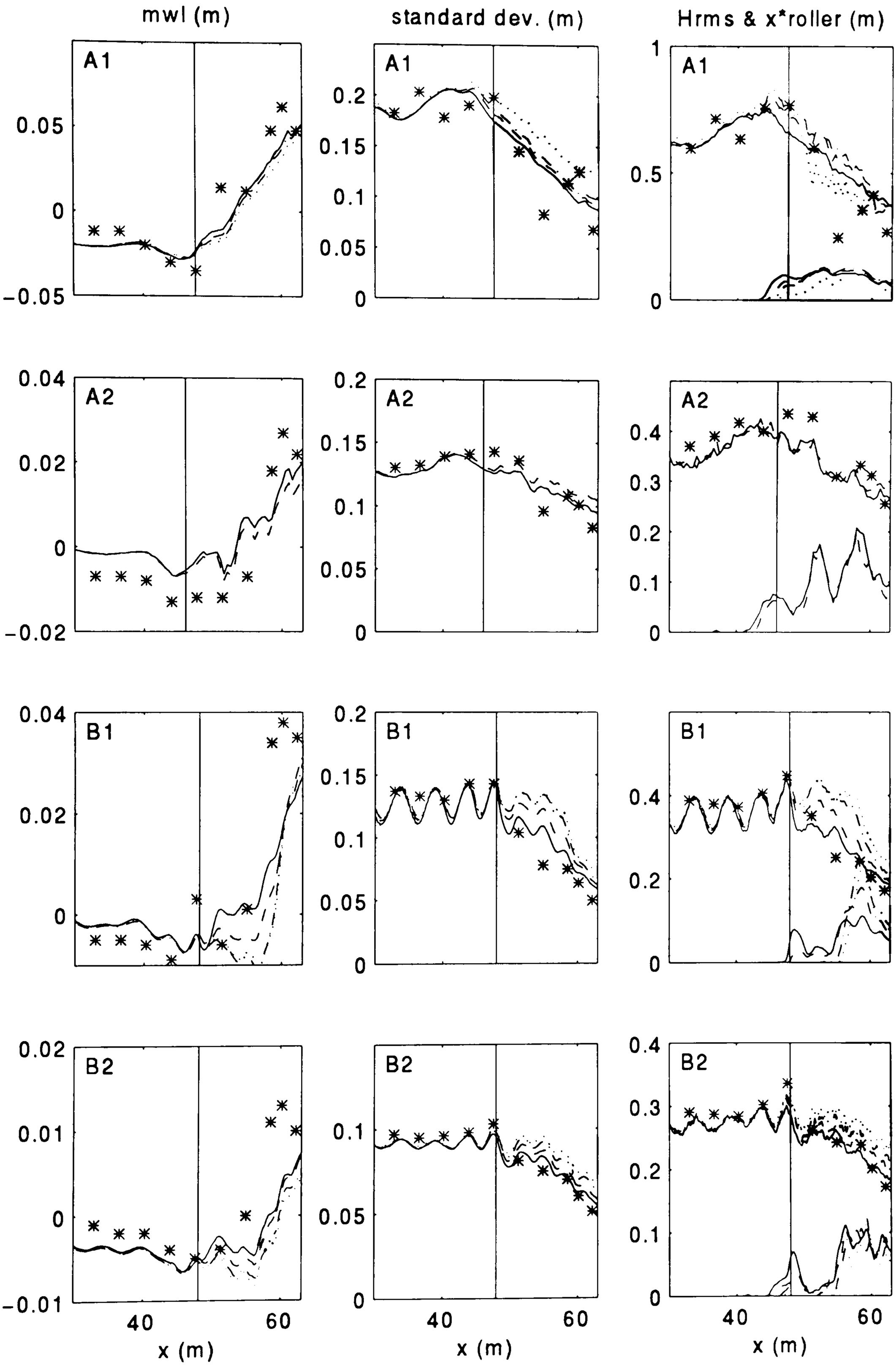

Figure 5.11 Effect of ϕ_B on the surface elevation (low order) statistics: *mwl* (left column), standard deviation (centre column), and *Hrms* and $\overline{\delta}$ (right column), for, from top to bottom row, A1, A2, B1 and B2. ——— $\phi_B = 17°$, - - - - - - $\phi_B = 20°$, -.-.-.- $\phi_B = 23°$, ... $\phi_B = 26°$, ✳ observed data. Results are plotted for x=30-63m.

Increasing ϕ_B for A2 lead to instabilities and no improvement on the prediction of the shoaling wave was possible here. This run shows little sensitivity to ϕ_B with respect to *Hrms*.

For B1 and B2, $\phi_B = 20^o$ leads to overestimations of the standard deviation and *Hrms* in the post-breaking region. This was seen to be a direct result of the incorrect prediction of the breaking location. Increasing ϕ_B further obviously increases the discrepancy. Reducing ϕ_B to 17^o gives a better reproduction of wave decay by inducing earlier breaking, but slightly underestimates *Hrms* in the breaking region. Notice that for B2, increasing ϕ_B to 26^o induces the waves to break much further shoreward with no improvement for *Hrms* at the breaking point. The results are dominated here by the weak nonlinearity assumption. For these 2 cases, keeping ϕ_B at 20^o and 'tuning' with the parameters that control wave decay may give better results in the inner surf zone, while still predicting breaking at the wrong location. The flexibility of the model may thus lead to results that can be misleading. This emphasises the need to carry out a thorough evaluation of the model in terms of breaking location, wave shape and reproduction of the wave-wave interactions.

The shift shoreward of the breaking point with increasing ϕ_B also results in a shift shoreward of the start of set-up, and in a further underestimation of the mean water level. Decreasing ϕ_B on the other hand tends to slightly improve mean water level predictions. For equivalent changes in ϕ_B, the short wave runs seem to be more sensitive to this parameter than the long wave runs. This is because a change of ϕ_B significantly affects the breaking location for these tests, in contrast with tests A1 and A2.

5.3.2 Depth-averaged velocity (low order) statistics

The effects of ϕ_B on the velocity predictions (figure 5.12) are fairly similar to those for the surface elevation. They show the same sensitivity to ϕ_B qualitatively: the increase in the surface elevation standard deviation as a consequence of an increase of ϕ_B is associated with an increase in the velocity standard deviation. The similarity is also quantitative as the relative increase (decrease) of the standard deviation for a ϕ_B changing from 20^o to 26^o (17^o) is the same for both the elevation and the depth-averaged velocity. ϕ_B has relatively little effect on the undertow predictions.

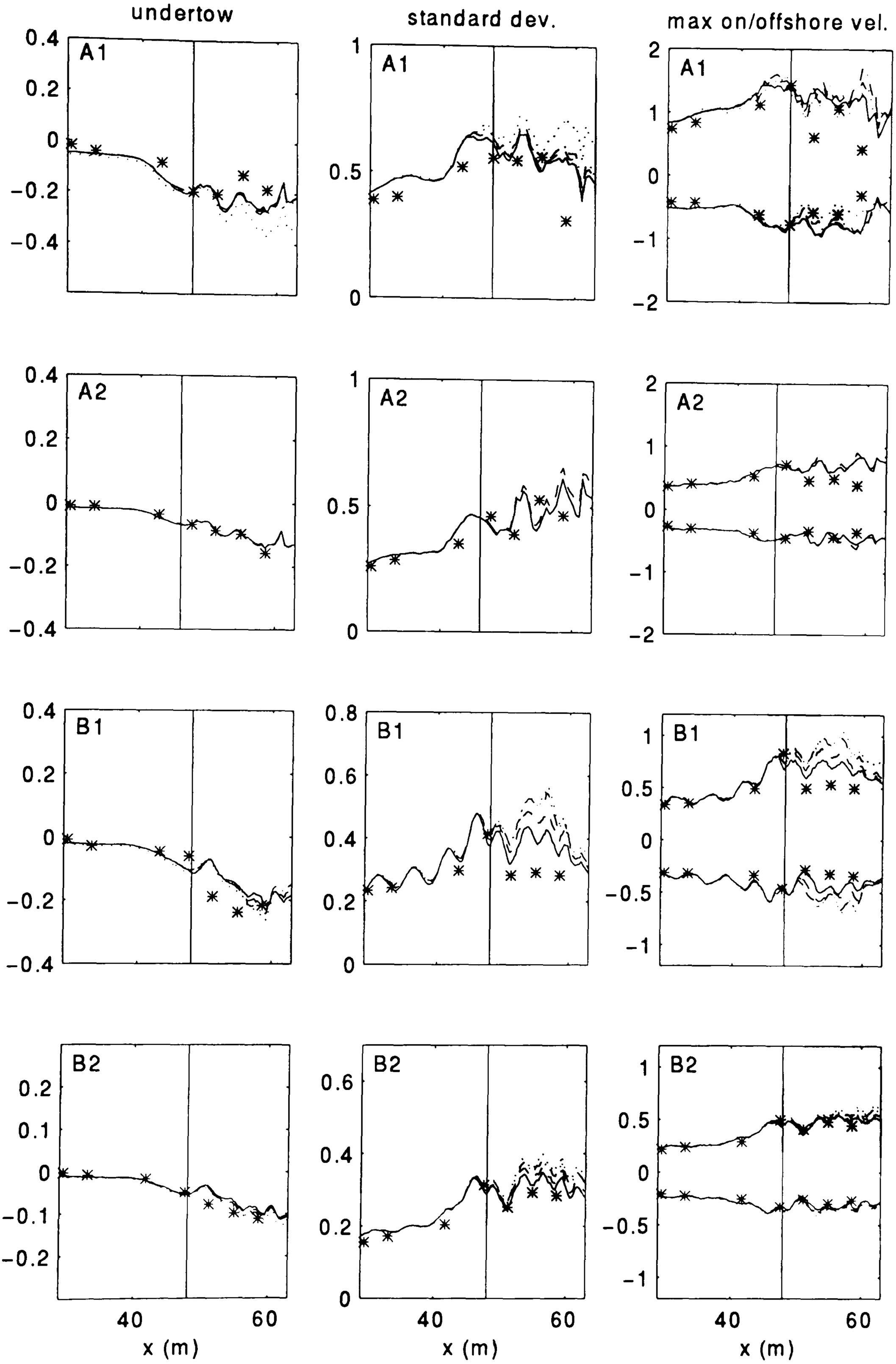

Figure 5.12 Effect of ϕ_B on the depth-averaged velocity (low order) statistics: undertow (left column), standard deviation (centre column), and mean maximum onshore and offshore velocities (right column). Legend as in figure 5.11.

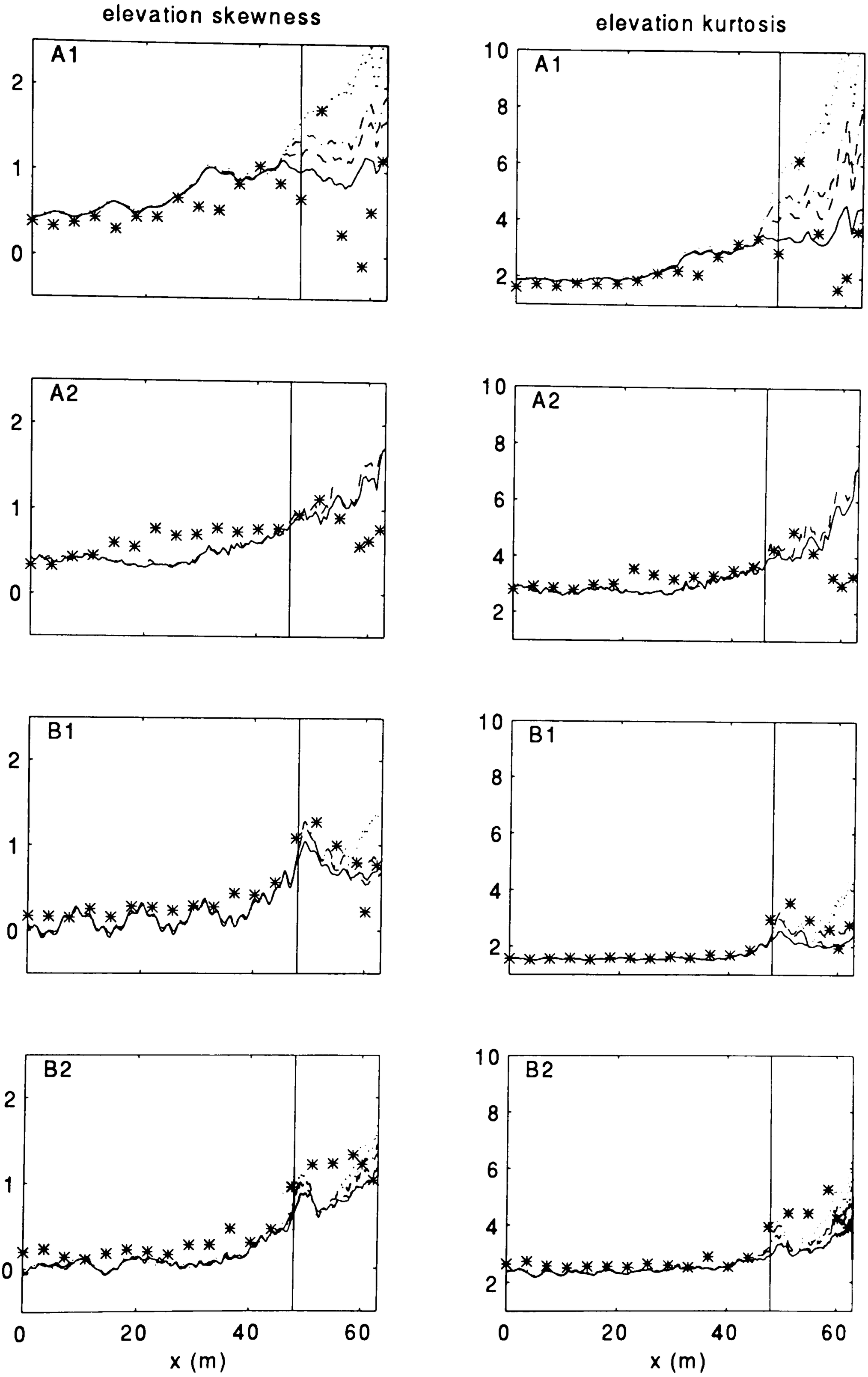

Figure 5.13 Effect of ϕ_B on the surface elevation high order statistics: S_η (left column), and K_η (right column). Legend as in figure 5.11.

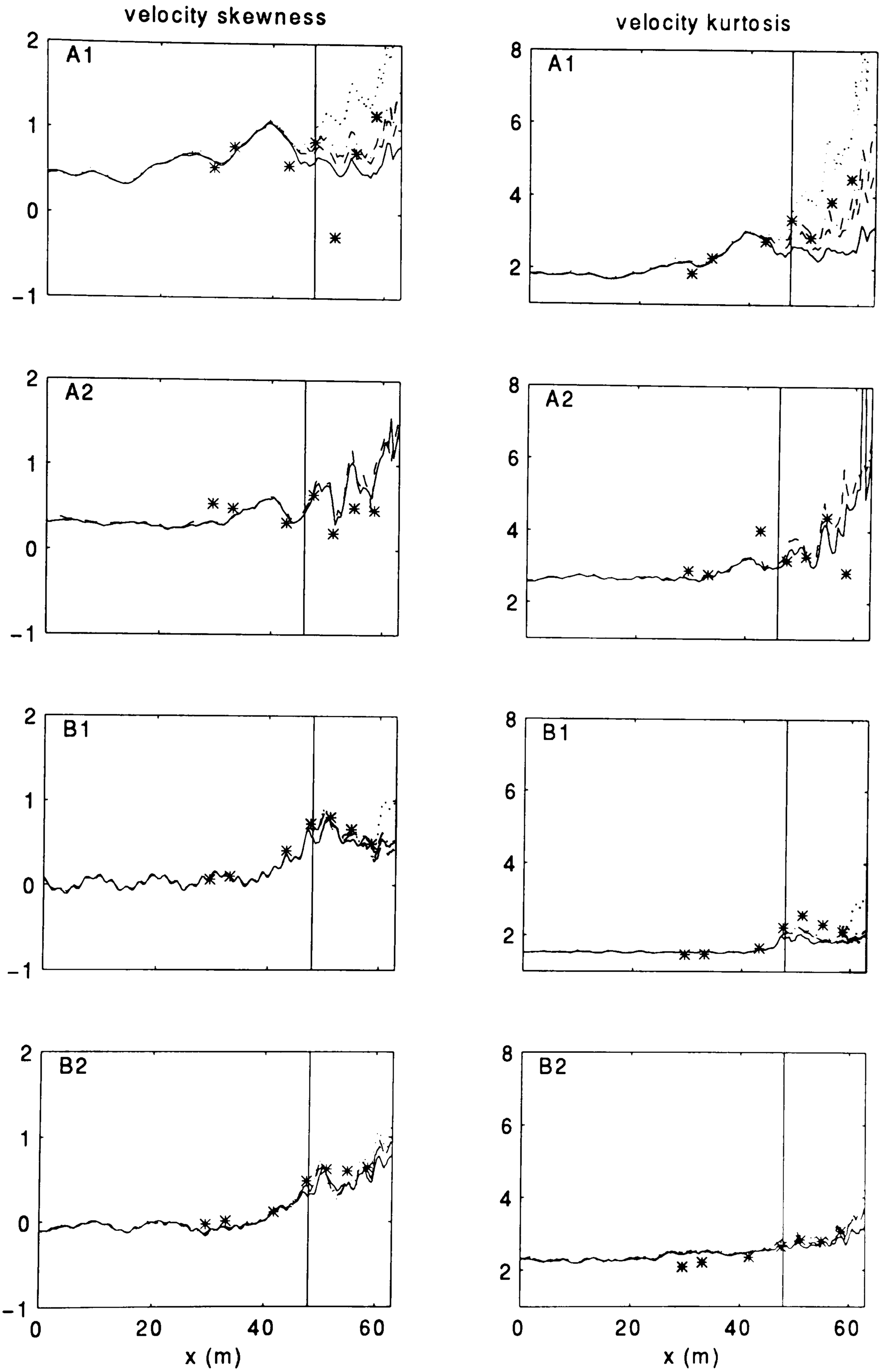

Figure 5.14 Effect of ϕ_B on the depth-averaged velocity high order statistics: S_U (left column), and K_U (right column). Legend as in figure 5.11.

5.3.3 Elevation and velocity skewness and kurtosis

It was shown that the results for low order statistics exhibit some sensitivity to ϕ_B. It is however on S_η and K_η (figure 5.13) that ϕ_B has the most significant effects.

S_U and K_U show the same sensitivity to ϕ_B as S_η and K_η both qualitatively and quantitatively. Results are shown on figure 5.14 for completeness.

S_η and K_η are generally best predicted with $\phi_B = 20°$. As ϕ_B increases, so do S_η and K_η. Again the effect of increasing ϕ_B is that the waves are allowed to shoal further, and therefore become more nonlinear. Thus it is expected that S_η and K_η should increase with increasing ϕ_B. However, an increase of ϕ_B by 6° only (condition A1) may result in a very significant increase in S_η and K_η, both being over-predicted in this case. The regular long waves run A1 exhibits the greatest sensitivity to ϕ_B. While increasing ϕ_B to 23° results in a slight improvement for the wave height, it produces a dramatic increase, and in this case overestimation, of S_η and K_η. In other words, efforts to improve the results for the wave height and the mean water level may yield the wrong wave shape. This, again, stresses the need to evaluate the model in all aspects, not only in terms of wave height and *mwl*.

The predicted S_η and K_η for case B1, which so far followed the trend obtained from the measurements, are seen to start increasing some distance after breaking if ϕ_B is set as high as 26°. These over-estimations of predicted S_η and K_η are due to the increasing presence of higher harmonics, generated during shoaling and breaking, which is associated with increasing ϕ_B. This will be discussed further in section 5.6.

5.4 The mild slope assumption and its implications

Throughout the comparisons carried out so far it has been possible to observe the prediction by the model of strong interactions of the waves with the bathymetry. For example, the modulations in the onshore and offshore velocities perfectly follow the bathymetry, increasing over the bars, and decreasing over the troughs. The predicted skewness and kurtosis also show strong coupling with the bathymetry, particularly for the irregular runs. Whilst this correlation between e.g. the velocities and the bathymetry is theoretically agreeable, the predicted interruption in the bar trough of the wave breaking process for cases B1 and B2 raises the following question: is this predicted instantaneous response to changes in the water depth a realistic representation of the actual wave field ?

This section provides a discussion of the effects of deviations from the assumption of slowly varying bathymetry. As an introduction, it is useful to emphasise why this assumption was made and its implications. First, the long wave assumption, the basis of classical Boussinesq models as well as of models based on the nonlinear shallow water equations, may be expressed as $kh << 1$, that is, the wave length is much longer than the water depth. This may be reinterpreted as implying that the wave properties vary little in a distance of the same order as the depth (Peregrine, 1972). This in turn has some implications regarding the bed slope. Using non-dimensional and scaled variables, Dingemans (1997) showed that the bottom slope h_x is $O(\mu^{1/2})$ at most, that is $h_x <= h/L$. In the derivation of the equations (section 2.2.4), the first derivative of h was considered small, i.e. $h_x << \mu^{1/2}$, and consequently higher derivatives and products of derivatives were neglected [1]. Since, despite improved dispersion, h/L is restricted itself, this imposes a very stringent restriction on the bottom slope and curvature.

Let us first consider the regular case B1. The bathymetry changes for this case show very strong features where it is expected that the requirement that the bathymetry be slowly varying is not met, and where the changes of curvature are such that their neglect by the model may affect the solution. Figure 5.15 shows the cross shore variation of the bed slope, curvature and beach parameter. It shows that the region of the bar trough does correspond to large values of these parameters. It appears from the results that the model responds instantaneously to quickly changing bathymetries. In contrast, it was observed in section 5.2.1 that the (laboratory) waves did not actually respond to the sudden change in water depth just shoreward of the bar. It appears that a violation of the mild slope assumption may result in an unrealistic instantaneous response to the water depth changes.

These observations lead to the idea that the *actual* bed profile could be modified to resemble the topography which the waves actually feel. In other words, the aim here is to estimate an *effective* bottom topography. Intuitively therefore, and on the basis of figure 5.15, it was decided to smooth the bathymetry from bar crest onshore. Figure 5.15 shows the new smoothed profile.

---

[1] Note that if it is assumed that $h_x = O(\mu^{1/2})$, higher derivatives and products of derivatives are now $O(\mu)$ and are thus retained. The resulting equations allow for larger slopes.

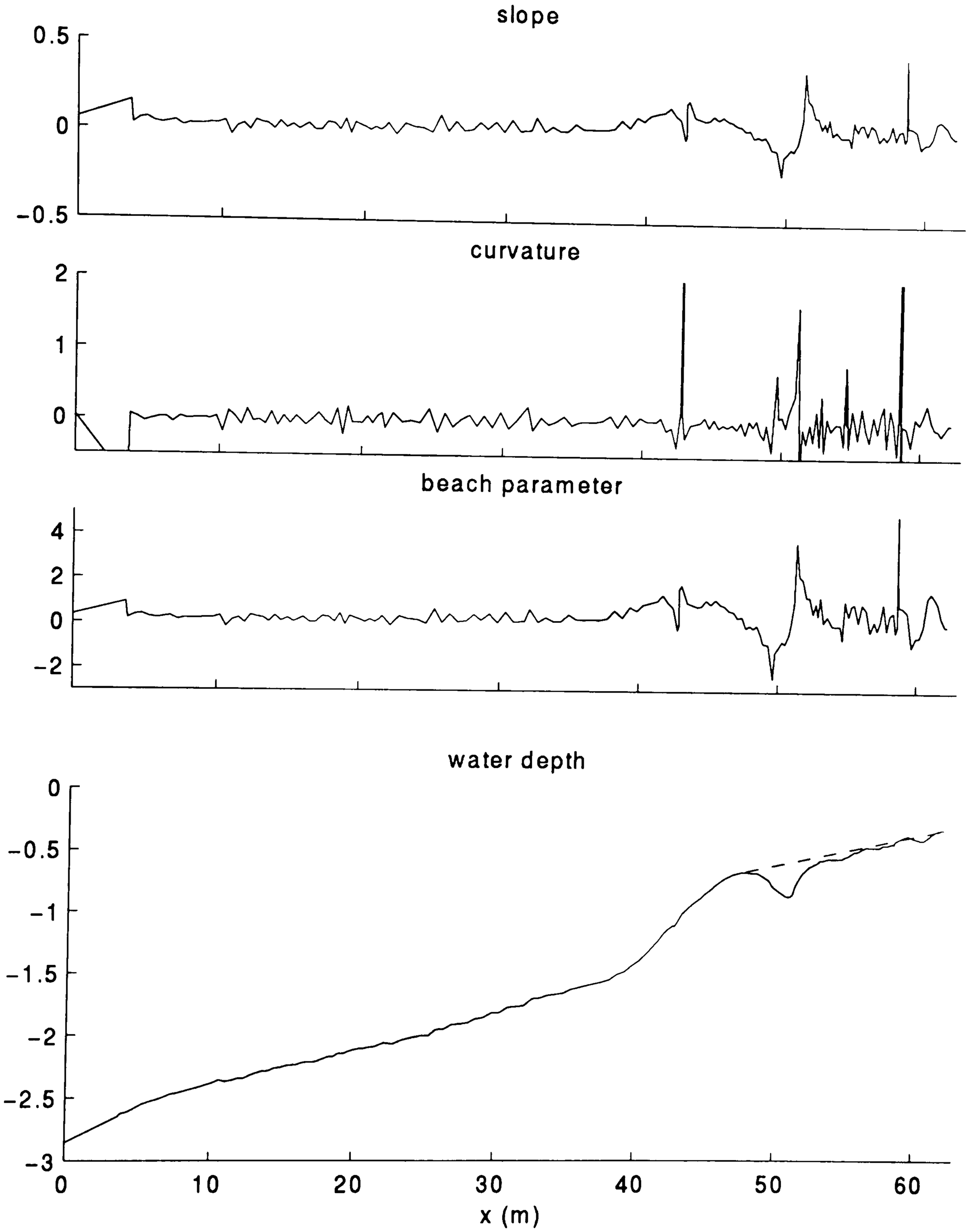

Figure 5.15 Cross-shore variation of, from top to bottom, the bed slope, bed curvature, beach slope parameter $S=h_xL/h$, and water depth for run B1. Actual (———) and effective (smoothed) (- - - - - -) beach profile .

Figure 5.16a shows the elevation statistics for both raw and smoothed profiles compared with measured data. It shows that the profile smoothing has resulted in a better prediction of

the location and intensity of wave breaking, which is no longer concentrated in the inner surf zone[1]. This in turn has resulted in a much better fit for Hrms, the maximum and minimum elevations, and the standard deviation. This improvement is reflected in excellent wave decay predictions and an attenuation of the cross-shore modulations. The latter is discussed in section 5.5. In addition, the set-up is initiated earlier, and is thus higher. As a result, a better fit for the *mwl* is obtained.

Profile smoothing has resulted in a smoother variation of S_η and K_η but brought no improvements. Surprisingly, in this particular case, S_η and K_η do not depend on the correctness of wave breaking prediction. The model limitations other than the mild slope assumption remain (namely limitation to weakly non linear waves, errors in phase celerity and shoaling for $kh > 4/5$). Consequently perfect results cannot be expected. It implies that, for this test, S_η and K_η are primarily sensitive to these model limitations rather than to the mild slope assumption. One may suggest that wave shape evolution for this case is dominated by triad interactions which do not depend on the wave breaking process.

Figure 5.16b show the velocity statistics for both raw and smoothed profiles compared with measured data. Improvements for velocity predictions appear as a decrease of both onshore and offshore velocities in the surf zone, resulting in a slightly better agreement with observations. Again no significant change to S_U and K_U appears.

The effect of smoothing the bathymetry for B2 is shown on figure 5.17a (elevation) and 5.18b (velocity). Profile smoothing has resulted in the same improvements as for B1, except that this time, improvements on S_η and K_η predictions also emerge, whereas S_U and K_U are now overestimated. This suggests that for this test, in contrast to B1, significant nonlinear transfers of energy (thus significant changes in wave shape) occur in the breaking region, and that the intensity of these transfers is depth (or bed slope) -dependent.

Smoothing the profile in the same way barely has any effect on cases A1 and A2. This is surprising since the restriction on bottom slope much more stringent for these long waves runs. Since the cross-shore variation of curvature for A1 and A2 is smoother, and the curvature is smaller , one may suggest that it is not the bottom slope but the change of curvature that affected the results for B1 and B2 .

---

[1] as defined by the observations

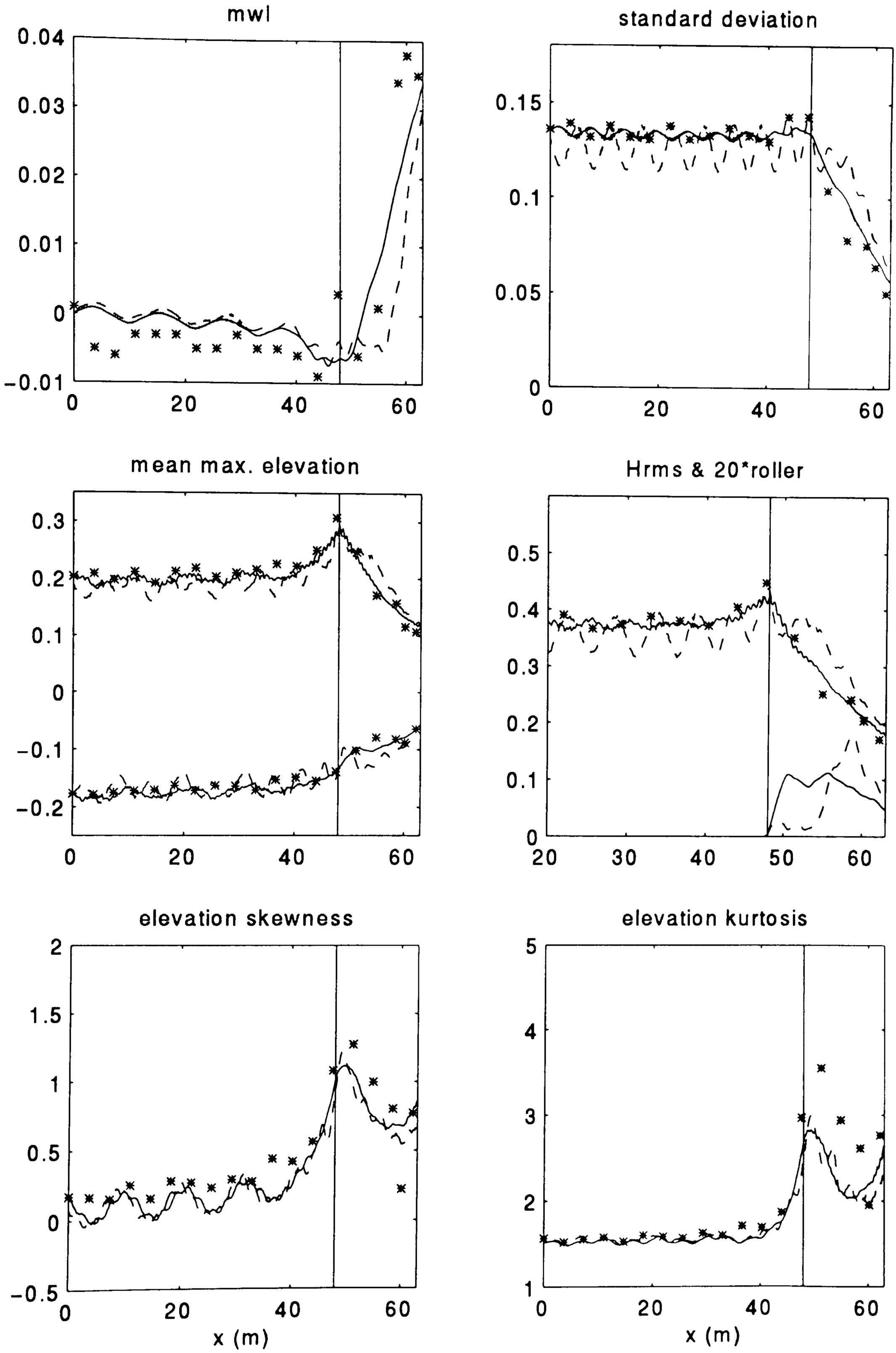

Figure 5.16a Effect of profile smoothing on the surface elevation statistics, run B1. Actual profile (------), effective profile (———).

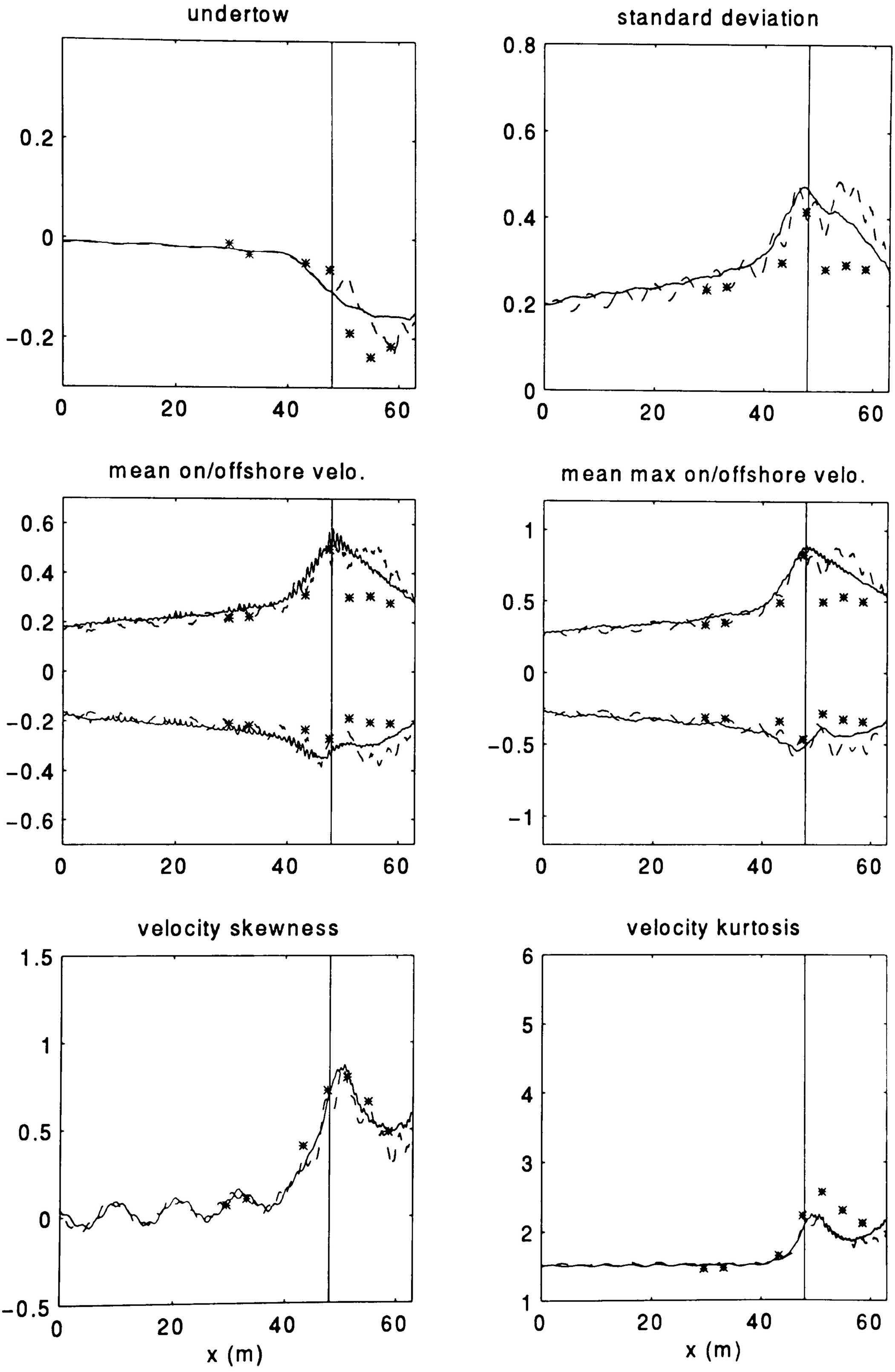

Figure 5.16b Effect of profile smoothing on the depth-averaged velocity statistics, run B1. Actual profile (------), effective profile (———).

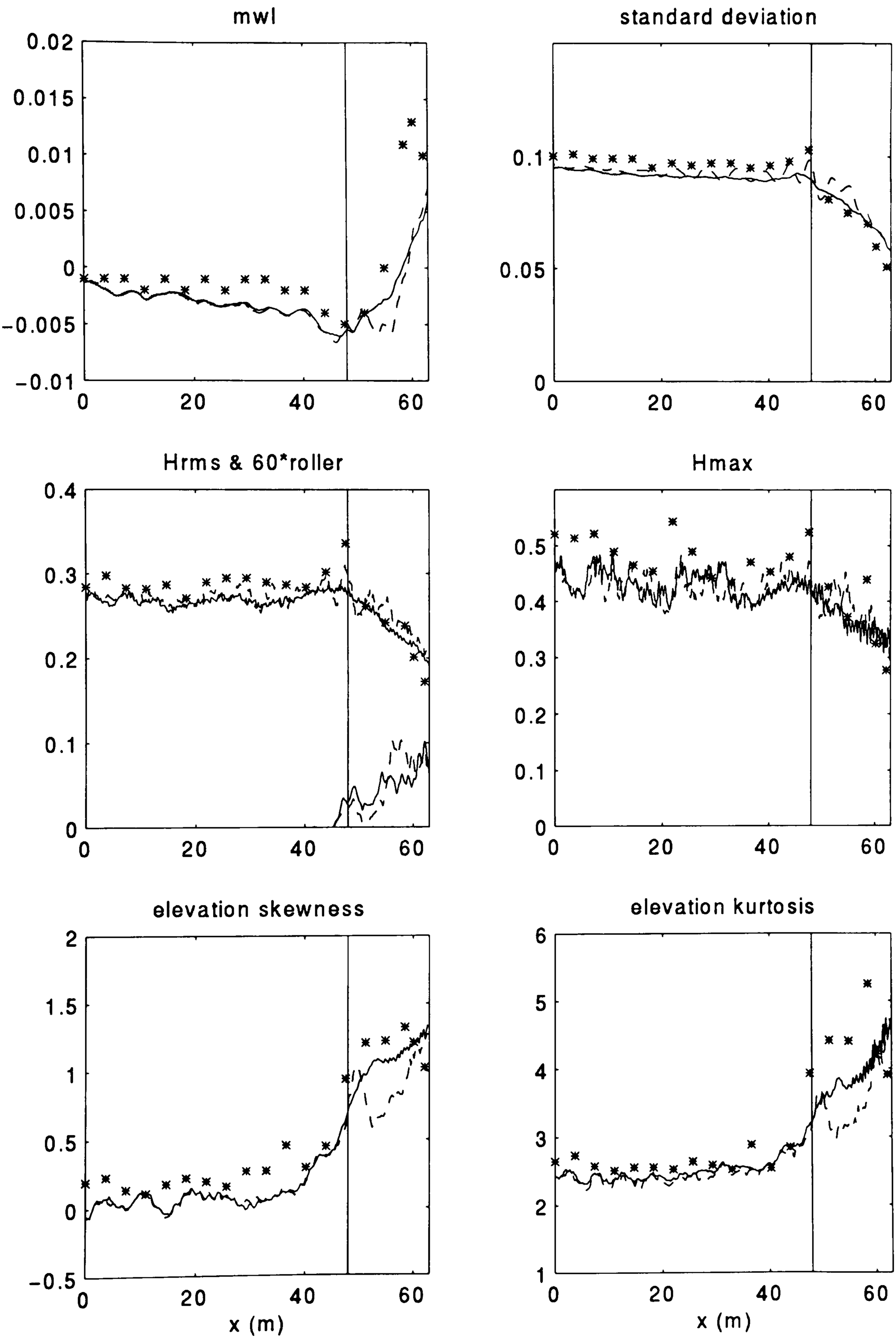

Figure 5.17a Effect of profile smoothing on the surface elevation statistics, run B2.
Actual profile (------), effective profile (———).

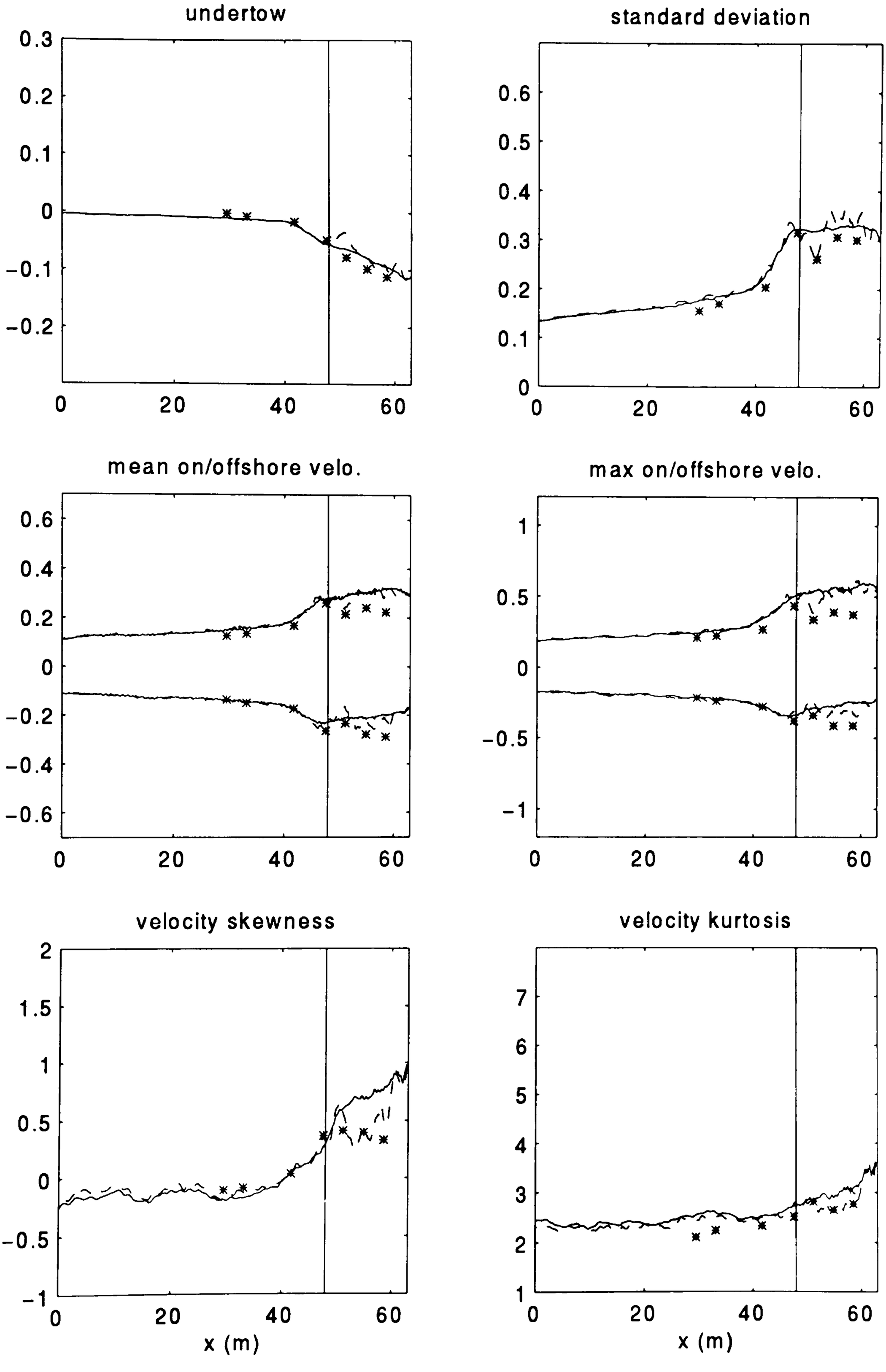

Figure 5.17b Effect of profile smoothing on the depth-averaged velocity statistics, run B2. Actual profile (------), effective profile (———).

5.5 Modulations in the spatial variation of statistics

A striking feature in the model results is the development of oscillations in the cross-shore variation of the surface elevation and velocity statistics, particularly in the case of both regular runs (see figures 5.2 & 5.8 for elevations, figures 5.4 & 5.9 for velocities). The eventuality that these modulations may be due to reflection from the sponge layer was ruled out during the tests on the efficiency of the sponge layer described in section 5.1.2. It is interesting to note that the measurements also show modulations in the cross-shore variation of the surface elevation statistics. These oscillations have the same wave length as those observed in the predictions, but are of smaller amplitude, and out of phase. Since the distance between two adjacent wave gauges is 3.66 m in the shoaling region, they are better defined for A1 (figure 5.2a), for which the wave length is longer. The presence of modulations both in the measurements and in the computations suggests two justifications for their appearance: they may be due to recurrence behaviour in nonlinear interactions (Boczar-Karakiewicz *et al.*, 1987), and/or they may be due to reflection from the slope. Another interesting point is that the wave length and amplitude of the oscillations for the standard deviation (or wave height) (figures 5.2 & 5.4) are different from those observed for the *mwl* and skewness (figures 5.8 & 5.9).

oscillations in the standard deviation and wave height

The possibility that the oscillations in the standard deviation may be due to nonlinear interactions is first examined. (Recurrent) triad interactions between the primary and bound second harmonic are characterised by a beat length given by (Dingemans, 1997):

$$L_r = \frac{2\pi}{k_2 - 2k_1} \tag{5.1}$$

where k_1 and k_2 are the wave number of the primary and first harmonic respectively. Thus the recurrence length for conditions A and B are 203 m and 7 m respectively, which does not correspond to the actual wave length of the observed oscillations (at 18 m and 5.5 m respectively). The predicted and measured power spectra at gauge 1 are compared, for all four runs, on figure 5.1. While interactions for B1 solely consist of self-interactions (the peak at the first harmonic is very weak), the picture for A1 is complicated by the fact that higher harmonics are already present in the field at gauge 1. Since equation (5.1) provides the beat length resulting from interplay between first and second harmonics only, the theoretical evaluation of L_r is uncertain.

It was thus decided to evaluate L_r numerically. Numerical experiments were also carried out in order to assess the significance of nonlinear interactions occurring over the flat bed. The incoming wave fields for both A1 and B1 were propagated over a flat depth with a depth equal to that at gauge 1. The cross-shore variation of the standard variation thus obtained displayed regular oscillations. For B1, the amplitude of these oscillations was about 1.5% of the standard deviation, whereas L_r was found to be 7 m. For A1, the amplitude of the oscillations was about 5.5% of the standard deviation. L_r for that run was not as clear, although a recurrence pattern was depicted every 165m. Table 5.2 tabulates these results. It is clear that the oscillations present in the results do not correspond to either theoretically or experimentally predicted oscillations due to nonlinear transfers of energy.

	1/ Actual oscillations		2/ oscillations due to triad interactions only flat bed test (theory)	
	A1	B1	A1	B1
length (m)	18	5.5	165 (203)	7 (7)
amplitude (m)	0.032	0.023	< 0.01	< 0.002
% standard dev	18 %	17 %	5.5 %	1.5 %

Table 5.2 - Amplitude and length of cross-shore modulations of the elevation standard deviation

1/ actual, that is oscillations over the flat bed section in front of the slope

2/ flat bed test, that is modulations for waves propagating over a flat bottom (i.e. modulations due to triad interactions only). The lengths in bracket are theoretical evaluations of recurrence in nonlinear interaction using equation (5.1).

The possibility that triad interactions may be responsible for these modulations is further put in doubt by the fact that the oscillations are of constant wave length. Boczar-Karakiewicz *et al.* (1987) showed theoretically that the propagation of a wave train over a sloping bed develops oscillations with decreasing beat length.

Bearing in mind the fact that the time domain Boussinesq equations allow waves travelling in both directions, it is possible that the oscillations observed both in the measured and predicted results may be due to reflections from the bed slope. The computed maximum elevations above and below the *mwl* (see e.g. figure 5.2b) show the wave envelope across the channel. The modulations of the wave envelope are characteristic of standing waves

patterns, with maxima and minima reached at the same (cross-shore) locations. Results in section 5.4 show that these modulations are indeed due to reflection from the slope. By changing the location and intensity of the breaking, the smoothing of the profile has resulted in a remarkable reduction in the modulations of the wave height (or standard deviation). Since the waves are breaking earlier, less energy is allowed to propagate shoreward and reflect.

The validity of these conclusions may be questioned by the fact that the oscillations do not damp away offshore. This is particularly striking for B1. It is interesting at this point to consider the effect of the treatment of the seaward boundary on the results. In the model, the waves reflected from the slope propagate seaward to the boundary where no allowance is made for seaward propagating waves to leave the domain undisturbed. Any outgoing wave is thus reflected back, which may result in the establishment of a standing wave field. Test B1 was run for a duration of 50 sec., at which time the first waves reach gauge 19. The results thus obtained show a clear damping of the reflected waves as they propagate offshore. It may thus be concluded that the fact that the amplitude of the modulation is constant along the tank for a longer test duration (175 sec) is due to the re-reflection at the wave generator of the reflected waves, thus creating a standing wave field.

In the case of oscillations dominated by reflection, the difference in the observed and simulated modulations may be explained by the difference in the intensity and location of reflection in the laboratory and numerical experiments. First, the model may not always predict the breaking location correctly (e.g. case B1). By allowing more energy to propagate into the surf zone, this may result in significant discrepancies in the magnitude and location, and thus effect, of reflection. Second, the observations include reflection from the slope beyond gauge 19, a region which the model ignores. The accuracy of the reproduction of reflection from the slope by the model is unknown. For case B1, the modulations in Hrms remaining after profile smoothing have the same amplitude and wave length as those observed in the measurements. This suggests that the amount and nature of the reflection in the simulations and in the model are equivalent. This in turn suggests two observations. First, the reflection responsible for these oscillations in the laboratory occurs before gauge 19. Second, in the physical tank, the seaward propagating waves were also reflected back at the wave generator. Note that, the wave generator is set to absorb outward going waves at the peak frequency f_p only, implying $f_{\text{reflected waves}} \neq f_p$..

oscillations in the skewness and mwl

Observation and analysis of the cross-shore modulations have concentrated on those observed in the standard deviation (or equivalently wave height) predictions. For test B1, the predicted *mwl*, S_η and S_U display oscillations of a different nature, with a longer wave length and higher amplitude. Furthermore, these oscillations do not disappear nor attenuate with profile smoothing, which implies that they may not be the result of reflection. Thus, while it has been established that the modulations in the standard deviation are predominantly due to reflection, as opposed to triad interactions, the question for the *mwl* and skewness oscillations remains open.

In order to investigate their origin, the length of the flat bed section at the toe of the slope, *FBL*, was changed. If these oscillations are dominated by triad interactions, they should change with varying *FBL*. Case B1 is examined here. *FBL* was originally set to 15 m (section 5.1.2). The recurrence length for B1 was theoretically and experimentally found to be 7m (table 5.2). *FBL* was thus changed to values ranging from 8 to 15 m. As shown on figure 5.18, this has resulted in shifts of the modulations in both the *mwl* and skewness, which suggests that these modulations are dominated by triad interactions. This is confirmed by the fact that (i) the cross-shore variation of the second harmonic amplitude displays modulations with the same wave length and amplitude and in phase (see figure 5.21), and (ii) these modulations do not disappear with profile smoothing.

Notice that a change of the length of the flat bed section in front of the slope results in no change in the location of nodes and antinodes for the oscillations in the standard deviation, which also retain the same amplitude and length. This confirms that these modulations are dominated by reflection, and not by triad interactions.

The origins of the oscillations have now been identified. The difference in nature of the modulations in the data and in the computed results can now be examined. The incoming wave field in the model is allowed to transform before reaching the slope. For A1 in particular (for which *FBL* does not correspond to the recurrence length) and for both irregular runs, this may have resulted in different recurring cycles. It is also possible that the treatment of the seaward boundary generates super-harmonics components, thus altering the cycle of nonlinear wave interactions.

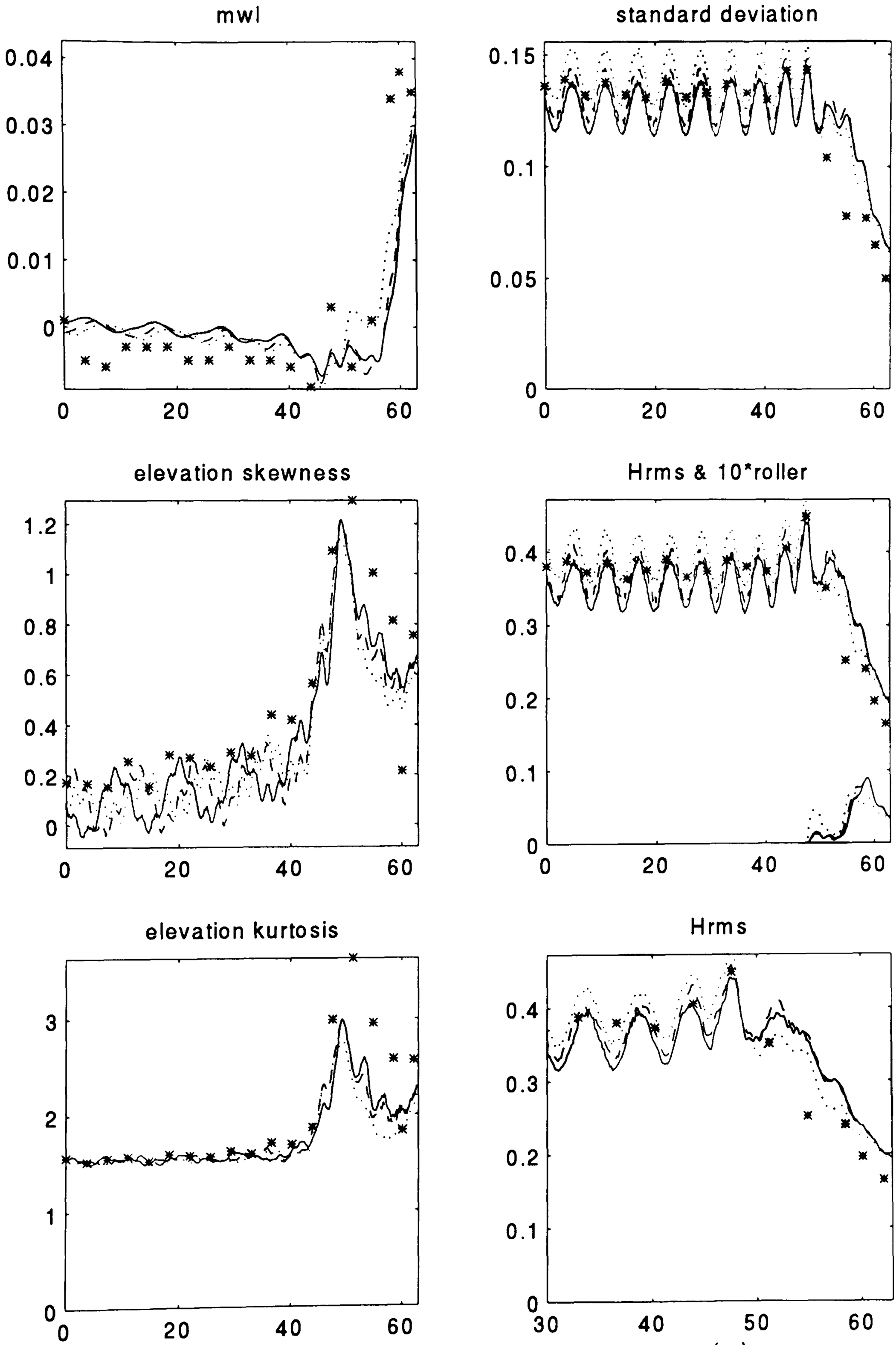

Figure 5.18 Effect of the length of the flat bed section, *FBL*, on the surface elevation statistics, run B1. *FBL* = 15m (————), *FBL* = 12.5m (- - - - - -), *FBL* = 11m (.....).

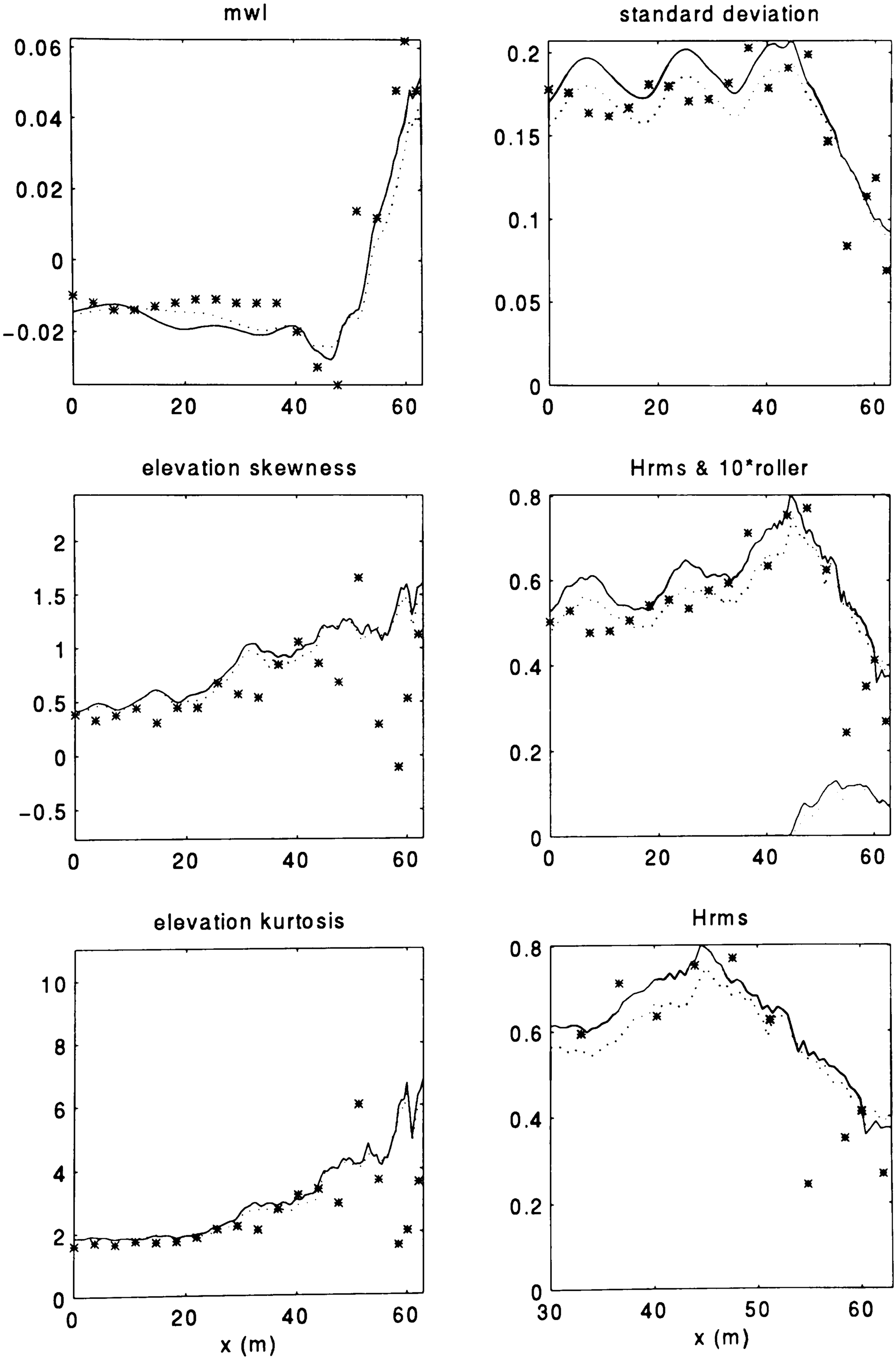

Figure 5.19 Effect of the length of the flat bed section, *FBL*, on the surface elevation statistics, run A1. *FBL* = 20m (———), *FBL* = 16m (.....).

5.6 Wave generation

In this section, the significance of *FBL* with respect to wave generation is investigated. Let us first examine the direct effect of *FBL* on wave generation. Comparison of the amplitude of the oscillations in the standard deviation due to triad interaction only (obtained from the flat bed test) and the standard deviation itself show that triad interactions occurring over the flat bed are very small. Table 5.2 shows that the amplitude of these oscillations is of the order of 5.5% and 1.5% of the standard deviation for A1 and B1 respectively. It may safely be assumed that this should not affect wave generation significantly.

In section 5.5, it was demonstrated that, because of the nonlinear transfers of energy occurring during propagation over the flat bed, changes in *FBL* resulted in shifts[1] of the oscillations that are dominated by these energy transfers, that is the oscillations in the skewness and *mwl*. In order to optimise wave generation, ideally, the flat bed length should be chosen such that the predicted and observed triad-interaction-dependent-modulations are in phase. However, it appears that changing the length of the flat bed has very little effect on the predictions in the surf zone (figure 5.18). This supports that assumptions made above that the triad interactions occurring over the flat bed sections have little effect on the wave generation. These observations were made for B1, but hold for case A1 as well, as shown in figure 5.19[2]. The irregular runs on the other hand showed no significant sensitivity to *FBL*. Choosing *FBL* so as to match observed and predicted modulations is thus not essential.

The combined effects of wave reflection (and the resulting standing wave field) and changes in *FBL* on the wave generation are now examined. It is now understood that, since the oscillations in the standard deviation are dominated by reflection[3], the location of maxima and minima (antinodes and nodes), and the amplitude of the oscillations remain the same with changing *FBL*. This, combined with the fact that the seaward boundary condition is fixed, results in shifts up or down of the standard deviation over the duration of the experiment (panel (1,2) figures 5.18 and 5.19). Note that this is likely to have occurred in the physical tank too. Figure 5.20 provides a close-up on the standard deviation in the generation region for both A1 and B1. For example, for test B1, with *FBL* = 14 m, the

---

[1] without any change of amplitude and length of oscillations

[2] note that for this case, changing *FBL* has had very little effect on the skewness oscillations, i.e. no shift. This is because the recurrence length for this run is long (165/203m) compared to the change in *FBL* (by 4m). Also note however that, with *FBL*=16m, over the duration of the experiment, the spectral peak was underestimated at gauge 1 because of phase mismatch between lab-model modulations. In other word, the best fit at gauge 1 does not correspond to best overall fit during shoaling. Also note that overestimation of the third harmonic spectral peak could not be corrected by changing *FBL*.

[3] and since the location and intensity of the reflection remains the same, regardless of *FBL*

generation point corresponds to an antinode, and the standard deviation is minimum. If *FBL* = 11 m, then the generation point corresponds to a node, and the standard deviation is maximum.

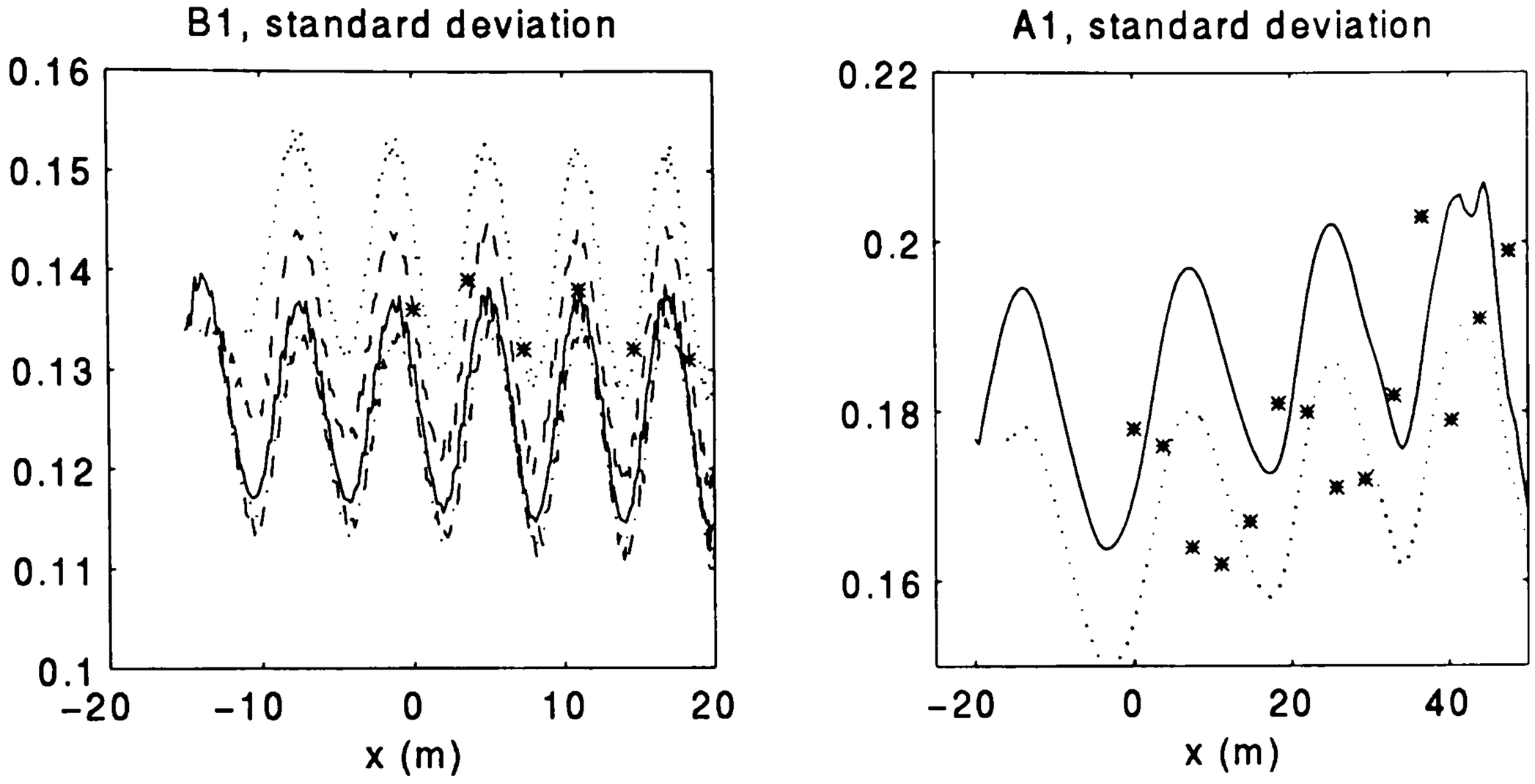

Figure 5.20 Combined effect of *FBL* and reflection on the elevation standard deviation, run B1 (left) and A1 (right). ✳ observed data.
Legend run A1: *FBL* = 20m (———), *FBL* = 16m (.....). *x* = -*FBL* to 50 m.
Legend B1: *FBL* = 15m (———), *FBL* = 12.5m (- - - - -), *FBL* = 11m (.....), *FBL* = 14m (- · - · - ·). *x* = -*FBL* to 20 m.

Note that the changes in the predictions in the surf zone for B1 resulting from changing *FBL* may now be ascribed to reflection, not the direct effect of changing *FBL*. The shifts up or down of the standing wave field for this test run result in changes in breaking location, hence changes in surf zone predictions. Hence the slightly better fit in the surf zone obtained with *FBL* = 11m is the result of overestimated wave heights in the shoaling zone (figure 5.18).

It appears from these observations that the wave field evolution over the flat bed due to triad interaction has little effect on wave generation and on the hydrodynamics in the surf zone. Wave generation is dominated by the effects of reflection, or more exactly, the combined effects of wave reflection and choice of *FBL*. Ideally, *FBL* should thus be chosen such that, for a given duration of the experiment, the wave generation is optimum.
It is emphasised however, that except for special cases like B1, for which breaking is problematic, the choice of *FBL* is not critical as the surf zone predictions are not affected. In the case where optimum wave generation is sought, it is clear that wave generation should

not be assessed in terms of power spectrum prediction, and that a more global approach is required. For example, for A1, optimum results in the shoaling zone are obtained with *FBL* = 16m. Note however that, with *FBL* = 16m, over the duration of the experiment, the spectral peak at gauge 1 is underestimated because of the phase mismatch between predicted and observed modulations. In other word, the best fit at gauge 1 does not correspond to best overall fit during shoaling. Also note that overestimation of the third harmonic spectral peak for that run could not be corrected by changing *FBL*.

5.7 Discussion

5.7.1 General performance of the model

This section provides a discussion on the general performance of model with respect to

- regular and irregular waves,
- long and short waves, and
- shoaling and breaking waves.

regular waves (A1,B1) and irregular waves (A2,B2)

On the basis of the four tests examined here it may be concluded that, overall, the model performs equally well for regular and irregular waves.

long waves (A) & short waves (B)

Contrary to expectations, the results for conditions B (short primary wave) are better than those for conditions A (long waves). This seems contradictory since the model is expected to perform better for long waves. However this can be explained by three reasons:

- wave generation for conditions B is relatively better (figure 5.1)
- the degree of nonlinearity is greater for A (table 4.1)
- given the steepness of the waves, a lot more reflection from the slope beyond gauge 19 is suspected to have occurred for A
- condition A is characterised by long waves, that is waves for which the phase mismatch between free and bound waves is small (increasingly non-dispersive waves). The triad interactions are thus more intense than for B, resulting in greater changes in wave shape. The resulting numerous super-harmonics, despite the improved dispersion characteristics, cannot be handled correctly by the model. This may be examined by assessing the model's performance for individual harmonics.

Let us first consider B1. The surface elevation time series were band pass filtered between 0.1-0.5 Hz (first harmonic), 0.5-0.9 Hz (second harmonic) and 0.9-1.3 Hz (third harmonic). The resulting standard deviation for the raw time series and these 3 harmonics is presented in figure 5.21. Apart from a marked overestimation in the surf zone for the first harmonic (due to re-shoaling, section 5.5), the predicted and measured results compared well. Figure 5.21 also shows the same results for the test carried out with a smoothed profile. The fit is improved, with a smoother variation and not as much overestimation of amplitude of the first harmonic.

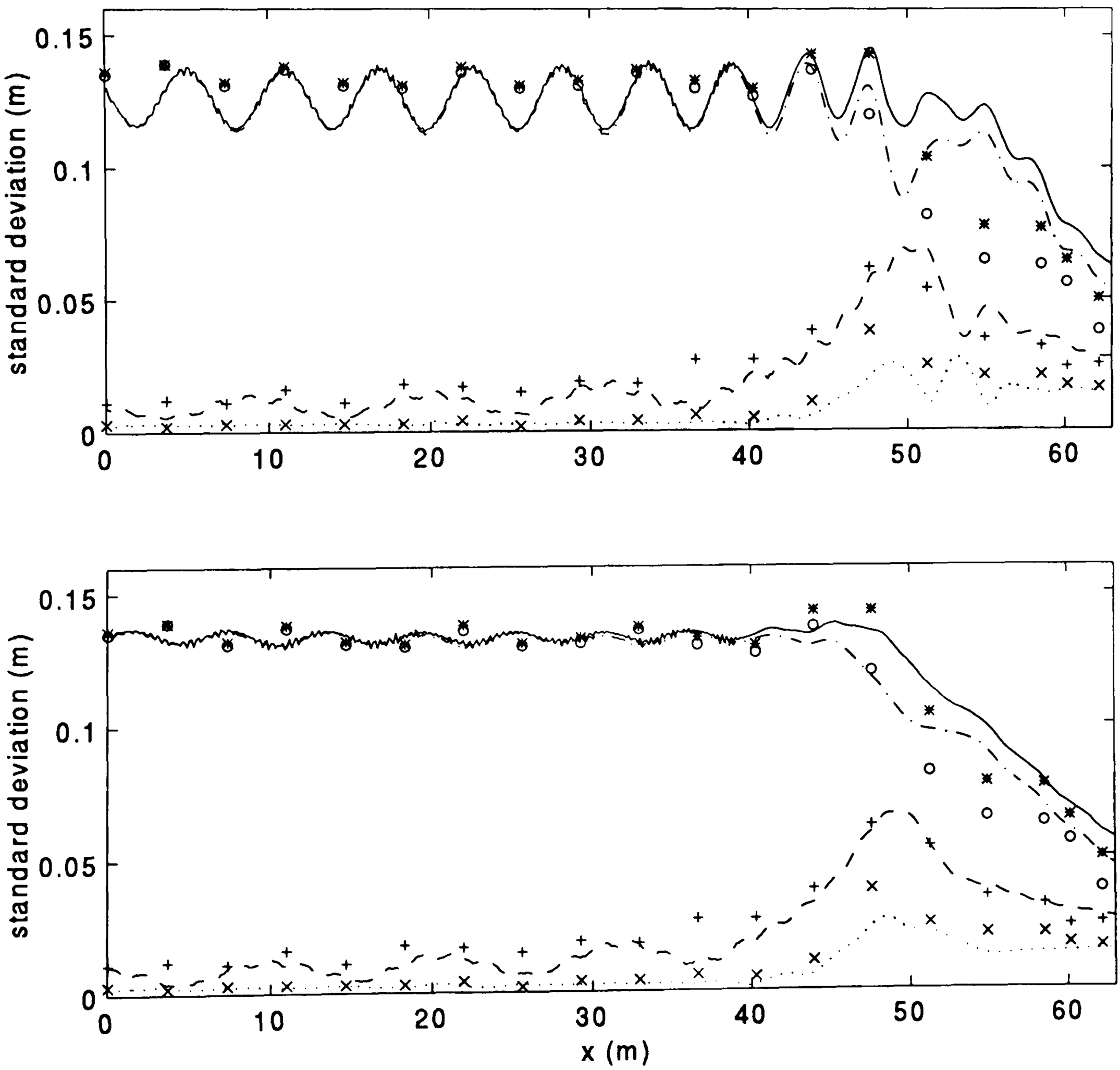

Figure 5.21 Cross-shore variation of the elevation standard deviation, for the first three harmonics, run B1. predictions with (top plot) actual profile, (bottom plot) effective profile.
total (——— , ✳), first harmonic a_1 (-·-·-·- , o), second harmonic a_2 (- - - - - - , +), third harmonic a_3 (..... , ×). The markers are the observed data, the lines are the predictions.

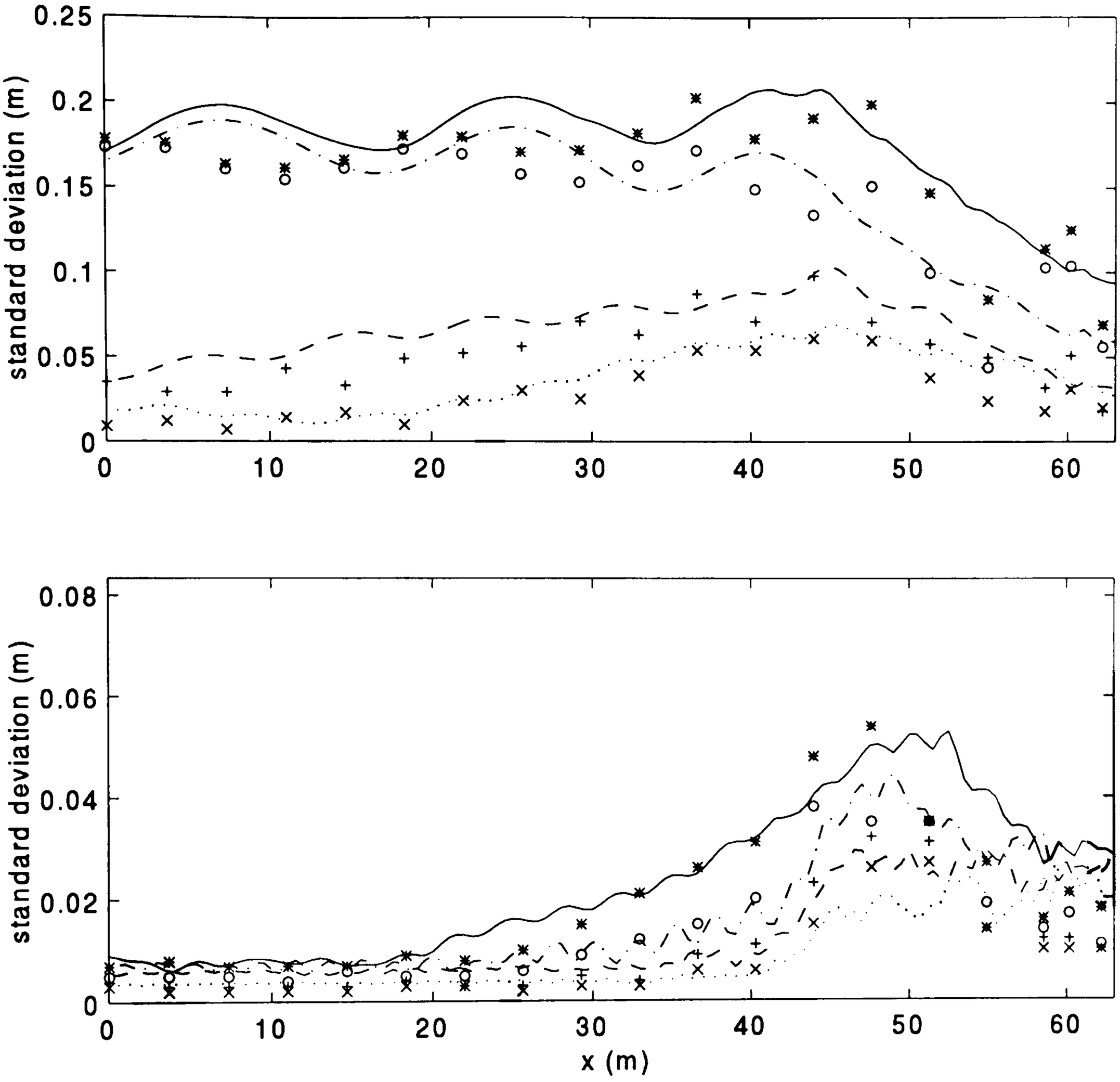

Figure 5.22 Cross-shore variation of the elevation standard deviation for the first 7 harmonics, run A1.
(top plot) first to third harmonic: total (———, ✳), first harmonic a_1 (-·-·-·-, ○), second harmonic a_2 (- - - - - - , +), third harmonic a_3 (....., ×).
(bottom plot) fourth to seventh harmonic: 4th harmonic a_4 (———, ✳), 5th harmonic a_5 (-·-·-·-, ○), 6th harmonic a_6 (- - - - - -,+), 7th harmonic a_7 (....., ×).
The markers are the observed data, the lines are the predictions.

The same analysis was carried out on A1 and is displayed on figure 5.22. The surface elevation time series were band pass filtered between 0.0625-0.1875 Hz..... up to the 7th super-harmonic. Figure 5.22 shows that the first and second harmonics are correctly predicted. The standard deviation of the third and higher harmonics are overestimated some distance after breaking (at $x \approx 50$m). Table 5.3 tabulates the location of the appearance of high harmonics for both A1 and B1 together with their kh values. For A1, $kh \approx 2$ for the third harmonic, which appears very early, at about 25 m. The third harmonic for condition B1 has $kh \approx 3.8$. One would thus expect the model to perform better for A1 than for B1 for

this harmonic. It is not the case however, because the third harmonic in A1 is more significant than the third harmonic in B1. For example, it represents approximately 35 % of the total energy at the breaking point for A1, against 18 % for B1. Moreover, the third harmonic develops and is present over a much longer distance for A1. Since A1 is characterised by yet higher harmonics, the poor performance of the model with respect to higher harmonics (figures 3.2 and 3.3) explains the improved results for B1.

A1			B1		
Harmonic nb	presence detected at gauge nb	*kh*	Harmonic nb	presence detected at gauge nb	*kh*
1	1	0.44	1	1	1.27
2	1	0.96	2	12	2.47
3	8	1.98	3	16	3.78
4	12	5.60			
5	13	14.50			
6	14	49.6			
7	15	-			
8	16	-			
9	16	-			

Table 5.3 *kh* values for each harmonics; run A1 and B1. The location of first appearance of the harmonics is determined from the predicted power spectrum (not shown).

shoaling and breaking waves

As expected, the model performs better in the shoaling zone than in the surf zone. The disagreements between the data and predictions are greatest for runs for which super-harmonic generation is intense, particularly for the skewness and kurtosis.

The Boussinesq equations contain frequency dispersion and amplitude dispersion terms that balance each other. In the breaking region, the waves become increasingly non-frequency dispersive, and amplitude dispersion dominates. Waves in this region have in fact successfully been modelled with the nonlinear shallow water equations. It is thus possible that the presence of the dispersion terms (high order 'Boussinesq' terms) induce errors in the wave shape prediction in the breaking region. It was recognised that the effect of the dispersion terms is to stabilise the wave profile by reducing the steepening of the wave front

(sec. 3.2.3). This would result in an underestimation of the asymmetry, and possibly, as a result, an over-estimation of the skewness.

Note however that observation of the time series shows that the predicted steepening of the wave front compares fairly well with the measured one. It is possible that the computations were stopped at a reasonable cross-shore location, that is at a location where dispersive effects in the equations are also present in the physical tank. Further investigation is now required to, in particular, evaluate asymmetry predictions. This is presented in chapter 6.

Definite causes for the discrepancies for the skewness and kurtosis in the surf zone were established in the previous section. Indeed the super-harmonics are increasingly present in the surf zone. The performance of the model for waves with large *kh* is known to result in (i) the incorrect phase celerity/wave number of high harmonics, (ii) incorrect linear shoaling. It appears from figure 5.22 that the transfer of energy to higher frequencies is over-estimated, hence the over-estimation of the skewness. The performance of the model with regards to the accuracy in predicting nonlinear transfer of energy is examined in chapter 6.

Finally, it appears from test A1 that a relatively good wave height and wave envelope prediction does not necessarily mean that the wave shape is right. On the other hand, it appears from B1 that good (normalised) wave shape prediction is not necessarily a sign of good wave height prediction. This also applies to the velocities.

5.7.2 Sensitivity to ϕ_B

The free parameters were chosen on the basis of laboratory measurements, but allowing for the fact that, since the model is limited to weakly nonlinear waves, it tends to underestimate the wave height in the breaking region (Schäffer *et al.*, 1993). Thus the breaking criterion was chosen accordingly. Despite this, and for the data studied in this chapter, the model appears fairly robust, and $\phi_B = 20^o$ does indeed give the best overall results.

In a recent paper, Madsen *et al.* (1997a) looked at the improvements obtained for the wave height and *mwl* by changing the free breaking parameters. It was shown here that similar improvements could be obtained, and that the sensitivity of the *mwl* and wave height to ϕ_B is moderate. The present study further establishes that the depth-averaged velocity statistics show the same sensitivity to ϕ_B, both qualitatively and quantitatively. In addition, it appears that this sensitivity is emphasised for the skewness and kurtosis of elevation and velocity predictions, especially for cases where the generation of higher harmonics is intense. The

danger is that an effort to optimise ϕ_B for a good fit for the wave height and *mwl* (as proposed by Madsen *et al.*, 1997a) may result in the wrong wave shape.

The reason for this sensitivity is now examined with case A1. The effect of ϕ_B on the elevation standard deviation is examined on figure 5.23. It is known that high *kh*, hence bad frequency dispersion and shoaling properties, result in the wrong phase celerity for higher harmonics (and therefore wrong wave shape), and wrong harmonic amplitude (over-prediction), respectively. Since increasing ϕ_B effectively results in the generation of more high harmonics, an increase in ϕ_B for a case like A1 results in significant changes to the wave shape.

It is clear that the extent of the sensitivity to ϕ_B depends on the stage of wave transformation process: if waves with large *kh* are already present at the breaking point (i.e. generated during shoaling) (case A1), or if increasing ϕ_B results in the generation of waves with large *kh* (case B1, $\phi_B = 26^o$) , then increasing ϕ_B yields large overestimations of the elevation and velocity skewness and kurtosis.

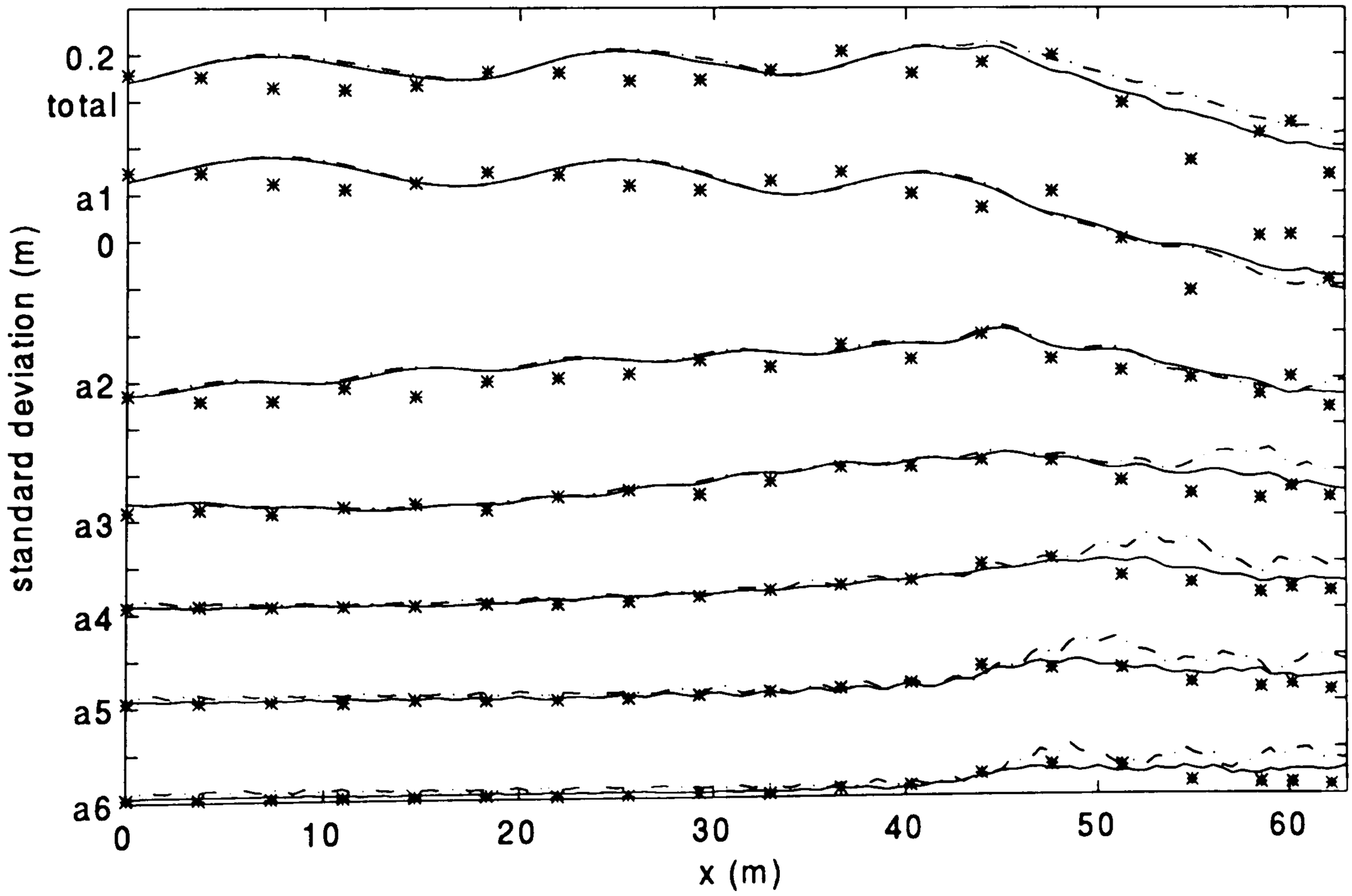

Figure 5.23 Effect of ϕ_B on the cross-shore variation of the elevation standard deviation, for the first six harmonics, run A1. $\phi_B = 20^o$ (———), $\phi_B = 26^o$ (- · - · - · -).

Given the sensitivity of the skewness and kurtosis of elevation and velocity on ϕ_B, the model must be applied with caution in cases for which triad interactions are intense (which happen to be long waves cases for which the model should perform best).

Finally, in the study of irregular and regular wave cases, Ozanne *et al.* (1997) found that, in contrast with the regular waves case, the irregular waves showed little or no sensitivity to ϕ_B. This trend is not repeated here. In terms of percentage difference, for the same change in ϕ_B, A1, A2 and B2 undergo the same increase in the elevation and velocity standard deviation.

5.7.3 Weak nonlinearity versus weak dispersion

In order to assess the dependence of the discrepancies between the predicted and measured results on the degree of nonlinearity ε, the difference between predicted and measured standard deviation, skewness and kurtosis of surface elevation were plotted against ε in figure 5.24. All four runs and each wave gauge are represented. Dependence on the degree of dispersion μ and on the Ursell number U_r are also shown in figure 5.24.

The difference for the standard deviation was normalised by the predicted standard deviation at gauge 14 (breaking point). The discrepancies are expected to increase with increasing ε, increasing μ, and increasing U_r. In other words, increasing discrepancies with increasing ε (increasing μ) show a correlation between errors and violation of the weak nonlinearity (weak dispersion) assumption.

Figure 5.24 shows that the discrepancies do indeed increase with increasing ε. Also notice that the degree of nonlinearity for tests A reaches as high as 0.38, compared to tests B (maximum ε at 0.24). This implies that it is for A runs that the violation of the weak nonlinearity assumption produces the most errors.

Figure 5.24 shows no sign of increasing errors with increasing μ, even for the short wave runs. Indeed, thanks to improved dispersion, no discrepancies are observed for large degrees of dispersion. The larger discrepancies associated with small μ are due to violation of weak nonlinearity.

An expected increasing discrepancy with increasing Ursell number is shown in figure 5.24. Note that good results are obtained even when ε and μ are not of the same order. The largest discrepancies are observed for largest ε, and thus largest U_r. It is not established whether

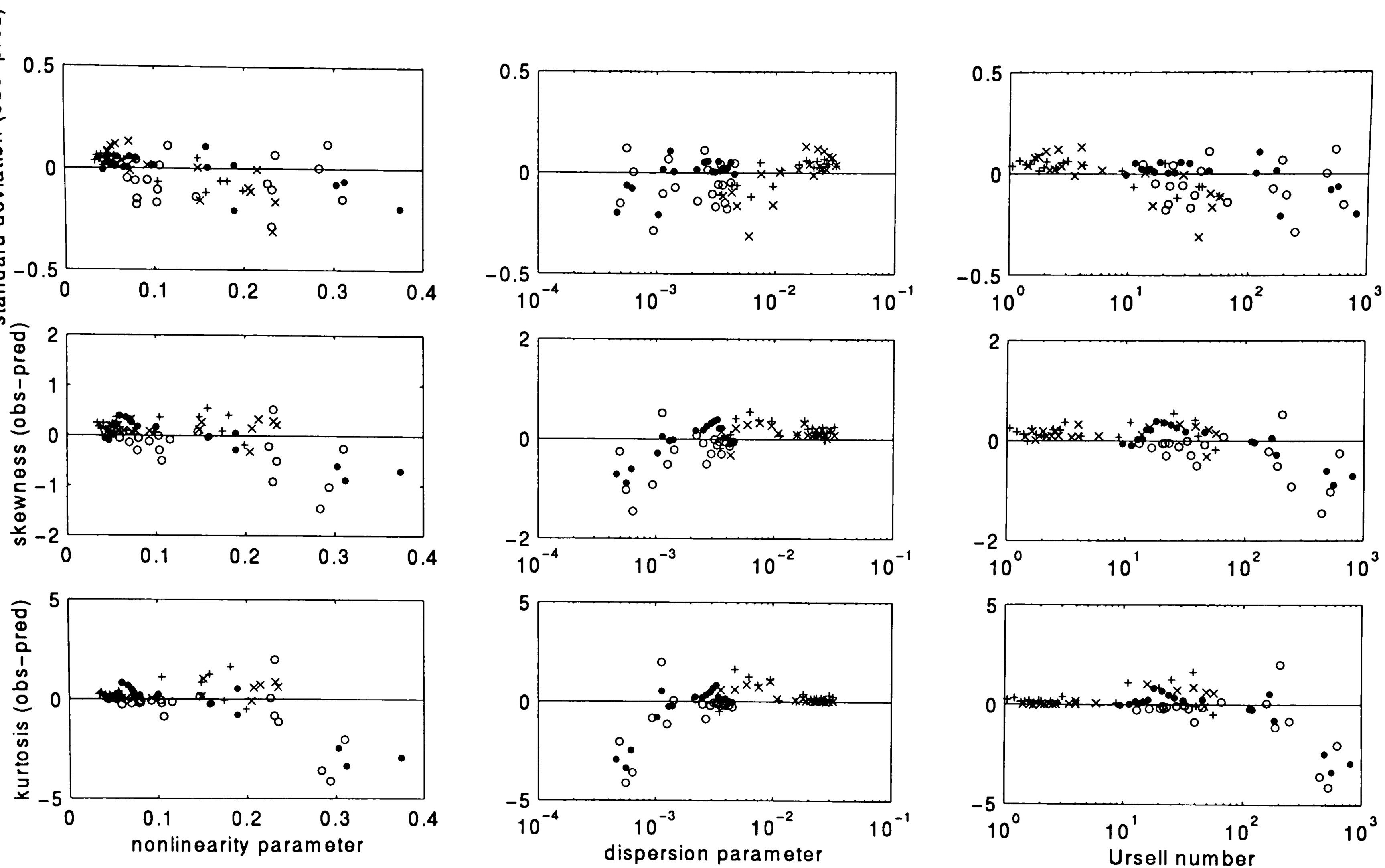

Figure 5.24 Difference between observed and predicted elevation standard deviation (top plot), skewness (middle plot), and kurtosis (bottom plot) *versus* ε (left column), *versus* μ (middle column), and *versus* $Ur = \varepsilon/\mu$ (right column. $\phi_B = 20°$. ε is calculated as the ratio of the elevation standard deviation and local water depth. The difference for the standard deviation is normalised by the standard deviation at gauge 14. ○ A1, • A2, × B1, and + B2.

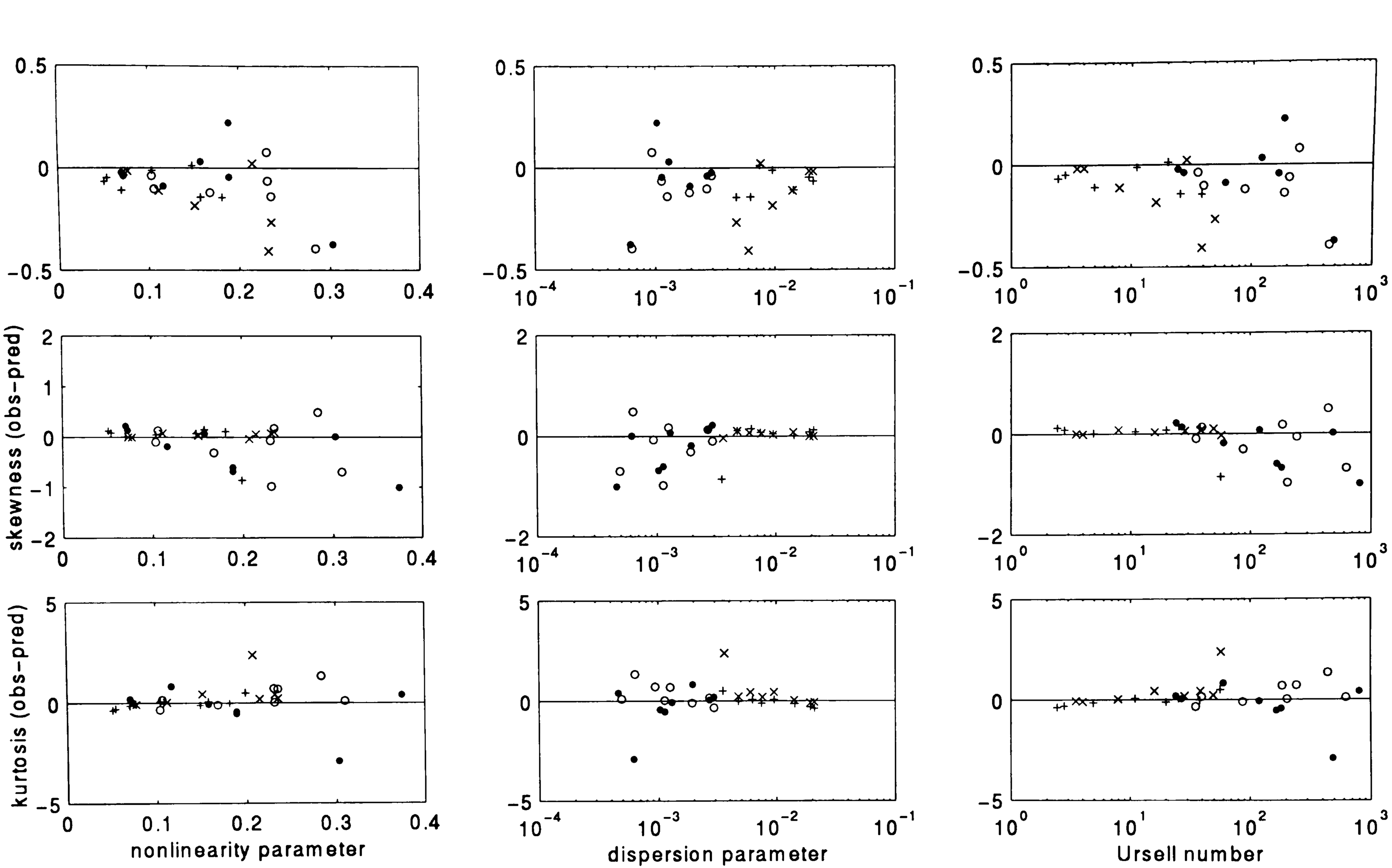

Figure 5.25 Same as fig. 2.25, depth-averaged velocity data.

discrepancies are the result of a violation of the weak nonlinearity assumption, or a result of the fact that ε and μ are not of the same order, or both.

Similar observations were made for the depth-averaged velocity statistics. They are shown in figure 5.25. The same remarks apply.

5.7.4 Towards a parameterization for the skewness and kurtosis of elevation and velocity ?

The predicted and measured elevation skewness and kurtosis are plotted against ε and μ (figure 5.26). Both the observations and the predictions indicate a dependence of S_η and K_η on μ and ε. A first order polynomial fit to both the predicted and the observed data is shown[1]. The same correlation also appears between S_U and K_U with μ and ε (figure 5.27).

The same trend is observed for regular and irregular waves, and short and long waves. A parameterization is tempting, although the scatter is still large. Such parameterization requires the testing of a wider range of wave characteristics and the inclusion of other parameters.

The improved performance of the model with velocity moment predictions, in contrast with elevation moments, is again apparent both in figures 5.25 and 5.27.

5.7.5 Summary of the various sources of discrepancy

The causes for the disagreements between the observation and predictions may be summarised as follows:

- The model limitations to weak dispersion and weak nonlinearity are major causes for disagreements. Note that, despite the improvements introduced to extend the accuracy of the linear dispersion relation, the model still yields inaccurate results for $kh > 5$.
- Errors in the measurements must also be accounted for. For example the difficulty to measure the surface elevation in the surf zone was found to be a possible cause for disagreements. Accurate positioning of the instruments is also essential, especially for rapidly evolving waves like test A1. Finally the measurement of wave shape with the resistance gauges may be inaccurate.
- The differences between laboratory and model conditions have also certainly contributed to discrepancies. The model does not reproduce hydrodynamics beyond gauge 19. and their effect on the modelled domain. Two processes are ignored that may explain discrepancies:

---

[1] The aim here is only to show trends. Fitting higher order polynomials will follow the data better but are not physically realistic. If a parametrisation is sought after, a more appropriate curve fitting should be used.

reflection - from the slope beyond gauge 19

undertow

The effect of these two processes on the wave shape are unknown. Note however that since S_U and K_U are well predicted, and since undertow is not simulated, it appears that the current oscillations are not perturbed by undertow.

• Finally, despite the correction for truncation errors, numerical errors are inevitable, and the effects of the stabilising numerical filter (sec 3.5.5) are not fully established.

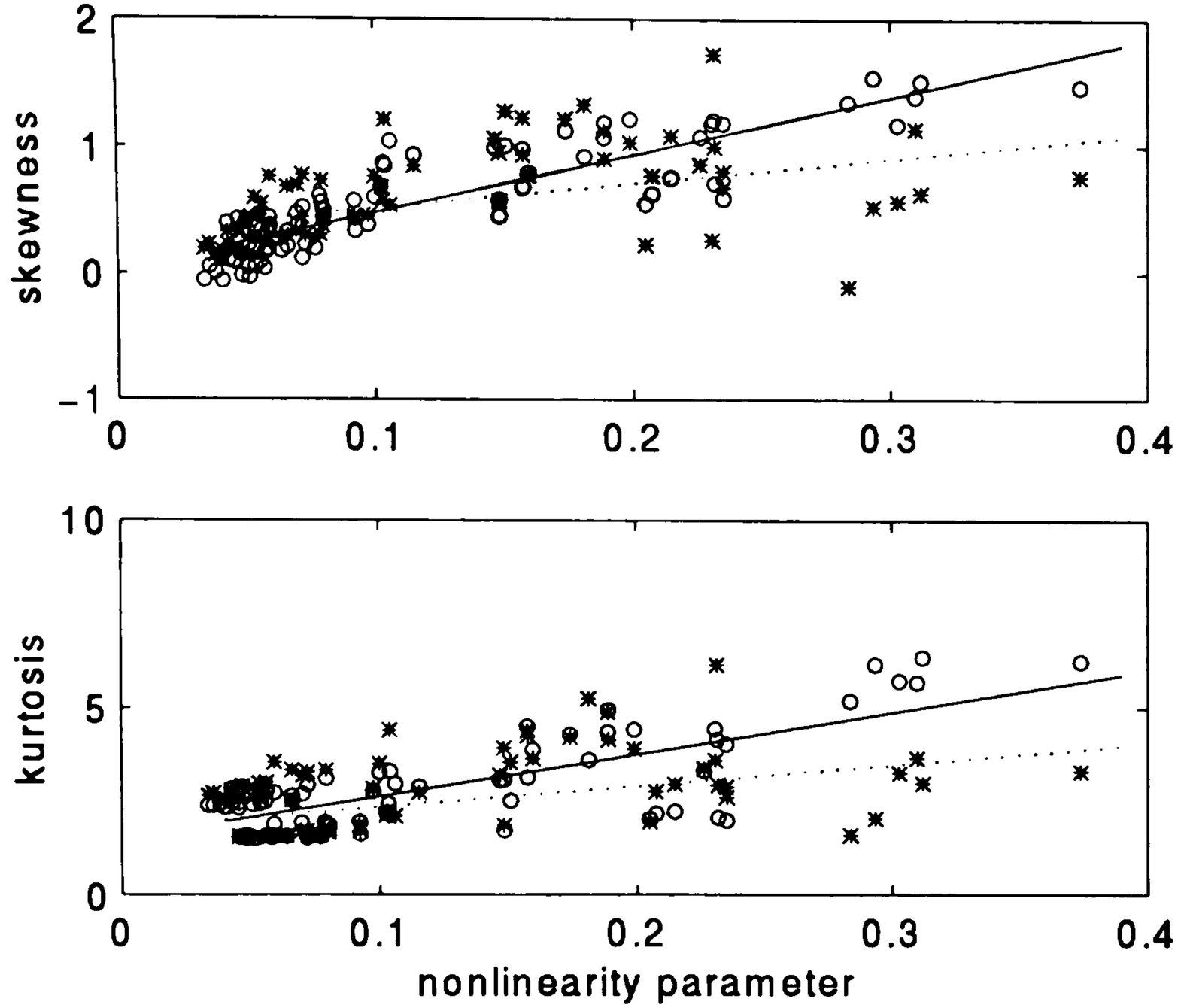

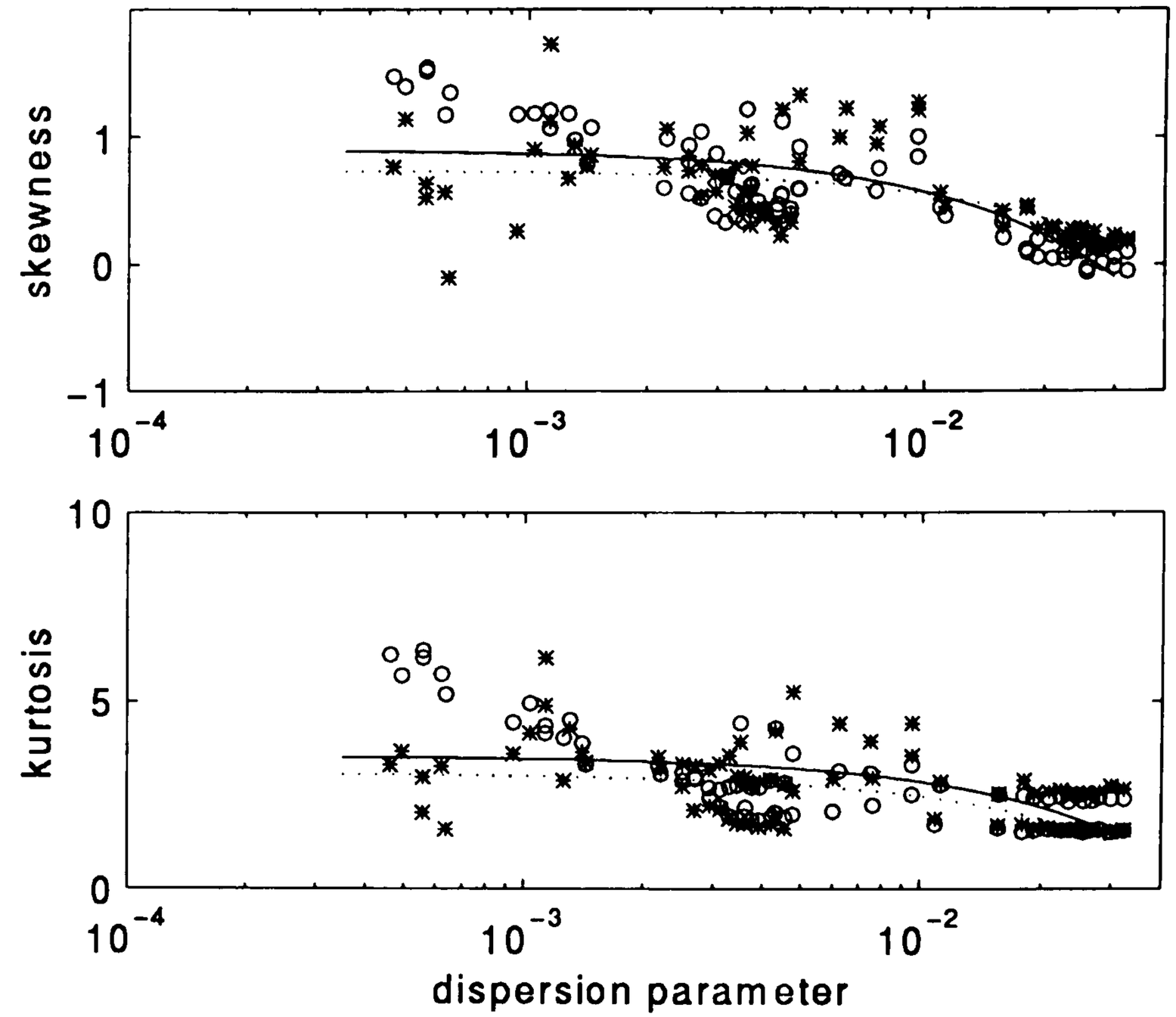

Figure 5.26 Predicted (○) and observed (✳) elevation skewness (top row), and kurtosis (bottom row) *versus* ε (left column), and *versus* μ (right column). $\phi_B = 20°$, all four runs are plotted for each 19 wave gauges. The plain and dotted lines are a first order polynomial fit to the predicted and observed data respectively.

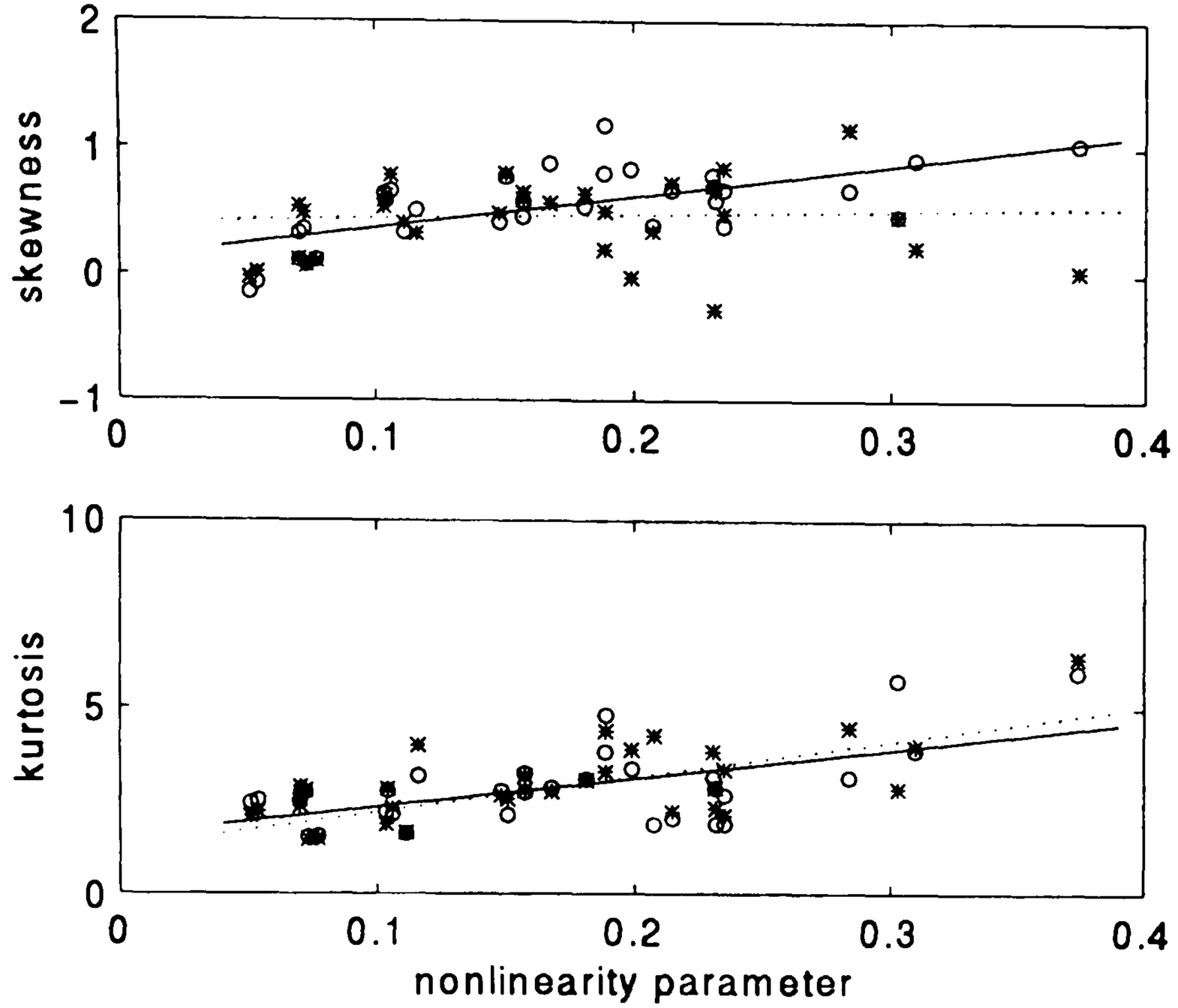

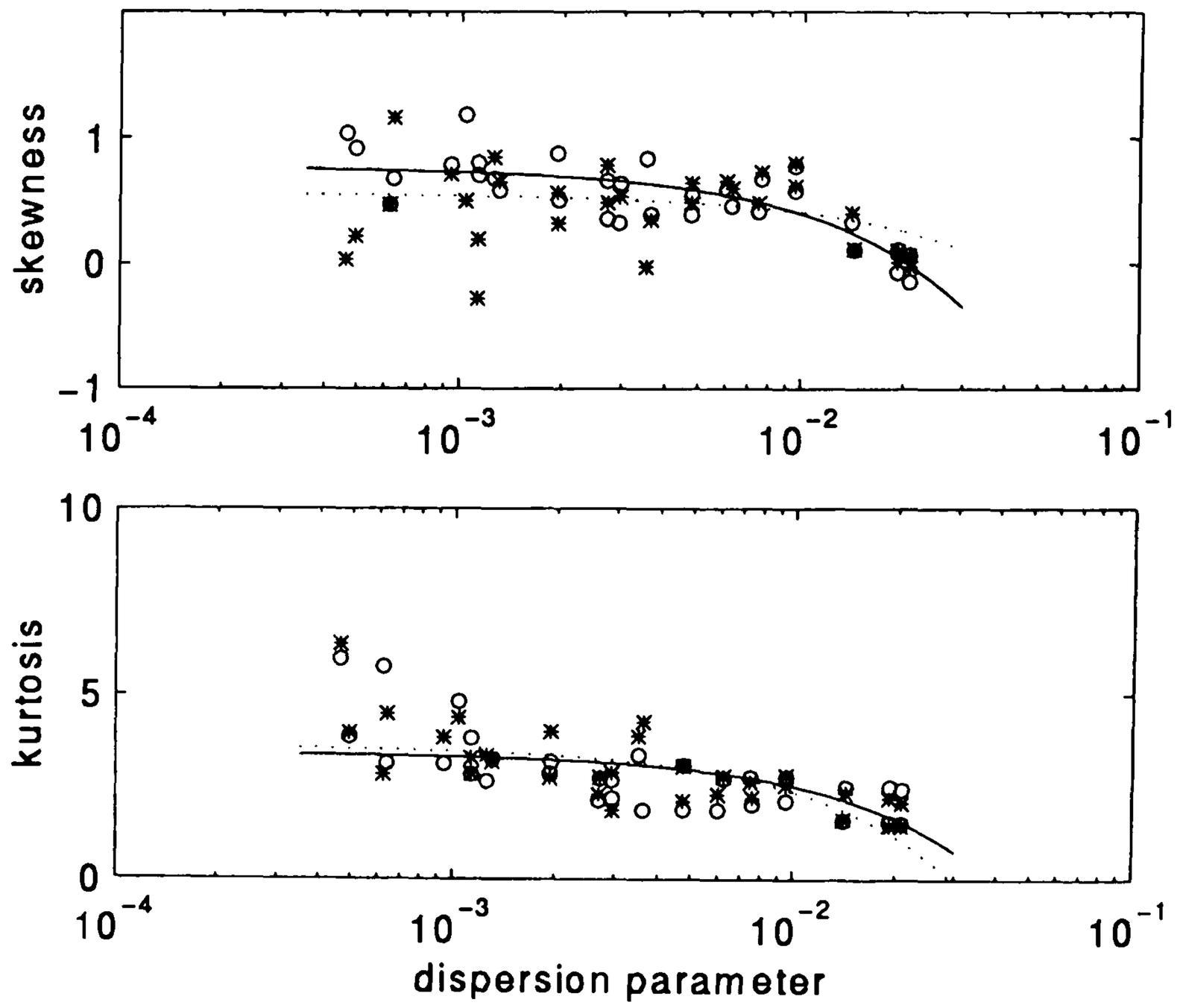

Figure 5.27 Same as figure 2.27, depth-averaged velocity data. All four runs are plotted for each 7 current meter arrays.

CHAPTER 6 MODEL - DATA COMPARISON: A BISPECTRAL ANALYSIS

6.1 Introduction

The departure, in shallow water, of the probability density function of the surface elevation and orbital velocity from a Gaussian distribution has so far been evaluated in terms of the third and fourth order statistical moments in a time domain analysis. In this chapter, a bispectral analysis is performed on the surface elevation and depth-averaged velocity data. This method was introduced by Hasselmann *et al.,* 1963, and subsequently applied by numerous investigators, in particular, by Elgar and Guza (1985b) for shallow water waves. The bispectral analysis provides information about the existence, nature and intensity of the wave-wave interactions. It provides a means of evaluating the skewness and asymmetry arising from triad interactions. These quantities were defined in section 1.2.1. The skewness may thus be re-evaluated, and a new quantity, the asymmetry, may be determined. In addition, the contribution to skewness and asymmetry arising from individual wave triads may be determined, thus providing a deeper insight into the differences between the model and data results. Finally, in the context of this study, the additional benefit of bispectral analysis is that it indicates the fraction of the energy present at a given set of frequencies that is due to triad interactions, thus distinguishing bound waves from free waves.

In section 6.2, the bispectrum is defined, and its properties relevant to this study are reviewed. Section 6.3 presents model-data comparison for total asymmetry, and section 6.4 looks at the contribution from selected wave triads to total skewness and asymmetry. Finally the results are summarised and discussed in section 6.5.

6.2 Bispectral analysis

6.2.1 Introduction to bispectral analysis

The bispectrum is formally defined as the Fourier transform of the third order correlation function of a time series $\eta(t)$ (Hasselmann *et al.*, 1963):

$$B(f_j, f_k) = \frac{1}{(2\pi)^2} \int_{-\infty}^{+\infty} \int S(\tau_j, \tau_k) e^{-i(f_j \tau_j + f_k \tau_k)} d\tau_j d\tau_k \tag{6.1a}$$

$$S(\tau_j, \tau_k) = E\left[\eta(t)\eta(t+\tau_j)\eta(t+\tau_k)\right] \tag{6.1b}$$

where τ is a lag, f is the frequency, $E[\ ]$ is the expected value, or average, operator. The bispectrum can also be expressed in terms of Fourier coefficients as:

$$B(f_j, f_k) = E\left[A_{f_j} A_{f_k} A^*_{f_{j+k}}\right] \tag{6.2}$$

where A_{f_j} is the complex Fourier coefficient of frequency f_j, and * denotes the complex conjugate. The bispectrum is zero if the average triple product of Fourier coefficients is zero. This occurs if the modes are independent of each other, that is, for the random phase relationships between Fourier modes in a linear wave field (Elgar and Guza, 1985b). On the other hand, if waves are present at f_j, f_k and f_{j+k}, and if there is a phase relation between the waves at these frequencies (i.e. energy is nonlinearly transferred from the interaction between two components to the third one), then the bispectrum is non-zero.

The bispectrum has real and imaginary components. It may be expressed in terms of its biamplitude and biphase:

$$B(f_j, f_k) = \left|B(f_j, f_k)\right| . e^{-i\beta(f_j, f_k)} \tag{6.3a}$$

where the biphase is

$$\beta(f_j, f_k) = \tan^{-1}\left\{\frac{\Im\left[B(f_j, f_k)\right]}{\Re\left[B(f_j, f_k)\right]}\right\} \tag{6.3b}$$

where $\Re\{\ \}$ and $\Im\{\ \}$ denote the real and imaginary parts respectively. The biamplitude indicates the nature and relative strength of the interactions, and the biphase gives a

measure of the relative importance of the real and imaginary parts of the bispectrum, which will be defined latter.

Using symmetry properties, the bispectrum can be uniquely described by its values in a bifrequency octant. For a digital time series with Nyquist frequency f_N, the bispectrum is uniquely defined within a triangle in a (f_1,f_2)-space defined on figure 6.1.

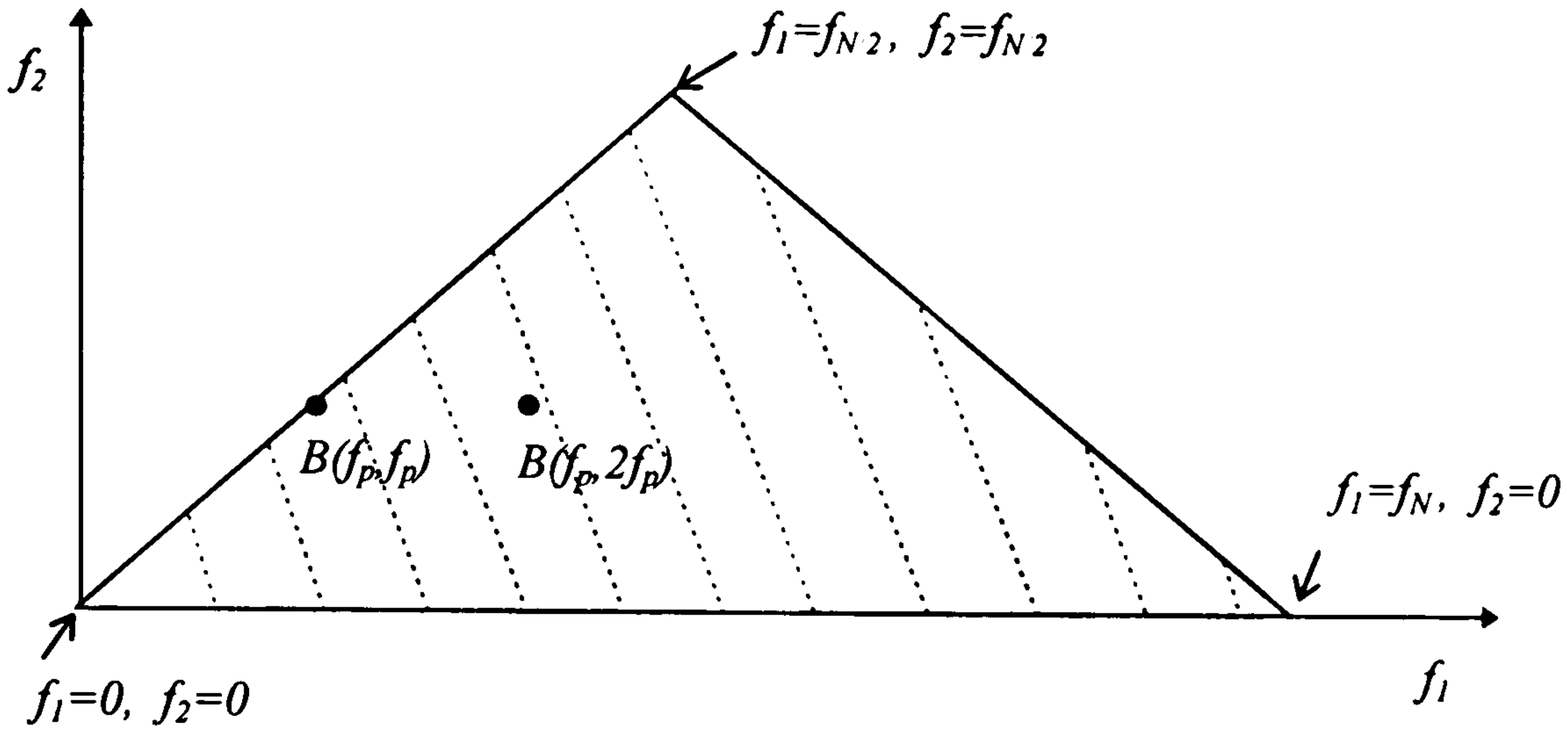

Figure 6.1. plan view of a unique bifrequency space

In this bifrequency space, for a wave train with peak frequency f_p, the convention adopted in this thesis is that a non-zero $B(f_p,2f_p)$ indicates nonlinear interactions between waves at f_p, $2f_p$ and $3f_p$. Note that the bispectral analysis does not indicate the direction of energy flow, hence a non-zero $B(f_p,2f_p)$ may indicate a sum interaction resulting in the transfer of energy to the third harmonic, i.e. $f_p + 2f_p \rightarrow 3f_p$, or a difference interaction modifying the first harmonic, i.e. $3f_p - 2f_p \rightarrow f_p$. Similarly, a non-zero $B(f_p,f_p)$ indicates phase coupling between primary and second harmonics (i.e., assuming $f_p + f_p \rightarrow 2f_p$, the self-self interaction of the waves at f_p forces waves at $2f_p$). Difference interactions can also occur that result in the generation of low frequency waves. These interactions are not considered in this analysis.

By analogy to equation (6.2), the power spectrum may be defined as

$$P(f_j)=E\left[A_{f_j}A^*_{f_j}\right] \tag{6.4}$$

The power spectrum indicates the contribution to the second order moment (variance) of $\eta(t)$ from the spectral component at f_j. The variance can thus be recovered from the integrated power spectrum. By analogy it can be shown that the bispectrum represents the

contribution to the third order moment from the spectral components at f_j and f_k , and that the third moment of $\eta(t)$ may be recovered from the integral of the real part of the bispectrum (Hasselmann *et al.*, 1963):

$$E\left[\eta^3(t)\right]=\int_{-\infty}^{+\infty}\int\Re\left\{B(f_j,f_k)\right\}df_j df_k \tag{6.5}$$

The skewness, or nondimensional mean cube, of $\eta(t)$ is obtained by normalising equation (6.5) by the variance to the power of 3/2 (Doering and Bowen, 1995):

$$S=\frac{E\left[\eta^3(t)\right]}{E\left[\eta^2(t)\right]^{3/2}} \tag{6.6}$$

Masuda and Kuo (1981) showed that the imaginary part of the bispectrum is related to the (vertical) asymmetry of the waves:

$$A=\frac{\int_{-\infty}^{+\infty}\int\Im\left\{B(f_j,f_k)\right\}df_j df_k}{E\left[\eta^2(t)\right]^{3/2}} \tag{6.7}$$

With these new definitions, the biphase may be interpreted as a measure of the relative importance of the skewness and asymmetry in the bispectrum.

The bispectrum may be expressed in a normalised form defined as the bicoherence spectrum given by Kim and Powers (1979):

$$b(f_j,f_k)=\frac{\left|B(f_j,f_k)\right|}{E\left[\left|A_{f_j}A_{f_k}\right|\right].E\left[\left|A_{f_{j+k}}\right|\right]} \tag{6.8}$$

Such normalisation ensures that $0 \le b \le 1$. Thus for a given triad, a zero bicoherence indicates normal independent modes, whereas a non-zero bicoherence indicates phase-coupled modes. While the bispectrum indicates the nature of the interactions, and their relative strength, the bicoherence spectrum (or normalised bispectrum) indicates the fraction of the power at e.g. *3fp* that is the result of phase coupling between waves at f_p and

$2f_p$, (assuming the flow of energy is $f_p + 2f_p \rightarrow 3f_p$), however small the interaction. In other words, if $b(f_p, 2f_p) = 1$, the forced waves at $3f_p$ are entirely due to the interaction of the waves at f_p and $2f_p$; that the third harmonic is travelling as a bound wave. $b(f_p, 2f_p) = 0.4$ indicates that 40% of the waves at $3f_p$ are due to the interaction of the waves at f_p and $2f_p$, and that the remaining of the third harmonic energy is travelling as free waves.

In this chapter, model-data comparisons consist of evaluations of the bispectrum in terms of its real and imaginary parts, and evaluation of the bicoherence. Skewness and asymmetry are calculated and compared for both elevation and velocity time series. More information regarding bispectral analysis may be found in Doering (1988) and Elgar and Guza (1985b).

6.2.2 Data analysis

To calculate the bispectrum, a Fast Fourier Transform method is used to calculate the product $\left[A_{f_j} A_{f_k} A^*_{f_{j+k}}\right]$ from discrete blocks of digital data that are ensemble averaged. The laboratory data, as received, had been decimated to 0.25 sec. It was thus decided to decimate the predicted time series to 0.25 sec also. The records were scaled for zero mean and broken down into segments of 64 sec (256 data points) each, with a 50% overlap. This resulted in a frequency resolution of 0.0156 Hz. No frequency averaging was applied. The cut-off frequency for the analysis was set to 2 Hz for all data. Note that this analysis is concerned with sum interactions only and that a 64 sec segment is therefore sufficient. The duration of the numerical experiment being limited, the length of the record for each run allowed ensemble averaging over 7 and 4 segments only, for cases A and B respectively. As a consequence the number of degrees of freedom, which is a function of the number of segments, is small, and the statistical stability of the bispectral estimates is low, especially for the irregular tests. Analysis of the statistical stability of the bispectral estimates is either vague or non-existent in the literature. It was indirectly assessed here by comparing the skewness estimated with the bispectral analysis to the exact skewness, that is the skewness obtained from the time domain analysis. A plot of the predicted total skewness evaluated from the time domain analysis versus the predicted total skewness evaluated from the bispectral analysis is shown on figure 6.2. The left hand plot is the elevation skewness; the right hand plot is the velocity skewness. The results show some scatter which can be shown to be related to e.g. the type of tapering window used, or the amount of overlapping. The reliability of the bispectral estimates is thus satisfactory. According to Elgar and Guza

(1985b), the number of degrees of freedom required for statistical stability decreases with increasing strength of the bispectral signal. It will be shown in section 6.5 that the bicoherence estimates indicate very strong interaction for all four runs for which it appears that the energy present at each harmonic frequency is entirely due to triad interactions. This further justifies the statistical stationarity of the estimates despite the small numbers of degree of freedom.

Lastly it is important to bear in mind the fact that this study consists of the comparison of laboratory and numerical results. It is not the exactitude of the estimates that is sought here, rather the validity of the comparison. Great care has been taken to ensure that those results are analysed in exactly the same way.

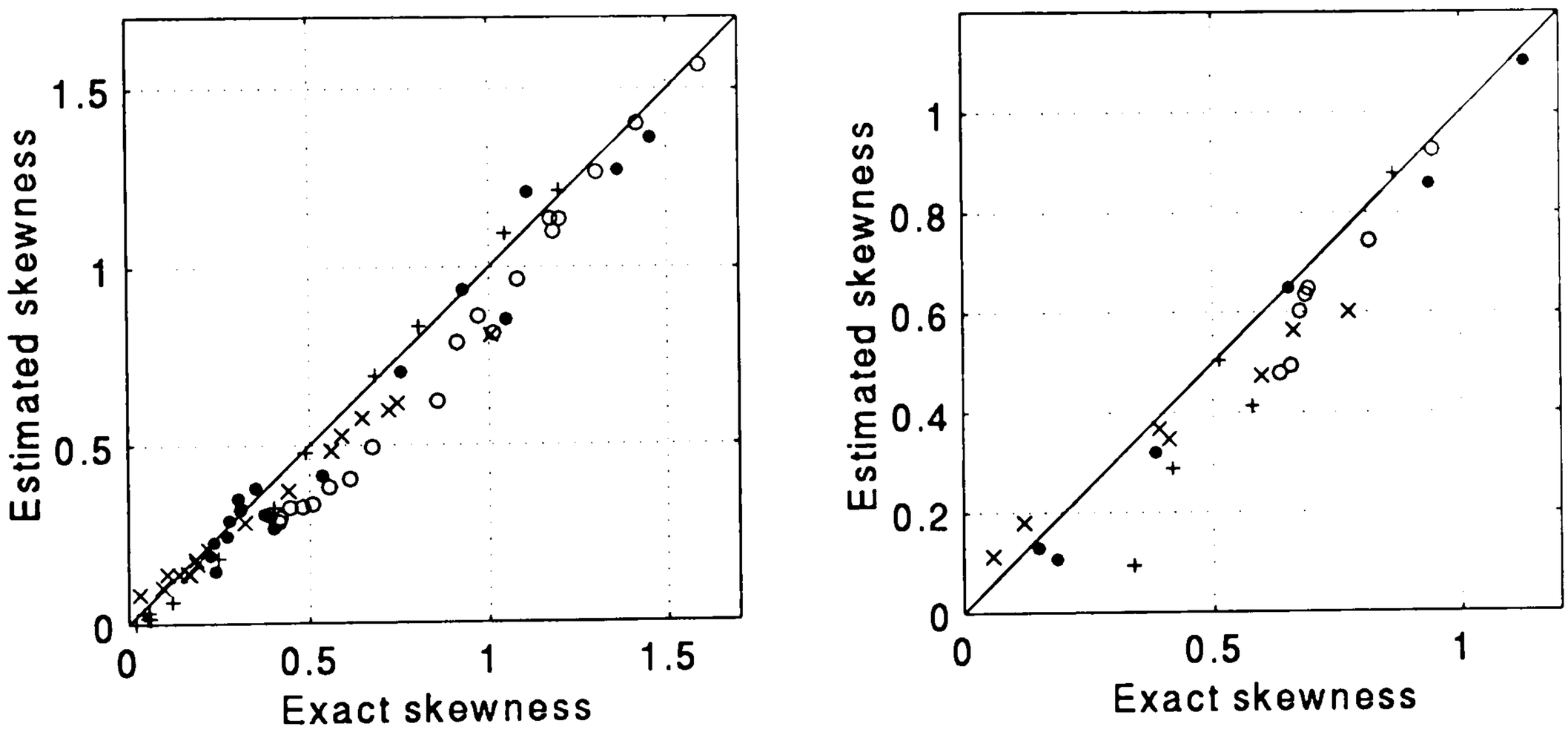

Figure 6.2 Predicted skewness estimated from the bispectral analysis *versus* exact predicted skewness. Surface elevation (left panel), depth-averaged velocity (right panel). ○ A1, • A2, × B1, and + B2.

6.3 Total effect of triad interactions on flow asymmetry

The evaluation of the wave shape so far has consisted of direct comparison of time series, and comparison of skewness and kurtosis evaluated from a time domain analysis. Bispectral analysis may be used to give further information on the wave shape: while the skewness may be retrieved from the real part of the bispectrum, a new quantity, the wave asymmetry (defined here as asymmetry with respect to the vertical) may be obtained from the imaginary part of the bispectrum. The relationship between flow asymmetry (as opposed to skewness) and sediment transport is not clear. One may suggest that the violent change of sign of the velocity in the case of a strongly asymmetrical wave profile may

result in the direction of the sediment movement initiated by the shoreward velocity to be reversed offshore. According to Nielsen (1992), several experiments, including those of King (1991), have shown that asymmetric waves produce net sediment transport. The asymmetry, or imaginary part of the bispectrum, is not only investigated here for its direct potential effects on sediment dynamics. Elgar and Guza (1985b) have shown that the imaginary part of the bispectrum is also a measure of the skewness of the first derivative of the time series, that is skewness of the acceleration in the case of a velocity time series. Hanes and Huntley (1986), using field data, first suggested that fluid acceleration had possible effects on suspended sediment transport. Since acceleration is directly related to the wave shape, both Hanes and Huntley's and King's finding corroborate each other.

Figure 6.3a shows the spatial variation of the predicted and observed elevation asymmetry, A_η, integrated and normalised according to 6.7. It was shown in section 6.2 that S_η and S_U were estimated with sufficient accuracy from the bispectrum. These estimates are shown in figure 6.3, along with asymmetry estimates. The reader is referred to figures 5.13 and 5.14 for a detailed cross-shore evolution of the exact skewness, for varying ϕ_B.

Since a negative asymmetry indicates a forward pitched profile, the increasing negative value of A_η indicates increasingly (vertically) asymmetrical wave profiles. The results for A1 and A2 are fairly good, particularly for A2. For A1, A_η is successively under-estimated in the outer surf zone, and over-estimated in the inner surf zone[1]. In contrast, the results for B1 and B2 show a good qualitative prediction of the cross-shore variation of A_η, but a underestimation in the surf zone. It appears that while the predicted S_η for A1 was overestimated in the surf zone (figure 6.3a, panel (1,1)), the predicted A_η for that case are comparatively good. On the other hand, the S_η predictions for B1 were almost perfect (figure 5.13, panel (3,1)), but A_η in the surf zone is underestimated. The improved results for A1 and A2, relative to B1 and B2, seem contradictory. Indeed (i) since the prediction of asymmetry relies on the correct prediction of the phase shift between the primary and its harmonics, and (ii) since A1 and A2 are runs for which high harmonics generation is intense and *kh* reaches values beyond 15, one would expect the results to be worse for these two cases.

[1] observed and predicted asymmetry are compared in absolute terms.

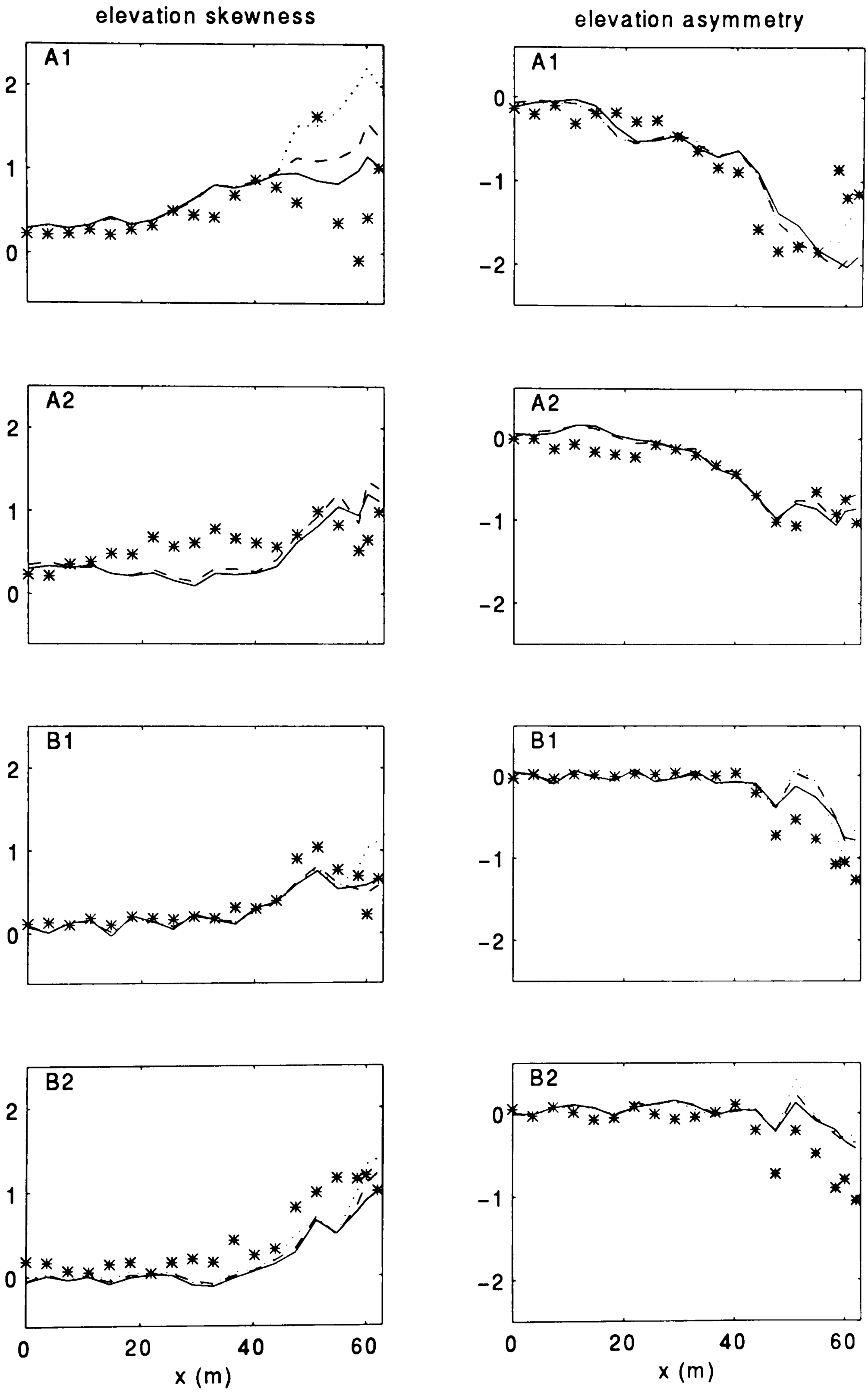

Figure 6.3a Cross-shore variation of the observed and predicted elevation skewness S_η (left column) and elevation asymmetry A_η (right column) estimated from the bispectral analysis. From top to bottom are tests A1, A2, B1 and B2. * observed data, _____ $\phi_B = 17°$, - - - - - - $\phi_B = 20°$, ... $\phi_B = 26°$.

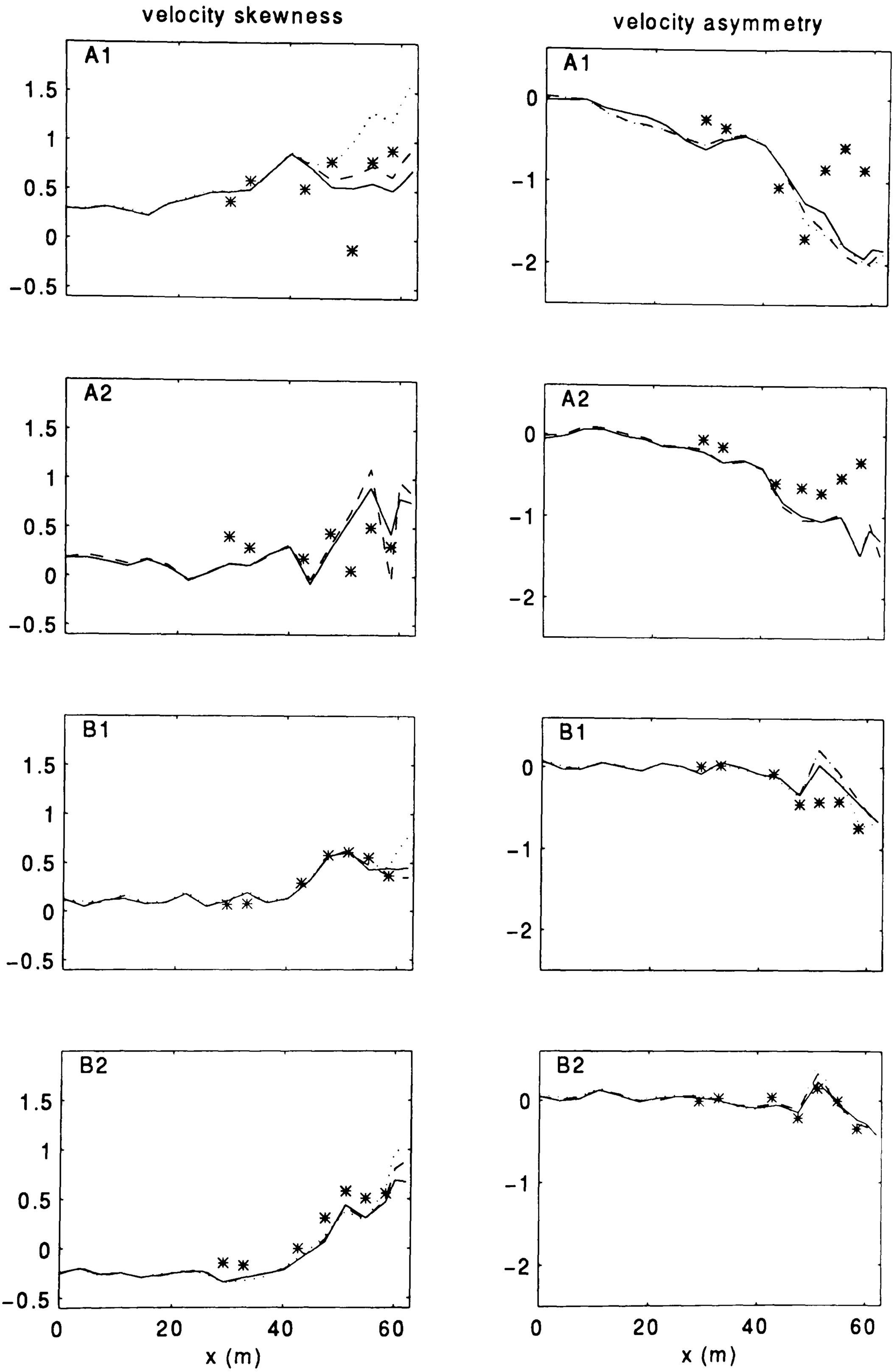

Figure 6.3b Cross-shore variation of the observed and predicted depth-averaged velocity skewness S_U (left column) and depth-averaged velocity asymmetry A_U (right column) estimated from the bispectral analysis. Legend as in figure 6.3a.

Another interesting feature lies with the effect of ϕ_B on the asymmetry. While increasing ϕ_B results in an increase in skewness, it appears to also result in a decreasing asymmetry. In other words, it seems that the increased presence of high harmonics results in decreased asymmetry. Furthermore, whilst the fit with laboratory data was improved with decreasing ϕ_B for the skewness, it appears that, for the asymmetry prediction, the fit is improved with increasing ϕ_B. Note that if a choice has to be made, accurate prediction of the skewness is preferred.

Figure 6.3b shows the spatial variation of the predicted and observed velocity asymmetry A_U. The predictions for A_U for cases A1 and A2 are larger than the observations in the surf zone (in contrast with A_η, for which the predictions and the observations were in better

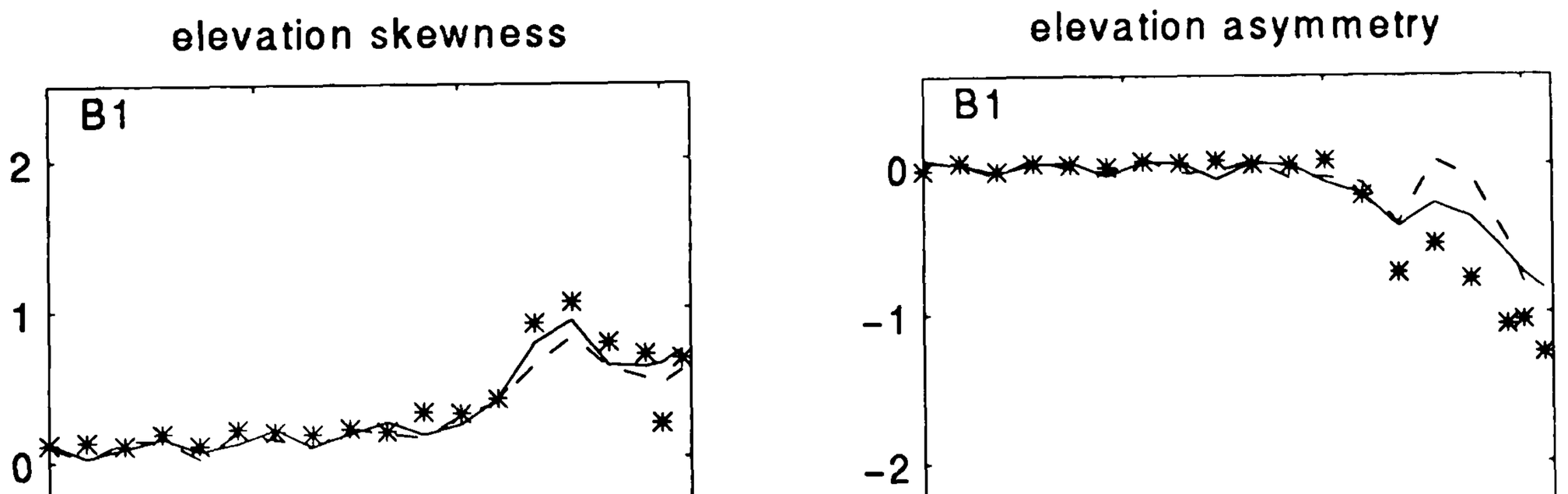

Figure 6.3c Effect of profile smoothing on the cross-shore variation of the observed and predicted elevation skewness S_η (left column) and elevation asymmetry A_η (right column) estimated from the bispectral analysis. For runs B1 (top panels), and B2 (bottom panels). $\phi_B = 20°$. * observed data, ——— effective profile, ------ actual profile.

agreement). The asymmetry predictions for B1 and B2 are good (and improved relative to A_η predictions). It is interesting to see that A_η and A_U for B1 and B2 follow the same trends, whereas A_η and A_U for A1 and A2 follow distinctly different trends. The model does not predict this change of trend. Also interesting is the fact that skewness and kurtosis follow the same spatial variation, not the skewness and asymmetry. Lastly, observation of the results for both A_η and A_U for case A1 show that the asymmetry is less sensitive to ϕ_B than the skewness.

The smoothing of the bathymetry for cases B1 and B2 was seen in section 5.4 to result in improved skewness and kurtosis predictions. The effect of profile smoothing on elevation and velocity asymmetry predictions is shown on figure 6.3c and 6.3d respectively. Profile smoothing has resulted in a smoother variation of A_η and A_U, and a better fit for B1.

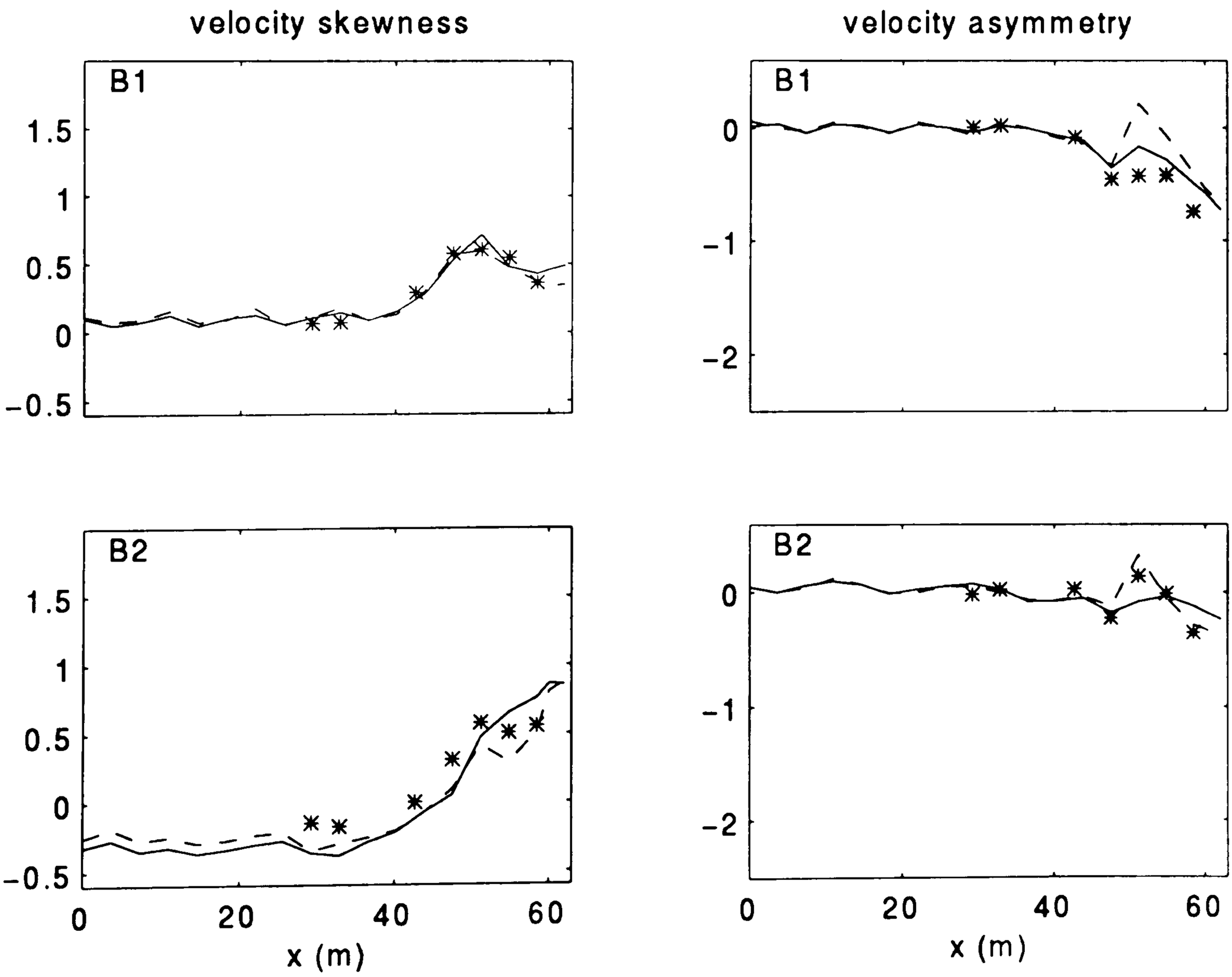

Figure 6.3d Effect of profile smoothing on the cross-shore variation of the observed and predicted velocity skewness S_U (left column) and velocity asymmetry A_U (right column) estimated from the bispectral analysis. For runs B1 (top panels), and B2 (bottom panels). Legend as in figure 6.3a.

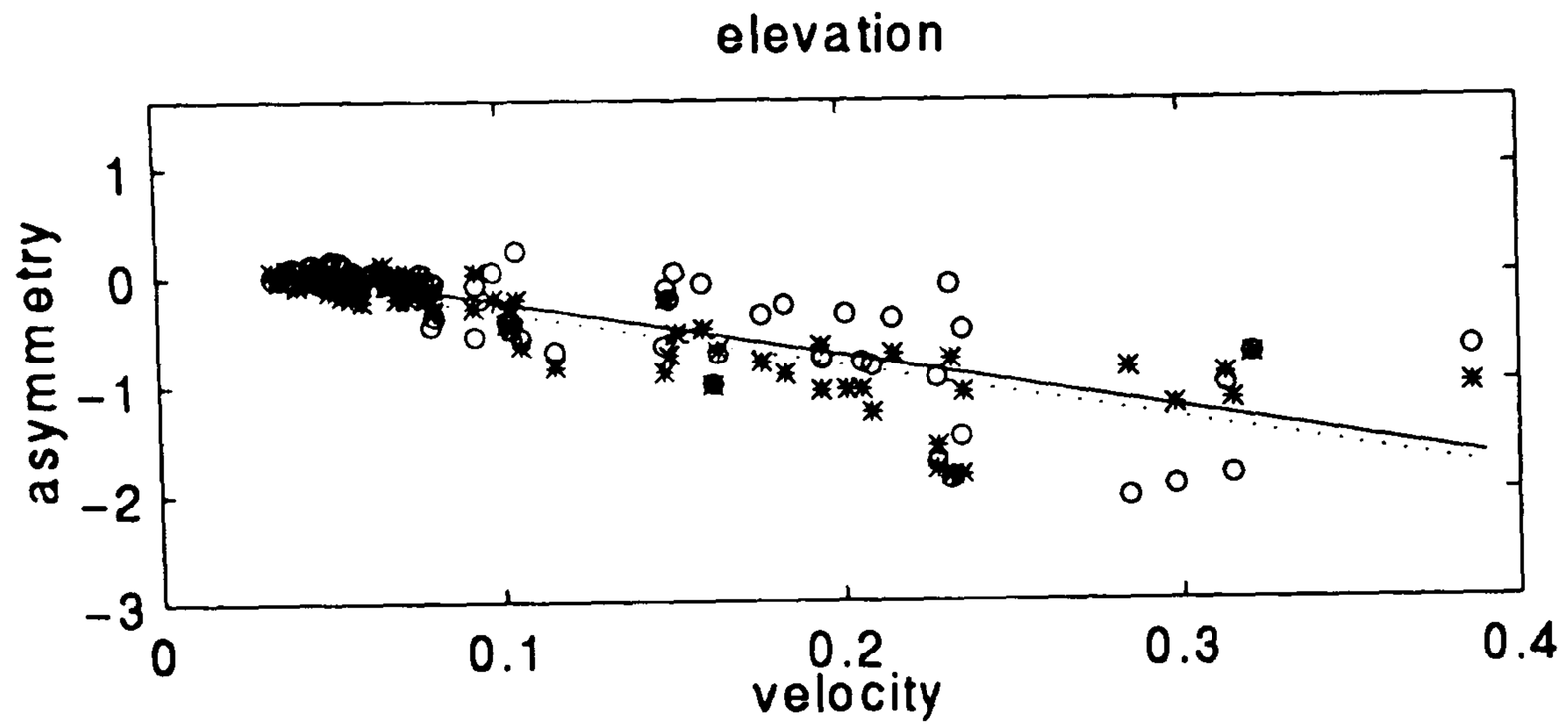

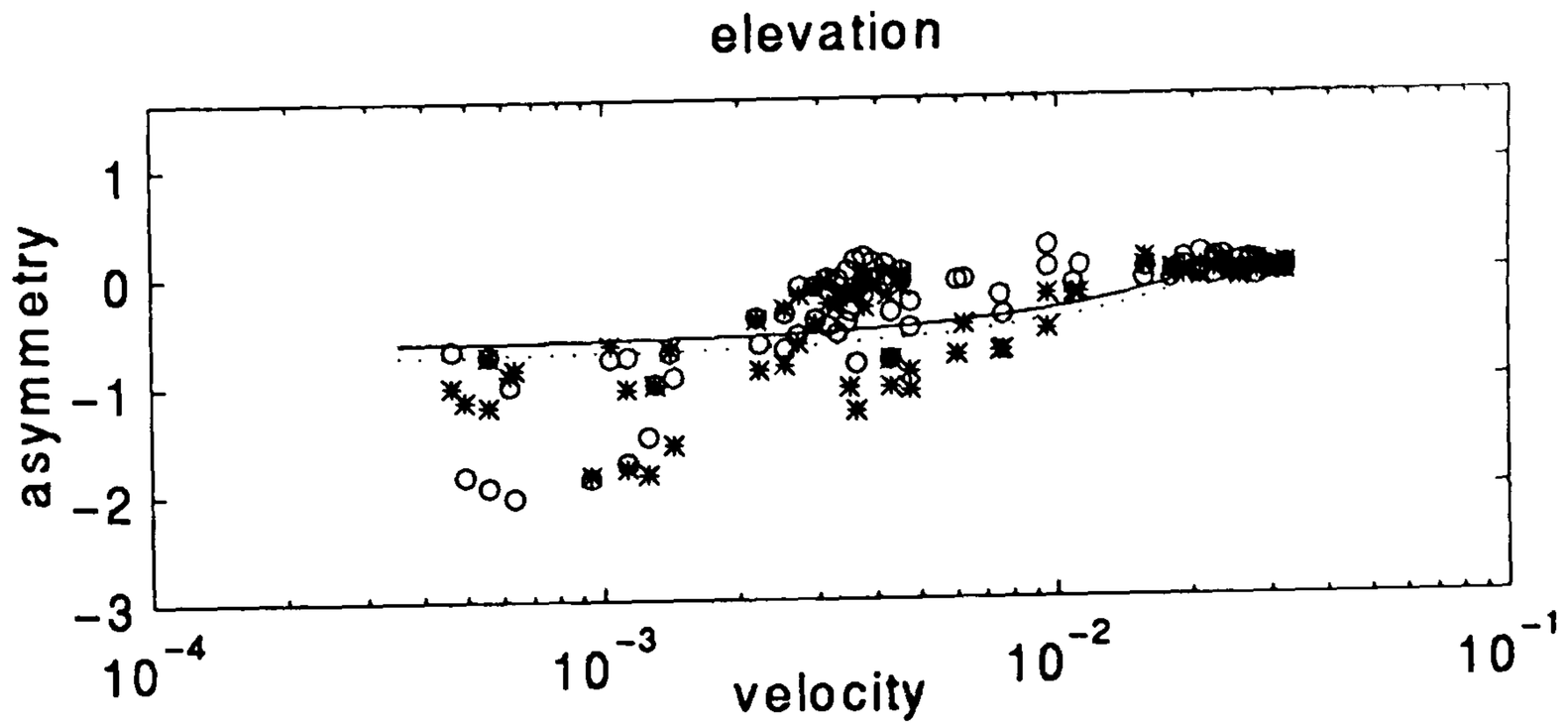

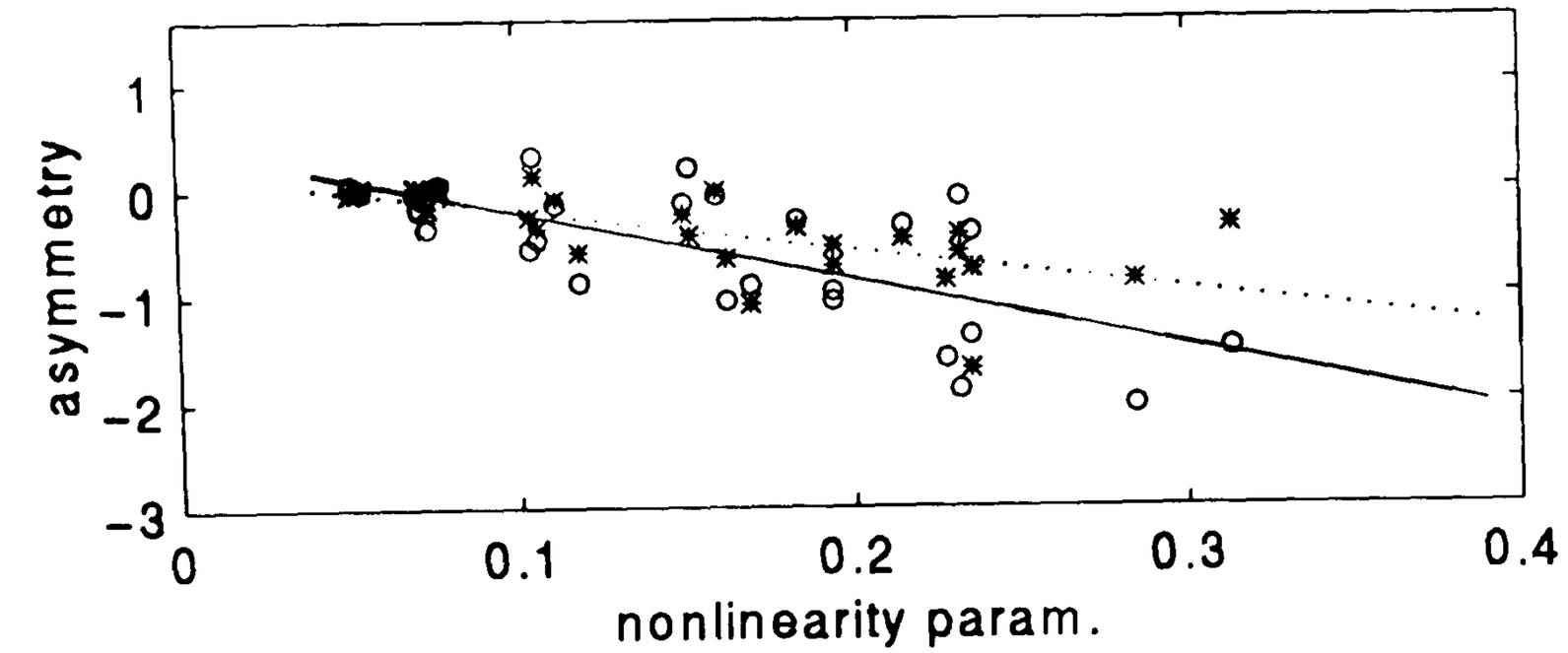

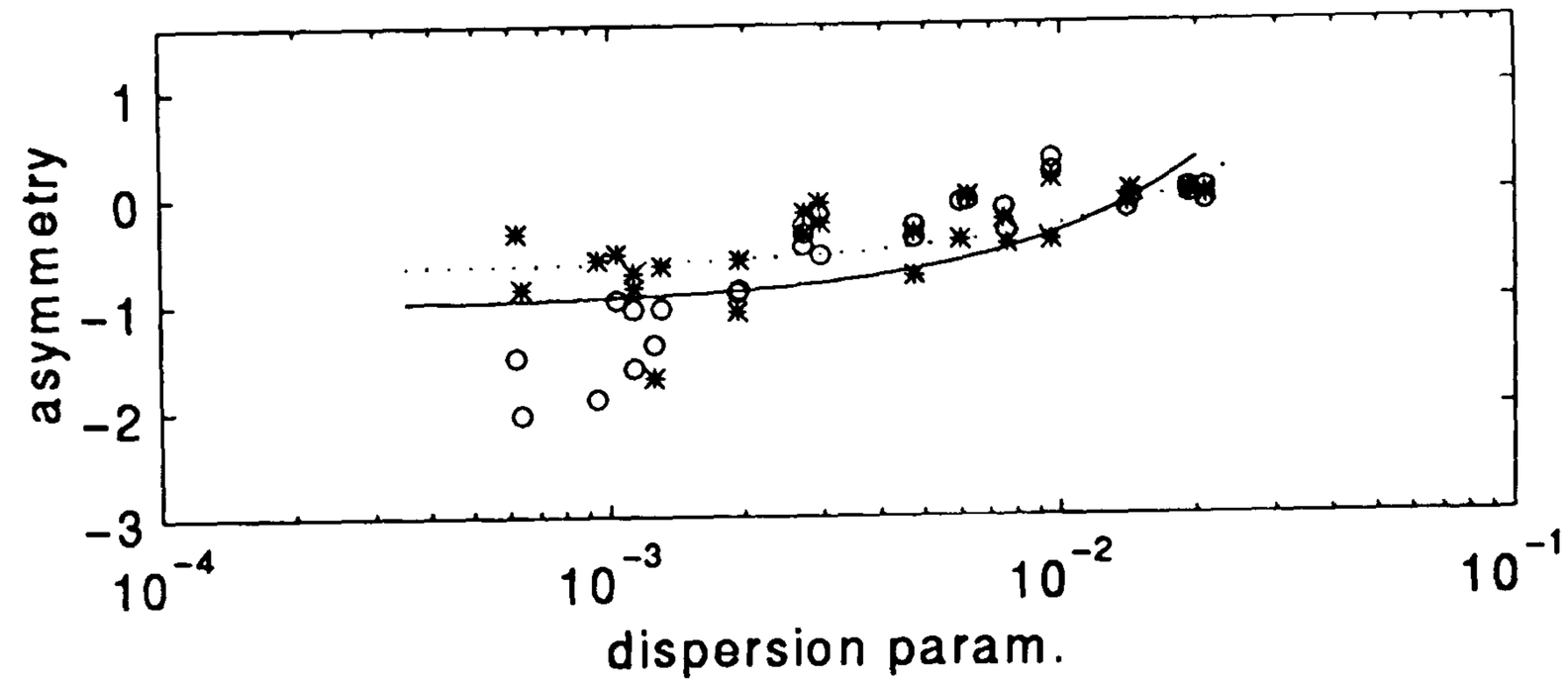

Figure 6.4a Predicted (○) and observed (∗) A_η (top row) and A_U (bottom row) *versus* ε (left column) and *versus* μ (right column). $\phi_B = 20°$, all four runs are plotted for each gauges. The plain and dotted lines are a first order polynomial fit to the predicted and observed data respectively.

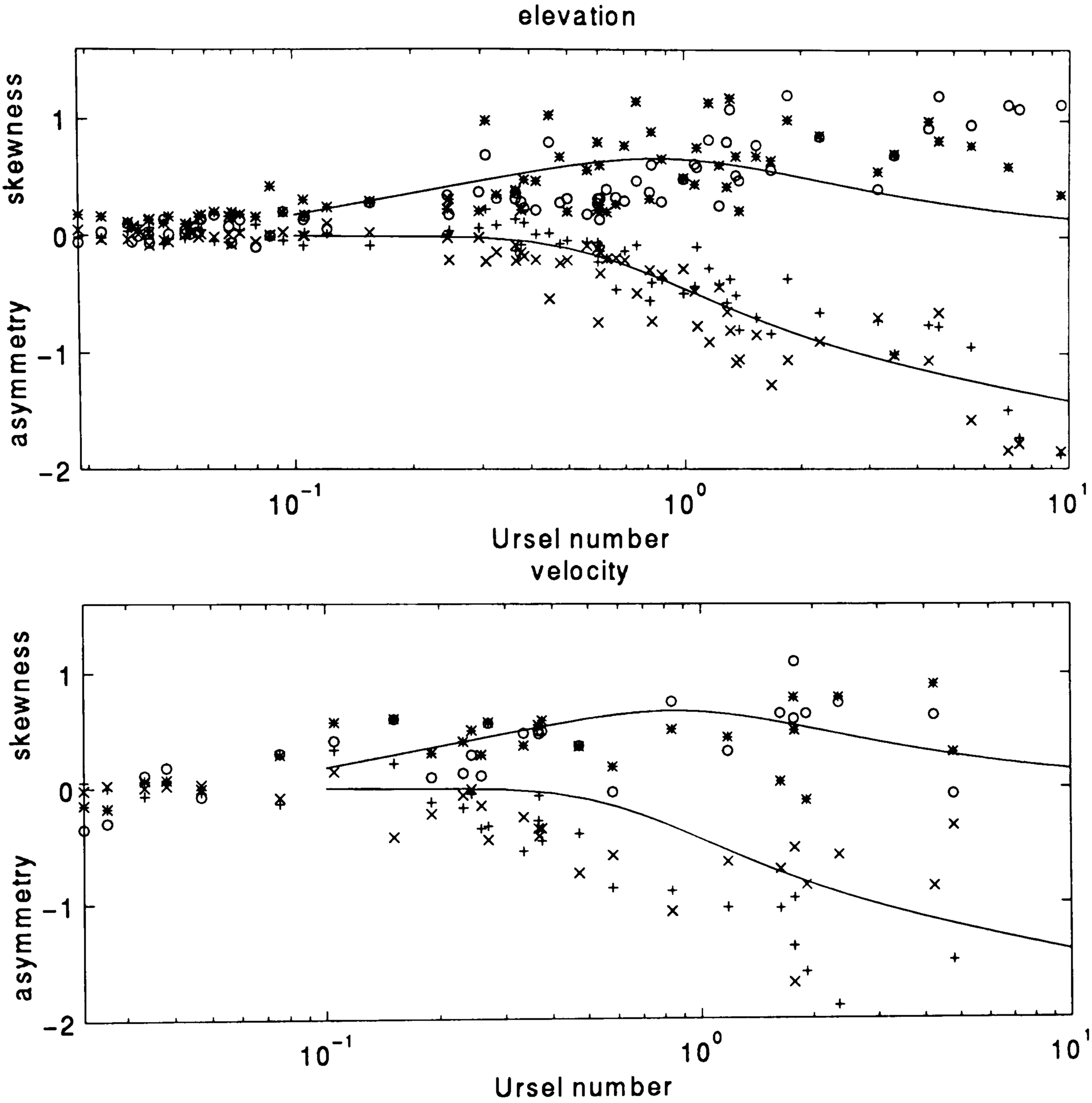

Figure 6.4b (top plot) S_η and A_η as a function of Ur, predictions (○ , +), observations (∗,×) respectively. (bottom plot) S_U and A_U as a function of Ur. $\phi_B = 20°$, all four runs are plotted for each gauges & current meter arrays. The plain lines are the parameterization proposed by Doering and Bowen (1995).

In section 5.5 some degree of correlation between S_η, S_U, K_η, K_U and ε and μ has been shown to exist (figures 5.26 and 5.27). The scatter being quite large, no attempt to parameterize this dependence was made. The same possible correlation between A_η, A_U and ε and μ is now sought after in figure 6.4a, and the same 'loose' correlation is obtained. A similar parameterization was introduced by Doering and Bowen (1995) where two expressions for A_U and S_U (arising from wind wave interactions) as a function of the Ursell number were obtained:

$$A_U = [0.8 + 0.62\log(U_r)]\sin\{[-90^o + 90^o \tanh(0.73/U_r)]\pi/180\}$$

$$S_U = [0.8 + 0.62\log(U_r)]\cos\{[-90^o + 90^o \tanh(0.73/U_r)]\pi/180\}$$

where the Ursell number is defined as:

$$Ur = \frac{3}{4}\frac{g}{8\pi^2}\frac{H_c T_p^2}{h^2}$$

H_c is a characteristic wave height. The data consisted of field measurements from four different sites and representative of a wide range of conditions. The scatter was still quite large, but the parameterization, obtained from a least square fit, is in accordance with theoretical expectations. Doering and Bowen (1995)'s expressions for A_U and S_U were fairly successfully applied to the cases studied here (figure 6.4b), with the same amount of scatter. Interestingly, this parameterization was also successfully applied to A_η and S_η. Indeed the shape of the wave profiles and velocity oscillation are seen to evolve in a similar way. In fact, the parameterization appears to fit the A_η better than A_U.

Note that all computations on figure 6.4b are with $\phi_B = 20^o$. For large ε, the skewness predictions were already seen to overestimate the observations. This is reflected in larger deviations from the parameterization for large Ursell numbers.

6.4 Contribution to skewness and asymmetry from single wave triads

The comparison of elevation and velocity skewness, and elevation and velocity asymmetry, that have been discussed so far are that of total estimates. In order to get a better insight of the model's performance, and establish where the discrepancies between laboratory and numerical results arise, an examination of the contribution to skewness and asymmetry from phase-coupling between individual harmonics is required.

In the following, a detailed description of bispectral evolution for case A1 is first given. This case was chosen in spite of the fact that the cross-shore variation of the skewness for this run is atypical (presumably because of reflection), and despite the consequent fact that the discrepancies between observed and predicted skewness are the largest (relative to the other 3 cases. It was selected because it presents intense wave-wave interaction activity relative to cases B1 and B2), and thus offers a good example of bispectral evolution. The model's capability to model triad interactions may therefore be fully assessed. Case A1 also has the advantage (over A2) to be a regular wave test for which the bispectral peaks are very well defined. Finally, this case has presented the most sensitivity to ϕ_B , and a detailed analysis for this case will demonstrate why this occurs.

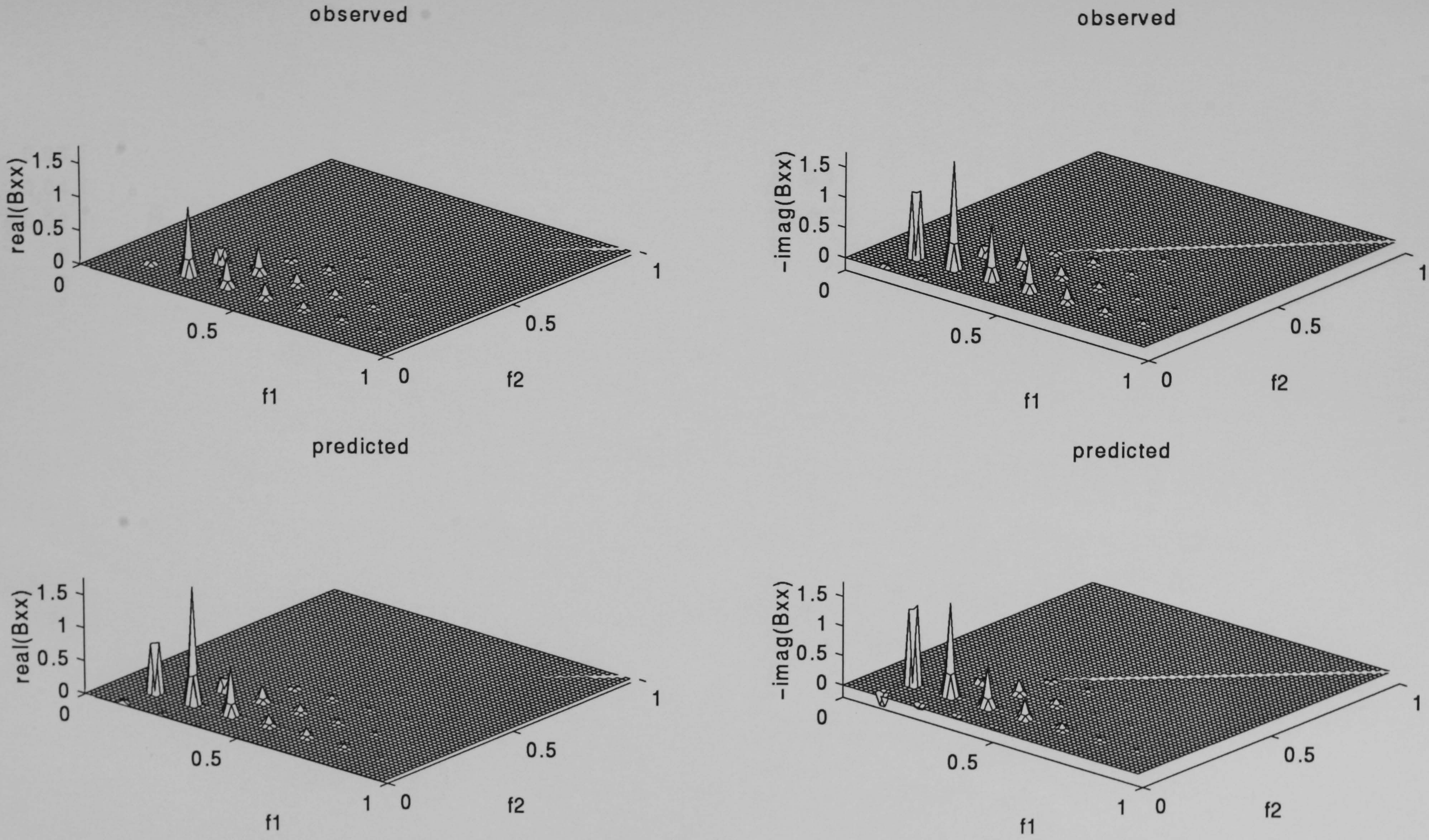

Figure 6.5 Dimensional real (left panels) and imaginary (right panels) parts of the bispectrum, run A1, gauge 13 (just before breaking). The top panels are the model predictions, the bottom panels are the observations. Note that the imaginary part has been multiplied by a factor of -1.

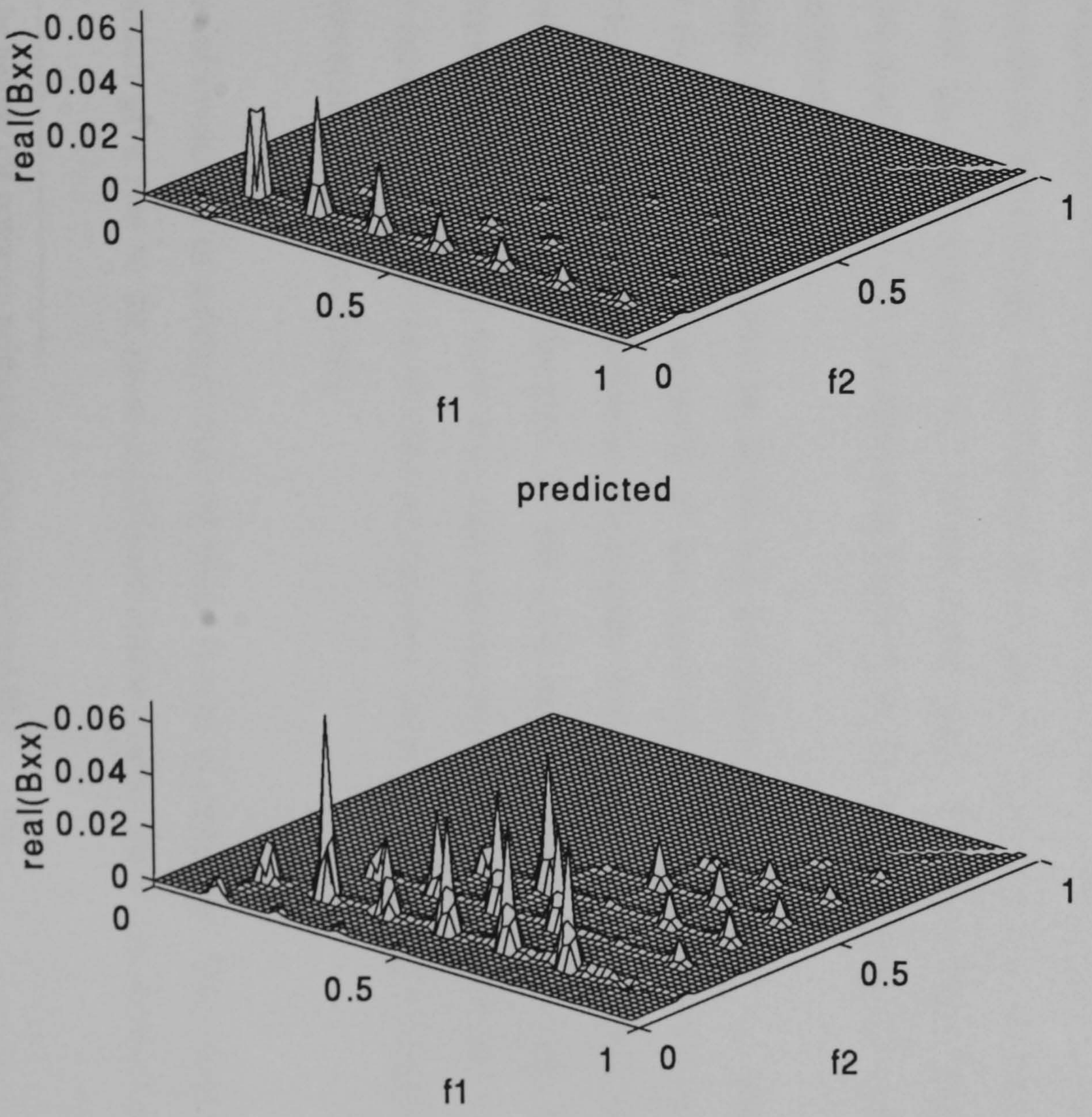

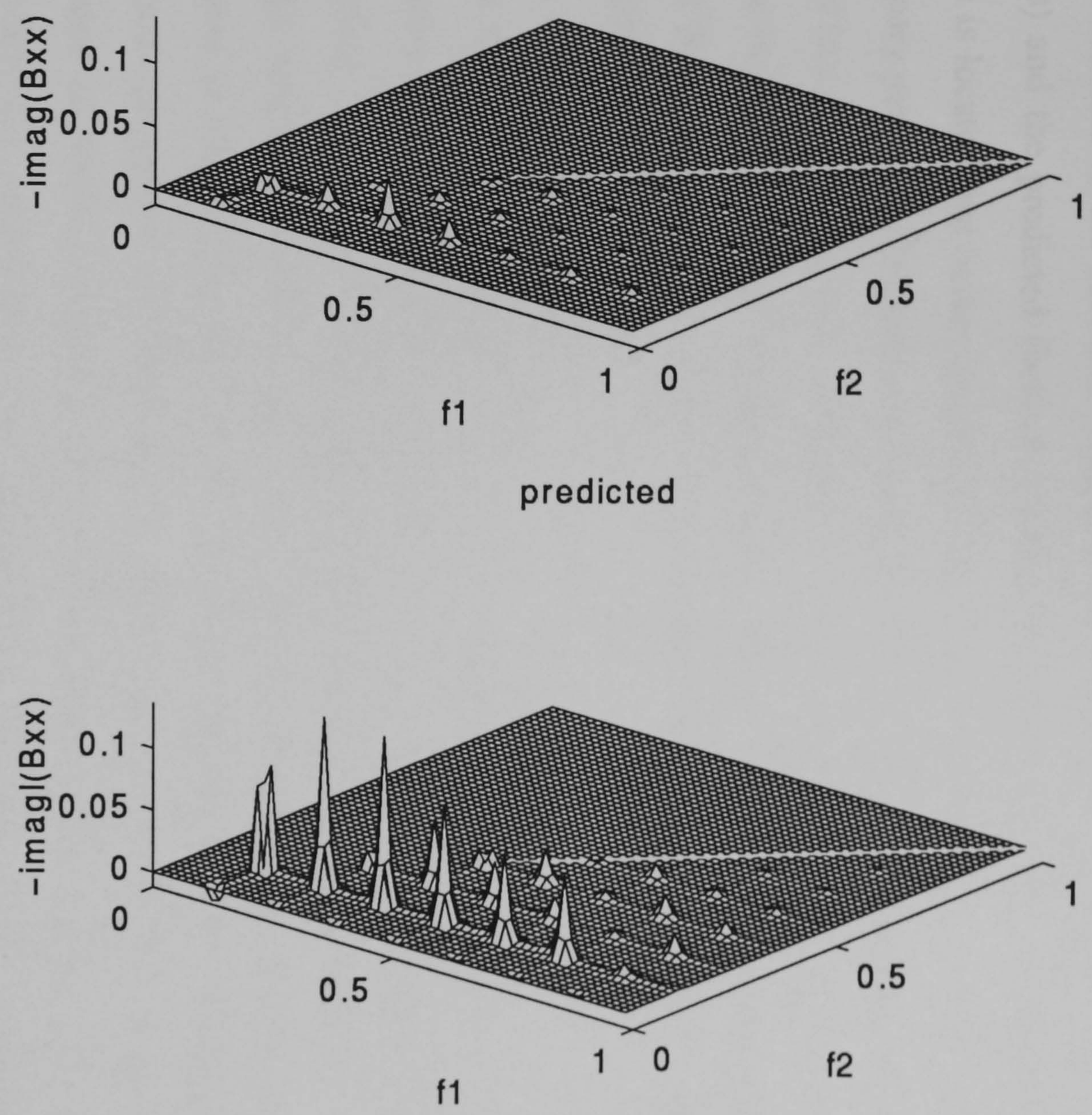

Figure 6.6 Same as figure 6.5, gauge 19.

Figure 6.5 shows the real and imaginary parts of the bispectrum for the measured (top panels) and the predicted (bottom panels) time series of surface elevation at gauge 13, which is located just before breaking. The predictions are with $\phi_B = 20^o$ [2]. Notice that the imaginary part of the bispectrum is multiplied by -1 to facilitate viewing. The bispectrum is plotted in a (f_1,f_2)-space with vertices at $(f_1 = 0 , f_2 = 0)$, $(f_1 = f_{N/2} , f_2 = f_{N/2})$ and $(f_1 = f_{N/2} , f_2 = 0)$, that is, half the unique bifrequency space. This was found to cover the most interesting part of the bispectrum (very little 'bispectral activity' is observed beyond 1 Hz), and again to facilitate viewing.

Let us first consider the real part of the bispectrum (panels (1,1) and (2,1)). From the laboratory data it appears that, at this gauge, the skewness arises mainly from the $(f_p, 2f_p)$ interaction. The rest of the skewness arises predominantly from the $(f_p, 3f_p)$, $(2f_p, 2f_p)$ and $(2f_p, 3f_p)$ interactions. Surprisingly, the (f_p,f_p) interaction gives rise to relatively little skewness at this gauge. This will be examined later (figure 6.8). Looking now at the predicted real part of the bispectrum it appears that the model gives a good qualitative prediction of wave-wave interaction. It is clear however the skewness is overestimated, particularly the contribution from the (f_p,f_p), $(f_p, 2f_p)$ and $(f_p, 3f_p)$ interactions. This is reflected in an overestimation of the total skewness (figure 5.13, panel(1,1)) at this gauge.

The imaginary part of the bispectrum for the measured time series (panel (1,2)) presents the same results as the real part, with the exception that the contribution to asymmetry from the (f_p,f_p) and $(f_p, 2f_p)$ interactions are of the same order. The prediction (panel (2,2)) is excellent qualitatively, but, as shown in figure 6.3a, the total asymmetry at this gauge is under-estimated.

The same data are presented on figure 6.6 for gauge 19. First it shows that the model largely over-estimates the intensity of the wave-wave interactions. This results in the generation of high harmonics that are not present in the measured time series, which clearly contributes to the over-estimation of the total skewness and asymmetry. Second, the overestimation of the total skewness (and asymmetry) is also shown clearly to arise from an over-estimation of the contribution to skewness (and asymmetry) for the phase-coupling also present in the observations.

The spatial evolution of a selected set of triads is now investigated. The triads selected are those which give rise to the most significant interactions. These are shown on figure 6.7.

---

[2] seen to be neither the optimum neither the worse case (fig 5.15 and 5.16)

Figure 6.8 shows the cross-shore variation of the band-integrated and normalised real part of the bispectrum for each of these 12 triads. The integration is carried out over the frequency bands as shown in figure 6.7. The band-integrated real part of the bispectrum was then normalised with the total (integrated) variance to the 3/2 power, thus giving the percent skewness or asymmetry. The predicted results are presented for ϕ_B = 17°, 20° and 26°. Note the scale of the y-axis varies from row to row. In addition, panels (1,1) and (1,2) show the total skewness (equation (6.5)) and the skewness resulting from interactions amongst short waves only (f > 0.06 Hz), respectively. These two plots show that the contribution to the total skewness from the difference interactions that result in bound low frequency waves is negligible. This was also found to be true for the other data.

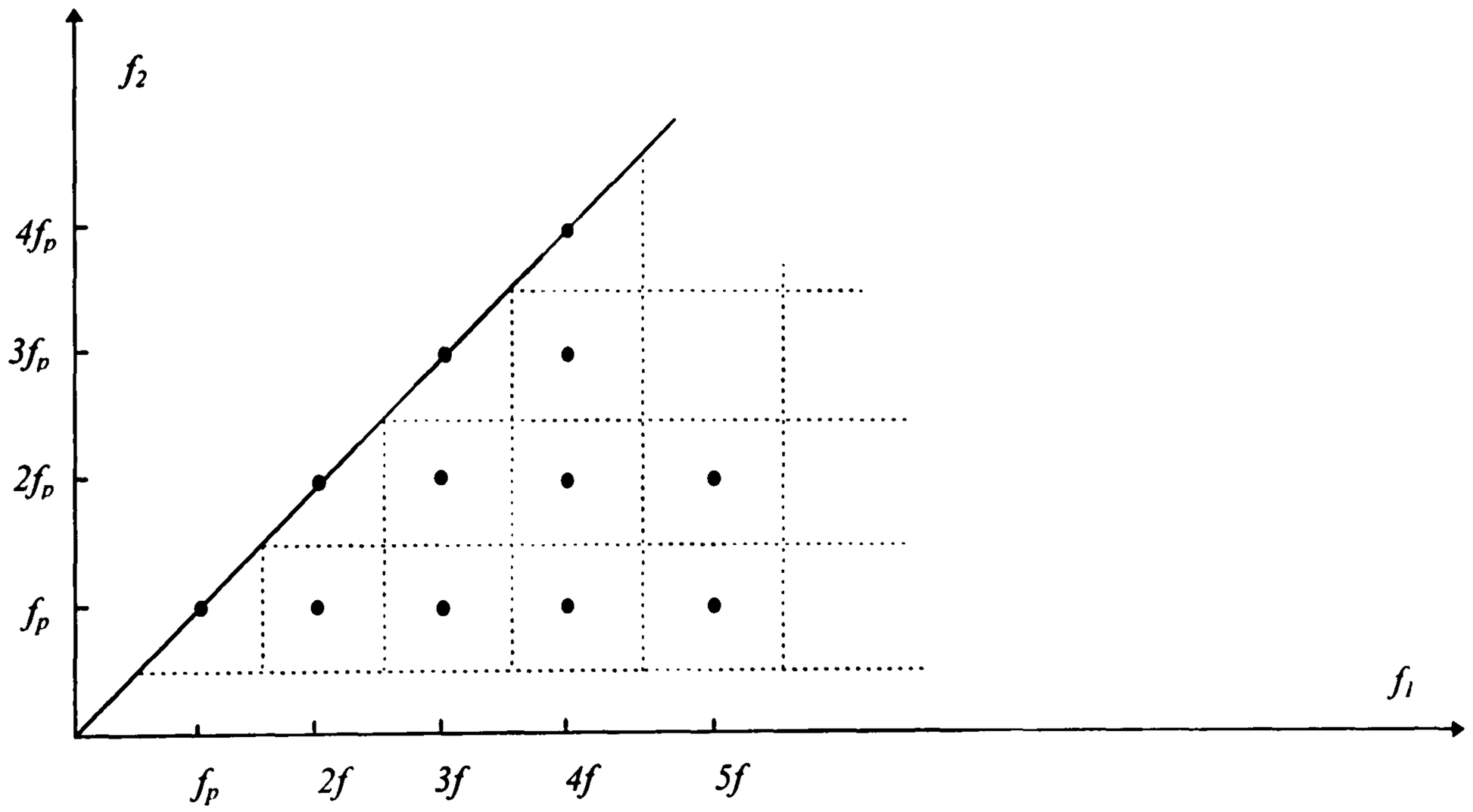

Figure 6.7. Identification of the 12 triads selected for investigation The dotted lines indicate the integration limits for each single wave triad.

Figure 6.8 shows the contribution to skewness predominantly arises from the (f_p,f_p) interaction up to gauge 11, after which the $(f_p,2f_p)$ interaction becomes the main source of skewness. A smaller contribution comes from the $(f_p,3f_p)$, $(2f_p,2f_p)$ and $(2f_p,3f_p)$ interactions, which develop further onshore during shoaling. The rest of the harmonics shown in figure 6.8 develop just prior to and during breaking. The model reproduces well this spatial variation of the contribution from each triad.

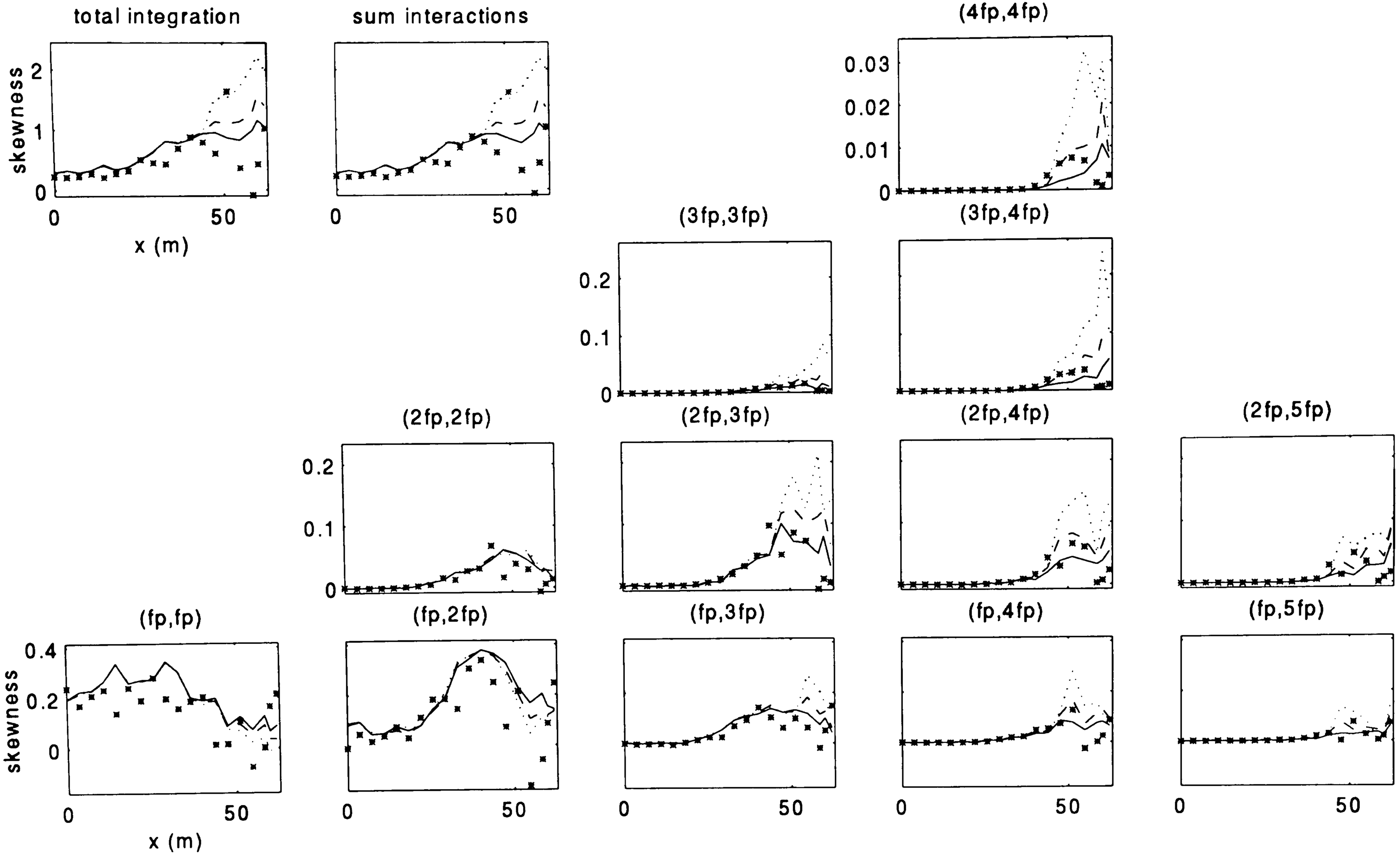

Figure 6.8 Spatial evolution of the normalised contributions to skewness for a selection of 12 triads, run A1. Also shown are the total skewness (panel (1,1)), and the skewness arising from wind-wave frequencies only (panel (1,2)). * observations, ——— $\phi_B = 17°$, - - - - - - $\phi_B = 20°$, ... $\phi_B = 26°$.

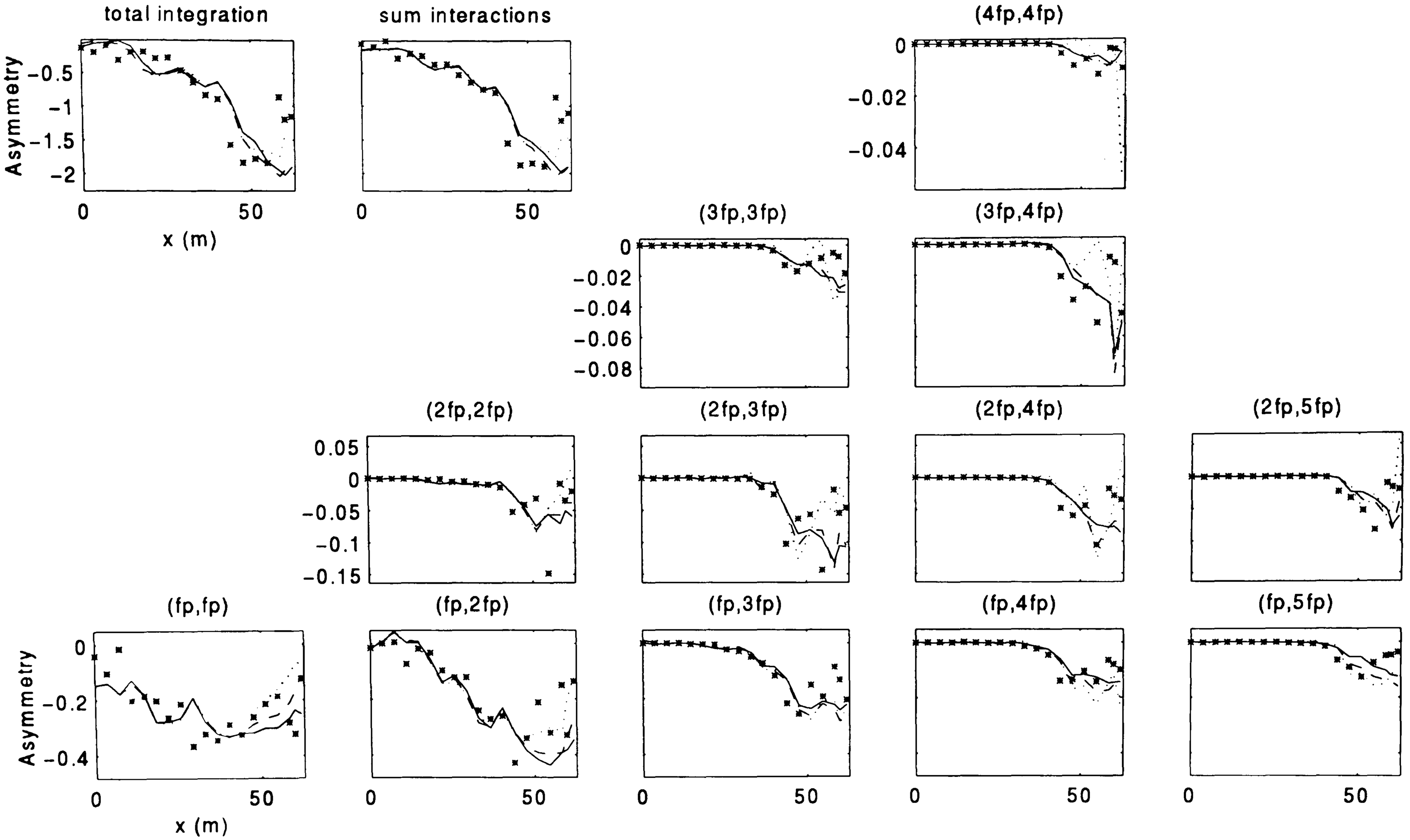

Figure 6.9 Spatial evolution of the normalised contributions to asymmetry for a selection of 12 triads, run A1. Legend as in figure 6.8.

The irregularity of the spatial variation of the measured skewness is reflected in the (irregular) spatial variation of the contribution to skewness arising from the (f_p,f_p) and $(f_p,2f_p)$ interaction, denoted $S_\eta(f_p,f_p)$ and $S_\eta(f_p,2f_p)$. Due to the atypical spatial variation of the measured skewness, it is difficult to conclude where the discrepancies between observed and predicted skewness arise from. On the other hand, an important characteristic of the model appears with the demonstration of the source of the dependence of the skewness on ϕ_B. It is evident that a change in ϕ_B greatly affects the predictions for the higher harmonics. Increasing ϕ_B from 20° to 26° results in a dramatic overestimation of the amplitude of the high order harmonics, and relatively little change to the amplitude of the low order harmonics e.g. $S_\eta(f_p,f_p)$ and $S_\eta(f_p,2f_p)$.

The negative skewness due to interactions involving primary and super-harmonics that is observed at gauge 16, and to a lesser extent at gauge 17 is unusual and inconsistent with expectations. These locations coincide with a minimum in the cross-shore variation of the observed wave height (figure 4.5), which was shown to be likely to be linked to wave reflection from the region beyond gauge 19. It is possible that reflection may be responsible for the negative skewness. This suggestion is supported by the fact the model, which ignores the region beyond gauge 19 and therefore fails to reproduce reflection from this zone, does not predict these negative contributions to skewness.

Furthermore, the model predictions for B1 with the raw bathymetry also yield the presence of negative contributions to skewness from the (f_p,f_p) interactions (not shown). These results are associated with a strong overestimation of wave reflection from the slope, and disappear when the profile is smoothed (i.e. when the reflection is reduced). This further corroborates the suggestion that wave reflection is responsible for negative contributions to skewness. Note that this suggestion implies that (i) the reflected waves are at the frequencies involved in the interaction concerned, and (ii) nonlinear interactions occurs between ingoing and outgoing waves.

To examine the effect of wave reflection on skewness, the skewness of a standing wave field of the form

$$\eta(t)=a_1\cos kx\sin wt+a_2\cos 2kx\sin 2wt$$

was considered. a_1 and a_2 are the amplitudes of the fundamental and second harmonic respectively. The computed results, shown in figure 6.10, reveal that indeed the skewness arising from sum interactions may be negative. The effect of reflection on the wave shape is unclear however, and needs to be investigated further.

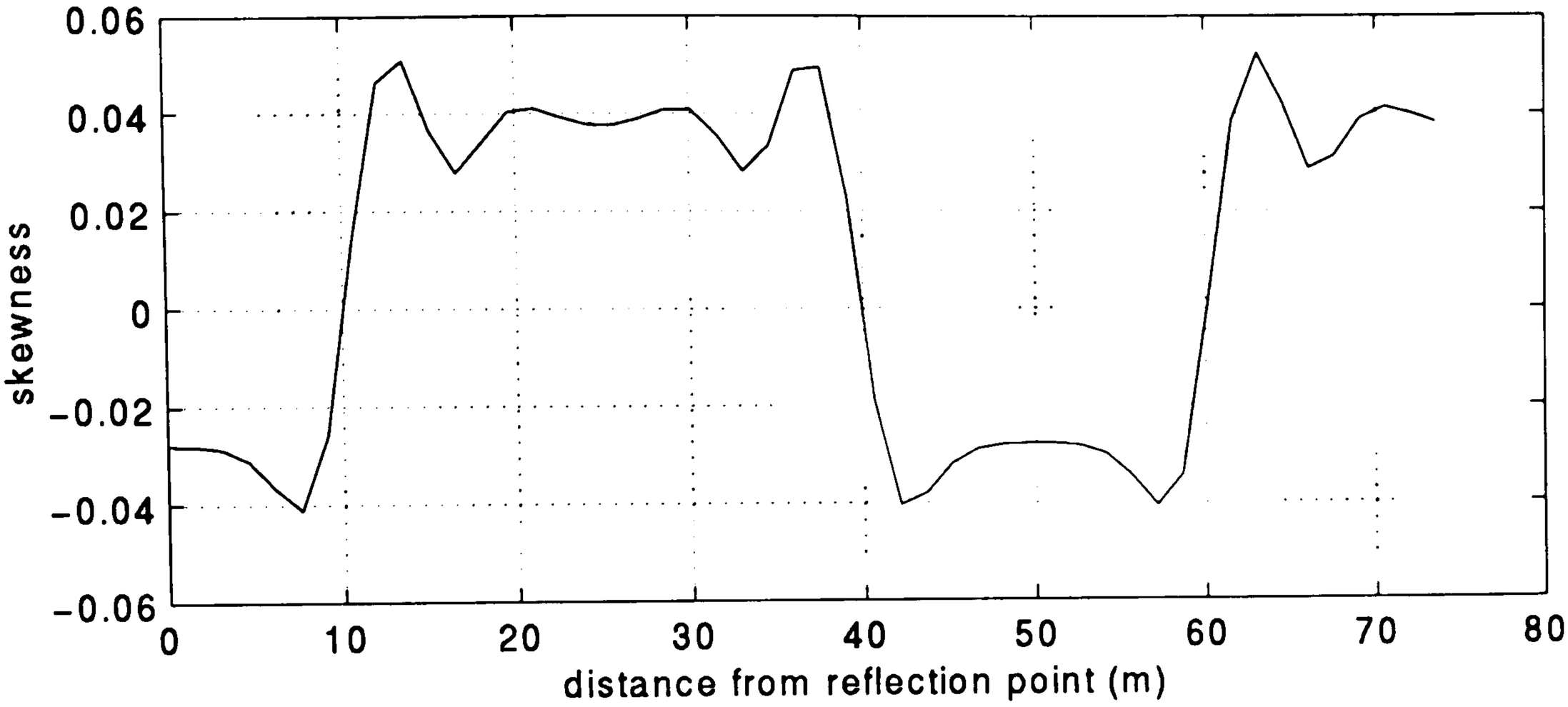

Figure 6.10 Spatial variation of the skewness of a standing wave field consisting of two harmonics with amplitudes 0.3m and 0.15m. $T = 8$s, $L = 50$m.

The predicted and observed asymmetry are presented in the same format in figure 6.9. Each of the triads investigated here makes the same relative contribution to A_η as for S_η. The effect of ϕ_B on the solution is less evident, although it appears that increasing ϕ_B generally results in a decrease of A_η. If $\phi_B = 17^\circ$ and 20° , the decrease of A_η after wave breaking is (i) underestimated for the low order harmonics, and (ii) not reproduced for the high order harmonics. If ϕ_B is increased to 26° however, the overall fit is much improved.

The same analysis on A2 shows that the over-estimation of the skewness at the last three wave gauges observed in section 5.2.3 (figure 5.8, panel(2,1)) is the result of an over-estimation of the contribution to skewness from the high order interactions. This confirms that the discrepancies for that run are due to the presence of high harmonics (with $kh > 5$, that is from the 5th harmonic) which the model cannot reproduce accurately.

The bispectral evolution for all the data is summarised in figure 6.11, which displays the predicted versus observed skewness arising from each triad, with $\phi_B = 20^\circ$. For B1 and B2 note that:

- the data is obtained with the smoothed profile.

- f_p = 0.33 Hz, and the integration limits (figure 6.7) have been changed accordingly.

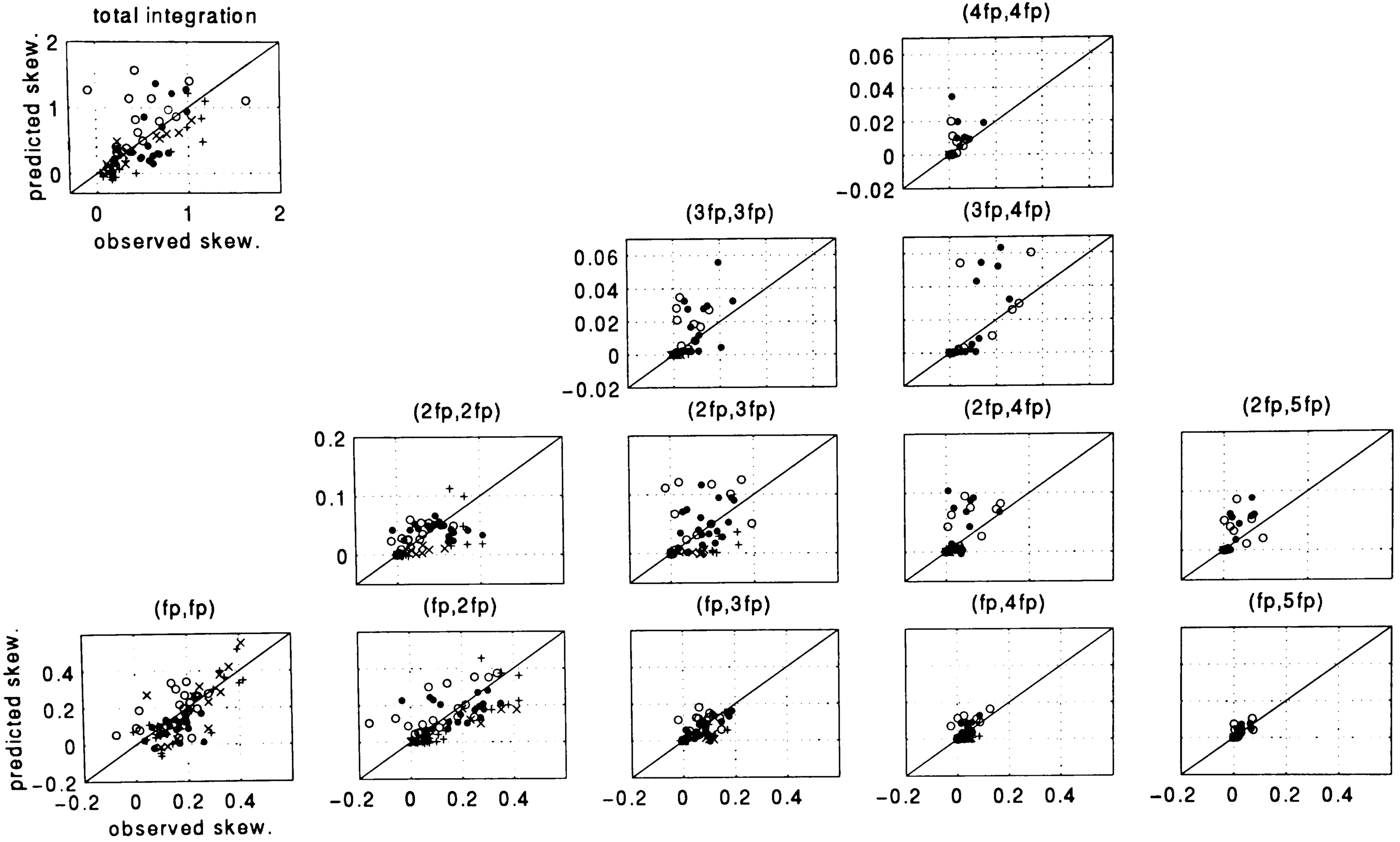

Figure 6.11 Predicted *versus* observed normalised contributions to skewness for a selection of 12 triads, for the 4 studied cases. Also shown is the total skewness (panel (1,1)). $\phi_H = 20°$. o A1, • A2, × B1, and + B2.

- ($4f_p, 4f_p$), ($4f_p, 3f_p$) and ($2f_p, 5f_p$) skewness and asymmetry are not calculated (and are set to zero) since for the analysis fc = 2 Hz and $6f_p$ = 2 Hz (see figure 6.7), and therefore these triads lie outside the domain of analysis. This limit is reasonable however since the most significant interactions for these runs are (f_p, f_p), ($f_p, 2f_p$), ($f_p, 3f_p$), ($2f_p, 2f_p$), and ($2f_p, 3f_p$).

A reasonable agreement, within the scatter, is obtained for the low order harmonics. Figure 6.11 also shows a clear over-prediction of the contribution to skewness from the high order harmonics. The largest discrepancies are for the largest contributions to skewness, that is, in the surf zone. Note that this is with $\phi_B = 20^\circ$ only.

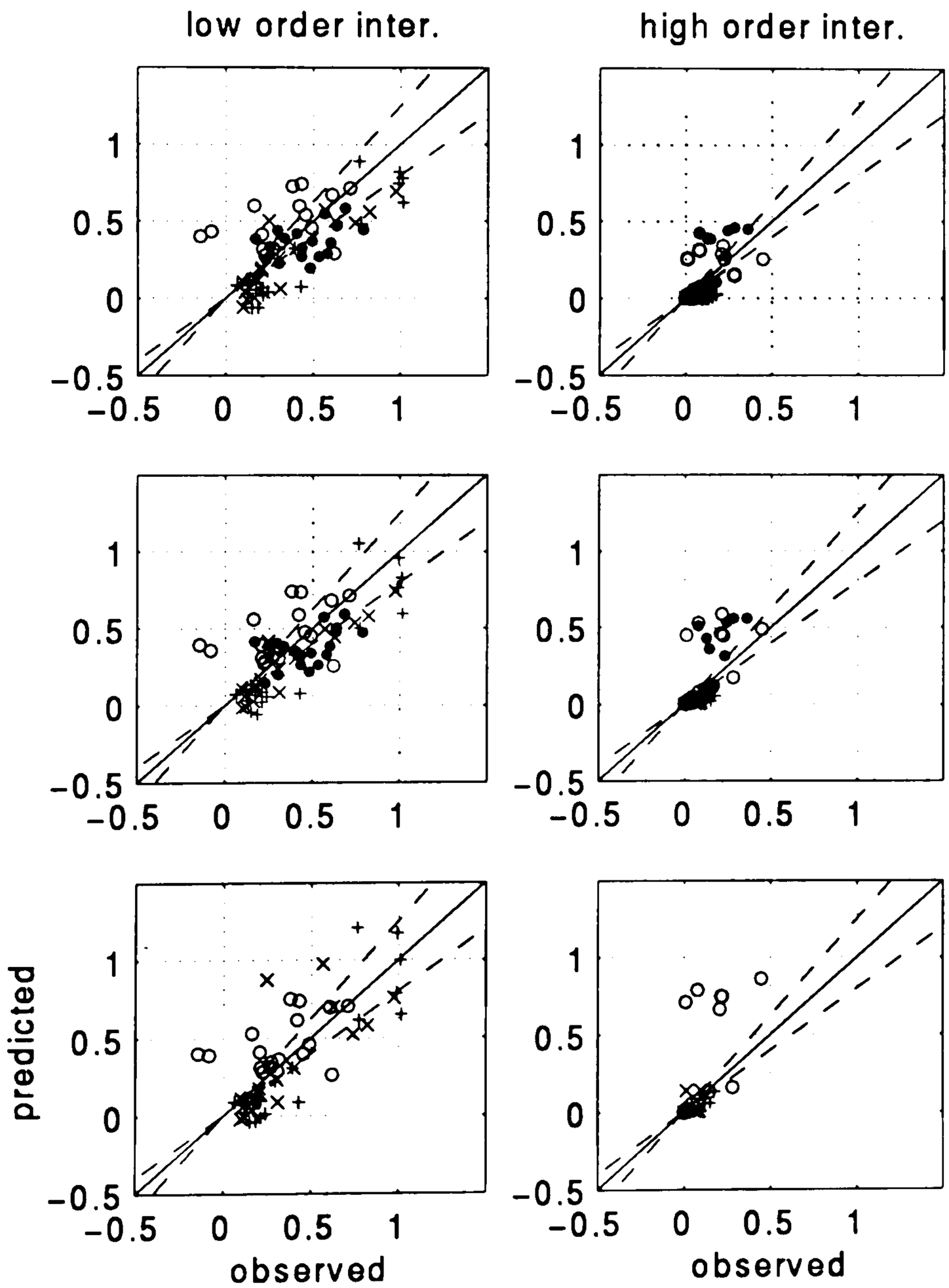

Figure 6.12 Predicted *versus* observed normalised contributions to skewness from (left column) low order interactions, and (right column) high order interactions, for the 4 studied cases. (top panels) ϕ_B = 17°, (middle panels) ϕ_B = 20°, (bottom panels) ϕ_B = 26°. Legend as in figure 6.11.

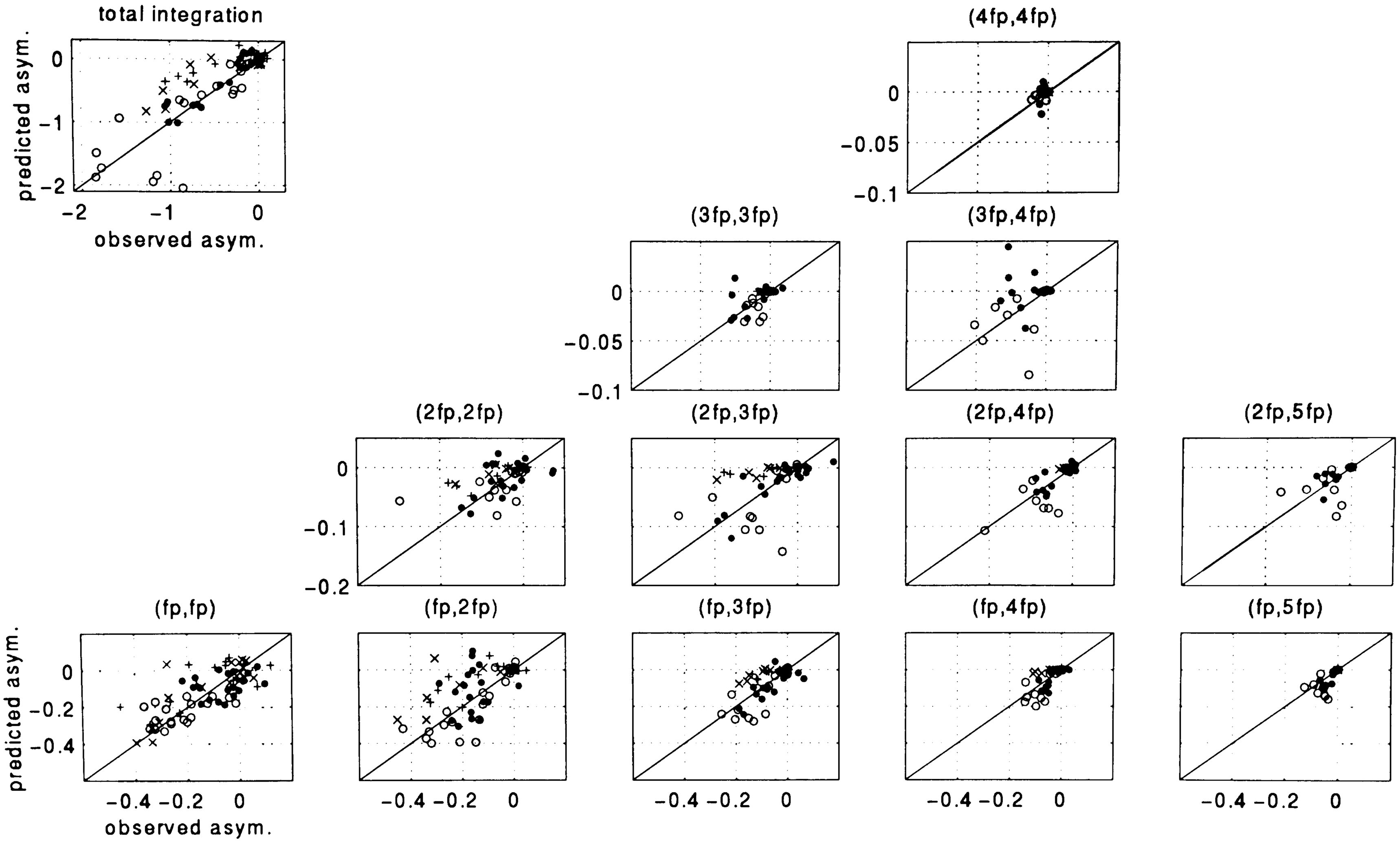

Figure 6.13 Predicted *versus* observed normalised contributions to asymmetry for a selection of 12 triads, for the 4 studied cases. Also shown is the total skewness (panel (1,1)). $\phi_B = 20°$. Legend as in figure 6.11.

Figure 6.12 shows the contribution to skewness from low order interactions, that is (f_p,f_p), $(f_p,2f_p)$, $(f_p,3f_p)$, and $(2f_p,2f_p)$, and high order interactions. The predictions with $\phi_B = 17^\circ$, 20° and 26° are presented. It appears that, for the low order contributions, the scatter remains the same with increasing ϕ_B. In contrast, the over-estimation clearly increases with increasing ϕ_B for the high order contributions. It is also consistently outside the 20% difference limit (dashed line). With $\phi_B = 26^\circ$ and for case A1, the predicted high order contributions become of the same order as the low order contributions.

The contribution to asymmetry for all the data is summarised in figure 6.13, where the predicted versus observed asymmetry arising from each single triads, with $\phi_B = 20^\circ$. The kh dependence of the results is less evident for this quantity.

6.5 Discussion

The results presented in this chapter are estimates of the surface elevation statistics. Estimates of similar statistics for the depth-averaged velocity can be shown to yield the same results, and similar discrepancies between observations and predictions.

The nonlinear transfers of energy amongst low order harmonics are well simulated. The transfers of energy to higher order harmonics are over-estimated. In addition, the bispectral analysis has shown that changes in ϕ_B mostly affect the high order harmonics[3]. Note that this can also be shown with the power spectra. The bispectral analysis shows clearly that the discrepancies observed in chapter 5 arise from the limitation of the model to the simulation of waves with small kh. Despite the extension of the accuracy of the linear dispersion relation for shorter waves, waves with large kh are not simulated accurately.

The skewness is a measure of the (cumulative) amplitude of the harmonics present in the field, while asymmetry depends on the phase shift of the harmonics with respect to the primary wave. In other words, an overestimation of the skewness indicates an overestimation of the amplitude of the harmonics. An overestimation of the asymmetry indicates an overestimation of the phase shift between the primary and its harmonics. Note however that the relationship is not that straightforward since the wrong prediction of the phase shift (i.e. wrong asymmetry) may result in the wrong skewness, and vice-versa.

[3] that is, assuming the direction of energy transfer is e.g. $f_p + 5f_p \rightarrow 6f_p$

Incorrect wave shape prediction is thus the result of the combined effects of incorrect prediction of linear shoaling, intensity of the nonlinear transfers and linear frequency dispersion. Each of these model limitations have been shown to be *kh* related.

Besides the physical limitations of the model, the over-estimation of the super-harmonics generation may be the result of the predictions being purely theoretical. In reality, other processes (leakage to other harmonics, phase shifts, noise, energy dissipation due to viscosity, *etc.*) may occur that may reduce the intensity of the nonlinear transfers.

Finally, the observations from the last three wave gauges (i.e. the capacitance gauges) appear to almost systematically break the trend in the spatial variation of the skewness and asymmetry for A1. It is possible that this is the result of errors in the measurements.

CHAPTER 7 - CONCLUSIONS

7.1 Summary and conclusions

Boussinesq-type models for non-breaking waves are widely used for coastal engineering applications. Their recent extension to the simulation of breaking waves has enlarged their possible range of application. In this thesis, a surf zone Boussinesq-type model was selected and implemented, and its performance was evaluated with high quality, large scale laboratory data. The model validation concentrated on parameters of importance to sediment transport predictions (velocity and wave shape[1] predictions), parameters which were neglected in previous studies of Boussinesq-type models.

Since in the derivation of the Boussinesq equations it is assumed that H/h is small, and since this ratio near the breaking point reaches values close to 1, the extension of Boussinesq models to the surf zone seems inconsistent. Despite this, several authors have extended their Boussinesq model to describe wave breaking without including additional (high order) terms to allow for more nonlinear waves. The resulting surf zone Boussinesq models yield surprisingly good results. This suggests that violation of the weak nonlinearity assumption is not as crucial as one might have expected. In fact, Dingemans (1994) has shown that the accuracy of the frequency dispersion properties is much more critical.

In the surf zone, the increasing intensity of triad interactions results in an increasing generation of super-harmonics, for which the performance of the model is limited in two related respects. Firstly, the incorrect prediction of the wave number mismatch between the primary and bound high harmonics when waves with kh > 4-5 are present results in an incorrect nonlinear transfer of energy. Secondly, if high harmonics with large kh are travelling as free waves, their phase celerity and shoaling are incorrectly predicted.

Using the bispectral analysis, it was shown that the discrepancies between the experimental data and numerical results arose predominantly from the inaccurate treatment of the high order super-harmonics. The exchanges of energy amongst the low order harmonics have been shown to be accurately reproduced. In the case where strong nonlinearities develop, the model tends to over-estimate the transfer of energy to the high order super-harmonics

[1] 'wave shape' encompasses both the surface elevation and the velocity vertical and horizontal asymmetries.

($kh > 5$) by more than 50% (with $\phi_B = 20^o$), and, as a result, yields an incorrect wave shape. It is important to stress that the development of strong nonlinearities results in the violation of both the weak nonlinearity and weak dispersion assumptions.

Another inconsistent aspect of the model transpired during this model validation: with the improved dispersion characteristics, the performance of the model for wave shape prediction was found to be better for the short wave tests compared to the long wave tests. This is unexpected since the model was originally derived for long waves, and subsequently extended to the simulation of shorter waves. Long waves propagating in decreasing water depths (thus becoming increasingly non-dispersive) undergo strong wave-wave interactions, and the resulting super-harmonics, or short waves, cannot be correctly simulated by the model. In other words, long waves, for which the model should perform best, are those that generate the greatest nonlinear exchange of energy. The resulting super harmonics are not treated correctly by the model. This clearly needs to be anticipated when applying the model.

The model, if applied within its (extended) limits, performs very well. The depth-averaged horizontal velocity predictions are promising, even in the surf zone. It was found that, although the velocity tends to be overestimated (by more than 20% in the surf zone), the velocity moments and the undertow are very well reproduced (generally within 20%). The model thus provides a suitable method of calculating these quantities (otherwise evaluated from field measurements) for application to sediment transport prediction.

The improved agreements between the observations and the predictions for the velocity moments, in contrast with the elevation moments for which differences up to 60% are found, suggests that disagreements for the latter may be due to the difficulty to measure surface elevations in the surf zone.

The evaluation of the high order moments has shown that the surface elevation and velocity time series both undergo the same distortions, both qualitatively and quantitatively. The same parameterization for the elevation and velocity moments may thus be applied.

The sensitivity analysis carried out on the empirical breaking parameters has shown that the results are mostly sensitive to the critical wave front slope ϕ_B. In a recent paper, *Madsen et al.* (1997a) looked at the improvements obtained for the wave height and *mwl* by changing the free breaking parameters. It was shown here that similar improvements could be

obtained, and that the sensitivity of the *mwl* and wave height to ϕ_B is moderate. The present study further establishes that the depth-averaged velocity statistics show the same sensitivity to ϕ_B as the elevation statistics, both qualitatively and quantitatively. In addition, it appears that this sensitivity is emphasised for the skewness and kurtosis of elevation and velocity prediction, especially for cases where the generation of higher harmonics is intense. In case A1, increasing ϕ_B so as to improve the wave height predictions resulted in marked over-estimations of the elevation and velocity skewness and kurtosis predictions. In case B1, increasing ϕ_B so as to improve the elevation and velocity skewness and kurtosis predictions resulted in increased over-estimations of the wave height and velocity predictions in the surf zone. The danger is that an effort to optimise ϕ_B for a good fit for the wave height and *mwl* (as proposed by Madsen *et al.*, 1997a) may result in inaccurate wave shape predictions. These are important results in the context of sediment transport predictions.

Ideally, an end-product of this sensitivity analysis would be a set of guidelines for choice of the breaking parameters. This was made difficult by the fact that optimum predictions of different quantities are obtained for different values of ϕ_B. Thus, given the subjectivity involved in selecting optimum values, and given the limited number of cases studied here, this has not been possible. Overall, a ϕ_B of 20^o is recommended.

As a result of the mild slope assumption (invoked by $h_x << \mu$, thus allowing the neglect of h_x^2 , h_{xx} , ... terms), the slope has to be small enough so that the wave properties (wave length) vary little in a distance of the same order as the depth. A consequence of the violation of the mild slope assumption is an unrealistically instantaneous response to water depth changes. Note that in this context, the accuracy of the bathymetry data in terms of small features is superfluous. The mild slope assumption is often overlooked, and the attention is focused on the nonlinearity and dispersion characteristics of the Boussinesq models. In this thesis it has been shown that a violation of the mild slope assumption can lead to substantial errors in the predictions, particularly in terms of wave shape. In particular, for B1 and B2, it has led to the simulation of wave breaking at the incorrect location. For those two cases, the smoothing of the bathymetry, to eliminate the water depth changes to which the waves cannot realistically respond to, has resulted in a better agreement with the data.

Discrepancies between predictions and observations were found to be the combined result of :

- a violation of the model assumptions of weak nonlinearity, weak dispersion[2], balanced nonlinearity and dispersion, and slowly varying bathymetry;
- inherent errors in the measurements;
- differences between the physical and numerical tanks (in particular the reflection from the swash zone and undertow are not simulated in the numerical model);
- numerical errors in the model (truncation errors, boundary conditions, wave generation).

In the cases studied here, these errors are greatest in the surf zone, where the effects of each of these factors (except the last one) are greatest. The cumulative error is typically limited to within 20 % for most quantities. Greater errors were obtained for the elevation moments (up to 60%) and for the depth average velocity (overestimated by up to 40%).

7.2 Future directions

The relative contribution to errors from the violation of the various assumptions inherent in the model has not been established. Recently, some work has been carried out in order to eliminate these assumptions. Models have been produced that allow for (i) higher order improved dispersion, and (ii) higher order non-linearity (for references see section 2.4). This has resulted in the developments of more advanced, but also more complex models, with higher order terms. The evaluation of models with higher order improved dispersion has been theoretical, and no numerical solution has been proposed for these new equations. The equations with higher order non-linearity have been solved in one dimension only, and their application has been limited to small computational domains. However, with the phenomenal progresses made in affordable computer power nowadays, these models are viable. Comparison of the predictions of the present model with (i) those of a fully dispersive model with the same limits on the degree of nonlinearity, and (ii) those of a fully nonlinear model with the same dispersion relation would help determine the relative effects of both these limitations.

The parameterization of the dependence of the skewness, kurtosis and asymmetry on Ur, or on ε and μ, is very attractive as it would provide a means to obtain these quantities which

[2] despite the extension of the accuracy of the linear dispersion relation

eliminates the use of a Boussinesq model and bispectral analysis (both of which are still very time consuming methods). The scatter obtained is still large however. It is possible that inclusion of a dependence on other quantities (e.g. beach slope, number of wave components interacting, *etc.*) may reduce this scatter.

In view of the effects of the violation of the mild slope assumption, it would be interesting to investigate the model behaviour if larger bed slopes are allowed (i.e. if some h_x^2 , h_{xx} , ... terms are retained). It would also be useful to formulate a technique by which the effective bathymetry could be obtained. Recently, with the development of video monitoring of beach evolution, a number of authors (Grilli, 1998; Dalrymple et al., 1998) have proposed means of evaluating the bathymetry from known wave characteristics (for example wave length and period) using *depth inversion* methods. At present, these methods are limited to shoaling waves on monotonically decreasing depths, and are thus not applicable to our case studies. Such developments are very attractive as in the future they could provide a means of determining the effective bottom topography for numerical modelling applications.

Further consideration of wave reflection is required. Two aspects need studying: reflection from the swash zone, which is not simulated by the model, and reflection from the remainder of the slope, present both in the physical and numerical tanks. Note that the latter assumes that reflection does occur from the slope. Further study is recommended in order to evaluate the extent of wave reflection from the swash zone in the laboratory, and its effects on the results, in particular on the wave shape. Also the model's capabilities of reproducing reflection from the slope needs to be evaluated.

As the undertow is not directly simulated by the model, its effects on the hydrodynamics are not accounted for in the numerical solution. Despite this, predictions for the velocity moments are good, which suggests that, in the cases studied here, undertow has little or no effect on the incoming waves. This requires further investigation.

The modelling of wave transformation in the nearshore region is not complete without the simulation of the swash oscillations. The extension to the shoreline of the model does not involve any difficulties as far as physical considerations are concerned. The problem lies with numerical difficulties, in particular with the introduction of a moving boundary. Recently, several approaches were presented to overcome this (sec. 2.4.3), and the

inclusion of such a boundary is recommended. In the context of this study, a direct advantage is that it would allow the simulation of reflection from the swash zone, and thus eliminate the uncertainties introduced with its neglect.

The theoretical and numerical development of models for nonlinear waves has recently accelerated and resulted in increasingly better models. The future is certain to see the flourishing of models capable of accurately modelling wave motion, and, with the improvements achieved in computing technology, these models will become readily available for engineering application. The difficulty in predicting nearshore hydrodynamics lies in the modelling of additional physical effects such as wave breaking, and associated turbulence, bed friction, percolation effects, *etc*. These processes are not fully understood, and are difficult to represent mathematically.

Considering the simplifications involved, the simulation of wave breaking in the model tested in this thesis is most satisfactory. In fact, an(other) interesting contradicting element of the model lies with the simulation of breaking waves. The surface roller concept invoked in the introduction of wave breaking assumes spilling breakers. On the other hand, the restriction of the model to weakly dispersive and weakly nonlinear waves implies that a/L << 1, which tends to characterise waves that break as plunging breakers.

Despite this inconsistency, the model yields relatively good results for both breaker types. This suggests that, in terms of the quantities evaluated in this thesis, plunging and spilling breakers may be evaluated with the same approximation. It is clear however that the turbulence induced in these two breaking modes is fundamentally different, and the mathematical representation of wave breaking, and its incorporation in a hydrodynamic model, still has a long way to go.

Finally, although 2D non-breaking Boussinesq models are now applied in engineering practice, it is rather surprising to note that no validation of these models with field data has been carried out (or documented...). Such testing needs to be done.

REFERENCES

Abbott M.B. and Basco (1985). Computational fluid dynamics. John Wiley & Sons. 425pp

Abbott M.B. and Rodenhuis G.S. (1972). A numerical simulation of the undular hydraulic jump. *Journal of Hydraulic Research* 10/3, 239-257.

Abbott M.B., McCowan A.D. and Warren I.R. (1984). Accuracy of short wave numerical models. *Journal of Hydraulic Engineering* 110 (10), 1287-1301.

Abbott M.B., Petersen H.M. and Skovgaard O. (1978a). Computations of short waves in shallow water. *Proc. 16th Inter.Coast.Eng.Conf. ASCE* 414-433.

Abbott M.B., Petersen H.M. and Skovgaard O. (1978b). On the numerical modelling of short waves in shallow water. *Journal of Hydraulic Research* 16/3, 173-204.

Bailard J.A. (1981). An energetics total load sediment transport model for a plane sloping beach. *Journal of Geophysical Research*. 86, C11, 10938-10954.

Battjes J.A. and Janssen J.P.F.M. (1978). Energy loss and set-up due to breaking of random waves. *Proc. 16th Int. Conf. on Coastal Eng., ASCE*, 569-587.

Beji S. and Battjes J.A. (1994). Numerical simulation of nonlinear wave propagation over a bar. *Coastal Eng*. 23, 1-16.

Berkoff J.C.W., Booij N. and Radder A.C. (1982). Verification of a numerical wave propagation model for simple harmonic linear water waves. Coastal Engineering, 6, 255-279.

Boczar-Karakiewicz B., Bona J.L. and Cohen D.L. (1987). Interaction of shallow-water waves and bottom topography. In *Dynamical problems in continuum physics* (edited by J.L Bona *et al.*). The IMA volumes in Mathematics and its applications, volume 4. Springer-Verlag. 131-176.

Bosboom J., Klopman G., Roelvink J.A. and Battjes J.A. (1997). Boussinesq modelling of wave-induced horizontal particle velocities. *Coastal Eng.*, 32, 163-180.

Bosboom J., Klopman G., Roelvink J.A. and Battjes J.A. (1997). Wave kinematics computations using Boussinesq models. *Proc. 25th Int. Conf. on Coastal Eng., ASCE*, 109-122.

Boussinesq J. (1872). Théorie des ondes et des remous qui se propagent le long d'un canal rectangulaire horizontal. *Journal de Mathématique Pures et Appliquées*, deuxième série, 17, pp55-108.

Brocchini M., Drago M. and Iovenitti (1992). The modelling of short waves in shallow waters. Comparison of numerical models based on Boussinesq and Serre equations. *Proc. 23rd Inter. Coast.Eng.Conf.* ASCE 76-88.

Chen Q., Madsen P.A., Schäffer H.A. and Basco D.R. (1998). Wave-current interaction based on an enhanced Boussinesq approach. *Coastal Engineering* 33, 11-39.

Chen Y. and Liu P.L.-F. (1995). Modified Boussinesq equations and associated parabolic models for water wave propagation. *J. Fluid. Mech.*, 288, 351-381.

Chen Y., Guza R.T. and Elgar S. (1997). Modeling spectra of breaking surface waves in shallow water. *Journal of Geophysical Research*. Pre-print.

Dalrymple R.A., Kirby J.T., Kennedy A.B. and Chen Q. (1998). Determining bathymetry from remotely sensed images. *26th Inter.Coast.Eng.Conf. ASCE* , Abstract.

Deigaard R. (1989). Mathematical modelling of waves in the surf zone. Progress Report No 69, Inst. of Hydrodynamics and Hydraulic Eng., ISVA Techn. Univ. Denmark. 47-60.

Dingemans M.W. (1994). Comparison of computations with Boussinesq-like models and laboratory measurements. prepared for MAST project 1: Waves, G8-M 32pp.

Dingemans M.W. (1997). Water waves propagation over uneven bottoms. Part 2 - Nonlinear wave propagation. Wiley, New York, 965pp.

Doering J.C. and Bowen A.J. (1995). Parametrization of orbital velocity asymmetries of shoaling and breaking waves using bispectral analysis. *Coastal engineering*, 26, 15-33.

Doering J.C. (1985). Wave-wave interaction in the nearshore. Ph D Thesis, Dalhousie University.

Eldeberky Y. and Battjes J.A. (1995). Parametrisation of triad interactions in wave energy models. *Coastal Dynamics*, 140-148.

Eldeberky Y. and Battjes J.A. (1996). Spectral modeling of wave breaking: Application to Boussinesq equations. *Journal of Geophysical Research*, 101, 1253-1264.

Elgar S., Guza R.T., Raubenheimer B., Herbers T.H.C and Gallagher E. (1997). Spectral evolution of shoaling and breaking waves on a barred beach. *Journal of Geophysical Research*. 102, C7, 15797-15805.

Elgar S, Freilich M.H. and Guza R.T. (1990). Model-data comparisons of moments of nonbreaking shoaling surface gravity waves. *J. Geophysical Research* 95/C9, 16055-16063.

Elgar S. and Guza R.T. (1986). Nonlinear model predictions of bispectra of shoaling surface gravity waves. *J.Fluid Mech.* 167, 1-18.

Elgar S. and Guza R.T. (1985a). Shoaling gravity waves: comparison between field observations, linear theory, and a nonlinear model. *J. Fluid Mech.* 158, 47-70.

Elgar S. and Guza R.T. (1985b). Observations of bispectra of shoaling surface gravity waves. *J. Fluid Mech.* 161, 425-448.

Engelund F. (1981). A simple theory of weak hydraulic jumps. Progress Report No 54. Inst. of Hydrodynamics and Hydraulic Eng., ISVA Techn. Univ. Denmark. 29-32.

Freilich M.H. and Guza R.T. (1984). Nonlinear effects on shoaling surface gravity waves. *Phil. Trans. R. Soc. Lond.* A 311, 1-41.

Freilich M.H., Guza R.T. and Elgar S.L. (1990). Observation of nonlinear effects in directional spectra of shoaling gravity waves. *J. Geophysical Research* 95/C6, 9645-9656.

Grilli S.T., Skourup J. and Svendsen I.A. (1989). An efficient boundary element method for nonlinear water waves. *Engng Anal. with Boundary elements*, 6, 97-107.

Grilli S.T. (1998). Depth inversion in shallow water based on properties on nonlinear shoaling waves. *26th Inter.Coast.Eng.Conf. ASCE* , Abstract.

Guza R.T. and Thornton E.B. (1985). Velocity moments in the nearshore. *Journal of Waterway, Port, Coastal and Ocean Engineering*, 111 (2), 235-256.

Hanes D.M. and Huntley D.H. (1986). Continuous measurments of suspended sand concentration in wave dominated nearshore environment. *Continental Shelf Res.*. 6 (4), 585-596.

Hasselmann K., Munk W. and MacDonald G. (1963). Bispectra of ocean waves. In *Time series analysis* (edited by M.Rosenblatt). Wiley, New York, 125-139.

Hauguel A. (1980). A numerical model of storm waves in shallow water. Proc. 17th Inter. Coastal Eng. Conf. 746-762,

Hibberd S. and Peregrine D.H. (1979). Surf and run-up on a beach: a uniform bore. *J.Fluid Mech.*, 95/2,323-345.

Hughes S.A. (1993). Physical modules and laboratory techniques in coastal engineering. Advanced Series on Ocean Engineering, Volume 7 (edited by P.L.-F. Liu). World Scientific. pp 567

Karambas Th.V., Southgate H.N. and Koutitas C. (1995). A Boussinesq model for inshore zone sediment transport using an energetics approach. *Coastal Dynamics '95*, ASCE, 841-849.

Karambas Th.V. and Koutitas C. (1992). A breaking wave propagation model based on the Boussinesq equations. *Coastal Engineering* 18, 1-19.

Kim Y.C. and Powers E.J. (1979). Digital bispectra analysis and its application to nonlinear wave interactions. *IEEE Trans. Plasma Science*, 1, 120-131.

King D.B.Jr (1991). Studies in oscillatory flow bedload sediment transport. Ph D Thesis, University of California, San Diego (Scripps), 183pp.

Korteweg D.J. and de Vries G. (1895). On the change of form of long waves advancing in a rectangular canal, and on a new type of long stationary waves. *Phil. Mag. and J. of Science* 39, pp422-443.

Kraus N.C. and McKee Smith J.,1994. SUPERTANK Laboratory Data Collection Project. US Army Corps of Engineers, Waterways Experiment Station, TR CERC-94-3.

Larsen J. and Dancy H. (1983). Open boundaries in short wave simulations - A new approach. *Coastal Eng.* 7, 285-297.

Long R.R. (1964). The initial-value problem for long waves of finite amplitude. *Journal of Fluid Mechanics* 20, 161-176.

Madsen P.A., Sørensen O.R. and Schäffer H.A. (1994). Time domain modelling of wave breaking, runup and surf beats. *Proc. 24th Inter.Coast.Eng.Conf. ASCE* 399-411.

Madsen P.A., Sørensen O.R. and Schäffer H.A. (1997a). Surf zone dynamics simulated by a Boussinesq type model. Part I. Model description and cross-shore motion of regular waves. *Coastal Eng.* 32, 255-287.

Madsen P.A., Sørensen O.R. and Schäffer H.A. (1997b). Surf zone dynamics simulated by a Boussinesq type model. Part II. Surf beat and swash oscillations for wave groups and irregular waves. *Coastal Eng.* 32, 289-319.

Madsen P.A. and Sørensen O.R. (1992). A new form of the Boussinesq equations with improved linear dispersion characteristics.Part 2:a slowly-varying bathymetry. *Coastal Engineering* 18, 183-204.

Madsen P.A. and Sørensen O.R. (1993). Bound waves and triad interactions in shallow water. *Ocean Eng.* 20/4, 359-388.

Madsen P.A. and Warren I.R. (1984). Performance of a numerical short-wave model. *Coastal Engineering* 8, 73-93.

Madsen P.A., Murray R. and Sørensen O.R. (1991). A new form of the Boussinesq equations with improved linear dispersion characteristics. *Coastal Engineering* 15, 371-388.

Masuda A. and Kuo Y.Y. (1981). A note on the immaginary part of bispectra. *Deep sea Res.*, 28,213-222.

McCowan A.D. (1987). The range of application of Boussinesq type numerical short wave models. *AIRH Congress* 378-384.

McCowan A.D. (1985). Equation systems for modelling dispersive flow in shallow water. 21st *IAHR Congress*, Melbourne, Australia 51-57.

McCowan A.D. (1981). Developments in numerical short wave computations. *Fifth Australian Conference on Coastal and Ocean Eng.*

McCowan A.D. (1978). Numerical simulation of shallow water waves. *Fourth Australian Conference on Coastal and Ocean Eng.*

Mei C.C. (1989). The applied dynamics of ocean surface waves. Wiley, New York, 740pp

Mei C.C. and Unlüata U. (1972). Harmonic generation in shallow water waves, in R.E. Meyer (ed)Waves on Beaches and Resulting Sediment Transport, Academic Press, New York. pp 181-202.

Nielsen P. (1992). Coastal bottom boundary layers and sediment transport. Advanced Series on Ocean Engineering, Volume 4 (edited by P.L.-F. Liu). World Scientific. 324 pp.

Nwogu O. (1993). Alernative form of Boussinesq equations for nearshore wave propagation. *Journal of Waterway,Port,Coastal and Ocean Engineering* 119/6, 618-638.

Nwogu O. (1996). Numerical prediction of breaking waves and currents with a Boussinesq model. *Proc. 25th Inter.Coast.Eng.Conf. ASCE.* 4807-4820.

Ozanne F, Chadwick A.C., Huntley D.A. and McKee Smith J. (1997). Wave transformation in the nearshore zone: comparison between a nonlinear model and large scale laboratory data. *Coastal Dynamics '97*, ASCE, 295-304.

Peregrine D.H. (1967). Long waves on a beach. *Journal of Fluid Mechanics* 27/4, 815-827.

Peregrine D.H. (1972). Equations for water waves and the approximations behind them, in *Waves on Beaches and Resulting Sediment Transport* (editor R.E. Meyer), Academic Press, New York. pp 95-121.

Petit H.A.H., Tönjes P., van Gent M.R.A. and van den Bosch P. (1994). Numerical simulation and validation of plunging breakers using a 2D Navier-Stokes model. *Proc. 24th Inter.Coast.Eng.Conf. ASCE* 511-524.

Rakha K.A., Deigaard R., Madsen P.A., Brøker I. and Rønberg J.K. (1996). Simulation of coastal profile development using a Boussinesq wave model. *Proc. 25th Inter.Coast.Eng.Conf. ASCE.* 3048-3061.

Russell P.E. (1993). Mechanisms for beach erosion during storms. Offprint, University of Plymouth.

Schäffer H.A., Madsen P.A. and Deigaard R. (1993). A Boussinesq model for waves breaking in shallow water. *Coastal Engineering* 20, 185-202.

Schäffer H.A. and Madsen P.A. (1995). Further enhancements of Boussinesq-type equations. *Coastal Engineering* 26, 1-14.

Schaper H. and Zielke W. (1984). A numerical solution of Boussinesq type wave equations. Proc. 19th Inter. Coastal Eng. Conf. 1057-1072,

Sørensen O.R., Schäffer H.A., Madsen P.A. and Deigaard R. (1994). Wave breaking and induced nearshore circulations. *Proc. 24th Inter.Coast.Eng.Conf. ASCE* 2583-2594.

Stive M.J.F (1980). Velocity and pressure field of spilling breakers. *Proc. 17th Int. Conf. on Coastal Engineering, ASCE.* 547-566.

Svendsen I.A., Yu K. and Veeramony J. (1996). A Boussinesq breaking wave model with vorticity. *Proc. 25th Inter.Coast.Eng.Conf. ASCE* 1192-1204.

Svendsen I.A. and Putrevu U. (1996). Surf zone hydrodynamics. in *Advances in coastal and ocean engineering*, edited by P.L.-F. Liu, Volume 2, World Scientific.

Svendsen I.A. (1984a). Wave heights and setup in a surf zone. *Coastal Eng.* 8, 303-329.

Svendsen I.A. (1984b). Mass flux and undertow in a surf zone. *Coastal Eng.* 8,347-365.

Svendsen I.A. (1974). Cnoidal waves over a gently sloping bottom. *Ph D Thesis, Techn. Univ. of Denmark*, ISVA series Paper 6, 181pp.

Wei G. and Kirby J.T. (1995a). Time-dependent numerical code for extended Boussinesq equations. *J.Waterway,Port,Coastal and Ocean Engineering* 121/5, 251-261.

Wei G. and Kirby J.T. (1995b). A coastal processes model based on time-domain Boussinesq equations. *Coastal Dynamics*.

Wei G., Kirby J.T., Grilli S.T. and Subramanya R. (1995). A fully nonlinear Boussinesq model for surface waves. Part1. Highly nonlinear unsteady waves. *J. Fluid Mech.* 294, 71-92.

Whitham G.B. (1974). Linear and non-linear waves. Wiley, New York

Witting J.M. (1984). A unified model for the evolution of non-linear waves. *Journal of Computational Physics* 56, 203-236.